Dissertation

submitted to the

Combined Faculties for the Natural Sciences and for Mathematics

of the Ruperto - Carola - University of Heidelberg, Germany

for the degree of

Doctor of Natural Sciences

presented by

M.Sc. Filip Tomasz
born in: Ilava, Slovakia

Oral examination: June 29th, 2005

Investigation of Exclusive Photoproduction of $\eta - \rho^0$ and $\pi^0 - \rho^0$ Meson Pairs at HERA

Referees: Prof. Dr. Karlheinz Meier
Prof. Dr. Ulrich Uwer

Abstract

Exclusive photoproduction of $\eta - \rho^0$ and $\pi^0 - \rho^0$ meson pairs is studied with the H1 detector at HERA. The analysis is based on data recorded in 1996-1997 and 1999-2000 data taking periods, corresponding to an integrated luminosity of 76.21 $\mathtt{pb}^{-1}$. The η and π^0 mesons are identified via their photonic decays in the backward calorimeter SpaCal, and the ρ^0 meson via its dominant decay into $\pi^+\pi^-$ pairs in the central tracking system of the H1 detector. The scattered proton or its remnant is not measured but is separated by a large rapidity gap from the ρ^0 meson.

The cross section for photoproduction of $\eta - \rho^0$ meson pairs is measured at an average photon-proton center of mass energy of $W \approx 208\,\mathtt{GeV}$ in the kinematical region defined by the rapidities of the η and ρ^0 mesons in the laboratory system: $-3.5 < Y_\eta^{lab} < -2$ and $-1.5 < Y_{\rho^0}^{lab} < 1.5$, photon virtualities $Q^2 < 0.01\,\mathtt{GeV}^2$ and inelasticity $0.3 < y < 0.65$. The cross section obtained is $\sigma^*(\gamma p \to \eta\rho^0 X) = (3.5 \pm 1.4(stat) \pm 1.3(syst))$ $\mathtt{nb}$. Due to the limited statistics no definitive statement is made to explain this process but the measured differential distributions are consistent with a contribution from Pomeron exchange.

In the analysis of photoproduced $\pi^0 - \rho^0$ meson pairs no significant ρ meson signal can be extracted. Therefore only an upper limit of the cross section is given as $\sigma^*(\gamma p \to \pi^0\,\rho^0\,X) < 8.6$ $\mathtt{nb}$ at 95 % confidence level, measured at an average photon-proton center of mass energy of $W \approx 180\,\mathtt{GeV}$ in the kinematical region defined by the rapidities of the π^0 meson and the $\pi^+\pi^-$ pair in the laboratory system: $-3.5 < Y_{\pi^0}^{lab} < -2$ and $-1.5 < Y_{\pi^-\pi^+}^{lab} < 1.5$, photon virtualities $Q^2 < 0.01\,\mathtt{GeV}^2$, and inelasticity $0.3 < y < 0.65$.

Zusammenfassung

Die exclusive Photoproduktion von $\eta - \rho^0$ und $\pi^0 - \rho^0$ Mesonpaaren wurde mit dem H1 Detektor bei HERA untersucht. Die Analyse basiert auf Daten, die in den Jahren 1996-2000 aufgenommen wurden und die einer integrierten Luminosität von 76.21 $\mathtt{pb}^{-1}$ entschprechen. Die η und π^0 Mesonen wurden durch ihre Zerfälle in zwei Photonen im Rückwärtskalorimeter (SpaCal) von H1 nachgewiesen, die ρ^0 Mesonen über ihren dominanten Zerfall in $\pi^+\pi^-$ Paare im zentralen Spurdetektor von H1. Das gesteuerte Proton oder seine Fragmente wurden nicht gemessen, allerdings wurde eine Rapiditätslücke zwischen dem zentralen ρ^0 und der Richtung des auslaufenden Protons gefordert.

Der Wirkungsquerschnitt für $\eta - \rho^0$ Photoproduktion wurde bei einer mittleren γp Schwerpunktsenergie von $W_{\gamma p} \approx 208\,\mathtt{GeV}$, einer Photon-Virtualität von $Q^2 < 0.01\,\mathtt{GeV}^2$ und einer Inelastizität von $0.3 < y < 0.65$ für die Rapiditätsbereiche $-3.5 < Y_\eta^{lab} < -2$ und $-1.5 < Y_{\rho^0}^{lab} < 1.5$ (definiert im Laborsystem), bestimmt. Er hat den Wert $\sigma^*(\gamma p \to \eta\rho^0 X) = (3.5 \pm 1.4(stat) \pm 1.3(syst))$ $\mathtt{nb}$. Aufgrund der geringen Statistik kann keine definitive Aussage über den zugrundeliegenden Reaktionsmechanismus gemacht werden. Die gemessenen differentiallen Verteilungen sind aber konsistent mit einem Beitrag vom Austausch der Pomerančuk-Trajektorie (Pomeron).

In der Analyse der Produktion von $\pi^0 - \rho^0$ Paaren konnte kein signifikantes ρ^0-Signal gefunden werden. Für den Wirkungsquerschnitt kann deshalb nur eine obere Grenze angegeben werden: $\sigma^*(\gamma p \to \pi^0\,\rho^0\,X) < 8.6$ $\mathtt{nb}$ (95% CL) bei einem mittleren $W \approx 180\,\mathtt{GeV}$, einer Photon-Virtualität von ebenfalls $Q^2 < 0.01\,\mathtt{GeV}^2$ und einer Inelastizität von $0.3 < y < 0.65$. Auch der kinematische Bereich, in dem die Mesonen nachgewiesen wurden, ist der gleiche wie bei $\eta - \rho^0$ Photoproduktion: $-3.5 < Y_{\pi^0}^{lab} < -2$ und $-1.5 < Y_{\pi^+\pi^-}^{lab} < 1.5$.

Contents

List of Figures

List of Tables

Introduction

This theses is devoted to the analysis of exclusive photoproduction of $\eta - \rho^0$ and $\pi^0 - \rho^0$ meson pairs at HERA using the H1 detector. Photoproduction processes in *ep*-scattering are induced by an interaction of quasi real photons emitted from colliding electron with the colliding proton. The scattered electron is detected at small angles to ensure low photon virtualities ($Q^2 \sim 0\,\mathtt{GeV}^2$). The hadronic structure of the photon allows it to interact with the proton via the strong interaction. The majority of these interaction are 'soft' processes in which particles produced have small ($< 1\,\mathtt{GeV}$) transverse momenta.

In a special class of soft interactions at high γp centre of mass energies ($W_{\gamma p} \approx 200\,\mathtt{GeV}$) the majority of the exclusive processes is induced by the exchange of a colour singlet object carrying quantum numbers of vacuum. Such processes are called diffractive. Due to the absence of a hard scale in soft processes perturbative quantum chromodynamics is not applicable in these reactions since the strong coupling constant is in general not small enough for the perturbation series to converge. Therefore phenomenological models based on Regge theory are used to describe the properties of these processes. In these models the colourless objects are attributed to the Pomerančuk trajectory ('Pomeron'). Experimentally, such interactions are characterized by a large rapidity gap without particle production between the hadronic final state and the proton or its remnant.

Double meson photoproduction can, in terms of Regge phenomenology, be interpreted in two ways: Either a high mass mesonic state is diffractively produced which subsequently decays or the meson measured in the central region of the detector is generated in a fusion process of a mesonic trajectory originating at the photonic vertex, and the Pomeron originating at the proton. In this analysis an attempt is made to distinguish between these mechanisms.

For the analysis presented, events were selected where the proton (or a low-mass proton excitation) loses only a very small fraction of its incoming momentum and escapes undetected in the beam pipe. This system is separated by a large rapidity region from the centrally produced ρ^0 meson whose decay products – $\pi^+\pi^-$ pairs – are measured in the central tracking system. The photons originating from η and π^0 meson decays are detected in the electromagnetic calorimeter SpaCal. The scattered electron is detected in the electron tagger which restricts the virtuality of the photon to $Q^2 \lesssim 0.01\mathtt{GeV}^2$.

Chapter 1

The H1 Experiment at the HERA Collider

In this chapter a short introduction to the HERA (Hadron-Elektron-Ring-Anlage) collider is presented. Also the H1 detector, which was used to measure the data analyzed in this thesis, and its components are briefly described.

1.1 The e-p Collider HERA

The collider HERA is situated at the DESY[1] laboratory in Hamburg. It is the first electron[2]-proton storage ring. At HERA protons and electrons are accelerated and stored in beam pipes of 6.3 km in circumference. The electrons are accelerated by superconducting cavities to 27.6 GeV and stored in the ring via conventional magnets. Also the protons are accelerated by superconducting cavities to 820[3] GeV but to store them in the ring super-conducting magnets with 4.6 T are needed. The maximum of the designed specific luminosity for the period 1994-2000 was $1.4 \cdot 10^{30}$ $\mathrm{cm}^{-2}\mathrm{s}^{-1}$. Protons and electrons are kept in bunches which subsequently collide with a period of 96 ns. The electron bunch length, width and height are about 10 mm, 0.3 mm and 0.04 mm, respectively, the proton bunch parameters are 110 mm, 0.3 mm and 0.08 mm. However not all bunches are collided. Non colliding bunches are known as a pilot bunches. They are used to estimate background from beam interactions with the residual gas in the beam pipe ('beam-gas' events) and those from collisions with the beam wall ('beam-wall' events).

1.2 The H1 Detector

The H1 detector is designed to measure the direction, energy and charge of the particles coming from electron-proton collisions, in almost hermetic coverage around the beam axis. The main obstruction comes from the beam pipe itself. The right handed H1 coordinate system is defined by the incoming proton direction to be $+z$ with the origin defined by the nominal interaction point. The positive y axis is oriented vertically upwards. The polar, θ, and azimuthal, ϕ, angles are defined correspondingly, such that θ is equal to zero in the

[1] Deutsches Elektron SYnchrotron

[2] between 1994 and 2000 HERA was mainly running with positrons. Only in 1998 and the first half of 1999, electrons were used. The term electron refers to both electrons and positrons in this thesis.

[3] from 1994 to 1997, the proton beam energy was 820 GeV, from 1998 to 2000, the energy was 920 GeV.

proton beam direction and ϕ is positive for positive values of y. Due to the asymmetry in the beam energies the H1 detector is asymmetric since the majority of particles produced are boosted along the proton direction, which is referred to as the forward region in the rest of the thesis.

The layout of the main components of the H1 detector [1] is shown in fig. 1.1. The reconstruction of the events relies on two particle detection methods: tracking to measure the momentum and the charge of the charged particles, calorimetry to measure the energy of the charged and also neutral particles. The central [2] and forward [3] tracking devices are located around the beam pipe [1]. They are situated in the strong field of 1.15 T produced by a superconducting coil [6] with a radius of 3 m, allowing charge and momentum to be measured from the curvature of the path. This field is compensated by another superconducting coil [7] in order not to influence the HERA beam. The electromagnetic and hadronic calorimeters [4], [5], [12], [13] surrounding the tracking devices are situated outside the trackers. Detection of muons is provided by the instrumented iron [10] in the central region and by muon chambers [9] and a toroid equipped by drift chambers [11] which are located in the most outside part of the H1 detector.

The H1 detector is completed with small angle electron and photon detectors dedicated to the luminosity measurement placed in the HERA tunnel. In the proton direction the devices for the measurement of the scattered proton and neutral particles are placed: the proton remnant tagger, the forward proton spectrometer and the neutron calorimeter.

1.3 The H1 Tracking System

The H1 tracking system shown in fig. 1.2 provides simultaneously trigger information, track reconstruction and particle identification. Track reconstruction is predominantly reliant on the drift chambers and triggering on the multiwire proportional chambers (MWPCs). Particle identification is based on measurements which are sensitive to the particle velocity, its charge and its momentum. The momentum and charge are measured from the curvature of the particle traversing in the magnetic field. The variable measured depending on the velocity is the loss of the particle energy over the distance traveled (dE/dx).

The MWPCs consist of many anode wires lying between cathode pads, with the volume in between filled by gas and spanned by an electrical field. The field is strong enough for very fast amplification of the ionization caused by the passage of charged particles. It allows very fast response times to obtain a trigger information. The charge accumulated on the sense wires is proportional to the initial ionization. In H1 this rôle is taken by the central inner proportional and central outer proportional chambers. The spatial resolution of the MWPCs is limited by the spacing of wires, and more accurate measurement can be performed via drift chambers.

In the drift chambers a set of sense anode and cathode wires are strung in a uniform electric field. In this field the electrons from ionization process move at nearly constant velocity towards the anode sense wires. Knowing the drift velocity, a precise measurement of the drift time allows to calculate the position of the passing particle with higher accuracy than the distance between the wires in the MWPC. Therefore the drift chambers are used for a precise spatial and momentum measurement of the tracks. The momentum

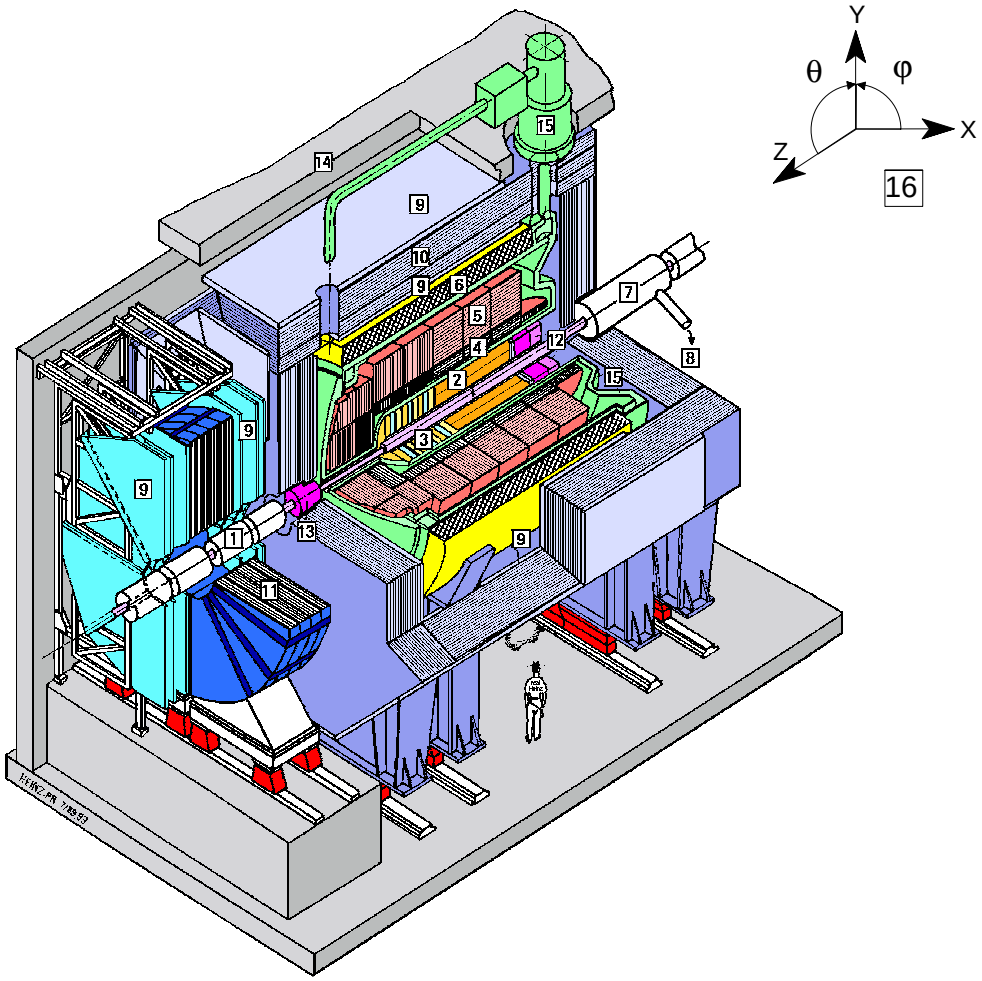

1	Beam pipe and beam magnets	8	Helium supply for 7
2	Central track detectors	9	Muon chambers
3	Forward track detectors	10	Instrumented iron yoke
4	Electromagnetic LAr calorimeter	11	Forward muon toroid
5	Hadronic LAr calorimeter	12	SPACAL and Backward DC
6	Superconducting coil (1.15 T)	13	Plug calorimeter
7	Compensating magnet	14	Concrete shielding
		15	Liquid argon cryostat
		16	H1 coordinate system

Figure 1.1: *Schematic view of the H1 detector.*

is measured from the curvature of the particle in the magnetic field. This rôle in H1 is performed by the central jet chambers, central inner and central outer z-chambers.

The tracking detectors are split into three major components - the central tracking detectors (CTD), the forward tracking detectors (FTD) and the backward drift chamber (BDC). They cover the angular range of $7° < \theta < 177.5°$. In particular, the CTD covers the range of $15° < \theta < 165°$, the FTD covers the range of $7° < \theta < 25°$ and the BDC covers the range of $153° < \theta < 177.5°$.

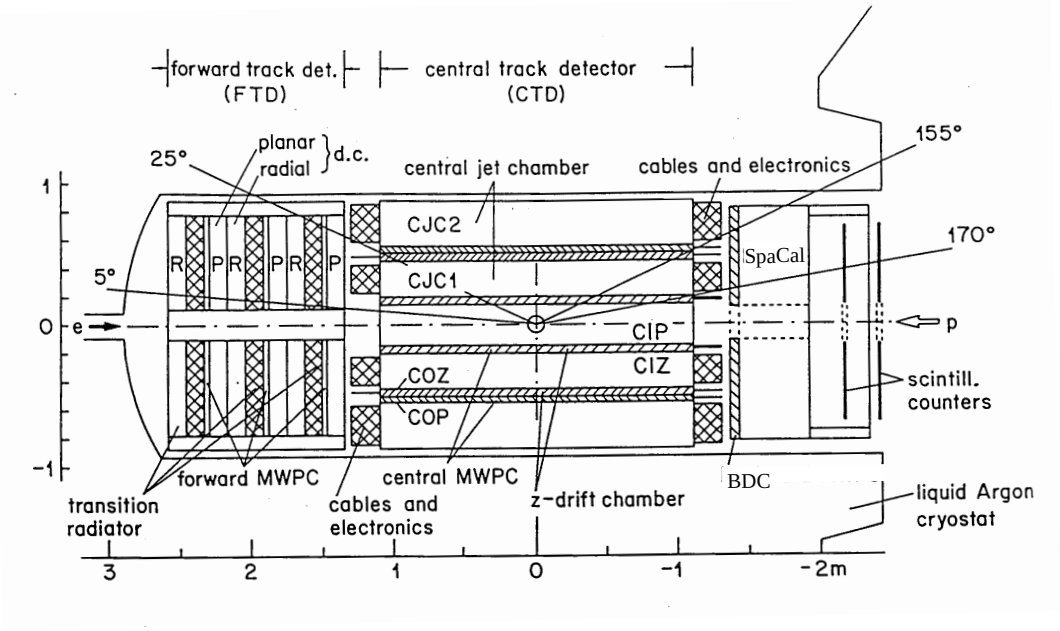

Figure 1.2: *An $r - z$ view of the H1 tracking system*

The Central Tracking System

The central tracking system consists of six chambers: the central inner proportional chamber (CIP), the central inner z-chamber (CIZ), the inner central jet chamber (CJC1), the central outer z-chamber (COZ), the central outer proportional chamber (COP), and the outer central jet chamber (CJC2). In the $r - \phi$ plane they are shown in fig. 1.3.

The two largest drift chambers CJC1 and CJC2 [2] are designed to give a most accurate measurement of the track position in the $r - \phi$ plane. They are equipped by a plane of anode sense wires strung parallel to the beam line with two adjacent cathode planes also made of wires. The chamber cell extends azimuthally from the sense wire plane to two adjacent cathode wire planes, and radially over the full CJC1 or CJC2 span. CJC1 consists of 30 cells with 24 radial sense wires each. CJC2 is made of 60 cells each containing 32 wires. The cells are tilted by approximately 30° so that the tracks pass through more than one cell which improves the track position resolution. Setting the cathode wires of each cell to a voltage proportional to the distance from the sense wire plane allows to create a uniform electric field and hence a constant drift velocity over almost the entire chamber

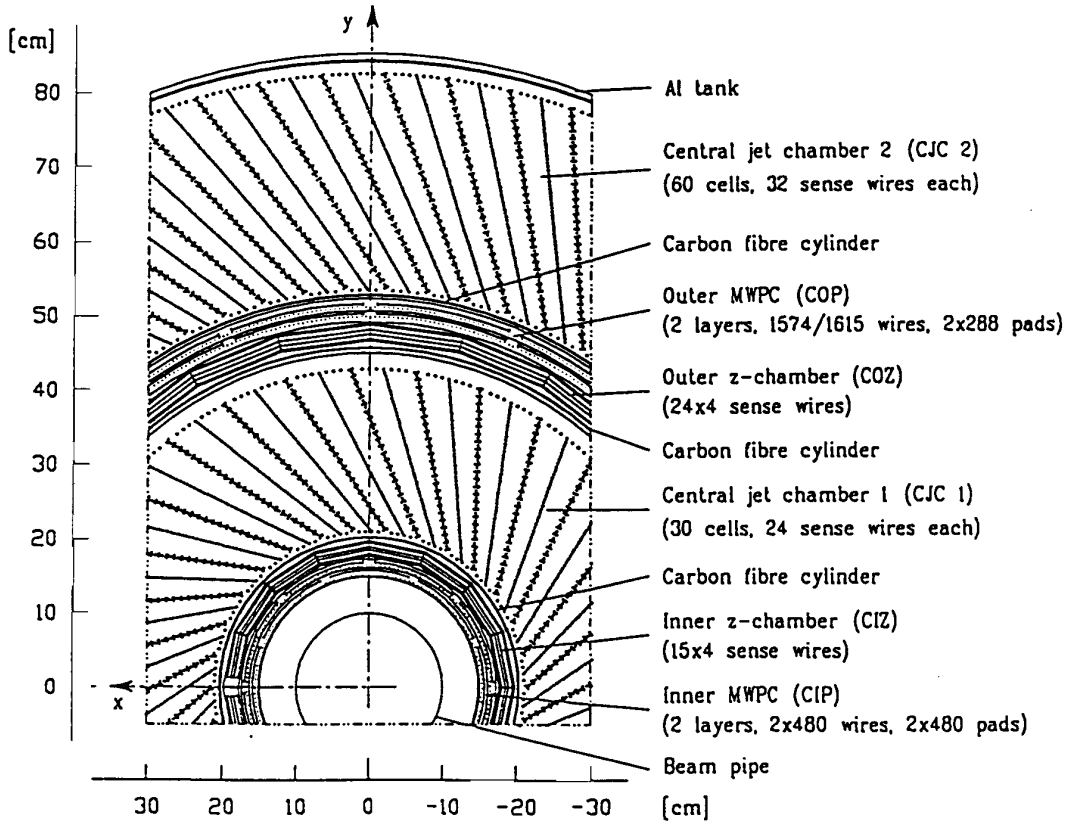

Figure 1.3: Section of the H1 central tracking system.

cell. In most of the drift region the electric field is constant to better than 1 %. Also at the first and last sense wires the inhomogeneity is below 2 %. For the drift velocity of 50 mm/μs at the nominal voltage in the gas used (a mixture of Ar-CO_2-CH_4) the resolution in the $r-\phi$ plane is known to 170 μm. Because of the high magnetic field, only the tracks with transverse momentum above 0.15 GeV will pass through both chambers. The momentum of the particle is measured with a relative resolution of $\sigma_p/p \leq (0.01 \cdot p)\,\mathrm{GeV}^{-1}$, the relative resolution of the $\mathrm{d}E/\mathrm{d}x$ measurement is 10 %, the absolute angular resolution is $\sigma_\theta = 21$ mrad and the spatial resolution is about 170 μm in the $r-\phi$ plane and 22 mm in the z direction.

The track recognition in the CJC is based mainly on the precise $r-\phi$ information. To improve the measurement in the z direction the track system is complemented by two thin drift chambers, the central inner and central outer z-chambers [3]. CIZ and COZ cover the polar angular range of $16° < \theta < 169°$ and $25° < \theta < 156°$. Their sense wires are perpendicular to the beam axis. The z-coordinate calculated from the drift time results in a resolution of 300 μm in the z direction and 30 – 60 mm in the $r-\phi$ plane. As a result the vertex resolution is 2 mm and the measurement of θ is improved to $\sigma_\theta = 2$ mrad. The combined track measurement of all four drift chambers improves the relative momentum resolution to $\sigma_p/p \approx (3 \times 10^{-3}\, p)\,\mathrm{GeV}^{-1}$ and $\sigma(\mathrm{d}E/\mathrm{d}x) \sim 6\,\%$.

The last two components of the central tracking system are MWPCs: the central inner

	θ [°]	$\sigma_{r-\phi}$ [mm]	σ_z [mm]	σ_θ [mrad]	$\frac{\sigma_p/p}{p}$ [GeV^{-1}]	$\sigma_{\frac{dE}{dx}}$ [%]
CJC1+CJC2	15–165	0.17	22	21	< 0.01	10
CIZ+(COZ)	16(25)–169(156)	30-60	0.3	2		
CJC+CIZ +COZ	–	0.17	0.3	2	3×10^{-3}	6
CIP	9–171					
COP	25–155					

Table 1.1: *H1 central tracker properties: Coverage of the polar angle θ, the spatial resolution in $r-\phi$, z and θ, momentum and dE/dx resolution.*

and outer proportional chambers [4] providing the z-vertex trigger. While the CIP is the innermost component, the COP is located between CJC1 and CJC2. The angular coverage of the CIP is $9° < \theta < 171°$, while COP covers the region of $25° < \theta < 155°$. They provide only trigger information and have no impact on the final track reconstruction. The information from CIP and COP is combined with that from a MWPC in the FTD to produce a z-vertex trigger.

In this thesis the selection of tracks is based on the central tracker devices only. The main parameters of these devices are summarized in tab. 1.1.

The Forward Tracking System

The forward tracking detector (FTD) [5] consists of three identical supermodules. Each of them includes three differently oriented planar drift chambers, a multiwire proportional chamber (MWPC), a transition radiator and a radial drift chamber. The layout of the FTD is shown in fig. 1.2 in the left-hand part. For the track measurement only the planar and radial drift chambers are used. The transition radiators are designed for the separation of electrons and pions. The trigger information is provided by MWPCs.

The Backward Drift Chamber

The backward drift chamber [6] is located in front of the electromagnetic part of the SpaCal calorimeter in order to provide an accurate measurement of the scattered electron. The spatial resolution in the radial coordinate is $\sigma(r) = 0.4\,\text{mm}$ and in the $r-\phi$ plane $\sigma(r-\phi) = 0.8\,\text{mm}$.

1.4 Calorimetry

At H1 there are four subdetectors which provide energy measurement: The liquid Argon Calorimeter (LAr), the backward Spaghetti Calorimeter (SpaCal), the Tail Catcher (TC) and the Plug Calorimeter (PLUG). In 1998, in the very backward region the VLQ calorimeter [26] was installed to detect scattered electrons at very low virtualities[4]: $0.15\,\text{GeV}^2 \lesssim$

[4] virtuality is defined as: $Q^2 = -(k-k')^2$, where k and k' are fourmomenta of the incoming and scattered electron, respectively. See also definition (2.6)

$Q^2 \lesssim 0.4\,\mathrm{GeV}^2$. The layout of the five calorimeters is shown if fig. 1.4. The two main calorimeters, SpaCal and LAr, cover the pseudorapidity range in the laboratory system of $-3.8 < \eta < 3.6$. The TC measures the energy leakage from the main calorimeters and the PLUG extends the acceptance in the forward region.

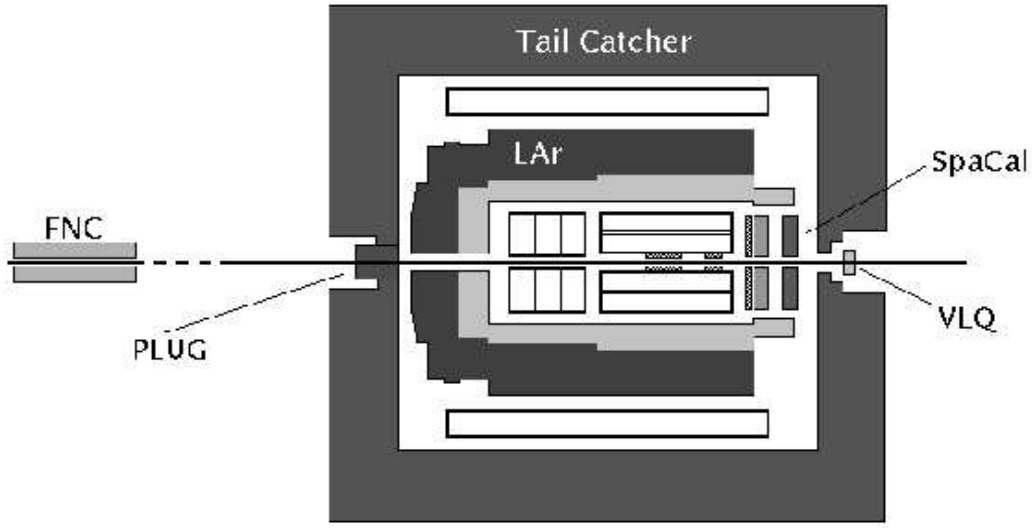

Figure 1.4: *Schematic view of the H1 calorimetry system.*

The principle of the energy measurement is based on the complete deposition of the particle energy in the passive material, so called absorbers, and a sample material where the deposition of energy is measured.

The shower induced by electromagnetically interacting particles like electrons or photons is governed by a combination of bremsstrahlung ($e \to e\gamma$) of electrons and pair production ($\gamma \to ee$) processes of the photons. Secondary particle production continues until the energy of the photons falls below the pair production threshold, and energy losses of the electrons other than bremsstrahlung start to dominate. The number of particles produced in the shower is proportional to the energy of the incident particle, $N \propto E_0$ [27], therefore the measurement of the total ionization in the sampling material provides a measurement of the incident particle energy. The electromagnetic interaction in a material is characterized by the radiation length, X_0 describing the behavior of the longitudinal development of the shower, and by the Molière radius R which defines the lateral spread of the shower. 95% of the shower energy in a homogeneous calorimeter is contained in a cylinder of radius $2R$ around the shower axis. A set of contiguous cells with non-zero energy deposition is called a cluster.

Strongly interacting particles passing through material lose energy via elastic and also inelastic scattering. The hadron showers are governed in their longitudinal structure by the nuclear interaction length λ and by the transverse momenta of secondary particles as far as the lateral width is concerned. Since for most materials $\lambda \gg X_0$ and $\langle p_t^{\mathrm{had}} \rangle \gg \langle p_t^{\mathrm{emc}} \rangle$

hadron showers are longer and wider. Part of the energy of the incident hadron is spent to break up nuclear bonds. This fraction of the energy is invisible in hadron calorimeters. Further energy is lost by escaping particles like neutrinos and muons as a result of hadron decays. Since the fraction of lost binding energy and escaping particles fluctuates considerably, the energy resolution of hadron calorimeters is systematically worse than that of electromagnetic ones.

1.4.1 The Liquid Argon Calorimeter

The largest calorimeter of H1 is the Liquid Argon Calorimeter (LAr) [7]. It is a non-compensating sampling calorimeter designed to measure the final state hadrons and the scattered electrons at very high Q^2, above 100 $\mathtt{GeV}^2$. It covers the full azimuthal angular region and the polar angle region $4^\circ < \theta < 154^\circ$. It is placed in a large cryostat inside the magnet solenoid which reduces the amount of dead material through which the particles must pass. The LAr is divided into the inner electromagnetic (EMC) and the outer hadronic parts (HAC).

Both sections use liquid argon as the sampling medium. The relatively high density of the liquid argon allows large ionization, and there is no need of charge amplification in an avalanche process. In the case of EMC, 2.4 $\mathtt{mm}$ thick plates of lead are used as absorbers with a similar gap size filled with liquid argon. The total thickness of the EMC varies between 20 (in backward direction) and 30 (in forward direction) radiation lengths. The stainless steel absorption plates in the HAC are 16 $\mathtt{mm}$ thick with 5 $\mathtt{mm}$ spacing filled with liquid argon. The total depth of both sections corresponds to 4.5 λ in the backward region and 8 λ in the forward region. The LAr is highly segmented with a total of approximately 45000 cells.

The energy resolution of the electromagnetic section is $\sigma_{emc}(E)/E \approx 12\%/\sqrt{E[\mathtt{GeV}]} \oplus 1\%$. The resolution of the hadronic LAr was determined to be $\sigma_{had}(E)/E \approx 50\%/\sqrt{E[\mathtt{GeV}]} \oplus 2\%$. By comparing the energy of electrons obtained from the momentum measurement by the tracking system and the energy measured by EMC, the electromagnetic energy scale is known to the level of 3%. The hadronic energy scale is known to approximately 4%. Since a response of the hadronic part to hadrons is about 30% smaller than the response to electrons of the same energy, the calorimeter is non-compensating.

1.4.2 The Spaghetti Calorimeter

The main purpose of the **Spa**ghetti **Cal**orimeter (SpaCal) [11] is to measure the energy of scattered electrons in the low Q^2 regime ($100 > Q^2 > 1$ $\mathtt{GeV}^2$). The SpaCal is situated in the backward region of the H1 detector (see figure 1.4) and is divided into two sections: the electromagnetic (EM) and hadronic (HA) one. It is (like the LAr calorimeter) a non-compensating sampling calorimeter in which the absorber consist of lead sheets with grooves into which scintillating fibres are laid used as the sampling medium. The light collected in the fibres is amplified by photomultiplieres (PMTs). The PMTs have to operate in the 1.2 $\mathtt{T}$ magnetic field created by the H1 solenoid, and so Hamamatsu fine-mesh-dynode types were chosen [21]. They provide a typical gain of 10^4.

The EM SpaCal covering the angular range of $153^\circ < \theta < 177.5^\circ$ consists of 1192 cells of lateral size of $40.5 \times 40.5\,\mathtt{mm}^2$. 2340 scintillating fibres with 0.5 $\mathtt{mm}$ in diameter laid in

26 grooved lead plates build up one EM cell. The active length of the cells is 250 mm with a lead:fibre ratio of 2.27 : 1. This yields a radiation length of 9.1 mm and 27 radiation length in total. The HA section is similar to the EM one but has fewer, 136, and larger, $120 \times 120\,\mathrm{mm}^2$, cells with a lead:fibre ratio of 3.4 : 1. The smaller granularity of the HA cells reflects the greater lateral size of hadronic showers. A characteristic transverse shower scale related to the Molière radius is 2.55 cm for the EM part and 2.45 cm for the HA part.

	EM SpaCal	HA SpaCal
nominal z position	-1500 mm	-2000 mm
number of cells	1192	136
Pb/Fibre Ratio	2.3 : 1	3.4 : 1
Fibre diameter	0.5 mm	1 mm
Cell size	$40.5 \times 40.5\,\mathrm{mm}^2$	$120 \times 120\,\mathrm{mm}^2$
Active length	25 cm	20 cm
Radiation length	0.91 cm	0.85 cm
Interaction Length	25 cm	20 cm
Molière Radius	2.55 cm	2.45 cm
PMT Gain at $\sim 1T$	$\sim 10^4$	$\sim 2 \times 10^4$
Spatial resolution	$(4.4/\sqrt{E} + 1.0)$ mm at centre $(3.8/\sqrt{E} + 1.0)$ mm at border	not measured
Time resolution, σ_t	0.38 ± 0.03 ns	0.83 ± 0.02 ns

Table 1.2: *Parameters of the SpaCal calorimeter*

The energy resolution of the EM part has been measured to be $\sigma_{em}(E)/E \approx 7.5\%/\sqrt{E[\mathrm{GeV}]} \oplus 1\%$ [12]. The depth of the EM and HA parts correspond to one interaction length, λ, for each detector. The hadronic resolution of the combined HAD and EM sections is $\sigma_{had}(E)/E \approx 30\%/\sqrt{E[\mathrm{GeV}]}$ [98]. The difference between the data and the simulation from QED Compton events, $ep \to ep\gamma$, [97] gives a relative energy scale uncertainty (data versus simulation) of 3% for a 5 GeV and 0.5% for a 27 GeV electron, respectively. The absolute energy scale uncertainty varies from 6% for 5 GeV and 1% for 27 GeV electron, respectively. These uncertainties reflect the known systematic uncertainties on the reconstruction of angles as well as the dead material in front of the calorimeter.

The spatial resolution for the impact point at the centre of a cell is $(\sigma_x^{em} = 4.4/\sqrt{E[\mathrm{GeV}]}+1)$mm and $(\sigma_x^{ha} = 3.8/\sqrt{E[\mathrm{GeV}]}+1)$mm [39] at the border of two cells. The better spatial resolution of a cluster with the impact point at the border of two cells is caused by the more equally shared energy between the cells. All the main properties of the SpaCal are summarized in table 1.2.

The SpaCal ToF/AToF window: The very fast response of the photomultiplieres used with a very precise time measurement allows the SpaCal trigger to veto non $e-p$ background. The separation of $e-p$ events from background is performed by the so called time-of-flight (ToF) window which defines the time window in which the time of the energy deposition is consistent with that produced from the interaction point. Upstream proton induced background (mainly due to beam-gas and beam-wall interactions) is dis-

tinguished from particles coming from an *ep* interaction by its time of arrival with respect to the bunch crossing clock. Because of the position of the SpaCal, proton induced background will reach the calorimeter before the products of the interaction by twice the time of flight from the calorimeter to the interaction region - 10 ns in the case of the EM part. This is shown in fig. 1.5 - the deposition of energy from background is much higher than from interaction products. This huge background would also cause a huge event rate which is avoided by using the time information in the trigger branch to veto these events by the ToF window, see fig. 1.6. The ToF window is adjustable in 0.4 ns steps via programmable delays which set the the start (for each channel) and the stop (common for 16 channels) of the window. The energy deposition which arrives within this window is referred to as 'in time' (ToF). Energy depositions outside this window are referred to as 'out of time' (AToF).

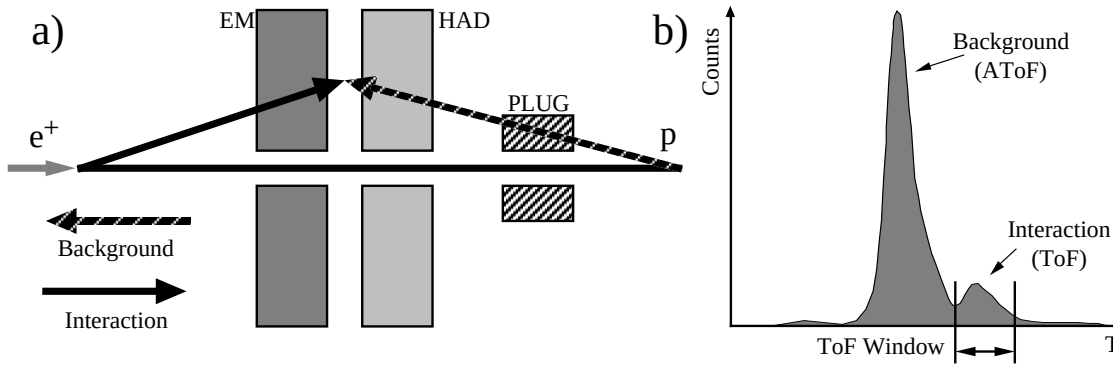

Figure 1.5: *In a) the path of the proton induced background and the path of a particle from the interaction point of protons and electrons is sketched. The path of the particles from background events traversing the SpaCal is shorter than that one from the interaction point. This situation as reflected in the SpaCal time measurement is shown in b). The earlier, much higher peak corresponds to the background events, while the lower and later peak corresponds to $e-p$ events. To suppress the huge background (by factor ~ 100) the time-of-flight (ToF) time window was defined for $e-p$ events.*

The arrival time information is provided to the SpaCal trigger chain via constant fraction discriminators (CFDs). According to this information either analogue sums of 2×2 channels are created to provide the information for an inclusive electron trigger (IET) or an energy sum of 16 channels to provide trigger bits for AToF trigger elements, see fig. 1.6. The adjustment of the ToF window is crucial for the correct separation of the $e-p$ physics from the background. A calibration procedure with the results for 1996-2000 data taking period described in [20] was developed in the framework of this thesis and can be used to adjust the ToF window.

The CFDs also provide information for the Time to Digital Converter (TDC) system [22, 23]. The CFD was designed to eliminate a problem of the crossing the threshold at the different times for the pulses with different amplitude which is known as a slewing

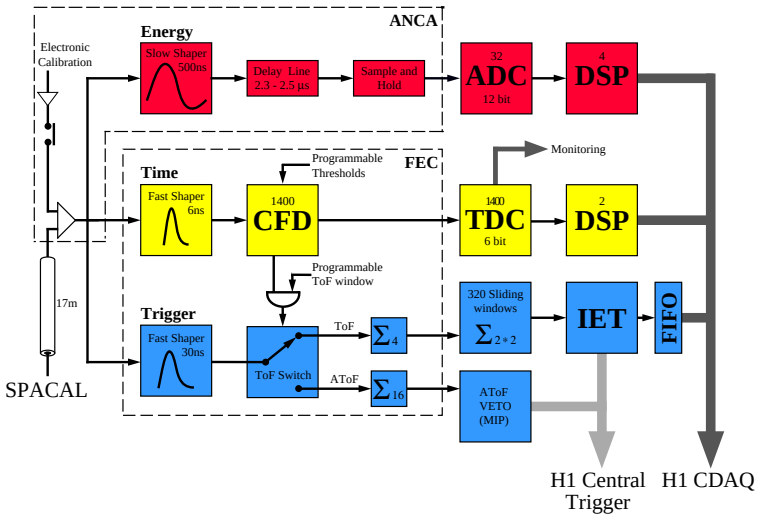

Figure 1.6: *Block scheme of the SpaCal electronics chain: Energy, time and trigger.*

	θ [°]	X_0	λ	$\frac{\sigma_E}{E[\mathrm{GeV}]}$	$\Delta E/E$
LAr (EM)	4–154	20–30		$12\%/\sqrt{E} \oplus 1\%$	3%
LAr (HAD)	4–154		$(4.5-8)^*$	$50\%/\sqrt{E} \oplus 2\%$	4%
SpaCal (EM)	153–177	27	1	$7.5\%/\sqrt{E} \oplus 1\%$	$(1-4)^{**}\%$
SpaCal (HAD)	159–178	28	1	$56(30)\%/E$	–

Table 1.3: *Properties of the SpaCal and LAr calorimeters: coverage of the polar angle θ, thickness in units of radiation lengths X_0 and in units of nuclear interaction lengths λ, the relative energy resolution σ_E/E, where E is measured in* GeV *and the energy scale uncertainty [9, 39, 40, 41].*
$56(30)\%$ *the value in the brackets denotes the resolution for the EM+HAD SpaCal parts.*
* *denotes the depth for HAD+EM LAr parts.*
** *an energy scale uncertainty of* 1% *for an electron of* 27 GeV *and* 4% *for a* 4 GeV *electron.*

effect. At the very low pulsamplitudes (equivalent to $< 500\,\mathrm{MeV}$) this effect is evident. This effect causes a shift for the time measurement of low energetic particles. The method developed in [20] corrects this shift and improves the time measurement for low energetic particles to be close to that measured for high energetic electrons at the beam test at SPS: $(0.38 \pm 0.03)\,\mathrm{ns}$ and $(0.83 \pm 0.02)\,\mathrm{ns}$ [98].

The most important parameters of the SpaCal and LAr calorimeters, used for cluster identification in this thesis are summarized in tab. 1.3.

1.4.3 The Tail Catcher and the Plug Calorimeter

The tail catcher (TC) [8] calorimeter provides a coarse measurement of the hadronic showers leaking out of the LAr. It covers almost the full solid angle. The energy resolution is 100% with a scale uncertainty, determined from cosmic muon data, of around 35%.

The plug calorimeter (PLUG) is designed to minimize the gap in acceptance for the energy flow between the beam pipe and the most forward part of the LAr calorimeter and therefore covers the extremely forward direction: $0.6° < \theta < 3°$. The energy resolution is estimated to be $\sigma(E)/E \approx 150\%/\sqrt{E[\mathrm{GeV}]}$ [10].

1.5 The Luminosity System

The main task of the luminosity system [14] (fig. 1.7) is to provide a fast online and precise offline luminosity measurement. The accurate determination of the luminosity is essential for the precise cross section determination of physics processes. The luminosity is measured via the rate of a process with a well known cross section, the Bethe-Heitler QED process [15]: $ep \to ep\gamma$.

The luminosity system is built from two Čerenkov detectors, the electron Tagger (eTag) and the Photon Detector (PD). The system is shown in fig. 1.7. The eTag is situated in the tunnel in electron direction at $z = -33\,\mathrm{m}$ from the nominal interaction point. The PD is located at $z = -103\,\mathrm{m}$. Due to the proton bunch structure the offline determined luminosity is corrected for the contribution from proton satellite bunches. In addition to the luminosity measurement the eTag provides trigger information for photoproduction events.

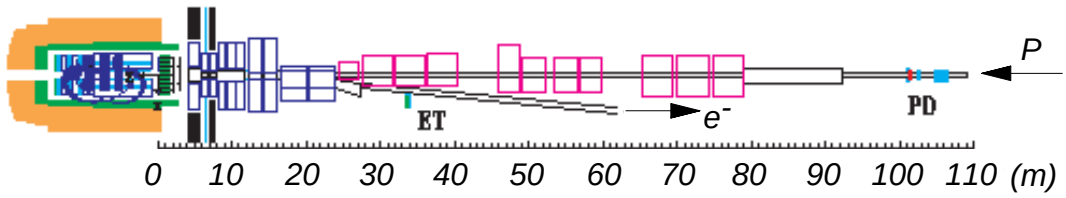

Figure 1.7: *The H1 luminosity system.*

1.6 The Very Forward Detectors

A number of detectors are placed in the accelerator tunnel in the proton beam direction. They are designed to detect the proton final state or its remnant, and are used to study diffraction. The proton remnant tagger is situated 24 m from the nominal interaction point in the forward direction. It covers the pseudorapidity range of $6 \lesssim \eta \lesssim 8$. The forward proton spectrometer (FPS) [16] consists of two stations located at 81 m and 90 m in the

proton direction from the nominal interaction point. They are designed to measure the final state protons in diffractive interactions at very low angles. The FPS has a small acceptance region for the protons which scatter at the angles lower than 0.5 mrad. The forward neutron calorimeter placed at 106m [17] detects neutral particles produced at angles of less than 0.8 mrad.

1.7 Further devices

1.7.1 The Muon System

The H1 muon system consists of two main detectors: The central muon detector (CMD) or 'instrumented iron' (also used as a tail catcher) and the forward muon detector (FMD) which are described in more detailed in [13].

1.7.2 The H1 Time-of-Flight System

The H1 Time-of-Flight System (ToF) [69] has been designed to distinguish background events from the physics interactions according to their time. The ToF systems, constructed from plastic scintillator, are located near the beam-pipe in the backward endcap of the return yoke (BToF), within the PLUG calorimeter (PToF) and near the FMD (FToF). In addition, the 'Veto Wall', a set of scintillators positioned behind the return yoke, detects particles from the proton beam-halo. This is a shower of mainly muons produced in the inelastic collisions of protons with residual gas.

1.8 Triggering and Data Acquisition

The aim of the trigger system is to separate physically interesting events from non-interesting *ep* processes and background arising due to interactions of the proton beam with the beam pipe or residual gas. Another reason for building the trigger system is the very fast bunch crossing interval of 96 ns. During that time the readout of all detector components is not possible due to the much longer response of the slowest subdetectors. A layered trigger system [73, 74] with three levels (L1, L2 and L4) is employed to solve that problem by buffering the information from subdetectors in a pipe line and making a decision whether to keep or to reject the event. The L1 and L2 trigger levels are online hardware triggers, L4 is an online software trigger. The software trigger level L3 has not been implemented yet. Each trigger level needs some time to make a decision, therefore the input rate is limited. The concept of the H1 trigger level is shown in fig. 1.8

Trigger Level L1

Almost each subdetector provides a trigger information coded in the so called 'trigger elements' which are logically combined (via 'AND' and 'OR') in 'subtriggers'. The latency of L1 is appear 2 μs. The decision to keep or to reject the events is based on the subtriggers. If an event is accepted at least by one subtrigger the pipelining is stopped, and the signal is passed to the second trigger level (L2).

Depending on the rate of events passing a subtrigger, they may be prescaled in order to control the output rate of the L1 trigger level. A prescale of d for a subtrigger means

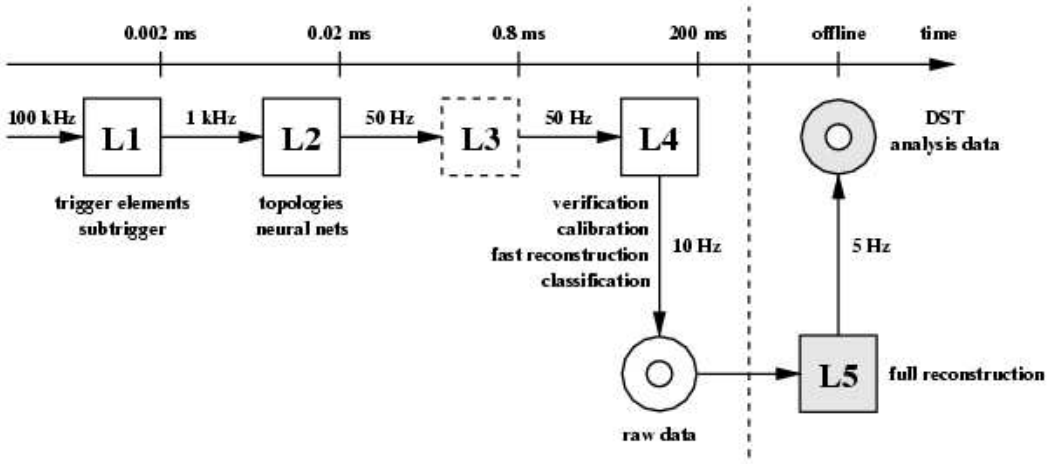

Figure 1.8: *The H1 trigger system*

that only every d-th event fulfilling the subtrigger conditions passes the trigger level L1. The trigger decision before prescaling is called 'raw subtrigger' and afterwards 'actual subtrigger'. The effect of the prescaling is taken into account by weighting the events in the data [75]. L1 typically reduces the rate from $\sim 100\,\mathtt{kHz}$ to $\sim 1\,\mathtt{kHz}$.

Trigger Level L2

The L2 trigger is divided into two sections: the topological (L2TT) [18] and the neural network (L2NN) trigger [19]. They use additional, more detailed, information from almost every subdetector. If a L1 subtrigger is to be validated by an L2 trigger condition and this condition is not fulfilled the event does not pass the trigger level L2. By this way the trigger level L2 reduces the event rate down to $50\,\mathtt{Hz}$.

Trigger Level L4

The L4 trigger is a multiprocessor farm performing a full reconstruction of the events passing L1 and L2. On the basis of this reconstruction further selection of the data is performed. A trigger verification in 1996 and 1997 mimicked the L1 trigger conditions which made the L1 and L4 trigger condition not independent. Therefore during the data taking period in 1998 the verification in its original sense was removed. In 1996 an event with at least one validated subtrigger was sufficient to pass the L4 trigger level. In 1997 the so called 'physics finders' (mainly for soft physics processes) and 'hard scales' (e.g. event with high p_t jets) were introduced. If an event did not fulfill any of the hard scales, like a track with high transverse momentum, it had to pass one of the finders, depending on the verified subtriggers. The event which did not fulfill any of the hard scales and also did not pass the corresponding finder, is according to its topology downscaled by by the so called L4 weights. In the data taking period 1998-2000 the classification was performed via finders and hard scales on L4. All data passing the L4 are permanently stored in the so called 'raw data' stream.

Trigger Level L5

After passing L4 the events are again fully reconstructed by the H1 reconstruction software H1REC [64] using updated calibration information. Until 1997 L5 also sorted the events into the classes - groups of events exhibiting similar physics signatures. The events assigned to one of the classes are written to Production Output Tapes (POTs) and a compressed format, Data Summary Tapes (DSTs). In 1998 the classification was moved to the L4 trigger level to decrease the amount of raw data. A summary of the requirements which the events have to fulfill in order to pass levels L1-L5 for the different data taking periods is given in table 1.4.

period	1996	1997	1999 – 2000
L1	L1 actual subtrigger	L1 actual subtrigger	L1 actual subtrigger
L2	(L2TT or L2NN)	(L2TT or L2NN)	(L2TT or L2NN)
L4	trigger verification	trigger verification hard scales ‖ finders	hard scales ‖ finders classification
event is stored to raw data stream			
L5	classification	classification	
event is stored to POTs and DSTs			

Table 1.4: *Requirements which the events have to fulfill in order to pass the trigger levels L1 - L4 for the data taking periods 1996-2000. L2TT and L2NN conditions have to be fulfilled only in the case if it is required by the subtrigger.*

1.8.1 L1 and L2 Trigger Elements

In the following the most relevant trigger elements used in this analysis are discussed.

- **SpaCal IET trigger:** the Inclusive Electron Trigger (IET) [24, 25] for the electromagnetic section provides the SpaCal trigger elements on the first trigger level. It employs the energy summed over 4×4 EM neighboring cells read out in the time-of-flight (ToF) window which selects the events from *ep* interaction. To avoid trigger inefficiencies from clusters with an impact point close to the edge of the 4×4 cells, the energy sum is performed in overlapping sliding windows. They are compared with three adjustable thresholds. During normal data taking periods in the years 1996-2000 the thresholds were: 0.5, 2, and 6 GeV. The IET trigger system is divided in two regions, central and outer, separated by a rectangle $-16 < x < 8$ cm and $-8 < y < 16$ cm. The trigger elements used in this analysis are:

  $$\begin{array}{lll} IET\_cen\_2, & IET > 1 & \text{with a threshold of 2 GeV} \\ IET\_cen\_3, & IET > 2 & \text{with a threshold of 6 GeV}, \end{array}$$

  where IET_cen_2 and IET_cen_3 denote IET trigger elements which require an energy deposition in at least one sliding window in the inner SpaCal region to be larger than 2 and 6 GeV, respectively. $IET > 1$ and $IET > 2$ denote IET trigger

elements which require an energy deposition in at least one sliding window in the outer SpaCal region to be larger than 2 and 6 GeV, respectively.

- **SpaCal R trigger:** The SpaCal also provides information to the second trigger level that is more granular in geometry than the IET trigger on the first level. In the topological trigger L2TT the following trigger elements are formed: R10, R20 and R30 which demand an energy deposition with a radial distance from the beam line greater than 10, 20 and 30 cm, respectively. Only the two last elements are used in this analysis.

- **zVtx trigger:** The zVtx trigger is a trigger system of the first trigger level and uses information from the central (CIP and COP) and forward (first layer of the FTD) multiwire proportional chambers to obtain the position of the event vertex in the z-direction. The trigger element $zVtx\_sig$[5] provided by this system is used in this analysis.

- **DCRϕ trigger element:** The DCRϕ trigger is also a trigger subsystem of the first level trigger. It uses ten of 56 sense wires of the CJC (seven of CJC1 and three of CJC2) and compares the digitized hits to a total of 10000 predefined masks in the $r - \phi$ plane. The only trigger element employed in this analysis, provided by the subsystem, is: DCRϕ_Thigh which requires at least one track with a transverse momentum greater than ~ 0.8 GeV.

[5] in the rest of the thesis the shorter notation $zVtx$ will be used

Chapter 2

Theoretical Overview

In this chapter, the theoretical foundations of the lepton-hadron and hadron-hadron interactions are reviewed. In the first part the kinematics and the kinematic regions of $e-p$ scattering at HERA are explained. In the second part an overview of diffraction in hadron-hadron interactions and in photoproduction at HERA is given. Finally, the phenomenological model of Regge theory is introduced.

2.1 Electron Proton Scattering at HERA

At HERA electrons[1] and protons are brought to collision with four-momenta $k = (E_e, \boldsymbol{k})$ and $p = (E_p, \boldsymbol{p})$ respectively:

$$k = (27.55, 0, 0, -27.55)\,\text{GeV} \quad ; \tag{2.1}$$

$$p = (820, 0, 0, 820)\,\text{GeV}\ , \text{ for the data taking period } 1994-1997 \text{ and} \tag{2.2}$$

$$p = (920, 0, 0, 920)\,\text{GeV}\ , \text{ for the data taking period } 1998-2000. \tag{2.3}$$

The incident energies of the colliding particles allow in general the exchange of a single boson V^* which can be a photon (γ) or Z^0 in the case of neutral current scattering, or a $W^{\pm}$ in charged current scattering. The processes are schematically shown in fig. 2.1.

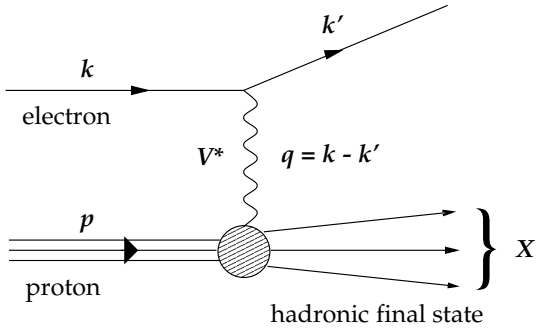

Figure 2.1: *Schematic diagram of the scattering of an electron off a proton.*

The outgoing hadronic final state is generically labeled X, which may be the original proton if the scatter is elastic, or a more complex object, if the scatter is inelastic.

[1] In the following the term electron is also used for positron for simplicity.

The kinematics of the event is parametrized in terms of the Lorentz invariant quantities s, W, Q^2, x, y and t, defined as:

- The square of the centre of mass energy of the `electron-proton` system:

$$s = (p + k)^2 \tag{2.4}$$

  which for the proton beam energies of 920 and 820 `GeV` has values of 102400 $\texttt{GeV}^2$ ($\sqrt{s} \approx 318\,\texttt{GeV}$) and 90200 $\texttt{GeV}^2$ ($\sqrt{s} \approx 300\,\texttt{GeV}$), respectively.

- The squared centre of mass energy of the $\gamma -$ `proton` system is equivalent to the invariant mass squared of the hadronic final state:

$$W^2 = (q + p)^2 \tag{2.5}$$

- The four-momentum transfer, q^2, is defined as:

$$q^2 = (k - k')^2 = -Q^2 \tag{2.6}$$

  where the quantity Q^2 represents the virtuality of the exchanged boson. It can also be interpreted as a measure of the strength of the interaction. By means of the Heisenberg uncertainty principle it is related to the resolution, i.e. a photon can resolve distances down to $\sim 1/\sqrt{Q^2}$.

- Bjorken's [91] dimensionless variable x:

$$x = \frac{Q^2}{2\,pk} \tag{2.7}$$

  in the infinite momentum frame of the proton is the longitudinal fraction of the proton momentum carried by the interacting parton.

- The second dimensionless Bjorken variable is the inelasticity, y. In the rest frame of the proton it gives the relative amount of energy transferred from the electron to the proton.

$$y = \frac{pq}{pk}\,. \tag{2.8}$$

- A further variable describing the four-momentum transfer is introduced in analogy to the virtuality Q^2, but referring to the proton vertex:

$$t = (p - X)^2\,. \tag{2.9}$$

  In the case where only one boson is exchanged, $t = q^2 = -Q^2$.

To characterize single particle quantities, 'rapidity' and 'pseudorapidity' are used which are defined as:

$$Y = \frac{1}{2}\, ln\frac{E + p_z}{E - p_z} \quad \text{and} \tag{2.10}$$

$$\eta = -ln(tan(\theta/2))\,, \tag{2.11}$$

respectively. E denotes a particle's energy, p_z its momentum component parallel to the beam axis and θ its angle w.r.t. the beam axis. The advantage of rapidity is Lorentz invariance of rapidity differences. The advantage of pseudorapidity is its dependence on

the polar angle θ only. Neglecting the mass of the particle ($m/E, m/p \to 0$) or for massless particles, rapidity and pseudorapidity of the particle are equal.

Assuming that the masses of the incoming particles are small compared to the centre of mass energy, the four variables s, x, y and Q^2 defined in equations (2.4) – (2.6) obey the relation

$$Q^2 = xys\,. \tag{2.12}$$

At fixed s the inclusive differential cross section can be completely described in terms of two independent variables which uniquely determine the kinematics and are usually x and Q^2 [103]:

$$\frac{\mathrm{d}^2\sigma(ep \to eX)}{\mathrm{d}x\,\mathrm{d}Q^2} = A\left[\frac{y^2}{2}xF_1(x,Q^2) + (1-y)F_2(x,Q^2) \pm (y - \frac{y^2}{2})xF_3(x,Q^2)\right]\,, \tag{2.13}$$

where $A = 4\pi\alpha_{elm}^2/xQ^4$ for electron with the electromagnetic coupling constant α_{elm}. F_i are the structure functions of the proton. F_1 and F_2 are related to the charge and magnetic moment of the partons in proton, respectively. F_3 is generated by the parity violating interactions which means it is non-zero for weak interactions.

2.2 Kinematical Regimes

The kinematical regimes at HERA can be characterized by two variables: transverse momentum of the particles in the final states, p_t, and the four-momentum transfer squared Q^2. Both variables separate the processes into two classes. The variable p_t defines soft and hard processes. The variable Q^2 distinguishes between the photoproduction and deep-inelastic scattering (DIS) regimes. The kinematical regions defined are sketched in figure 2.2 and described in the following:

- Soft processes are characterized by an energy scale in the order of the hadron size $R \sim 1\,\mathtt{fm}$ which means that p_t^2 and the square of the momentum transfer are generally small: $\sim 1/R^2$ which is in the order of a few hundreds MeV. From a theoretical point of view, the presence of the large scale make the calculations of these processes non-perturbative, and perturbative quantum chromodynamics (QCD) is not applicable. The approach which has been adopted since the 60's to describe soft processes is Regge theory [76, 52, 78].

- Hard processes are characterized by a hard energy scale. In this processes the momentum transfer and p_t^2 are large (> 1 GeV). This allows to use perturbative QCD.

- The photoproduction processes are characterized via an energy scale defined by Q^2 which is in the order of the hadron size $R \sim 1\,\mathtt{fm}$. In the photoproduction regime the photon virtuality of the photon $Q^2 \ll 1\,GeV^2$ and the photons may be considered as real.

- The regime of $Q^2 > 1\,\mathtt{GeV}^2$ is referred to as deep inelastic scattering (DIS). A virtual photon in DIS processes is capable to resolve the partons inside the proton, and therefore DIS is used mainly to investigate the proton structure. Measurements of the structure function can be found for example in [79, 80, 81] with the theoretical models in [83].

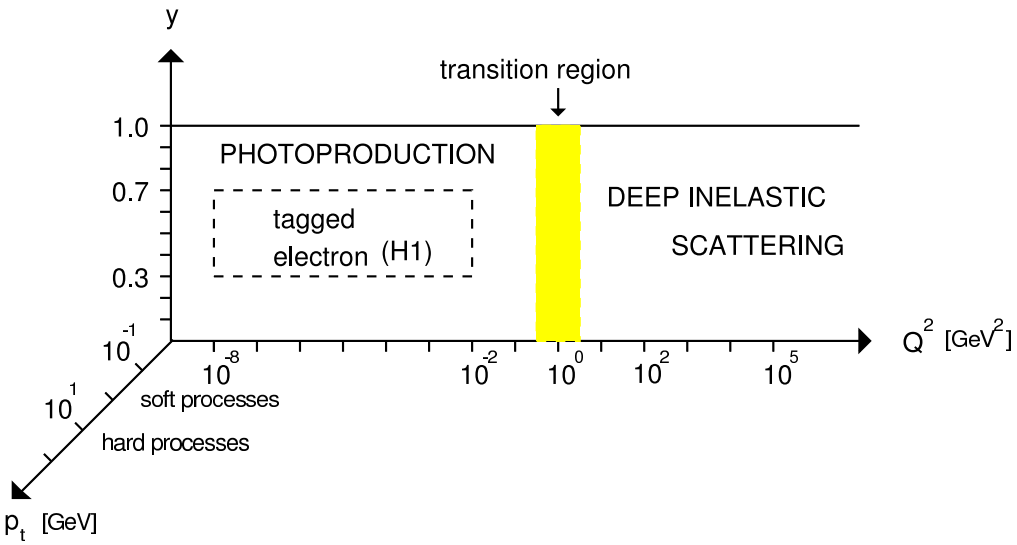

Figure 2.2: *Kinematical regimes at HERA in the electron-proton scattering.*

The analysis presented here is performed in the photoproduction regime where the electron is scattered at very small angles. The covered region is $Q^2 < 0.01\,\mathtt{GeV}^2$ in virtuality and $0.3 < y < 0.65$ in the inelasticity which is shown in fig. 2.2. The transverse momenta of the particles are usually $p_t \lesssim 1\,\mathtt{GeV}$.

2.3 From $e-p$ Scattering to Photoproduction

In the interaction of electrons and protons at HERA energies the dominant processes are when the electron as a source of virtual photons emits a quasi-real photon ($Q^2 \ll 1$) which subsequently interacts with the proton. The dominance of the photoproduction processes is evident from equation 2.13 from which a dependence: $1/Q^4$ follows. In the following the transition from the ep cross section to the photoproduction cross section is discussed.

Neglecting the contributions from the exchange of $W^{\pm}$ and Z bosons which are significant only for $Q^2 \gtrsim M^2_{Z,W^{\pm}}$, the cross section can be factorized into terms characterizing the flux of photons emitted by the electron and a term representing the photon-proton scattering. The photon-proton scattering is a sum of the cross sections for transversely and longitudinally polarized photons:

$$\frac{\mathrm{d}^2\sigma(ep \to eX)}{\mathrm{d}y\,\mathrm{d}Q^2} = \Phi(y, Q^2)\left(\sigma_T^{\gamma p} + \sigma_L^{\gamma p}\right), \tag{2.14}$$

where Φ represents the flux factor of virtual photons, σ_T and σ_L are the cross sections for transversely and longitudinally polarized photons. In the photoproduction region ($Q^2 \approx 0$)

the quasi real photons have only a transverse polarized component which contributes to the cross section. For the connection between photoproduction and inclusive ep cross section one obtains:

$$\frac{\mathrm{d}^2\sigma(ep \to eX)}{\mathrm{d}y\,\mathrm{d}Q^2} = \Phi_{WWA}\,\sigma^{\gamma p \to X}, \tag{2.15}$$

where Φ_{WWA} is the photon flux factor in the Weizsäcker-Williams-approximation:

$$\Phi_{WWA}(y,Q^2) = \frac{\alpha_{elm}}{2\pi Q^2}\left[\frac{1+(1-y)^2}{y} - \frac{2(1-y)}{y}\left(\frac{Q^2_{min}}{Q^2}\right)\right], \tag{2.16}$$

with $Q^2_{min} = m_e^2 y^2/(1-y)$ is the lower limit of Q^2 for the given inelasticity y. The integral over the kinematic limits defined for this analysis ($0.3 < y < 0.65$ and $Q^2 < 0.01$ $\mathtt{GeV}^2$) gives the photon-flux in the electron: $\mathcal{F}_{e/\gamma} = \int_{0.3}^{0.65}\int_{Q^2_{min}}^{0.01} \Phi_{WWA}(Q^2,y)\mathrm{d}Q^2\mathrm{d}y = 0.0132$.

To describe photoproduction the model of the photon structure from [36] has been adopted. In first approximation the photon can be treated as a point-like particle. In the second approach, quantum mechanics allows for fluctuations of photons into quark-antiquark or lepton-antilepton pairs. The quark-antiquark pair can build bound or non-bound states. The hadronic fluctuations are split into a part of low and high virtualities[2]. However, the quantum numbers of this hadronic component must match the respective quantum numbers of the photon ($Q = B = S = 0$, $J^{PC} = 1^{--}$). Therefore for the bound states only the vector mesons ($VM = \rho^0, \omega, \phi, J/\psi, \Upsilon$) are allowed. The low virtuality part can be therefore approximated by the sum of vector mesons. Due to the high p_t the high virtuality part can be calculated perturbatively. With this classification the photon can be expressed by:

$$|\gamma\rangle = c_{bare}|\gamma_{bare}\rangle + \sum_{V=VM} c_V|V\rangle + \sum_q c_q|q\bar{q}\rangle + \sum_{\ell=e,\mu,\tau} c_\ell|\ell^+\ell^-\rangle\,, \tag{2.17}$$

where the coefficients c_i is related to the couplings. All photon components may subsequently interact with the protons. The contribution from lepton-antilepton interaction with the proton is due to the relative smallness of the electromagnetic/weak coupling negligible. The above photon wave function corresponds to the existence of three main event classes [38]:

1. If the bare photon $|\gamma_{bare}\rangle$ interacts with partons inside the proton directly one deals with direct processes. A typical process of this kind is boson-gluon fusion which is shown in fig. 2.3 b).

2. The wave function $|V\rangle$ corresponds to the vector meson dominance (VMD) [68] processes in which the photon turns into a vector meson before the interaction, and thus all processes allowed in hadronic physics may occur. The essence of the VMD model is low virtuality of the quark-antiquark pairs. This part of the cross section can be expressed via the VMD model as a sum of meson-proton cross sections:

$$\sigma^{\gamma p}_{\mathrm{VMD}} = \sum_V \frac{4\pi\alpha_{elm}}{f_V^2}\sigma^{Vp}_{\mathrm{tot}}\,, \tag{2.18}$$

   where f_V is the respective coupling of the meson to the photon. The process is shown in fig. 2.3 a).

[2] The term "virtuality" here refers to the amount of "off-shellness" that comes in addition to the virtuality q^2 of the photon.

3. In the so called anomalous process one of the non-bound quarks/antiquarks subsequently interacts with a parton of the proton which is demonstrated by fig. 2.3 c). A characteristic of these processes is high virtuality of the quark-antiquark pairs.

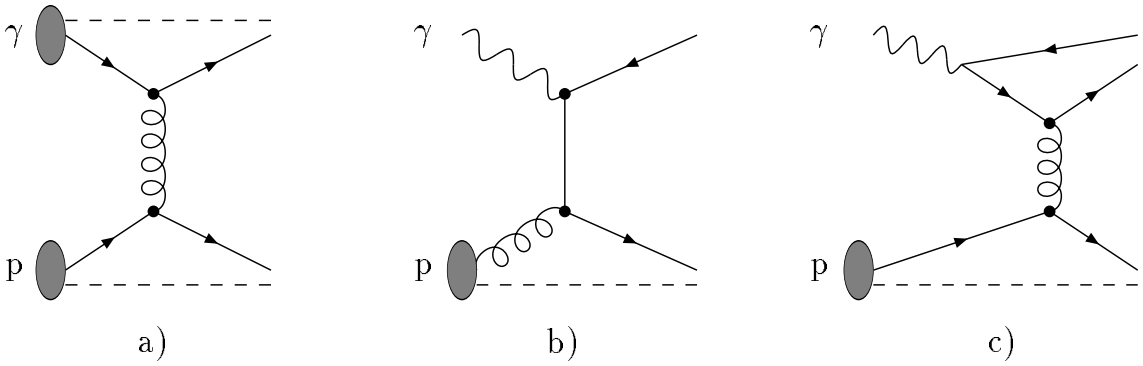

Figure 2.3: *Contributions to γp interactions: a) Vector Meson Dominance (VMD) process, b) direct, and c) the anomalous process (according to [84]).*

Based on this classification, the total photon-proton cross section can be written as:

$$\sigma_{\text{tot}}^{\gamma p} = \sigma_{\text{VMD}}^{\gamma p} + \sigma_{\text{direct}}^{\gamma p} + \sigma_{\text{anomalous}}^{\gamma p} \,. \tag{2.19}$$

2.4 Diffraction

The notation 'diffraction' has been introduced in the 17-th century by Grimaldi [90] at the occasion of optical observations. Since the 50's [43, 44], the optical analogy plays an important rôle also in high energy physics. The term is in strict analogy with the optical phenomenon that occurs when a beam of light meets an obstacle or crosses a hole whose dimensions are comparable to its wavelength.

Defining diffraction in a unique way is difficult, but generally two definitions of hadronic diffractive processes can be formulated:

1. A reaction at high energies in which no quantum numbers are exchanged between the interacting particles. In other words, the particles diffused have the same quantum numbers as the incident particles. It is a necessary condition for the process to be diffractive, but not a sufficient one. This definition allows a classification of the following types of the diffractive processes:

   - elastic scattering: the incident and outcoming particles are the same:

     $$A + B \to A' + B' \,. \tag{2.20}$$

     The process is schematically shown in fig. 2.4 a).
   - single dissociation[3]: one of the incident particles comes out unchanged after the collision while the other one gives rise to a bunch of final particles (or to a resonance) with the same quantum numbers (fig. 2.4 b) and c)):

     $$A + B \to A' + X_B, \quad A + B \to X_A + B' \tag{2.21}$$

[3] in literature the terms single/double diffraction are often used instead of single/double dissociation.

- double dissociation: each incident particle gives rise to a bunch of final particles (resonances) with the same quantum numbers (except the spin) as the incident particles (fig. 2.4 d)):

$$A + B \to X_A + X_B \,. \tag{2.22}$$

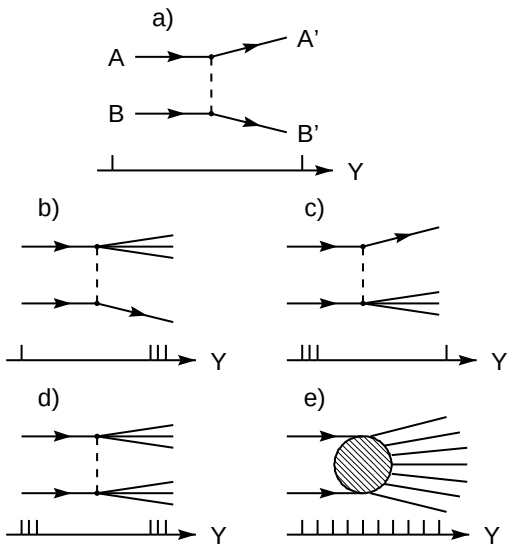

Figure 2.4: *Classification of diffractive processes: a) elastic, b) and c) single dissociative, d) double dissociative, d) non diffractive. Below each process the rapidity distribution* (Y) *is shown.*

For the single or double dissociative processes it is difficult to find the quantum numbers for not fully reconstructed states. This problem can be omitted by the second definition of a diffractive process [45]:

2. A diffractive process is characterized by a large, non exponentially suppressed, rapidity gap in the final state. A rapidity gap ΔY is meant to be a rapidity difference between final state particles A' (X_A) and B' (X_B). Then the diffractive processes are characterized by a constant rapidity difference distribution $\mathrm{d}N$:

$$\frac{\mathrm{d}N}{\mathrm{d}(\Delta Y)} \sim \text{constant} \,, \tag{2.23}$$

and non-diffractive processes are exponentially suppressed (see fig. 2.4 e):

$$\frac{\mathrm{d}N}{\mathrm{d}(\Delta Y)} \sim e^{-\Delta Y} \,. \tag{2.24}$$

The requirement of a large rapidity gap is again not sufficient to characterize diffraction, and one has to demand also the rapidity gap to be non exponentially suppressed.

The traditional theoretical framework for diffraction is Regge theory which is described in the following.

2.5 Regge Theory

In the study of soft hadron-hadron interactions, where no hard scale is present and perturbative QCD is not applicable, phenomenological models often give the best descriptions available. A consistent description of such processes is offered by Regge[4] theory which describes the hadronic reactions at high energies in terms of the exchange of 'objects', called 'Reggeons' ($I\!R$). A short introduction is given below.

Regge phenomenology was introduced in the beginning of the 60's [76, 77] in the pre-QCD era. It is based on the S-matrix formalism assuming unitarity of the S-matrix, analyticity and crossing symmetry.

1. Unitarity of the S matrix: The scattering matrix is unitary which means that the probability that some process will happen is unity: if S is the operator that transforms an initial state $|i\rangle$ into some final state $|f\rangle$ by $|f\rangle = S|i\rangle$, unitarity is expressed as: $S^\dagger S = \mathbb{1} = SS^\dagger$.

2. Analyticity: the variables s and t characterizing the process can be extended into the complex plane and the scattering matrix $S(s,t)$ can be expressed via these complex variables.

3. Crossing symmetry: Crossing symmetry is a consequence of the analyticity assumption and states that if the scattering matrix of the process $A + B \to C + D$ with $s = (P_A + P_B)^2$ and $t = (P_A - P_C)^2$ is known, also the crossed reaction $A + \bar{C} \to \bar{B} + D$ with $s' = (P_A + P_{\bar{B}})^2$ and $t' = (P_A - P_{\bar{C}})^2$ is known. Making use of the analyticity leads to the exchange of $s \to t'$ and $t \to s'$ and the same scattering matrix for both processes:

$$S_{AB\to CD}(s,t) = S_{A\bar{C}\to\bar{B}D}(t',s') \tag{2.25}$$

   Hence the crossing symmetry implies that s-channel resonance production can be described by the same amplitude as a t-channel exchange mechanism, providing that the variables s and t are interchanged on crossing. The generalized s and t channel processes, as defined in this discussion, are shown in fig. 2.5.

In the s-channel, all possible resonances which can be produced by the interaction are linked by a linear trajectory in a two dimensional space defined by the mass squared and angular momentum. In Regge theory, the angular momentum is extended to the complex plane, $\alpha(t)$, with physically observable t-channel resonances. They occur only at physical values of spin, such that $Re(\alpha(t))$ is an integer or half integer, known as Regge poles. The linear trajectories can be parametrized as:

$$\alpha(t) = \alpha(0) + \alpha' t\,. \tag{2.26}$$

Each family of bound states or resonances having the same quantum numbers (except spin) correspond to a single Regge trajectory, also called Reggeon. The basic known trajectories are the baryon, meson and Pomeron trajectories, with intercepts $\alpha(0)$ approximately < 0, < 0.5 and 1.08, respectively. The π, ω, ρ and ω as meson trajectories and the Pomeron trajectory are depicted in fig. 2.5.

[4] named after the Italian physicist Tullio Regge

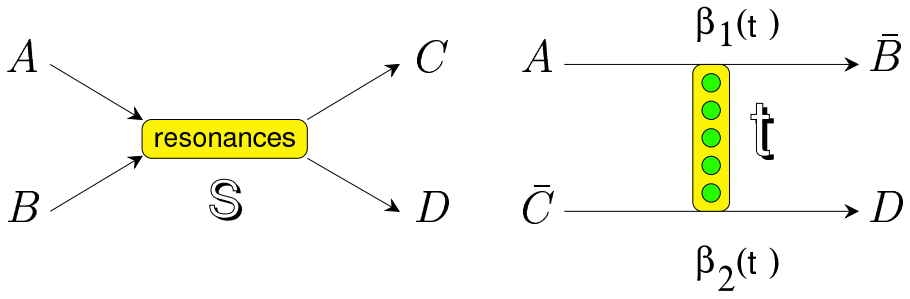

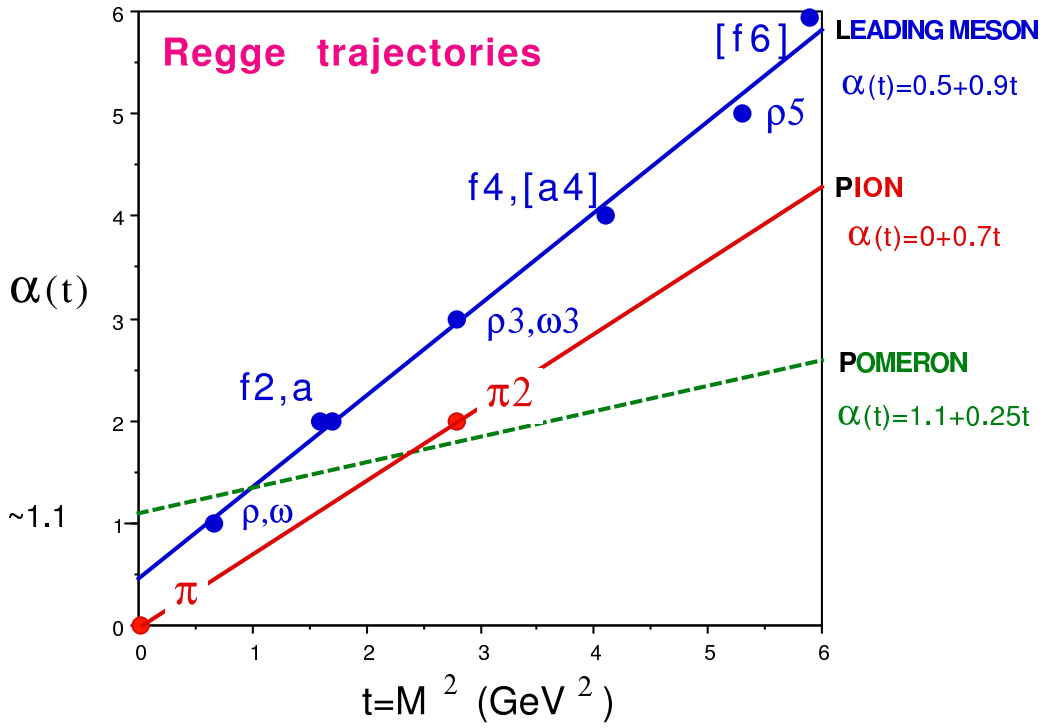

Figure 2.5: *In upper plots: An illustration of the relationship between a) the s channel process $AB \to CD$ and the corresponding b) t channel process $A\bar{C} \to \bar{B}D$. $\beta_1(t)$ and $\beta_2(t)$ stand for the residue.*
Lower plot: Regge trajectories in the two dimensional plane of angular momentum versus mass squared, so called Chew-Frautschi diagram. The π trajectory with an intercept close to zero, meson trajectories (ρ, ω) with an intercept of 0.5 *and the Pomeron trajectory with an intercept of* 1.08, *are shown.*

2.5.1 Elastic and Total Cross Sections

Assuming the asymptotic limit ($s \to \infty, t/s \to 0$) the single leading trajectory contribution to the scattering amplitude is:

$$A(s,t) = f(t) \left(\frac{s}{s_0}\right)^{\alpha(t)} \tag{2.27}$$

where $f(t)$ includes $\beta(t) = \beta_1(t)\,\beta_2(t)$ (see fig. 2.5), which describes the residue related to the hadronic form factors, and the part independent of t. s_0 denotes the scale relative to which s must be large. It gives for the elastic cross section:

$$\frac{\mathrm{d}\sigma_{\mathrm{el}}^{AB}}{\mathrm{d}t} = \frac{|A(s,t)|^2}{16\pi^2 s^2} = \frac{\beta_1^2(t)\beta_2^2(t)}{16\pi^2}\left(\frac{s}{s_0}\right)^{2(\alpha(t)-1)} = F(t)\left(\frac{s}{s_0}\right)^{2(\alpha(t)-1)} . \tag{2.28}$$

where $F(t)$ includes all the t dependences. Assuming one single Reggeon exchange with a linear trajectory according to eq. (2.26) and the parameterization $\beta(t) \sim \beta_0 e^{-b_0|t|}$ the elastic cross section becomes:

$$\frac{\mathrm{d}\sigma_{\mathrm{el}}^{AB}}{\mathrm{d}t} = C\left(\frac{s}{s_0}\right)^{2\alpha(0)-2} e^{-b|t|} = \left.\frac{\mathrm{d}\sigma}{\mathrm{d}t}\right|_{t=0} e^{-b_0|t|} , \tag{2.29}$$

with

$$b = b_0 + 2\alpha' \ln(s/s_0) . \tag{2.30}$$

One observes that the width of the forward peak decreases as the energy increases. This is known as the shrinkage of the diffraction peak. In the following s_0 will be fixed at $s_0 \sim 1$ $\mathtt{GeV}^2$.

The Optical Theorem [90] relates the elastic forward amplitude $AB \to A'B'$ to the total cross section $AB \to X$ by:

$$\sigma_{tot} = \frac{1}{s}\mathcal{I}m(A(s,t=0)^{AB\to A'B'}) \sim \frac{1}{s}\beta_1(0)\beta_2(0)s^{\alpha(0)} \tag{2.31}$$

$$\sim s^{\alpha(0)-1} . \tag{2.32}$$

The energy dependence shows that trajectories with an intercept greater than one will lead to a rise of the total cross section, for $\alpha(0) = 1$ the total cross section will be constant and for $\alpha(0) < 1$ the total cross section will decrease. Especially at lower energies it is possible that not only one trajectory will contribute to the cross section. In this case the cross section is given by a sum over all contributing of the trajectories:

$$\sigma_{tot} \sim \sum_i g_i s^{\alpha_i(0)-1} , \tag{2.33}$$

where g_i is the respective contribution of the trajectory to the total cross section. The basic trajectories are discussed below.

2.5.2 Meson Trajectories

All of the observed meson trajectories have intercepts in the region of $\alpha(0) \lesssim 0.5$. Thus the cross section of the processes associated with these trajectories fall rapidly with increasing centre of mass energy, as indicated by eq. (2.32). The leading meson trajectories are the ω and ρ trajectories. All meson trajectories have the same quantum numbers as the real particles:

$$\rho: \quad B = Q = S = 0\,, \quad I = 1, \quad P = -1,\, C = -1,\, G = +1\,, \xi = -1\,, \tag{2.34}$$

$$\omega: \quad B = Q = S = 0\,, \quad I = 0, \quad P = -1,\, C = -1,\, G = -1\,, \xi = -1\,, \tag{2.35}$$

where B, Q, S, I, P, C, G and ξ denote the baryon number, charge, strangeness, isospin, P-parity, C-parity, G-parity and the signature of the trajectory, respectively. Their respective trajectories [50] are:

$$\alpha_\rho(t) \approx \alpha_\omega(t) = \alpha(0) + \alpha' t \approx 0.5 + 0.9t \tag{2.36}$$

Due to the same intercept of the ρ and ω trajectories their total cross sections have according to eq. (2.32) the same dependence on s:

$$\sigma_{tot} \sim s^{-0.5}\,, \tag{2.37}$$

which leads to a total cross section decreasing with energy. The elastic cross section can be calculated according to eq. (2.29).

2.5.3 The Pomerančuk Trajectory

The Regge trajectories discussed above have intercepts below 0.5. Because of the $s^{\alpha(0)-1}$ dependence, the total cross section decreases. However, early observations [51] showed that as $\sqrt{s}$ increases above ~ 10 GeV, the total hadronic cross section starts to be rather constant. In order to explain the constant form of the cross section a new trajectory with an intercept of one was introduced [52, 53] and named Pomeron ($I\!P$) [5].

In the 90's Donnachie and Landshoff [46] performed a fit of the total proton-proton and proton-antiproton cross sections assuming the Pomeron to be the leading trajectory at high energies with an intercept of $\alpha_{I\!P}(0)$ and a meson leading trajectory with the intercept of $\alpha_{I\!R}(0)$ by the function:

$$\sigma_{\mathrm{tot}}^{(-)p\,p} = X^{(-)p\,p} s^{\alpha_{I\!P}(0)-1} \pm Y^{(-)p\,p} s^{\alpha_{I\!R}(0)-1}\,. \tag{2.38}$$

The first term $X^{(-)p\,p}$ corresponds to the processes induced by Pomeron exchange and the second term $Y^{(-)p\,p}$ corresponds to the trajectories with $C = 1$ and $C = -1$ trajectories, respectively. The fit yields: $\alpha_{I\!R} \sim 0.55$ for the intercept of the leading meson trajectory and:

$$\alpha_{I\!P}(0) = 1.08, \quad \alpha'_{I\!P} = 0.25\,\mathrm{GeV}^{-2} \quad \Rightarrow \quad \alpha_{I\!P}(t) = 1.08 + 0.25\,t \tag{2.39}$$

[5] named after the Russian physicist Isaak Yakovlevič Pomerančuk

for the intercept and slope of the Pomeron trajectory.

The Pomeron carries the quantum number of the vacuum:

$$Pomeron: \quad B = Q = S = 0\,, \quad I = 0, \quad P = +1,\, C = +1,\, G = +1\,, \xi = +1\,, \tag{2.40}$$

which means that in processes induced by Pomeron exchange no quantum numbers are exchanged and also spin flip on the quark level is forbidden [49]. Therefore e.g. the exclusive production of axial vectors ($J^{PC} = 1^{+-}$ e.g. b_1 meson) at HERA is not possible via Pomeron exchange. However, the spin state of the final state can be changed due to possible angular momentum transfer, when e.g. the proton becomes an excited state N^*: $p \to N^*$.

Due to the intercept of 1.08, the Pomeron is the leading trajectory at high energies with a cross section gently rising:

$$\sigma_{tot} \sim s^{+0.08}\,, \tag{2.41}$$

In analogy to the meson trajectories, the possibility of bound states lying on the Pomeron trajectory arises. However so far there is still no evidence of any resonance to lie on this trajectory. Although glueballs are supposed to be candidates for such states [57]. Another approach [58, 59, 60] describes the Pomeron as a colourless system of two gluons that interact with the partons of the scattered particle.

2.5.4 The Odderon Trajectory

The Odderon[6] was introduced by Lukaszuk and Nicolescu in 1973 [61, 62]. The Odderon is conceived as the $C = P = -1$ partner of the Pomeron. Another difference to the Pomeron is its negative signature, $\xi = -1$, which would entail differences between the cross section of pp and $\bar{p}p$: $\Delta\sigma = \sigma^{pp} - \sigma^{\bar{p}p} \not\to 0$ for $s \to \infty$ and would violate the Pomerunčuk theorem [63]. The other quantum numbers remain the same:

$$Odderon: \quad B = Q = S = 0\,, \quad I = 0, \quad P = -1,\, C = -1,\, G = +1\,, \xi = -1\,, \tag{2.42}$$

The consequence of the change of the sign of parity in the processes induced by the Odderon is a requisite of the angular momentum transfer ($\Delta l > 0$), via $P = (-1)^{\Delta l}$ (Gribov-Morrison rule [54, 55]), while for the processes induced by Pomeron exchange an angular momentum transfer is not necessarily required and can also be zero: $\Delta l \geq 0$.

So far all attempts to find the Odderon failed [101, 96, 99, 100].

2.6 Double Reggeon Exchange

So far only processes with single Reggeon exchange were discussed. In principle also processes with more than one trajectory may happen with the fusion of trajectories into some

[6] **Odd**-under-crossing-Pom**eron**

hadronic final state. These processes offer a possibility to search for some exotic states like hybrids (mixing of quarks and gluon: $q\bar{q}g$), pure gluonic states called glueballs (gg) [56] and for instance the Odderon [100].

Assuming elastic scattering of hadron A off hadron B with the exchange of two trajectories, one at the vertex of hadron A and the other at the vertex of hadron B, with the fusion of the two trajectories into a hadronic final state X, one can write:

$$A + B \overset{T_1+T_2\to X}{\longrightarrow} A' + X + B', \tag{2.43}$$

where X refers to the final state produced in the fusion process of the trajectories T_1 and T_2. The process is schematically shown in fig. 2.6. The variables t_1 (t_2), and $\beta_1(t_1)$ ($\beta_2(t_2)$) denote the square of the momentum transfer at the upper (lower) vertex, and the residuum related to the T_1 (T_2) trajectory flux from A (B), respectively. The flux gives the probability to find the trajectory in the particle A or B. s_1 and s_2 are the squares of the centre of mass energies of the subsystems $A'X$ and $B'X$, respectively. $\sigma(T_1 + T_2 \to X)$ is the cross section for the production of X in the fusion of the two trajectories.

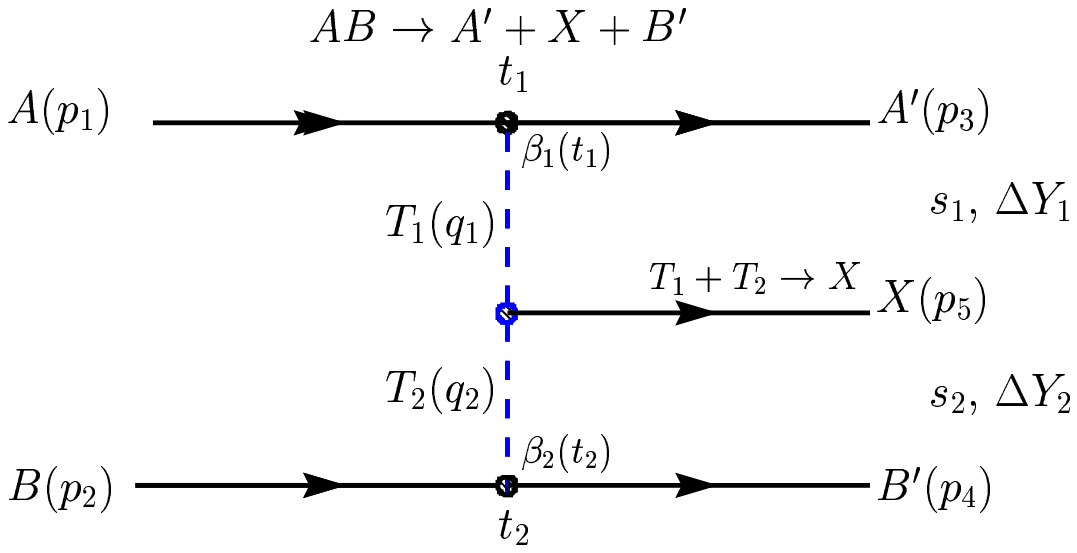

Figure 2.6: *Double Reggeon exchange.*

Assuming in the factorization of the total scattering amplitude $A_{tot} \sim A_1 \cdot A_2$ [28] with A_1 (A_2) being the scattering amplitude for the upper (lower) vertex:

$$A_1(s_1, t_1) \sim s_1^{\alpha_1(t_1)} \tag{2.44}$$
$$A_2(s_2, t_2) \sim s_2^{\alpha_2(t_2)}, \tag{2.45}$$

one may obtain an s dependence for the upper and lower vertices in the form:

$$\sigma_1^{tot} \sim s_1^{\alpha_1(0)-1} \tag{2.46}$$
$$\sigma_2^{tot} \sim s_2^{\alpha_2(0)-1}, \tag{2.47}$$

and also the elastic cross sections in the form:

$$\frac{\mathrm{d}\sigma}{\mathrm{d}t_1} = \left.\frac{\mathrm{d}\sigma}{\mathrm{d}t_1}\right|_{t_1=0} e^{-b_1|t_1|}, \tag{2.48}$$

$$\frac{\mathrm{d}\sigma}{\mathrm{d}t_2} = \left.\frac{\mathrm{d}\sigma}{\mathrm{d}t_2}\right|_{t_2=0} e^{-b_2|t_2|}. \tag{2.49}$$

where $s_1 = (P_{A'} + P_X)^2$ and $s_2 = (P_{B'} + P_X)^2$ are the squared centre of mass energies of the subsystems $A'X$ and $B'X$, respectively. Using $ln(s) \sim \Delta Y$ [90] one obtains the total cross section also as a function of rapidity difference:

$$\sigma_1^{tot} \sim e^{(\alpha_1(0)-1)\,\Delta Y_1} \tag{2.50}$$

$$\sigma_2^{tot} \sim e^{(\alpha_2(0)-1)\,\Delta Y_2}, \tag{2.51}$$

where ΔY_1 (ΔY_2) is the rapidity difference between subsystems A' and X (B' and X): $\Delta Y_1 = Y_{A'} - Y_X$ ($\Delta Y_2 = Y_{B'} - Y_X$). According to the definition of diffractive and non-diffractive processes (eq. (2.23) and (2.24)) the reactions induced by trajectories with a intercept close to one (Pomeron trajectory) are diffractive, while the processes induced by trajectories with a intercept lower than one are non-diffractive (e.g. meson and baryon trajectories).

2.7 Signatures of Double Meson Photoproduction

In this section, the investigated process and its signatures are introduced together with the reconstruction of the kinematic variables defining the processes.

2.7.1 Event Signature

This analysis is devoted to the search of exclusive double meson photoproduction, namely:

$$\begin{array}{llllll} \gamma p \to & \eta\ \rho^0 X & \text{with} & \eta & \to \gamma\gamma & \rho \to \pi^-\pi^+, \\ \gamma p \to & \pi^0\rho^0 X & \text{with} & \pi^0 & \to \gamma\gamma & \rho \to \pi^-\pi^+, \end{array} \tag{2.52}$$

shown in fig. 2.7. The η and π^0 mesons will be identified via its dominant photonic decays: $\eta(\pi^0) \to \gamma\gamma$ and the ρ meson via its dominant decay into charged pion pairs: $\rho \to \pi^-\pi^+$.

Here and in the following the variables s, W, s_1, s_2, t_1 and t_2 are used to characterize the investigated processes:

- s is the centre of mass energy squared of the $e-p$ system:

$$s = (P_e + P_p)^2, \tag{2.53}$$

- W is the centre of mass energy of the $\gamma - p$ system:

$$W^2 = (P_\gamma + P_p)^2, \tag{2.54}$$

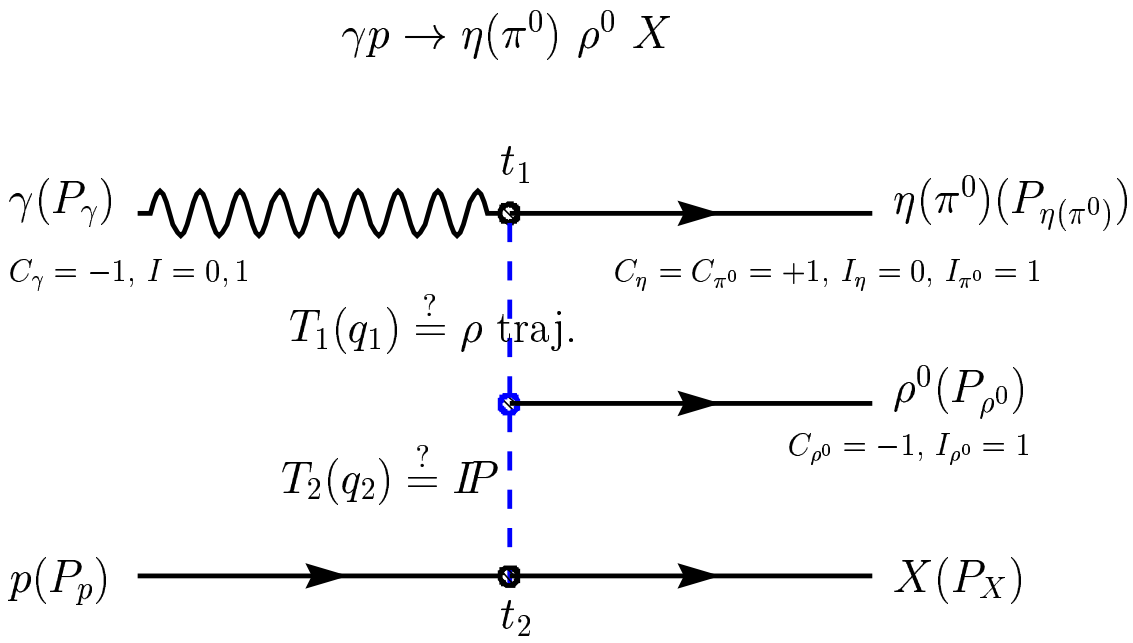

Figure 2.7: *Double meson photoproduction at HERA: the central meson can be produced either in a fusion process of T_1 and T_2 trajectories or originates from high mesonic state which subsequently decays into two mesons or stems from the fragmentation of the non-bound quark-antiquark states.*

- s_1 is the square of the centre of mass energy of the $\eta(\pi^0) - \rho^0$ subsystem:

$$s_1 = (P_{\rho^0} + P_{\eta(\pi^0)})^2, \tag{2.55}$$

- s_2 is the square of the centre of mass energy of the $\rho^0 - p$ subsystem:

$$s_2 = (P_{\rho^0} + P_X)^2, \tag{2.56}$$

- t_1 is the four-momentum squared at the photon vertex:

$$t_1 = (P_\gamma - P_{\eta(\pi^0)})^2, \tag{2.57}$$

- t_2 is the four-momentum squared at the proton vertex:

$$t_2 = (P_p - P_X)^2. \tag{2.58}$$

The existence of such kind of a process at very high γp CMS energies ($W \approx 200\,\mathrm{GeV}$) involves Pomeron exchange at at least one vertex. Due to C parity and isospin conservation the Pomeron exchange can take place only at the lower, proton, vertex. In Regge phenomenology one possible explanation of the upper, photon, vertex could be Reggeon exchange. In order not to violate C parity and isospin at the upper vertex and to produce a ρ^0 meson in the fusion process with the Pomeron, the Reggeon has to have negative parity (like the photon) and isospin one: $C_{T_1} = -1$ and $I_{T_1} = 1$. Therefore the candidate for a leading Reggeon is the ρ-trajectory.

Another possible explanation could be the processes in which the photon fluctuates into bound or non-bound states. In the former case the photon fluctuates into a vector meson which via the proton interaction is diffractively excited and subsequently decays into $\eta-\rho^0$ or $\pi^0-\rho^0$ states. The mechanism of their production are described in chapter 3.2.1. Both processes are simulated in the Monte Carlo generators Pythia and RapGap. Their contribution to the total signal is estimated in the chapters 5 and 6. In the process where the photon fluctuates into a non-bound state of the quark-antiquark pair the fragmentation of the pair may lead into production of $\eta-\rho^0$ or $\pi^0-\rho^0$ states. In this case the process at the photon vertex would be described by a quark propagator instead of a ρ trajectory exchange between the photon and the ρ vertex.

2.7.2 Kinematical Reconstruction

To reconstruct the kinematical quantities defined in chapter 2.7.1 on the detector level several methods can be used [102]. In this analysis the electron is measured and therefore the 'electron method' is employed in which the kinematics is determined by measuring the energy, E'_e, and the polar angle, ϑ_e, of the scattered electron. If E_e is the energy of the colliding electron and the masses of the electron and proton are neglected, then for s, the inelasticity, y, the photon virtuality, Q^2, and Bjorken x, one obtains:

$$
\begin{aligned}
s &= 4\,E_e\,E_p\,, && (2.59)\\
y &= 1-\frac{E'_e}{E_e}\sin^2\vartheta_e/2\,, && (2.60)\\
Q^2 &= 4E_eE'_e\cos^2\vartheta_e/2 \quad \text{and} && (2.61)\\
x &= \frac{E_eE'_e\cos^2\vartheta_e/2}{E_p\left(E_e-E'_e\sin^2\vartheta_e/2\right)}\,, && (2.62)
\end{aligned}
$$

respectively. In the photoproduction regime the electron is deflected only by a very small angle and equations (2.60) – (2.62) simplify significantly, in the approximation $\vartheta_e \approx 180°$:

$$
\begin{aligned}
y &\approx 1-\frac{E'_e}{E_e}\,, && (2.63)\\
Q^2 &\approx 0 \quad \text{and} && (2.64)\\
x &\approx 0\,, && (2.65)
\end{aligned}
$$

respectively. The photon-proton centre of mass energy for $Q^2 \to 0$ can be approximated by

$$W = \sqrt{ys}\,. \qquad (2.66)$$

To reconstruct the square of the four-momentum transfer at the photon, t_1, and proton, t_2, vertices it will be assumed that $p_{z,\eta(\pi^0)} \approx p_{z,\gamma}$ and $p_{z,X} \approx p_{z,p}$. Then t_1 and t_2 can be obtained via the transverse momentum of the $\eta(\pi^0)$ meson and the transverse momentum of the $\eta(\pi^0)-\rho^0$ system [90], respectively:

$$
\begin{aligned}
t_1 &= -\left(\boldsymbol{p}_{t,\eta(\pi^0)}\right)^2\,, && (2.67)\\
t_2 &= -\left(\boldsymbol{p}_{t,\rho^0+\eta(\pi^0)}\right)^2\,. && (2.68)
\end{aligned}
$$

This approximation has to be used since neither the emitted photon from beam electron nor the final state X are measured and t_1 and t_2 can not be calculated directly from eq. (2.57) and (2.58).

The centre of mass energy squared of the subsystem $\eta(\pi^0) - \rho^0$, s_1, will be reconstructed via the four-momenta of the $\eta(\pi^0)$ and ρ^0 mesons. Since the final state X is not measured, the following approximation will be used for the determination of s_2: the four-momenta of the final state X are assumed to be the same as for a colliding proton, $P_X^i = P_p^i$. Then s_1 and s_2 can be reconstructed via:

$$s_1 = (p_{\eta(\pi^0)} + p_{\rho^0})^2 = (E_{\eta(\pi^0)} + E_{\rho^0})^2 - (\boldsymbol{p}_{\eta(\pi^0)} + \boldsymbol{p}_{\rho^0})^2 \text{ and} \tag{2.69}$$

$$s_2 = (p_{\rho^0} + p_p)^2 = (E_{\rho^0} + E_p)^2 - (\boldsymbol{p}_{\rho^0} + \boldsymbol{p}_p)^2 , \tag{2.70}$$

respectively.

The four momenta of the photons from η or π^0 meson decays are calculated by

$$p_\gamma = \left(E_\gamma, E_\gamma \frac{\Delta x}{D}, E_\gamma \frac{\Delta y}{D}, E_\gamma \frac{\Delta z}{D} \right) , \tag{2.71}$$

where D is the distance of the centre of gravity of the energy deposition in the detector w.r.t. the interaction point:

$$D = \sqrt{(\Delta x)^2 + (\Delta y)^2 + (\Delta z)^2} \tag{2.72}$$

with

$$\Delta x = x - x_{vtx} \quad ; \quad \Delta y = y - y_{vtx} \quad ; \quad \Delta z = z - z_{vtx} .$$

The coordinates x, y and z correspond to the centre of gravity of the energy deposition in the detector. The coordinates $[x_{vtx}, y_{vtx}, z_{vtx}]$ refer to the reconstructed interaction point. The masses of the η and π^0 mesons are reconstructed from the invariant mass of the $\gamma - \gamma$ system calculated as:

$$m_{\gamma\gamma} = \sqrt{\left(\sum_{i=1}^{2} E_i \right)^2 - \left(\sum_{i=1}^{2} \boldsymbol{p}_i \right)^2} , \tag{2.73}$$

where the sum runs over two photons from η or π^0 mesons.

The four momenta of the charged pions from ρ^0 meson decay are calculated as

$$p_{\pi^\pm} = \left(\sqrt{(m_{\pi^\pm})^2 + p_x^2 + p_y^2 + p_z^2}, p_x, p_y, p_z \right) , \tag{2.74}$$

where p_x, p_y, p_z are momenta reconstructed by the H1 software and $m_{\pi^\pm} = 139.57$ `MeV` is the nominal value for the mass of the charged pion [37].

The variable $E - p_z$ will denote the difference between the energy and the z component of the momentum summed over all particles in the final state, in this case two pions, two photons and a scattered electron:

$$E - p_z = \sum_i (E - p_z)_i \tag{2.75}$$

where the sum runs over all particles i in the final state. Due to energy-momentum conservation in a fully contained event its value is twice the electron beam energy:

$$\Sigma(\text{final state}) = \Sigma(\text{initial state}) = \underbrace{(k^0 - k^3)}_{55\,\text{GeV}} + \underbrace{(P_p^0 - P_p^3)}_{0} = 55\,\text{GeV}\,. \tag{2.76}$$

Chapter 3

Monte Carlo Models

For the measurement of a cross section, the detector effects on the process to be measured have to be determined, and the contribution from background processes has to be estimated. Both tasks are accomplished by computer programs, so called Monte Carlo generators (MC). The MC simulation consists of three steps: First generating interactions of certain processes according to their cross-sections takes place and four-vectors of particles are calculated. These are subsequently passed to another program that simulates the detector (particle interactions with the detector material), its imperfections and the decay of unstable particles. The detector simulation at H1 is provided by the program package H1SIM [70] based on the package GEANT [71]. At this level the simulation of some trigger elements (IET, DCR_ϕ) is also derived. At the last level the result of the previous simulation step is processed by the same reconstruction software as the data, H1REC [64].

For the analysis presented in this thesis three event generators are employed, where two (Pythia and RapGap) are used for the background estimation, and one (ToyGen) for describing the signal processes. In this chapter, all generators are presented.

3.1 The Signal Event Generator ToyGen

In this analysis the processes under study are exclusive photoproduction of $\pi^0 - \rho^0$ and $\eta - \rho^0$ meson pairs, respectively. In the Regge terminology the processes may be described by ρ-trajectory exchange at the photon vertex and the Pomeron exchange at the proton vertex. The η and π^0 are produced at the photon vertex and the ρ^0 meson is produced from a fusion process of ρ- and Pomerančuk- trajectories.

The event generator ToyGen [30] is used as the signal Monte Carlo model for the analysis. It offers the possibility to simulate exclusive double meson production in the photoproduction regime via an exchange of different Regge-trajectories. It was designed to provide the simulation of the processes on a qualitative level in the sense of description of their kinematics rather than allowing prediction of cross-sections. Therefore it is used mainly as a tool for the estimation of detector efficiencies. Nevertheless, it allows quite a satisfactory description/comparison with the data. The possibility to modify several parameters of the program allows a qualitative description of the exclusive production of any two mesons $\mathtt{M}_1$ and $\mathtt{M}_2$:

$$ep \to (e' + \gamma)p \overset{\gamma \to \mathtt{M}_1 + T_1}{\longrightarrow} (e' + \mathtt{M}_1 + T_1)(X + T_2) \overset{T_1 + T_2 \to \mathtt{M}_2}{\longrightarrow} e'\mathtt{M}_1\mathtt{M}_2 X, \tag{3.1}$$

where $\mathtt{M}_1$ and $\mathtt{M}_2$ refer to the meson produced at the photon vertex and to the meson produced in the fusion process of trajectories T_1 and T_2, respectively. In the corresponding diagram (fig. 3.1) for sake of simplicity the electron is not shown and the photon is considered as the beam particle.

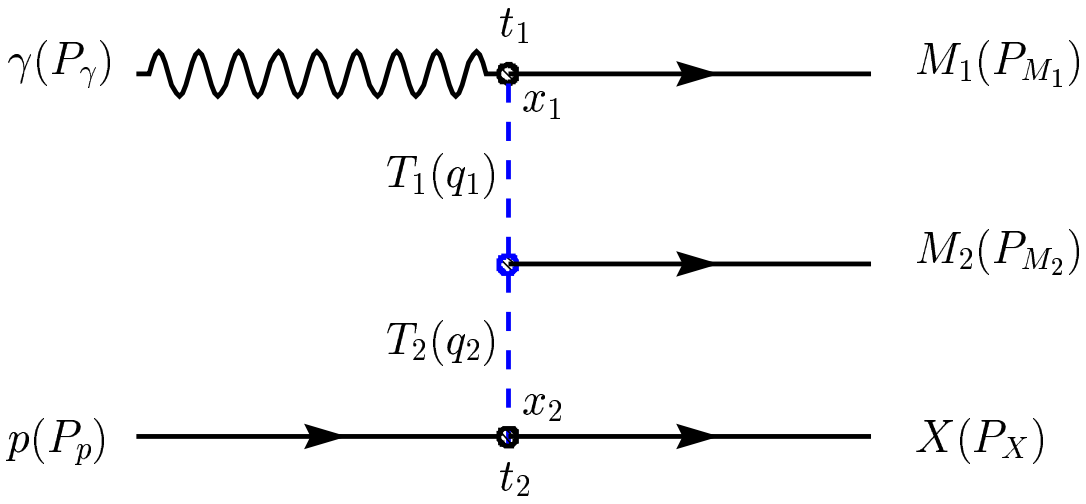

Figure 3.1: *Diagram of exclusive double meson production at HERA as modeled by ToyGen.*

The ToyGen MC model is based on double-pomeron exchange ($T_1 = T_2 = I\!P$) with various parametrisations of the Pomeron flux factors taken from other MC's, RAPGAP [31] and POMPYT [29]. The Pomeron flux factor in the proton is well known from p-p experiments. Since the Pomeron flux in the photon is unknown, the presented model assumes the same flux parametrisation for the Pomeron in the photon as in proton. The Ingelmann-Bruni parametrisation of the Pomeron flux [31] is employed in both cases:

$$f_{I\!P/\gamma}(x_{I\!P_1}, t_1) \;=\; f_{I\!P/p}(x_{I\!P_2}, t_2) \;=\; \frac{1}{2}\,\frac{1}{2.3}\,\frac{1}{x_{I\!P_{1(2)}}}\left(6.38e^{8t_{1(2)}} + 0.424e^{3t_{1(2)}}\right). \tag{3.2}$$

The variables $f_{I\!P/\gamma}(x_{I\!P_1},\, t_1)$ and $f_{I\!P/p}(x_{I\!P_2},\, t_2)$ denote the Pomeron flux factor in the photon and proton, respectively, $x_{I\!P_{1(2)}}$ ($x_{I\!P_{1(2)}} = x_{1(2)}$) denotes the longitudinal momentum fraction carried by the Pomeron, and $t_{1(2)}$ marks the squared four momentum transfer at the photon vertex, $t_1 = (P_\gamma - P_{M_1})^2$ and at the proton vertex $t_2 = (P_p - P_X)^2$, respectively.

In the investigated processes the π^0 and η mesons are related to the $\mathtt{M}_1$ meson produced in the upper, photon, vertex and hence stem from the photon. The ρ^0 ($\mathtt{M}_2$) results from the fusion process of the two T_1 and T_2 trajectories which requires that the T_1 trajectory has to carry the quantum numbers of the ρ^0 meson. Since there is no prediction for the ρ trajectory flux in the photon, the presented model cannot be used for a prediction of the cross section. However the modification of the flux at the photon vertex, $f_{I\!P/\gamma}$, to estimate detector efficiencies which is the main purpose of the Monte Carlo model. The necessary

modifications of $f_{I\!P/\gamma}$ will be discussed in the following.

Firstly, in order to study the populated regions the original fluxes from 3.2 were assumed. The $\eta - \rho^0$ and $\pi^0 - \rho^0$ processes have been generated in the photoproduction kinematical region with the standard diffractive cuts: $x_{I\!P_{1(2)}} < 0.05$ and $|t_{1(2)}| < 1\,\mathtt{GeV}^2$. Kinematical constraints applied to the generated events are summarized in table 3.1. The corresponding distributions are shown in fig. 3.2 a)-f) for the $\pi^0 - \rho^0$ sample and g)-l) for the $\eta - \rho^0$ sample, respectively. The first row concerns always the photon vertex and the second one the proton vertex in both samples. The first column shows the Bjorken $x_{1(2)} = x_{I\!P_{1(2)}}$ of the Pomeron at the photon (proton) vertex, the second one describes the variable t at the given vertex and the third column illustrates either the rapidity of the backward or the central meson.

The rapidity distributions show that the π^0 and η mesons are produced strongly in the backward direction. π^0 mesons go to rapidities of $Y_{\pi^0} \to -6$, while the η mesons are produced to $Y_\eta \to -4.5$. For both mesons only a very small part of the events lies in the SpaCal acceptance ($-3.5 < Y_{SpaCal} < -1.5$). The ρ^0 mesons are produced mostly forward. The backward region of the CJC acceptance ($Y_{CJC} \to -1.5$) is also very sparsely populated by ρ^0 meson production.

Comparing the rapidity distributions of the η and the ρ^0 measured in data (dots) shown in Appendix C in fig. C.1 g) and h) for the $\eta - \rho^0$ sample, and the generated rapidity distributions in 3.2 i) and l), one observes that the backward (η) as well the central (ρ^0) mesons in MC sample do not cover the region where the signal in the data occurs. Therefore it is not possible to calculate the detector efficiency with these generated events in the region seen in data.

From the aspects of detector efficiency studies, discussed in chapter 4.6, it is necessary to cover the full acceptance region of the SpaCal and CJC. Taking this into account the following modifications of the kinematics at the photon vertex have been done:

- the Pomeron flux at the photon vertex has been modified in t_1 by setting the coefficients in the exponential function in eq. (3.2) to zero ($8 \to 0,\ 3 \to 0$):

$$f'_{I\!P/\gamma}(x_1, t_1) = \frac{1}{2}\frac{1}{2.3}\frac{1}{x_1}\left(6.38e^{0t} + 0.424e^{0t}\right) . \tag{3.3}$$

  The variable $f'_{I\!P/\gamma}(x_1, t_1)$ defines the new (not Pomeron anymore) flux in the photon. Also the upper limit for $|\mathtt{t_1}|$ was changed to $|t_1| < 6\,\mathtt{GeV}^2$. It allows higher p_t value of the backward meson and hence also a larger scattering angle.

- the upper limit for the fraction of longitudinal momentum carried by the trajectory T_1 in the photon has been increased to $x_1 < 0.5$ in order to allow higher longitudinal momentum of the T_1 trajectory and thus to allow the central meson to be produced more backward.

The behavior of kinematics at the proton vertex remained unchanged. In the following the ToyGen simulation after these modifications will be called ToyGenMod.

All changes at the photon vertex are summarized in table 3.2. The corresponding distributions are shown in fig. 3.3. Now the backward mesons populate the full SpaCal region and the central meson the full CJC acceptance region for both samples $\pi^0 - \rho^0$ and $\eta - \rho^0$. The efficiency is investigated with this simulation in chapter 4.6.

variable	photoproduction cuts	
y	$0.3 < y < 0.7$	
Q^2	$< 0.01\,\mathrm{GeV}^2$	
variable	photon vertex	proton vertex
$x_{I\!P}$	< 0.05	< 0.05
$\lvert t\rvert$	$< 1\,\mathrm{GeV}^2$	$< 1\,\mathrm{GeV}^2$

Table 3.1: *Kinematical restrictions on the generated $\pi^0 - \rho^0$ and $\eta - \rho^0$ samples using original Pomeron flux from (3.2).*

variable	modification of photon vertex
$f'_{I\!P/\gamma}(x_{I\!P_1}, t_1)$	$e^{0t} + e^{0t}$
x_1	< 0.5
$\lvert t_1\rvert$	$< 6\,\mathrm{GeV}^2$

Table 3.2: *Modification of kinematics at the photon vertex of the generated $\pi^0 - \rho^0$ and $\eta - \rho^0$ samples.*

3.2 Background Generation

3.2.1 The Generator Pythia

Pythia [32] is a powerful event generator developed mainly for high-energy e^+e^-, $p\bar{p}$ and ep interactions. It is based on leading order (LO) matrix elements, parton showers and the Lund hadronization [33, 35]. Pythia contains a rich selection of physics processes, e.g. soft and hard QCD processes, deep inelastic scattering, photon induced processes, and many others, with more than 200 different subprocesses. The physics model employed by the generator to describe photoproduction is described in [38, 36].

It is expected that Pythia can describe the behavior of inclusive data distributions. The inclusive data sample was selected by the cuts described in table 3.3. These inclusive cuts play a rôle of the preselection for the final selection of the investigated processes (chapter 4). The data sample is compared with a Pythia sample, after applying the same cuts, shown in fig. 3.4. The data are shown by dots and the Pythia distributions by the solid-line histogram. In a) the invariant track-track mass[1] is compared. The Pythia MC describes the data reasonably except the mass window of the ρ^0 meson. In b) the number

[1] the term track-track mass will denote the invariant mass of the system of two particles corresponding to the reconstructed tracks.

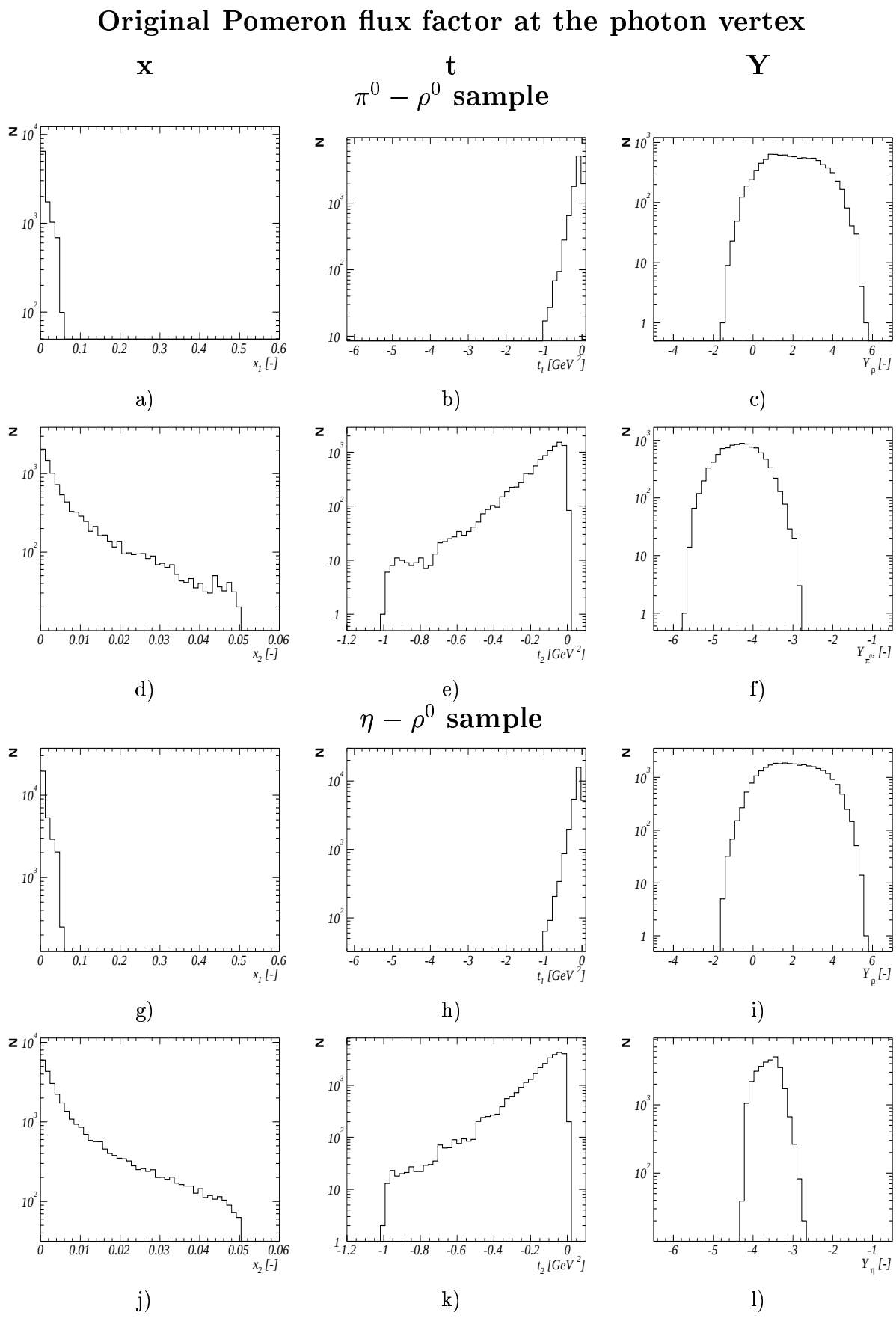

Figure 3.2: *Kinematical distributions generated using original Pomeron flux for the $\pi^0 - \rho^0$ a)-f) and the $\eta - \rho^0$ g)-l) samples. First column corresponds to the longitudinal momentum fraction of the Pomeron trajectory for the photon (first row) and proton vertex (second row), respectively. The second column shows the four-momentum transfer at photon (first row) and proton (second row) vertex and third column the rapidity of the ρ^0 and π^0 (η).*

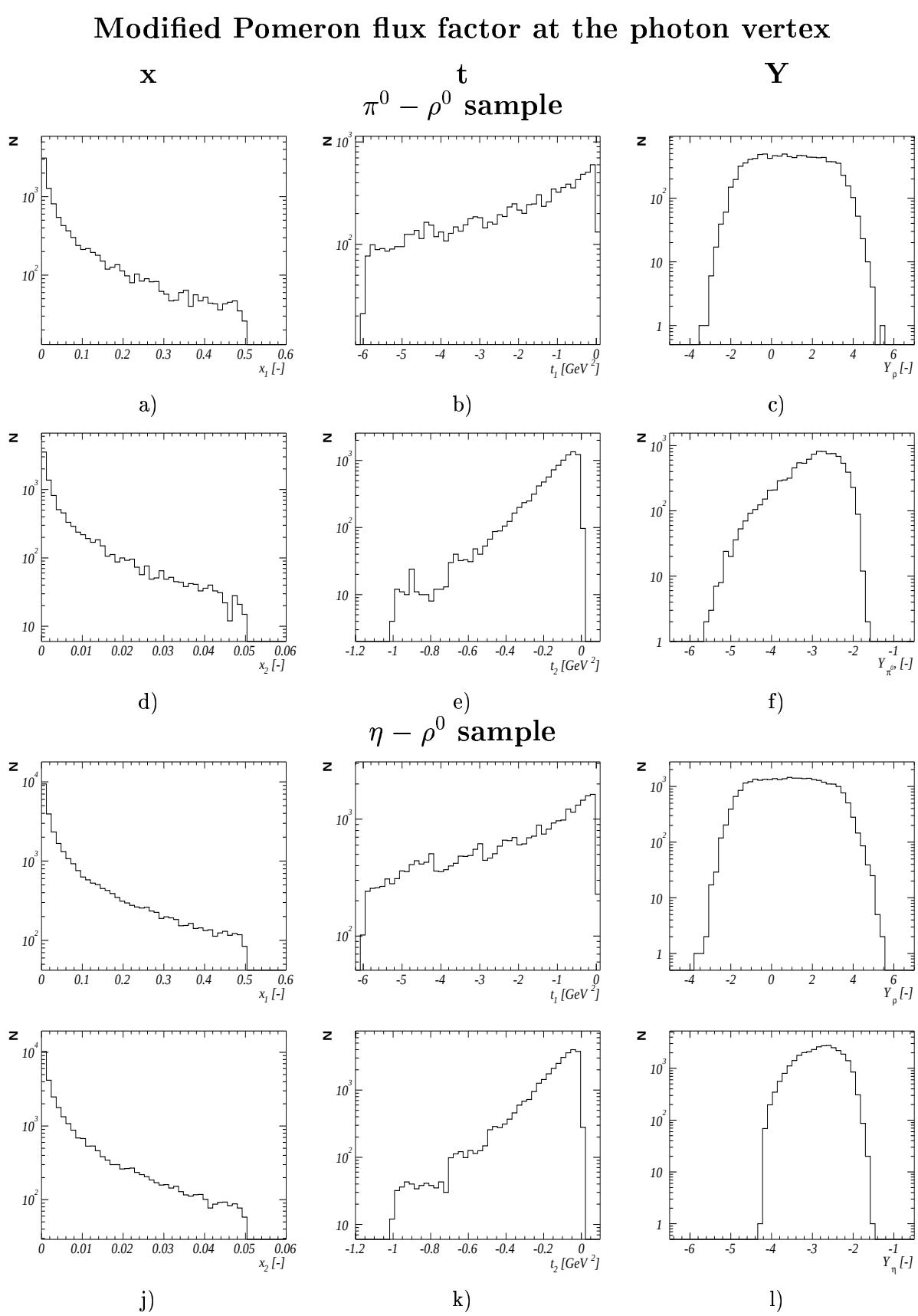

Figure 3.3: *The same kinematical variables as in fig. 3.2 but after modifications to the Pomeron flux on the photon side (table 3.2).*

of photon candidates detected in the SpaCal calorimeter is shown. The distribution exhibits an agreement between data and Pythia for $N_\gamma > 2$. Since the main characteristics of ep interactions is multiparticle production (typically in the order of tens) the main emphasis in Pythia is given in this direction. Therefore it is not unexpected that Pythia is not capable to describe very low multiplicities. Another possible reason is the existence of unknown processes or processes not implemented in Pythia. In d) the number of LAr clusters which are not associated with one of the two tracks is shown, in e) $E - p_z$ variable and in e) the z-coordinate of the vertex. In the last three distributions the Pythia lies slightly, but systematically below the data due to the differences at low multiplicities.

cut	motivation
$0.3 < y < 0.7$	tagged photoproduction
$Q^2 < 0.01\,\mathrm{GeV}^2$	photoproduction
$N_{forward\,LAr\,clusters} = 0$	diffraction with limited proton dissociation
$N_{CJC\,tracks} = 2$	investigated processes
$1 < N_{SpaCal\,photons} < 10$	investigated processes

Table 3.3: *Cuts applied to the data and Pythia for their comparison.*

The photon structure [38] implemented in Pythia allows for photon dissociative events in which the photon turns into a vector meson ($V = (\rho^0, \omega)$) and subsequently into a diffractivelly excited state called V_{diff}. The diffractive excitation into V_{diff} takes place due to the photon interaction with the proton. The process is sketched in fig. 3.5. This kind of a process simulated by Pythia contributes to the investigated processes via: $\gamma p \to \eta(\pi^0)\rho^0 X$ through the ρ^0_{diff} decay: $\rho^0_{diff} \to \rho^0\,\eta(\pi^0)$. Since the *total* cross-section for diffractive $\rho^0\,\eta$ production will be determined, independently of its origin, the processes leading to $\eta\rho$ are excluded from the Pythia sample. The new model of Pythia is called PythiaMod. The treatment with the Pythia and PythiaMod models is discussed in chapters 5 and 6.

3.2.2 The Generator RapGap

RapGap (short for Rapidity Gap) [31] is a MC suited to describe Deep Inelastic Scattering (DIS), including diffractive DIS and LO direct and resolved (however only for transverse polarized virtual photons) processes. Standard hard scattering partonic cross section and parton showers are combined with the LUND string fragmentation model using the JETSET package [33, 35, 34]. The RapGap MC does not provide any model of soft underlying interactions in terms of multiple interactions.

The description of diffraction is based on the hard-pomeron model via two gluon exchange. In rapidity gap events the proton stays intact or becomes a low mass diffractive state, called p'. Within diffraction RapGap describes photoproduction as well as deep inelastic scattering. The emphasis in the analysis is on photoproduction.

Also RapGap is employed as a background MC in the analysis. In this model the main source of background to the investigated processes is expected from the quark scattering of the photon on a quark from the Pomeron and from the boson (photon) - gluon fusion shown in figure 3.6 a) and b), respectively. In a) the lowest order process for scattering

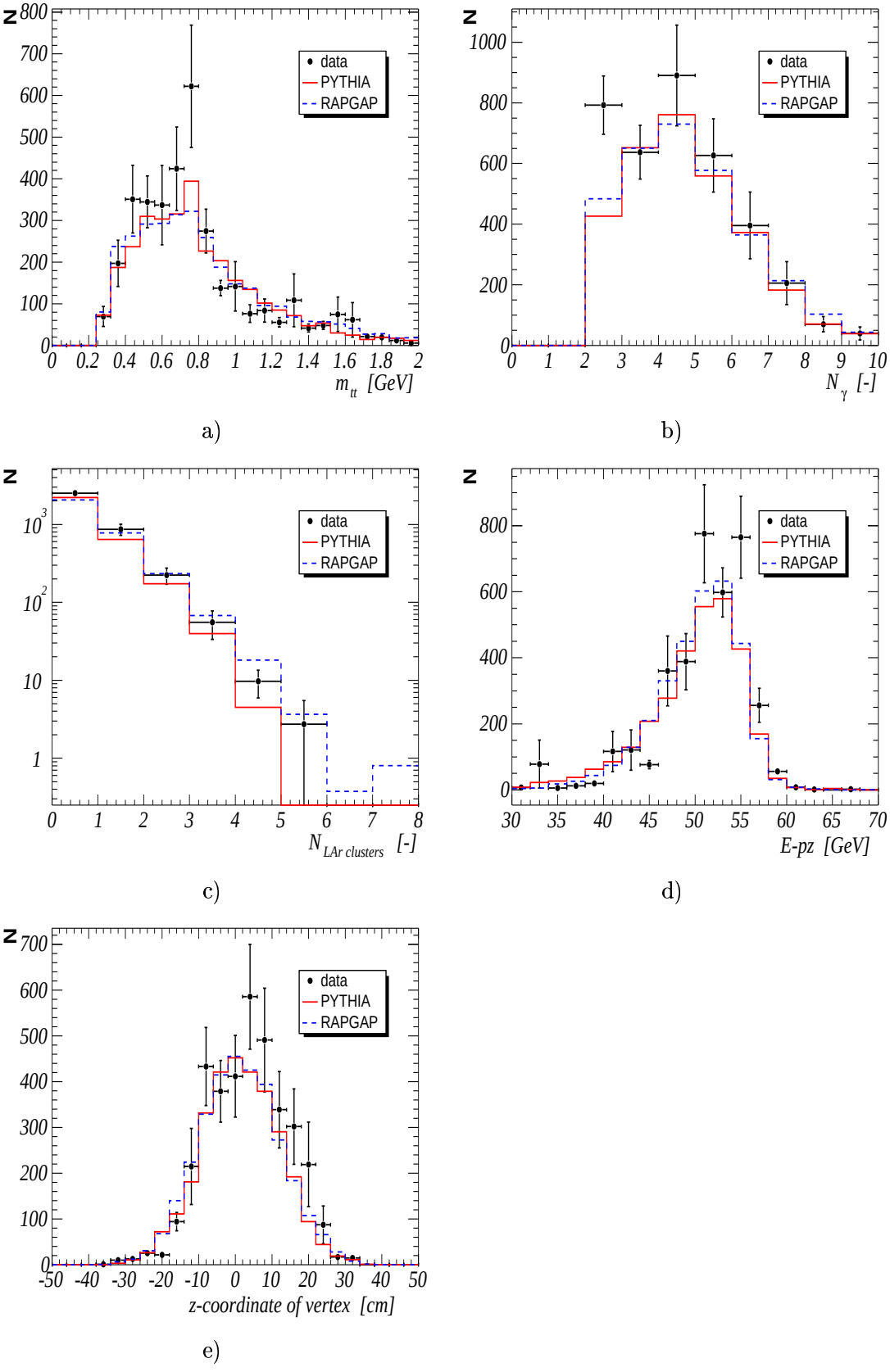

Figure 3.4: *Comparison of data to Pythia (solid-line histogram) and RapGap (dashed-line histogram) for the inclusive selection shown in table 3.3. a) indicates the invariant track-track mass, b) the number of photon candidates in the SpaCal calorimeter, c) the number of clusters in LAr calorimeter which are not associated with any track, d) variable $E - p_z$, e) z-coordinate of the vertex.*

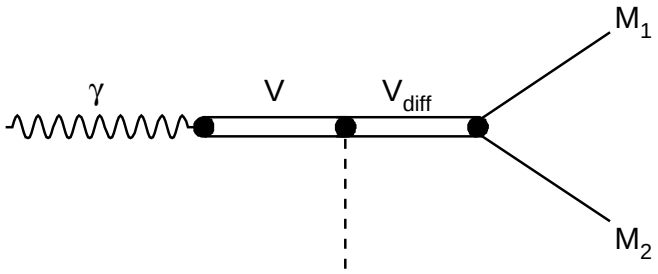

Figure 3.5: Diffractive dissociation as modeled by Pythia: *A photon is turned into a vector meson V according to VMD and subsequently interacts with the proton. This interaction excites the vector meson into a state called V_{diff}, that decays into two mesons* `M1` *and* `M2`.

quark, $ep \to e'q\bar{q}p' \to e'Xp'$, is illustrated. If the photon reacts with a quark q from the Pomeron, $I\!P$, an antiquark $\bar{q}$, of the same flavor but with opposite color is left. The scattered quark q' together with the left antiquark then fragments into a state `X`. This process is unfortunately in the photoproduction regime ($Q^2 \to 0$) incalculable in QPM and therefore not simulated by RapGap. If the photon reacts with a gluon from the Pomeron, a color octet remnant is left, here treated as a single gluon. This Pomeron remnant together with the $q\bar{q}$ from the hard interaction forms also a color singlet state X. This boson gluon fusion (BGF) from a resolved Pomeron is sketched in b).

The BGF has been simulated by RapGap under the assumption that only light quarks (LQ: u,d,s) and antiquarks are produced. In the comparison between the inclusive data sample and background MC's, applying the cuts in tab. 3.3 is shown in fig. 3.4. RapGap and Pythia agree with the data and therefore provide a reasonable tool for the background description. Also RapGap contributes to the investigated processes via fragmentation of the `X` state into $\eta - \rho^0$ and $\pi^0 - \rho^0$ state. However this contribution is one order smaller than from Pythia.

3.3 Monte Carlo Sets

In this section an overview over the kind and the amount of generated events is given for the signal MC ToyGen and both background MC's Pythia and RapGap. All samples were generated in the photoproduction regime requiring $Q^2 < 0.01\,\mathtt{GeV}^2$ and $0.25 < y < 0.85$ ($0.3 < y < 0.7$ for ToyGen).

Since the ToyGen signal MC does not provide any prediction of the cross-section the number of events is given instead of the integrated luminosity. For the $\pi^0 - \rho^0$ sample 250000 events were generated for the 1996 and also for the 2000 data taking period. The simulation for 1997 and 1999 data taking periods was omitted since the running conditions in 1997 were similar as for 1996 and in 1999 as for 2000 data taking period. Also for the $\eta - \rho^0$ sample the events were simulated and reconstructed only for 1996 and 2000, namely 200000 per year. The total amount of generated luminosity for background MC's is $59.61\,\mathtt{pb}^{-1}$ for Pythia and $37.38\,\mathtt{pb}^{-1}$ for RapGap, respectively. They are summarized

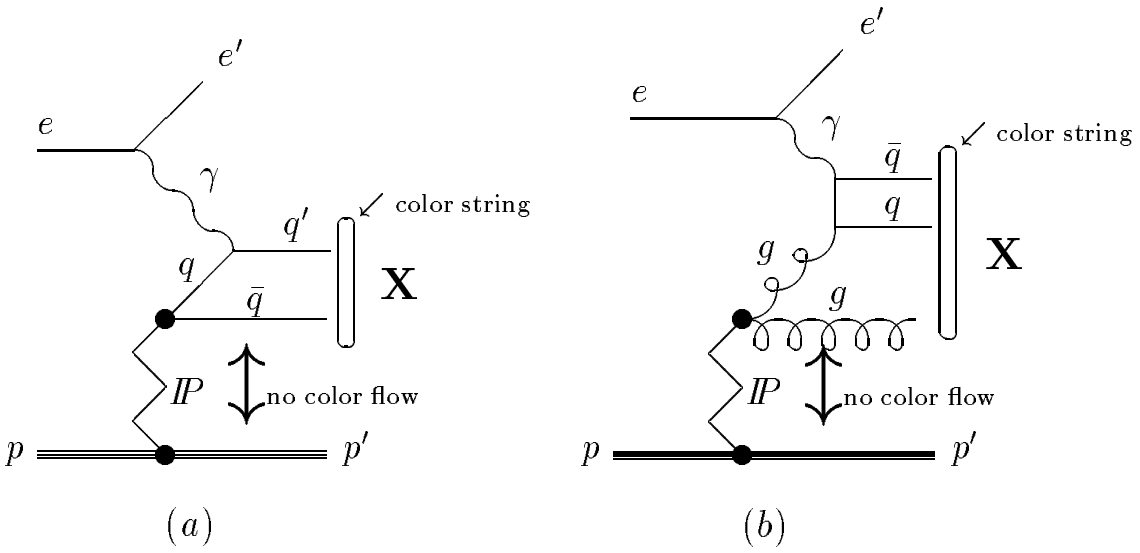

Figure 3.6: *a) lowest order $\mathcal{O}(\alpha_{elm})$ process for scattering quark of photon. b) $\mathcal{O}(\alpha_{em}\alpha_s)$ for boson (photon) gluon fusion with resolved Pomeron. The Pomeron remnant is a color octet gluon.*

	MC			
	ToyGenMod		Pythia	RapGap
generated process	$\gamma p \to \pi^0 \rho^0 p'$	$\gamma p \to \eta \rho^0 p'$	$\gamma p \to$ *anything*	$\gamma p \to q\bar{q}gp'$ (q =LQ)
kin. restrictions	$Q^2 < 0.01\,\mathtt{GeV}^2$, $0.3 < y < 0.7$		$Q^2 < 0.01\,\mathtt{GeV}^2$, $0.25 < y < 0.85$	
	Statistics			
year	Number of events		Integrated luminosity [$\mathtt{pb}^{-1}$]	
1996	250000	200000	17.08	9.33
1997	–	–	12.72	9.34
1999	–	–	12.49	9.32
2000	250000	200000	17.32	9.39
Total	500000	400000	59.61	37.38

Table 3.4: *Summary on the processes generated by ToyGen, Pythia and RapGap: kind of the generated process, restrictions on the kinematics of the process and its statistics for 1996, 1997, 1999, 2000.*

in table 3.4.

For the Monte Carlo sets to be directly compared to the data, the corresponding distributions are scaled by factors $\mathcal{L}_i = \mathcal{L}_{data}/\mathcal{L}_{MC}$, where $\mathcal{L}_{MC}$ is the luminosity for MC shown in table 3.4.

Chapter 4

Data Selection

In this chapter the selection of data will be discussed: Firstly the signatures of the investigated processes in the H1 detector are described, then, run quality criteria and the trigger selection.

The H1 experiment is collecting a huge amount of events originating from a large variety of physics processes in so called *luminosity runs* under nearly constant experimental conditions. The run period of data taking between filling and dumping of electrons or protons is called *luminosity fill*. Since not all data for this analysis have the appropriate run quality, quality criteria for the runs are discussed in this chapter. For any analysis of exclusive processes only a subset of this large amount of data, defined by the topology of the investigated processes, is needed. These selection criteria defined by the topology of exclusive double meson photoproduction are described as well.

Each event had to pass the H1 trigger system which means that the event has been taken with certain trigger conditions, defined by subtriggers. To control the amount of output data from different trigger levels, the subtriggers can be prescaled. The treatment of the prescale factors applied to the subtriggers used is also discussed. Since with rising number of subtriggers the calculation of the prescale corrections becomes very complicated, an appropriate number of subtriggers with acceptable prescales is chosen.

At the end the efficiency is investigated from two different points of view: firstly constraints on the rapidities of the π^0, η and ρ^0 mesons to exclude inefficient detector regions are determined and secondly the correction factors for the cross sections are obtained.

4.1 Signatures and Event Selection in the H1 Detector

In order to study exclusive double meson photoproduction, one looks for an exclusive coincidence between a ρ^0 meson in the central detector region and a π^0 (η) meson in the backward region.

Since the central tracking system provides excellent momentum measurement the dominant decay mode of the ρ^0 meson leading into $\pi^+\,\pi^-$ pairs is used for the identification of the ρ^0 mesons:

$$\rho^0 \to \pi^+\pi^-, \quad BR(\rho^0 \to \pi^+\pi^-) \sim 100\,\%,$$

where BR denotes the branching ratio of the $\rho^0 \to \pi^+\pi^-$ [37]. The charged pions passing the active chamber volumes produce hits which are combined into tracks by the H1 reconstruction software package, H1REC. The tracks are used to determine the interaction vertex using the central tracking detectors (CTD). The presence of a magnetic field allows to determine momentum and the sign of the charge of the particle. Exactly two tracks with unlike-sign charges reconstructed from the primary vertex are required.

On the other hand H1 provides good measurement of electromagnetically interacting particles in the backward electromagnetic calorimeter SpaCal. Therefore the decay modes of the backward mesons π^0 and η leading into pure multi-photon final state are used for their identification:

$$\begin{aligned} \pi^0 \to \gamma\gamma, \quad & BR(\pi^0 \to \gamma\gamma) = 98.8\,\% \\ \eta \to \gamma\gamma, \quad & BR(\eta \to \gamma\gamma) = 39\,\% \end{aligned}$$

BR denotes the branching ratio for a given decay [37]. Each of the photons is detected as an electromagnetic cluster. Thus η and π^0 mesons are identified via two electromagnetic clusters. In order to be able to reconstruct the kinematics and to suppress DIS background, when the scattered electron produces an electromagnetic shower in the SpaCal and is misidentified as a photon, the electron has to be detected in one of the electron taggers. Out of three electron taggers with different inelasticity acceptances provided by H1 the tagger located at 33 meters from the interaction point has been chosen because of its largest acceptance in y ($0.3 < y < 0.65$) [94]. The signatures with a schematic view of the important devices of H1 are depicted in figure 4.1 and listed in table 4.1.

signature	device
existence of a primary vertex	CTD
$N_{central\,track} = 2$ reconstructed from the primary vertex, $q_1 \cdot q_2 = -1$	CTD
detected electron	eTag_{33}
$N_{cluster} = 2$	SpaCal

Table 4.1: *Event selection summary of the investigated processes with the devices in which the final state particles are detected.*

The region in which all decay products can be detected is defined by the geometrical acceptance of the detector components. Since the reconstruction of the tracks is based on the CJC, the rapidity acceptance for the tracks is limited via the CJC acceptance: $-1.5 < Y_{track} < 1.5$. The rapidity of the clusters is limited due to the SpaCal acceptance: $-3.5 < Y_{cluster} < -1.5$, see fig. 4.1. The limits on the rapidities applied to the clusters and tracks due to the detector acceptances are summarized in table 4.2.

In order to assign the SpaCal clusters to photons, tracks to the charged pions, and energy deposition in the electron tagger to the electron efficiently, the selection criteria for photon, pion and electron candidates are discussed in the following.

4.1.1 From Clusters to Photons - Selection Criteria

The π^0 (η) mesons are identified via their purely photonic decays. The two photons produce electromagnetic showers in the backward calorimeter SpaCal. Although DIS back-

$$\begin{array}{|c|}\hline -1.5 < Y_{track} < 1.5 \\ -3.5 < Y_{cluster} < -1.5 \\ \hline \end{array}$$

Table 4.2: *The cuts applied to the rapidity of the tracks and clusters due to subdetector acceptances.*

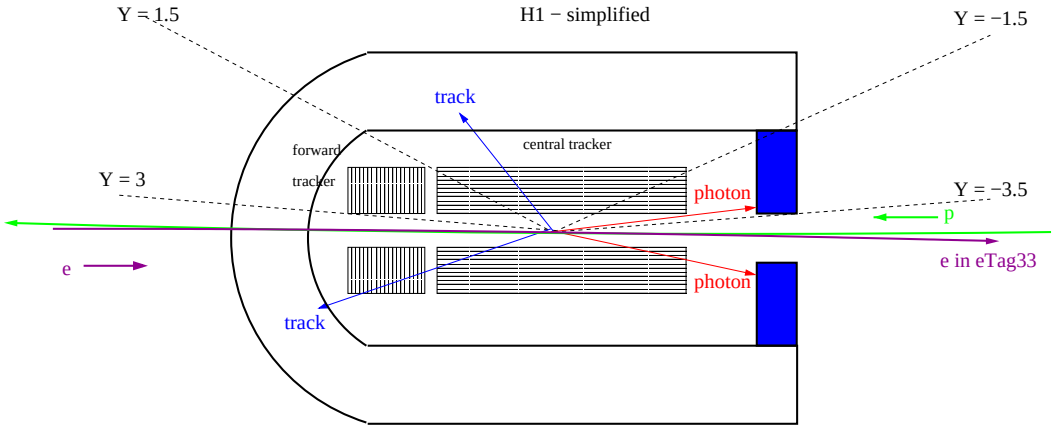

Figure 4.1: *The signatures of the investigated processes at H1, two clusters in the SpaCal coming from the π^0 or η and two unlike-sign tracks in the central tracking system coming from the ρ^0. The electron is measured in the electron tagger located at 33 m from the nominal interaction point.*

ground should be efficiently suppressed by requiring an electron in the tagger, diffractive background leading to jets in the SpaCal, mostly charged pions, has to be eliminated. A good possibility to distinguish between photons and hadrons are the transverse and longitudinal shapes of the SpaCal showers. Photons produce much more compact clusters than hadrons. The consequence is a difference in the cluster radius. In addition to the cluster radius requirement a cut on the ratio between the cluster energy deposited in electromagnetic and hadronic SpaCal is imposed to reject hadronic showers. In order to ensure reliable energy measurement a cut on the radial distance of the cluster from the beam line and a noise cut are imposed. The selection criteria for photon candidates are summarized in table 4.3.

motivation	cut
to separate hadrons and photons	$R_{cluster} \in (0,3)$ cm $E^{had}_{cluster} / E^{em}_{cluster} < 0.01$
noise cut	$E^{em}_{cluster} > 100$ MeV
fiducial cut	$RD_{cluster} \in (8,75)$ cm

Table 4.3: *Summary of requirements to select a photon candidate with fiducial cut on the radial distance of the cluster from the beam line.*

Here denote:

- $E^{em}_{cluster}$ and $E^{had}_{cluster}$ - cluster energy deposited in the electromagnetic and hadronic part of the SpaCal, respectively. As photon candidates are treated only those clusters for which the contribution from the hadronic part is less than 1%,. The efficiency of the cut has been studied in [65]. A cut of 100 MeV on the electromagnetic cluster energy corresponding to $\sim 3\sigma_{\text{noise}}$ [66] is applied to reject noise.

- $R_{cluster}$ - cluster radius. Only clusters with a finite radius $R_{cluster} > 0$ and $R_{cluster} < 3$ cm [65] are considered to be photon candidates.

- $RD_{cluster}$ the radial distance of the energy deposition from the beam line. The fiducial cut $RD_{cluster} \in (8,\ 75)$ cm is required to avoid shower leakage at the borders of the SpaCal.

Clusters with $E_{cluster} < 100$ MeV are ignored and considered as noise. Due to an acceptance overlap between CJC and SpaCal the charged pions from the ρ meson decay, defined in next chapter, can produce a cluster in the outermost part of the SpaCal. To save such events, clusters associated with one of the tracks are ignored for the photon selection, independent of their hadronic energy fraction. Otherwise events with a cluster with a large hadronic energy fraction are assumed to be contaminated by hadrons and are excluded. The events with clusters violating the 'fiducial cut' condition suffer from energy leakage and are also excluded.

4.1.2 From Tracks to Pions - Selection Criteria

The ρ^0 meson is identified through its dominant pionic decay. The decay products π^+ and π^- are detected in the central jet chamber (CJC). The charged pions passing the CJC produce hits from which tracks are reconstructed. One example of a CJC track is shown in fig. 4.2. The main track quality parameters defining the tracks in H1 are plotted

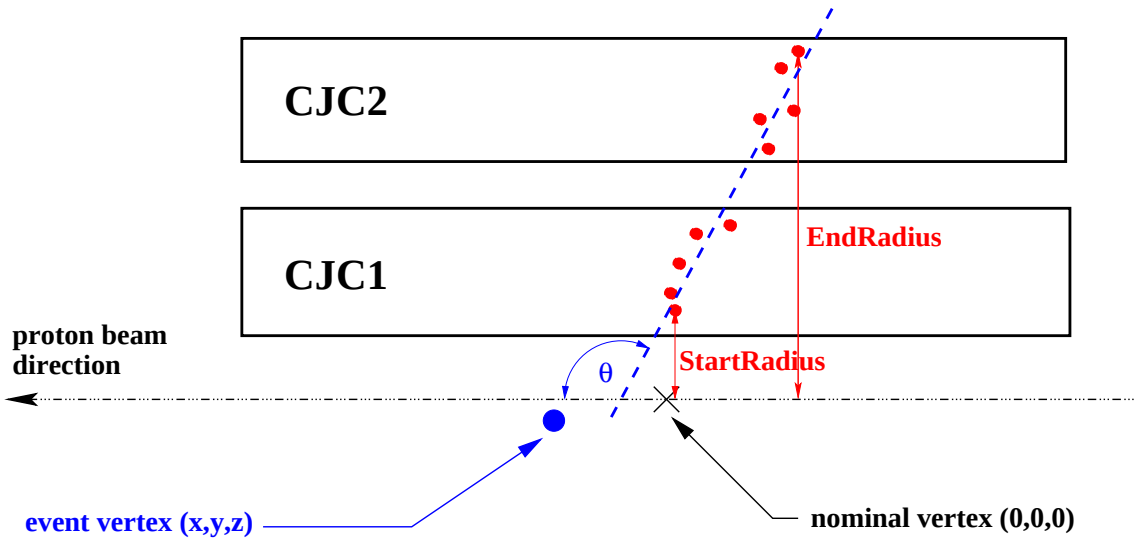

Figure 4.2: *CJC track in z-R plane*

in fig. 4.3. The parameter *dca* is defined as the distance of closest approach in the x-y plane to the nominal vertex position [x = 0, y = 0]. The main kinematical variables for a track classification are its polar, θ, and azimuthal, ϕ, angle, respectively, and transverse momentum p_t with respect to the beam direction. Both, azimuthal and polar angles are considered with respect to the reconstructed vertex. Only tracks fulfilling certain quality criteria are considered as pion candidates. In this analysis the standard H1 software package from Lee West [72] is used to select 'good tracks'. It contains a set of cuts on kinematical and quality parameters which are summarized in table 4.4, where:

- p_t - transverse momentum of track; 150 MeV is the lowest value at which tracks can be reliably measured by the CJC.
- θ - polar angle of the track (fig. 4.2); cuts of 20° and 160° are imposed by the acceptance limits of the CJC.
- StartRadius (fig. 4.2); radial distance of the first hit produced by the tracks in the x-y plane to the nominal vertex position. By setting an upper limit on the StartRadius one avoids that the track starts far from the interaction point. The cut of 50 cm demands the beginning of the track in CJC1.
- *dca* (fig. 4.3) - distance of closest approach calculated with respect to the primary vertex. By setting an upper limit the tracks lying far from the vertex in the x-y plane are rejected. An upper limit of 2 cm is considered with respect to the nominal vertex.
- $\mathrm{R_{lenght}}$ - track length in the x-y plane. It is the radial difference between the last hit, EndRadius, and first hit, StartRadius, in the CJC. The cut removes short tracks.
- RPTHPHTH - variable used to remove unreliable parts of the central tracks which were split into two tracks due to reconstruction problems.

Track selection	$p_t > 0.15\,\mathrm{GeV}$ $20.0° < \theta < 160.0°$ $\mathrm{StartRadius} < 50.0\,\mathrm{cm}$ $\lvert\mathrm{dca}\rvert < 2.0\,\mathrm{cm}$ $\mathrm{R_{lenght}} > 10.0\,\mathrm{cm}$, for $\theta < 150.0°$ $\mathrm{R_{lenght}} > 5.0\,\mathrm{cm}$, for $\theta > 150.0°$ $\mathrm{RPTHPHTH} = 1.0$
Background rejection	$\lvert z\_Vtx\rvert < 30\,\mathrm{cm}$
Pion hypothesis	$m = 139.57\,\mathrm{MeV}$

Table 4.4: *Summary of the requirements to select a good track. It is assumed that all particles produced the tracks are charged pions.*

In this analysis no method for identification of the mass of the particles is used and therefore it is assumed that all particle candidates obtained from the track selection are charged pions (have a mass of charged pions $m = 139.57\,\mathrm{MeV}$).

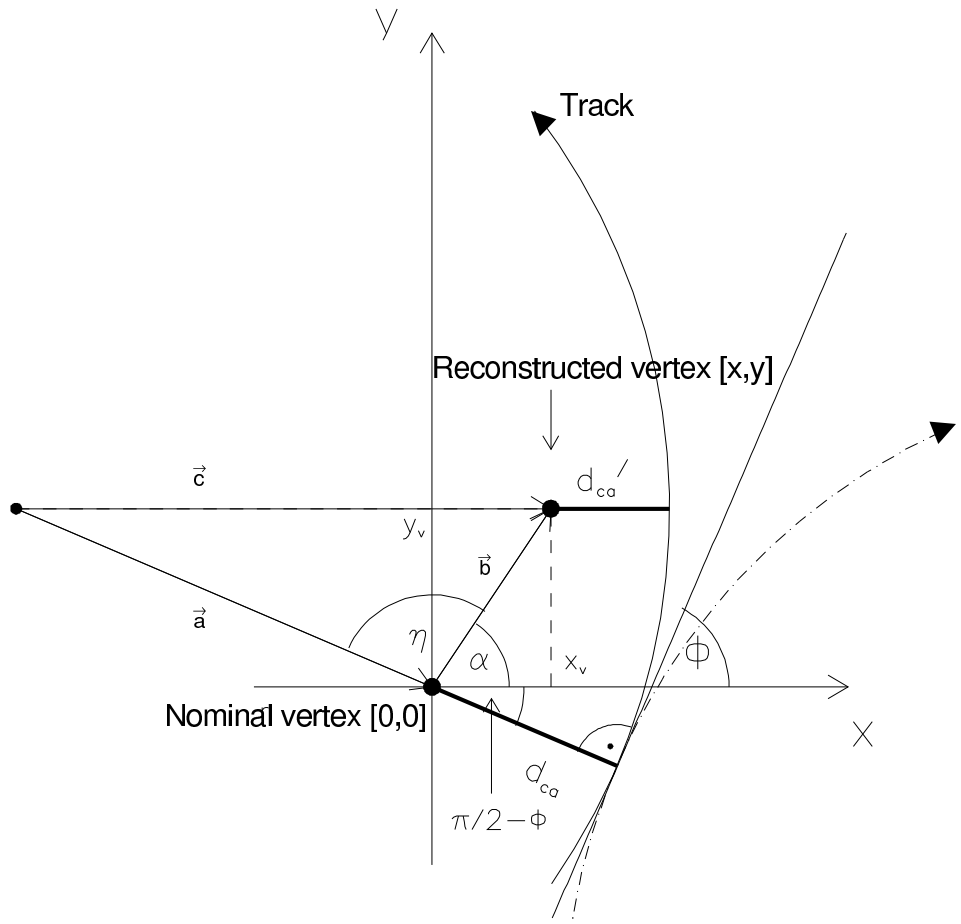

Figure 4.3: *Track reconstruction: The curve illustrates the reconstructed track. Also important variables for the track definition are shown: the nominal* $[0,0]$ *and reconstructed* $[x,y]$ *vertex, the distance of closest approach* `dca` *with respect to the nominal vertex position and the azimuthal angle* Φ.

Both tracks have to be reconstructed from the primary vertex. In order to reject interactions from satellite bunches the z-coordinate of the vertex (z-Vertex) has to be within 30 `cm` of the nominal vertex. A comparison between the simulated and data z-Vertex distributions is shown in figure 4.4.

4.1.3 Photoproduction Selection - Electron Selection

Photoproduction events are selected by demanding the scattered electron to be detected in the electron tagger eTag_{33}. This restricts the photon virtuality to $Q^2 < 0.01\,\texttt{GeV}^2$ and the inelasticity roughly to $0.3 < y < 0.65$ (see fig. 4.5). To select a 'good electron' the criteria shown in table 4.5 are applied.

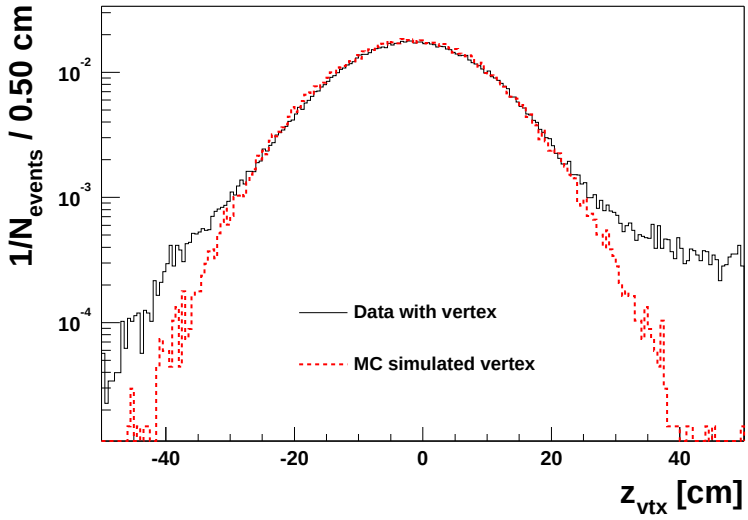

Figure 4.4: *z-coordinate of the vertex with respect to the nominal vertex* $(0, 0, 0)$

$0.3 < y < 0.65$
$X_{eTag33} < 6.5\,\mathtt{cm}$
$E_{PD} < 2\,\mathtt{GeV}$

Table 4.5: *Summary of the requirements to select 'good electron'*

The variables used are:

- y denotes the inelasticity defined in eq. (2.8), The inelasticity region (0.3, 0.65) has been chosen to ensure the acceptance to be higher than 10% (see fig. 4.5).
- X_{eTag33} denotes the x coordinate of the impact point of the electron, the cut of $6.5\,\mathtt{cm}$ is applied to minimize the energy leakage at the border of the tagger
- E_{PD} is the energy measured in the photon detector. In the Bethe-Heitler (BH) process, used for luminosity measurements, the photons are detected in the photon detector whereby the electron can scatter into the electron tagger. In this topology the photon energy in BH events is higher than 2 `GeV`, therefore to avoid overlap between a BH event and a photoproduction event, the energy in the photon tagger is required to be less than 2 `GeV`.

4.1.4 Electron Tagger Acceptance

The efficiency ϵ_{eTag33} of the electron as a function of inelasticity y was determined with the help of the software package QPETAC [92]. QPETAC supplies a run dependent tagger acceptance as a function of inelasticity y if the electron is scattered into the fiducial region $X_{eTag33} < 6.5\,\mathtt{cm}$. As an example for one run in 1996 the acceptance is shown in figure 4.5. The mean efficiency is $\langle \epsilon_{eTag33} \rangle \approx 0.5$ which means that on average the tagger detects only every second electron. This value is also used for the cross section determination.

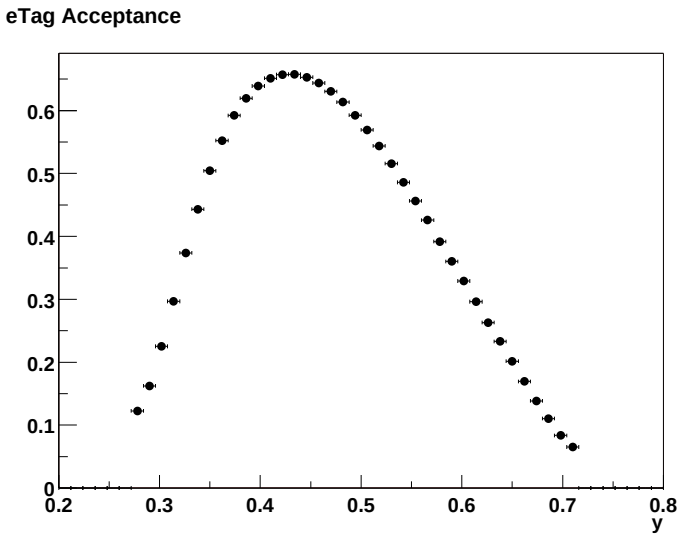

Figure 4.5: *Electron tagger acceptance as a function of the inelasticity y defined in (2.8)*

Since H1 does not provide a simulation of the electron tagger and the corresponding trigger elements, the MC events in the tagged photoproduction have to be weighted according to their acceptances ϵ_{eTag}.

4.2 Final Selection

In addition to the preselection (table 4.1) further cuts are applied: In order to ensure a rapidity gap between the proton or its remnant and the ρ^0 meson no activity in the forward region of the LAr calorimeter was demanded. To ensure exclusivity of the investigated processes no activity in the central LAr calorimeter, aside the clusters assotiated with the tracks from $\pi^{\pm}$, was required. Under 'no activity' one understands no LAr cluster above 500 MeV. Another condition to ensure exclusivity and a fully measured event, except the scattered proton, is a cut on $\mathtt{E} - \mathtt{p}_z$, defined in eq. (2.75), to be between 50 and 60 GeV. The final selection is summarized in table 4.6.

motivation	final cuts
diffraction at proton vertex	$\mathrm{N}(\mathrm{E}_{LAr\_cluster} > 500\,\mathtt{MeV}) = 0$ in forward LAr
exclusivity	$\mathrm{N}(\mathrm{E}_{LAr\_cluster} > 500\,\mathtt{MeV}) = 0$ in central LAr not conected to any track
fully measured event	$50\ \mathtt{GeV} < \mathtt{E} - \mathtt{p}_z < 60\ \mathtt{GeV}$

Table 4.6: *Final selection summary to ensure exclusivity, diffraction at the proton vertex and a fully measured event.*

4.3 Run Selection

The present analysis is based on the data accumulated by the H1 detector during four years, 1996-2000, except 1998. In 1998, HERA switched from running with positrons to electrons. The background conditions could not be improved adequately to run reasonably with the tracking detectors. Therefore the data teakig period of the year 1998 is omitted.

The runs used for the present analysis had to pass the following quality cuts:

- **Excluded runs:** The following run periods were excluded from the data sample 1996 - 2000 taken by the H1 experiment:
  - at the end of 1997 and 1999, so called 'minimum bias'[1] runs with different trigger settings
  - runs with a shifted z-position of the vertex in 2000 due to different kinematics of the events
  - all runs $Run > 257601$ in 1999 [67]: in October 1999, one wire in the inner central jet chamber (CJC1) broke and caused a 'hole' of approximately 20° in ϕ.
  - The run period upto run 157877 in 1996 because of different trigger settings (see chapter 4.4).
  - The run period in 1999 with running with electrons
- **Run quality: Medium or good.** Each run can be classified as 'Good', 'Medium', or 'Poor' according to the current status of detector components. Poor runs have been excluded, since many detector components didn't work properly over a significant part of run time.
- **Trigger phase > 1**: At the beginning of each luminosity fill, the trigger phase one is set up. During this phase the trackers are ramped and very high prescales are applied. Different trigger phases during data taking within one lumi fill correspond to different prescale factors. Because of high prescales the phase 1 is excluded.
- **High voltage (HV) sub-detector status.** The HV status of the detector components used for the analysis (LAr, SpaCal, CJC, ToF) had to be fully functional during more than 80% of the full run time. Events in accepted runs with some components not working, were excluded from the analysis, and the luminosity of the run was correspondingly corrected.

The collected luminosity for the different data taking periods and the impact of the run selection criteria are summarized in table 4.7. H1 has collected 117.26 $\mathtt{pb}^{-1}$ over the four years 1996, 1997, 1999 and 2000. About 65% of the data sample survives the run selection which means about 76 $\mathtt{pb}^{-1}$ to be analysed. The main reduction of the luminosity is caused by the 'excluded runs' condition and the 'trigger phase' requirement, about 10%. The reduction due to the 'run quality' selection is about 7.3% and the 'HV subdetector status' about 5%. Since raw luminosity also includes sattelite bunches, therefore has to be corrected for analyzed z-Vertex range.

4.4 Trigger Selection

For choosing a proper subtrigger combination aspects like trigger efficiency, L1 subtrigger prescales and the number of triggers play a key role. The prescale is an important issue

[1] the events taken with more inclusive trigger conditions

		1996	1997	1999 e^+p	2000	Sum
proton beam energy	[GeV]	820	820	920	920	
Total raw luminosity	[pb^{-1}]	9.89	27.95	19.33	60.09	117.26
Excluded runs (see text)	[pb^{-1}]	7.35	24.91	14.2	59.26	105.72
G+M Runs	[pb^{-1}]	7.11	21.61	13.34	56.02	98.08
Trigger Phase 2-4	[pb^{-1}]	6.88	17.08	11.16	52.35	87.47
HV ok + corr	[pb^{-1}]	6.10	16.33	9.99	48.00	80.42
z-Vtx	[pb^{-1}]	5.67	15.23	9.54	45.78	76.21

Table 4.7: *Integrated luminosity from 1996-2000.*

mainly because of statistics collected by a given subtrigger. The number of selected subtriggers is restricted because of the calculation difficulty of the L1 prescale correction (see chapter 4.5). According to the topology of the processes and as a compromise among all above mentioned issues the following trigger combination was chosen:

$$\begin{array}{lll} s50 & & \text{Run} \leq 193433 \\ s50 \;\|\; s61, & & \text{Run} > 193433 \end{array} \tag{4.1}$$

Subtrigger s50 was a special trigger for backward meson photoproduction. Subtrigger s61 was a general inclusive SpaCal trigger designed to measure the scattered electron in DIS.

	1996 Run > 157877	1997	1999 e^+p :Run< 257601 /2000
s50 Run > 157877	L1: eTag && (IET> 1||IET_cen_2) L2: $R20$	L1: eTag && (IET> 1||IET_cen_2) L2: $R20 \rightarrow R30$ in Run = 198827	L1: eTag && (IET> 1||IET_cen_2) L2: $R30$
⟨L1 prescale⟩	1.16	1.65 / 1.51	1.26 / 2.06
s61 since 28.6.97 Run > 193433		DCRϕ_Thigh && $zVtx$ && (IET> 1||IET_cen_2)	DCRϕ_Thigh && $zVtx$ && (IET> 1||IET_cen_2)
⟨L1 prescale⟩		1.0	1.03 / 1.16

Table 4.8: *Definition of the subtriggers s50 and s61 with their averaged L1 prescales.* $R20 \rightarrow R30$ *denotes the change of the subtrigger condition.* 1.65 / 1.51, 1.26 / 2.06 *and* 1.03 / 1.16 *denote the* ⟨*L1 prescale*⟩ *for different run periods.*

The exact definition of the subtriggers are shown in table 4.8, where || and && mean logical 'OR' and 'AND', respectively. The subtriggers contain trigger elements of three different detector systems: IET derived from SpaCal clusters, DCRϕ from CJC information and zVtx from the proportional chambers. All subtriggers contain in addition global trigger elements which ensure that the events come from a nominal bunch crossing and not from an interactions behind or in front of the H1 detector. The definition of the trigger elements which the subtriggers consist of is discussed in chapter 1.8.1.

The runs before 157877 have been excluded because of a different s50 subtrigger setup (TE IET_cen_2 has been included into the subtrigger since this run). The data in the run periods 1996 and 1997 (up to run 193433) have been selected by subtrigger s50 only. Starting with the run 193433 the events have been selected by the subtrigger combination 's50 || s61'. The averaged L1 prescales over a year for both subtriggers are shown in table 4.8. In the 1997 period prescale factors 1.65 and 1.51 for $s50$ corrospond to the period of Run $<$ 198827 (L2TT:$R20$) and Run $>$ 198827 (L2TT:$R30$). For the determination of the correction on the prescales and the trigger efficiency the data sample in 1997 has been split into three periods according to the change of $R20$ in the run 198827 to $R30$ and including subtrigger s61 from the run 193433 onwards: Run $<$ 193433, 193433 $<$ Run $<$ 198827 and Run $>$ 198827. This separation of the run periods according to any change of subtrigger settings is essential for the TE efficiency determination and correction of prescaling.

In the following the trigger efficiencies and the correction of the data for the trigger effciency are determined.

4.4.1 Trigger Element Efficiencies

The efficiencies of trigger elements are usually not 100%. These inefficiencies can be determined in two ways: 1) Either the trigger efficiencies will be obtained from Monte Carlo and applied to the data or 2) the correction on the trigger efficiencies are obtained directly from the data sample. The efficiencies of main trigger elements (TE) will be studied in the following. The efficiencies of global trigger elements have been studies in many analyses [87, 88], they are close to 100%.

The large amount of data available for the trigger efficiency determination allows to obtain inefficiencies from data and to correct the data with them. For the trigger element efficiency determination a data sample independent of the data sample taken with the investigated (tested) trigger is needed. Therefore another event sample has been selected by so called reference subtriggers. The efficiency is then determined as the ratio between the total number of the events selected by the investigated TE and by the reference subtrigger additionally and the number of events selected by the reference subtrigger, as a function of the quantity x:

$$\epsilon(x) = \frac{N_{test\&\&ref}(x) \ \&\& \ \texttt{particle\_candidate}}{N_{ref}(x) \ \&\& \ \texttt{particle\_candidate}}. \tag{4.2}$$

If the efficiency is below 100% the error is [89]:

$$\Delta\epsilon(x) = \sqrt{\frac{\epsilon(x)(1-\epsilon(x))}{N_{ref}}}. \tag{4.3}$$

If $\epsilon = 100\%$ the lower limit for a 67% confidence level for the efficiency was used:

$$\epsilon_{min}(x) = (1 - 0.67)^{1/N_{ref}} \tag{4.4}$$

where x is a variable with respect to which the efficiency is determined (i.e. cluster energy, p_t, θ, ...). $N_{test\&\&ref}$ is the number of the events accepted by the investigated trigger element 'AND' the reference subtrigger, N_{ref} is the number of the events accepted by the reference subtrigger. '`particle_candidate`' will be in this analysis either 'good track' defined in 4.4 or a photon candidate described in 4.3, depending on the trigger element studied.

4.4.2 Trigger Efficiency of Subtrigger s50

In the subtrigger s50 the L1 SpaCal trigger elements (TE's) $IET > 1$ and IET_cen_2 are supplemented by the L2TT condition $R20$ ($R30$) demanding the cluster to have a radial distance from the beam line, RD, larger than 20 (30) `cm`.

The trigger efficiency of subtrigger s50 is determined via the efficiencies of all its trigger elements: $IET > 1$, IET_cen_2, $R20$, $R30$ and $eTag$. Since the trigger efficiency of the electron tagger is included in the electron tagger acceptance (through QPETAC) the efficiency of s50 depends on the efficiencies of the independent SpaCal trigger elements: IET[2] (ϵ_{IET}), and R (ϵ_{R}), only, as their product $\epsilon_{s50} = \epsilon_{IET}\,\epsilon_R$. Since $IET > 1$ and IET_cen_2 have the same thresholds their efficiency has been studied commonly applying logical 'OR' between them in eq. (4.2). The trigger efficiency ϵ_{IET} is studied as a function of the energy of the 'hottest cluster'[3] $\epsilon_{IET} = \epsilon_{IET}(E_{hot})$. The trigger efficiency ϵ_R is studied as a function of the radial distance RD of the furthest cluster[4] RD, $\epsilon_R = \epsilon_R(RD)$. In both cases subtriggers s83 and s84, not containing any SpaCal trigger elements, are used as the reference subtriggers:

$s83: \; DCRPh\_Tc\&\&zVtx\_sig\&\&eTAG$
$s84: \; DCRPh\_Tc\&\&zVtx\_sig\&\&(LU\_ET\_44\&\&!LU\_PD\_low\&\&!LU\_WatVet)$

The total efficiency of s50, $\epsilon_{s50}(E, RD)$, is given as the product of the independent efficiencies of $\epsilon_{IET}(E_{hot})$ and $\epsilon_R(RD)$:

$$\epsilon_{s50}(E, RD) = \epsilon_{IET}(E)\,\epsilon_R(RD) \tag{4.5}$$

The efficiency determination of $\epsilon_{IET}(E)$ is shown in figure 4.6 a), using formula 4.2 with `particle_candidate` to be a photon candidate defined by the cuts in table 4.3. As an example for 1996 the events accepted by the combination of reference subtriggers '$s83 \parallel s84$' are shown by the solid histogram and the events accepted by $IET > 1 \| IET\_cen\_2$ trigger elements additionally by the dashed histogram as a function of the energy of the hottest cluster. The ratio of both histograms is shown in figure 4.6 b) as black full points. The same procedure has been used for the determination of efficiencies for $R20$ and $R30$. They are depicted in figure 4.6 c) $\epsilon_{R20}(RD)$ as an example for 1996 and d) $\epsilon_{R30}(RD)$ for 2000. For the $R20$ and $R30$ distributions the energy of the furthest cluster has to exceed 2.5 `GeV` to be independent of the cluster energy condition.

The efficiencies were fitted with the Fermi function

$$\epsilon_{IET}(E) = \frac{\epsilon_{max\_IET}}{\exp\left(\frac{E_{Th}-E}{E_{widht}}\right)+1} \tag{4.6}$$

and

$$\epsilon_R(RD) = \frac{\epsilon_{max\_R}}{\exp\left(\frac{RD_{Th}-RD}{RD_{width}}\right)+1} \tag{4.7}$$

where ϵ_{max_IET} (ϵ_{max_R}), E_{Th} (RD_{Th}) and E_{widht} (RD_{width}) denote the parameters of the Fermi fit:

[2] In this subsection the common notation IET is used for $IET > 1$ and IET_cen_2, and R for $R20$ and $R30$.

[3] the cluster with the maximum energy

[4] cluster with biggest radial distance from the beam line

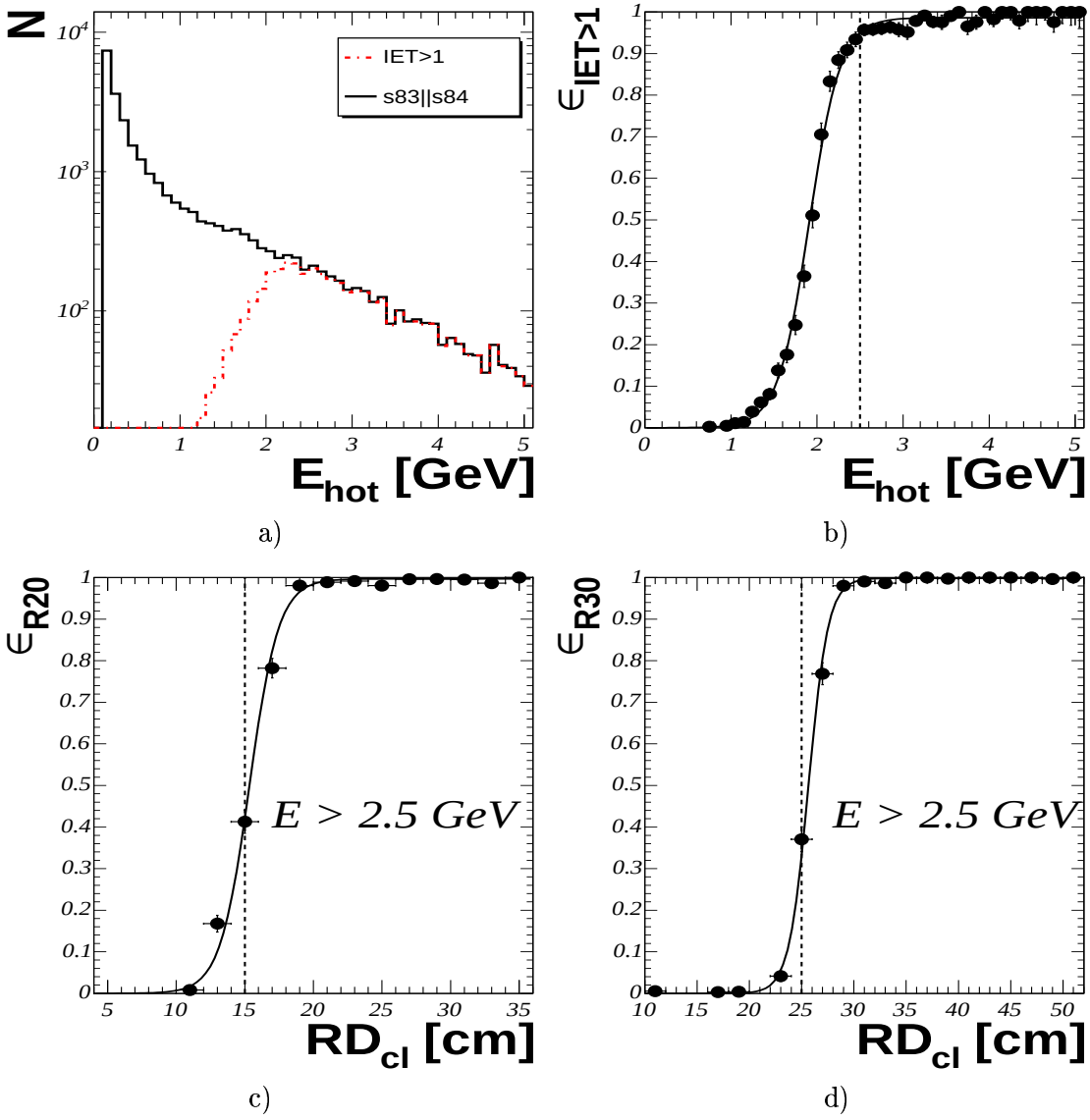

Figure 4.6: The trigger element efficiencies of IET, $R20$ and $R30$ elements: *a)* the solid (dashed) histogram illustrates the energy distribution of the hottest cluster selected by reference subtriggers s83||s84 ((s83||s84) && IET). Parts b), c) and d) show trigger element efficiencies for data of IET> 1 || IET_cen_2, $R20$ and $R30$, respectively. The curves show the fit functions. The vertical dashed lines indicate the energy and radius limits applied in the analysis.

- ϵ_{max_IET} (ϵ_{max_R}) is the maximum efficiency of the IET (R) trigger element.
- E_{Th} (RD_{Th}) is the energy (radial distance) threshold for the IET (R) trigger element.
- E_{widht} (RD_{width}) denotes the width of the threshold.

Inserting 4.6 and 4.7 into 4.5 one gets for the total efficiency of s50:

$$\epsilon_{s50}(E, RD) = \frac{\epsilon_{max\_IET} \quad \epsilon_{max\_R}}{\left[\exp\left(\frac{E_{Th}-E}{E_{widht}}\right)+1\right]\left[\exp\left(\frac{RD_{Th}-RD}{RD_{width}}\right)+1\right]} \tag{4.8}$$

From the efficiency distributions one observes that the maximum efficiency of subtrigger s50 demands at least one cluster with the energy above 2.5 GeV and radial distance above 20 (30) cm. The impact of these cuts on the statistics of the final ($\eta - \rho^0$) sample is shown in figure 4.7: where the energy versus radial distance of all clusters for the events selected by subtrigger s50 is plotted: In a) for the events in the run period selected by the $R20$ and in b) selected by the $R30$ condition. While the requirement on the cluster energy of 2.5 GeV does not reduce the statistics, the requirement on the radial distance reduces the statistics significantly. Therefore, to save statistics, the lower cuts corresponding to an efficiency of more than 40% have been chosen: a cut of 15 cm for the run period Run $<$ 193433 selected by $R20$ and a cut of 25 cm for the run period Run $>$ 193433 selected by $R30$ condition. The cuts and their impact on the efficiency are summarized in table 4.9.

The trigger element efficiencies of ($IET > 1 \parallel IET\_cen\_2$), $R20$ and $R30$ trigger elements for all year periods are shown in Appendix A in figure A.1 in the first, third and fourth row. All the fit parameters with χ^2/ndf of the SpaCal TE's are listed in table A.1. The distributions show the stability of all fit parameters for all trigger elements over the run period 1996-2000. The maximum efficiency of IET is $\epsilon_{max\_IET}(E) \sim 98\%$ for 1996 and very close to 100%, for other of years. The maximum efficiency for the L2TT trigger element, R, is $\epsilon_{max\_R}(RD) \sim 100\%$ over all periods.

cut	ensured efficiency
$E > 2.5$ GeV	$\epsilon_{IET}(E > 2.5\text{GeV}) > 98\%\, \epsilon_{max\_IET}(E)$
$RD > 15$ cm for $R20$	$\epsilon_{RD}(RD > 15\text{cm}) > 40\%\, \epsilon_{max\_R}(RD)$
$RD > 25$ cm for $R30$	$\epsilon_{RD}(RD > 25\text{cm}) > 40\%\, \epsilon_{max\_R}(RD)$

Table 4.9: *Summary of the cuts applied to the events selected by subtrigger s50. The cuts ensure at least* 40% *efficiency of the subtrigger* s50.

Since not for all events a trigger efficiency of 100% is ensured, the events with an efficiency lower than 100% have to be corrected. If the energy of the cluster is E_i and its radial distance RD_i, the probability, that the cluster will fire subtrigger s50 is $\epsilon_{s50}(E_i, RD_i)$. The total probability for an event that at least one cluster sets subtrigger s50 is:

$$p_{\text{s50}} = 1 - \prod_{i=1}^{N(clusters)} (1 - \epsilon_{s50}(E_i, RD_i)) \ . \tag{4.9}$$

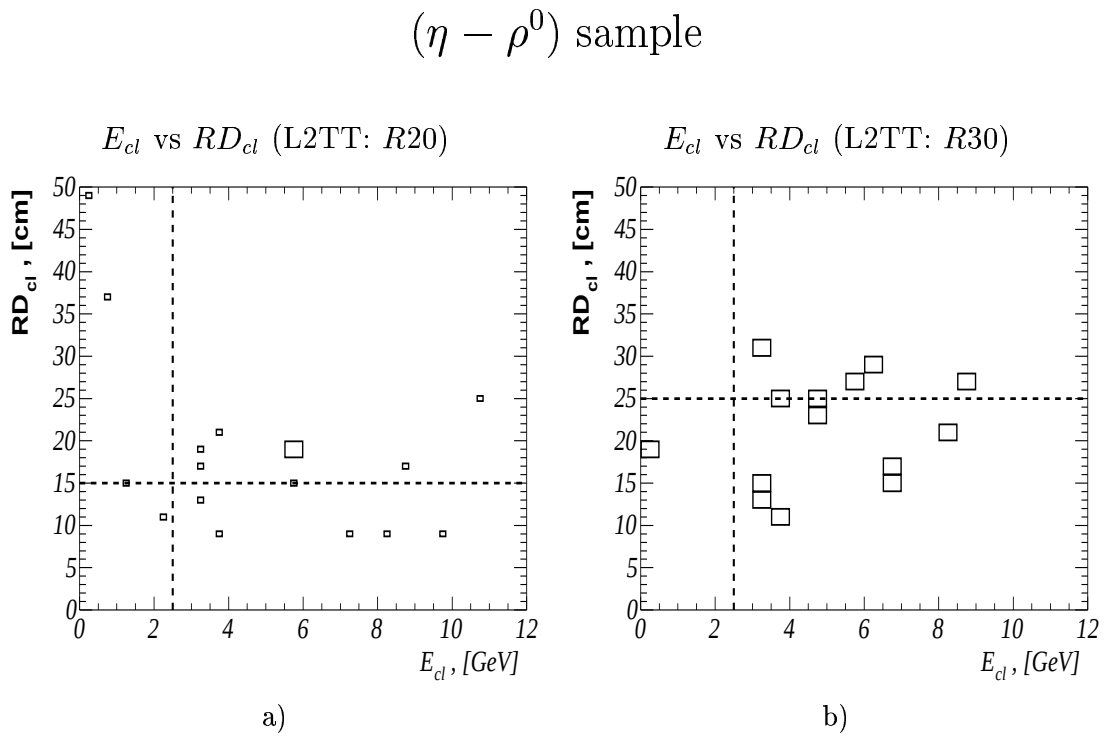

Figure 4.7: *T*he energy versus radial distance of all clusters for the $(\eta - \rho^0)$ sample is plotted for the data sample after final cuts selected by subtrigger s50 contained a) $R20$ condition and b) $R30$ condition. The dashed lines demonstrate the requirement on the energy (vertical one) and the radial distance (horizontal one) of the cluster.

The product runs over two clusters stemming from the π^0 or η reconstructed in the SpaCal. To correct the events selected by subtrigger s50 for the efficiency, the event weight is given by p_{s50}^{-1} from eq. (4.9).

4.4.3 Trigger Efficiency of Subtrigger s61

The efficiency of subtrigger s61 is determined through its trigger elements: $IET > 2$, IET_cen_3, DCR_ϕ and $zVtx$. The efficiencies of the SpaCal trigger elements IET[5] are determined in the same way as for subtrigger s50 using the same reference subtriggers s83 and s84. In figure 4.8 a) the efficiency (determined according to equation 4.2) for IET trigger element is shown as an example for the 2000 data taking period. The points illustrating the efficiency as a function of the energy of the hottest cluster, $\epsilon_{IET}(E_{hot})$, are fitted with the Fermi function from eq. (4.6).

The efficiency of the DCRϕ trigger element, $\epsilon_{DCR\phi}$, can be studied as a two dimensional function of transverse momentum p_t and polar angle θ of the 'highest p_t track'[6],

[5] In this subsection the common notation IET for $IET > 2$ and IET_cen_3 is used. Since $IET > 2$ and IET_cen_3 have the same thresholds their efficiency has been studied commonly applying logical OR between them in eq. (4.2).

[6] the track with the highest p_t

$\epsilon_{DCR\phi} = \epsilon_{DCR\phi}(p_{t\,high}, \theta_{high})$ if the p_t and θ are uncorrelated which is assumed.

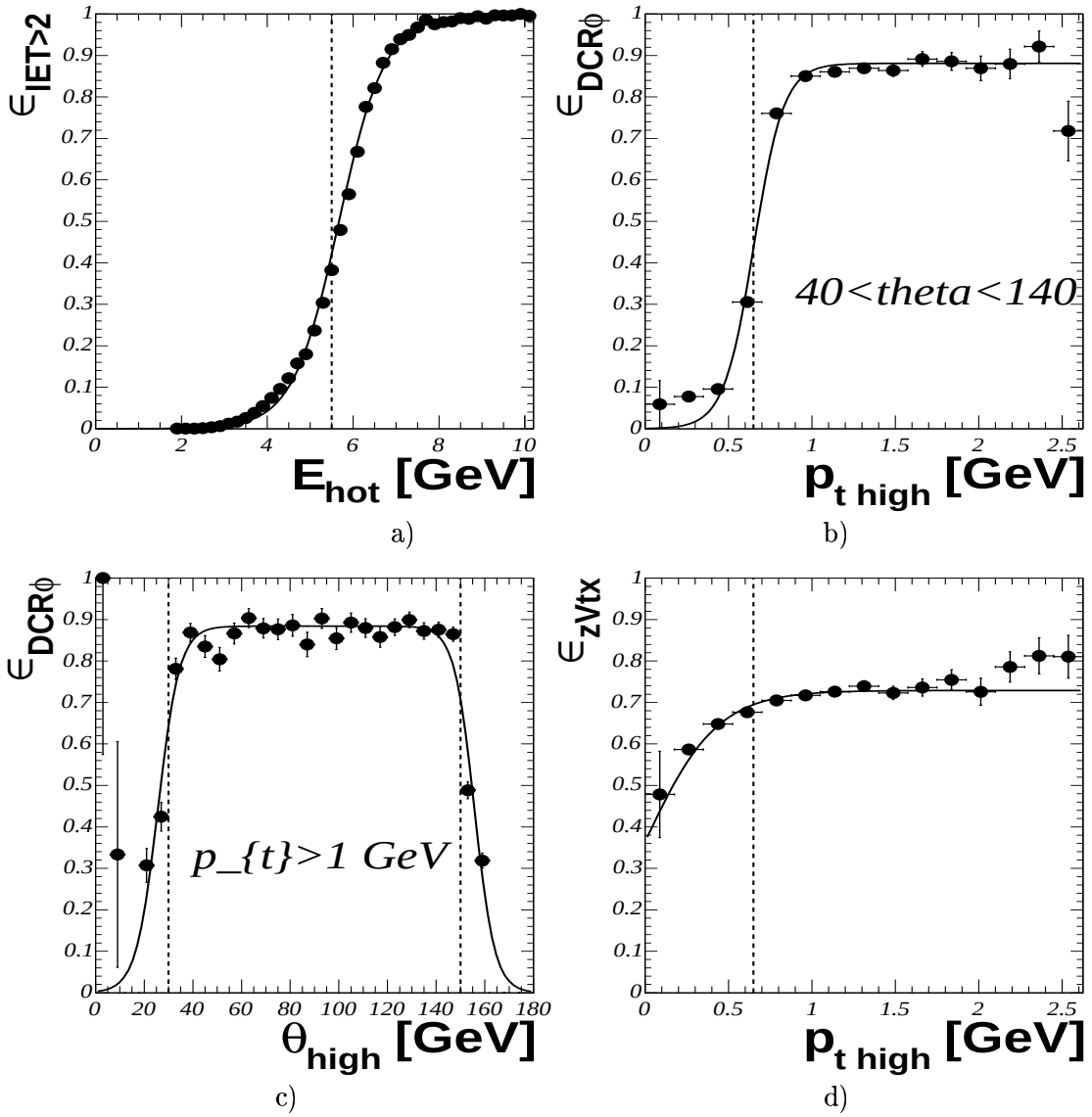

Figure 4.8: *The trigger element efficiencies of IET, DCRϕ and zVtx trigger elements: a) IET as a function of the energy of the hottest cluster, b) and c) DCRϕ as a function of transverse momentum and polar angle of the highest p_t track, respectively, and d) zVtx as a function of tranverse momentum of the highest p_t track.*
The curves demonstrate the fit functions. The dashed lines illustrate the limits on the energy of the hottest cluster, transverse momentum and the polar angle of the highest p_t track applied in the analysis.

The distribution in figure 4.8 b) shows the efficiency of the DCRϕ trigger element as a function of transverse momentum of the highest $p_{t\,high}$ track, $\epsilon_{DCR\phi}(p_{t\,high})$, as an example for the year 2000. Thereby one requires the polar angle of this track to be between 40° and 140° to be independent of the inefficient region in θ_{high}. The distribution in figure

4.8 c) shows the efficiency of the DCRϕ trigger element as a function of the polar angle of the highest p_t track, $\epsilon_{DCR\phi}(\theta_{high})$ as an example for the year 2000. Here one demands the transverse momentum of the track to be above 1 GeV to be independent of the inefficiency caused by low p_t tracks. In this kinematic region ($p_t > 1\,\mathtt{GeV}$ and $40^\circ < \theta < 140^\circ$) $\epsilon_{DCR\phi}(p_{t\,high}, \theta_{high}) = \epsilon_{max\_DCR\phi}$. The $\epsilon_{DCR\phi}(p_{t\,high})$ distribution has been fitted with the Fermi function

$$\epsilon_{DCR\phi}(p_{t\,high}) = \frac{\epsilon_{max\_DCR\phi}}{\left(\exp\left(\frac{p_{t\,Th1} - p_{t\,high}}{p_{t\,width1}}\right) + 1\right)} \tag{4.10}$$

and $\epsilon_{DCR\phi}(\theta)$ has been fitted with the 'double Fermi function':

$$\epsilon_{DCR\phi}(\theta) = \frac{\epsilon_{max\_DCR\phi}}{\left(\exp\left(\frac{\theta_{Th1} - \theta}{\theta_{width1}}\right) + 1\right)\left(\exp\left(\frac{-\theta_{Th2} + \theta}{\theta_{width2}}\right) + 1\right)} \tag{4.11}$$

where θ_{Th1} (θ_{Th2}) and θ_{width1} (θ_{width2}) are the corresponding thresholds and widths, respectively.

The efficiency of the trigger element $zVtx$, ϵ_{zVtx}, is also studied as a function of $p_{t\,high}$, $\epsilon_{zVtx} = \epsilon_{zVtx}(p_{t\,high})$. For the $\epsilon_{DCR\phi}$ and ϵ_{zVtx}, s50 is used as reference subtrigger which does contain neither $DCR\phi$ nor $zVtx$ conditions. Figure 4.8 d) shows the efficiency $\epsilon_{zVtx}(p_{t\,high})$ as a function of $p_{t\,high}$. The fit was performed with the Fermi function.

The efficiencies of all trigger elements of subtrigger s61 for the run period 1997-2000 (except 1998) are shown in Appendix A in figures A.1 (for ϵ_{IET}) and A.2 (for $\epsilon_{DCR\phi}$ and ϵ_{zVtx}). All fit parameters with χ^2/ndf are listed in table A.1. The fit parameters exhibit the stability of all trigger elements. The maximum efficiency of trigger elements $IET > 2 \,||\, IET\_cen\_3$ is $\epsilon_{max\_IET}(E) \sim 100\%$ over all years. The maximum efficiency of the $DCR\phi$ trigger element lies for different run periods between $\epsilon_{max\_DCR\phi} \in (84.5 - 89.5)\%$. The $zVtx$ trigger element exhibits its maximum for different periods in the interval: $\epsilon_{max\_zVtx} \in (71.2 - 74.5)\%$.

Also for the data selected by s61 it is not possible to make cuts hard enough to ensure the maximum efficiency of trigger elements due to the loss of significant statistics. From the efficiency distributions one obtains that the maximum efficiency of subtrigger s61 demands at least one cluster with an energy above 7.5 GeV and at least one track with θ between 40° and 140° and $p_t > 1\,\mathtt{GeV}$. In figure 4.9 *a*) the p_t versus polar angle θ for all tracks and in *b*) the energy of the hottest cluster for the events of the $(\eta - \rho^0)$ sample selected by s61 are depicted. The requirement on the maximum efficiency of $DCR\phi$ would exclude a dominant part of the statistics. To save statistics the lower limits of the cuts have been chosen to ensure an efficiency of the trigger element larger than 50%: a minimum cluster energy of 5.5 GeV, $30^\circ < \theta < 150^\circ$ for the polar angle of the track and $p_t > 0.65\,\mathtt{GeV}$ for the transverse momentum of the track. The cuts with the ensured efficiency are summarized in table 4.10. Since not always the hottest cluster and the highest p_t track has to set the trigger element the cuts applied will concern all the clusters and tracks. It means that for the events selected by subtrigger s61 it is demanded: at least one track with a transverse momentum above 0.65 GeV and polar angle between 30° and 150° and at least one cluster with an energy above 5.5 GeV. The cuts applied to the angle and the transverse momenta of the tracks ensure their uncorrelation and the efficiency $\epsilon_{DCR\phi}$ could be

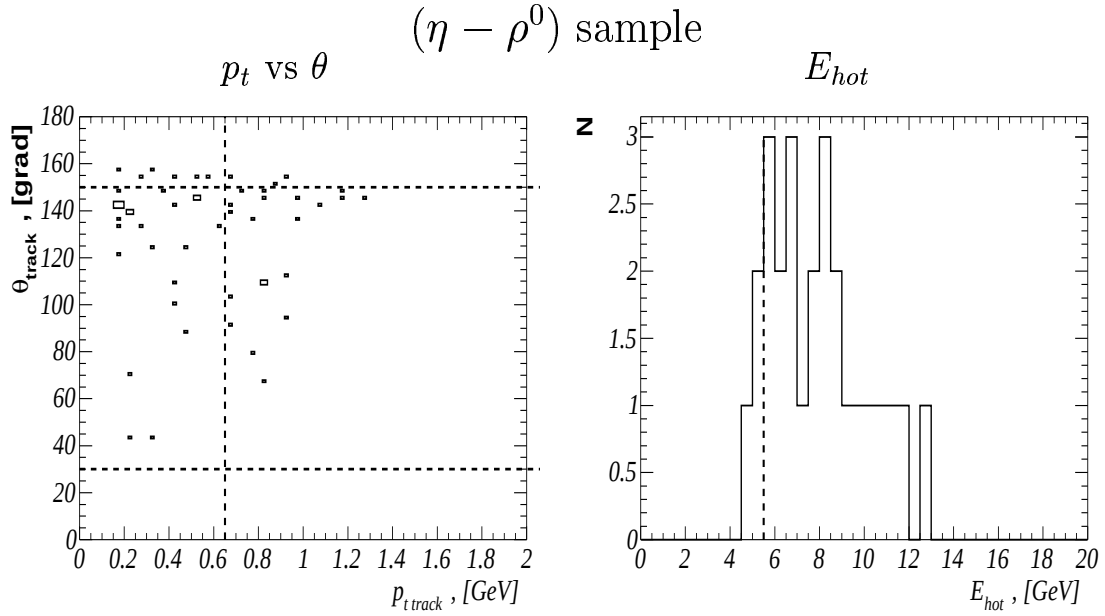

Figure 4.9: *T*he impact of the cuts applied to the track and clusters of the events selected subtrigger s61 of the $(\eta - \rho^0)$ sample: In a) p_t versus polar angle θ of all tracks. The vertical dashed lines indicate the cuts on the minimum p_t of the tracks the horizontal ones the cuts on the polar angle θ of the tracks. In b) the energy of the hottest cluster is plotted. The vertical dashed line indicates the cuts on the minimum cluster energy.

cut	ensured efficiency
$E > 5.5\,\mathtt{GeV}$	$\epsilon_{IET}(E > 5.5\,\mathtt{GeV}) > 50\%\,\epsilon_{max\_IET}(E)$
$30° < \theta < 150°$	$\epsilon_{DCR\phi}(30° < \theta < 150°) > 50\%\,\epsilon_{max\_DCR\phi(\theta)}$
$p_t > 0.65\,\mathtt{GeV}$	$\epsilon_{DCR\phi}(p_t > 0.65\,\mathtt{GeV}) > 50\%\,\epsilon_{max\_DCR\phi(p_t)}$
	$\epsilon_{zVtx}(p_t > 0.65\,\mathtt{GeV}) > 98\%\,\epsilon_{max\_zVtx(p_t)}$

Table 4.10: Summary on the cuts because of s61 efficiency *to ensure at least* 50% *of the maximum of the trigger element efficiencies.*

studied as $\epsilon_{DCR\phi} = \epsilon_{DCR\phi}(p_{t\,high}, \theta_{high})$.

Also the data which passed the subtrigger s61 have to be corrected for the trigger efficiency. The probability that at least one of the SpaCal clusters coming from $\pi^0(\eta)$ meson with energy E_i will set the trigger element IET is in analogy to formula 4.9:

$$p_{IET} = 1 - \prod_{i=1}^{N(clusters)} (1 - \epsilon_{IET}(E_i)) \ . \tag{4.12}$$

p_{IET} is the probability that either $IET > 2$ or IET_cen_3 trigger element fired.

Similarly the probability that one of the tracks originating from the ρ^0 meson decay will fire the DCRϕ trigger element is:

$$p_{DCR\phi} = 1 - \prod_{i=1}^{N(tracks)} (1 - \epsilon_{DCR\phi}(p_{t\,i}, \theta_i)) \ , \tag{4.13}$$

and the probability that one of the tracks stemming from the ρ^0 meson decay will fire the $zVtx$ trigger element is

$$p_{zVtx} = 1 - \prod_{i=1}^{N(tracks)} (1 - \epsilon_{zVtx}(p_{t\,i})) \ . \tag{4.14}$$

The total probability for an event to fire the subtrigger s61 is the product of the probabilities 4.12, 4.13 and 4.14:

$$p_{\mathrm{s61}} = p_{IET>2} \cdot p_{DCR\phi} \cdot p_{zVtx}. \tag{4.15}$$

The weight $w_{s61} = p_{s61}^{-1}$ has been applied to the events in the data sample selected by subtrigger s61.

4.4.4 Data Corrections on Trigger Inefficiencies

Since in this analysis it is not possible to choose the cuts as high as necessary to ensure the maximum efficiency of the trigger elements the data have to be corrected. For the determination of the correction factor one has to distinguish the following trigger combinations:

- the event has been accepted only by one subtrigger (s50 or s61). Then the event gets the weight p^{-1} defined in equation 4.9 or 4.15 according to the fired subtrigger.
- the event has been accepted by both subtriggers s50 and s61.
  In general the weight for events selected by N independent subtriggers is given by a product of probabilities of all subtriggers that fired:

$$p_{N(subtriggers)} = \prod_{subtrigger}^{N(subtriggers)} p_{subtrigger} \cdot \tag{4.16}$$

  The two subtriggers s50 and s61 are correlated due to the SpaCal IET condition (see table 4.8). But the efficiency of the IET condition in subtrigger s50 is 100% (table 4.9) and therefore there is no correlation between these two subtriggers and formula 4.16 can be used to weight the events in which both subtriggers fired.

4.5 L1 Prescales and Data Corrections

Depending on run and background conditions the level one subtriggers are prescaled to control the output rate. The subtriggers involved were downscaled by an automatic procedure [85] adjusting prescaling factors depending on the background conditions in order to provide the optimum use of the delivered luminosity. A combined event weight, necessary

for the simultaneous use of N subtriggers with different downscaling factors, is computed as [75]:

$$w_{pr}^{-1} = 1 - \prod_{i=1}^{N(subtriggers)} \left(1 - \frac{r_i}{Pr_i}\right) . \tag{4.17}$$

The product runs over subtrigger s50 or subtrigger combination s50||s61, r_i is:

$$r_i = \begin{cases} 1 & \text{if the raw subtrigger s50, s61 is set in the event} \\ 0 & \text{otherwise} \end{cases} , \tag{4.18}$$

and Pr_i are the prescaling factors of the subtriggers in the run in which the event was taken. Equation 4.17 shows, the higher the number of the downscaled subtriggers, the more possible combinations of subtriggers set in the event have to be distinguished. It makes the calculations more difficult. The weight w_{pr}^{-1} reduces for the events accepted by only one subtrigger to its prescale $w_{pr}^{-1} = Pr_i$. Very low L1 prescale (close to 1) of subtrigger s61 allows to apply $w_{pr}^{-1} = Pr_{s61}$ also to the events in which the raw subtrigger s50 'AND' s61 is set.

4.6 Total Efficiency

In order to determine the cross section several corrections for the detector effects (in addition to the trigger inefficiencies) have to be taken into account. Usually they are included in the so called *total efficiency*. Due to the poor statistics of the data sample available for its determination, the efficiency will be determined by means of the signal Monte Carlo events. In this analysis the ToyGenMod MC event generator (see chapter 3.1) is employed. In the first step the efficiency will be determined to restrict the analyzed kinematical region of the production of the $\pi^0(\eta)$ and ρ^0 mesons where the efficiency is reasonably high in order to avoid large extrapolation factors. In the second step the efficiency will be determined to correct the data for the cross section calculations.

Two main contributions to the total efficiency ϵ_{tot} are examined: The geometrical acceptance, ϵ_{geom}, and the detector efficiency, ϵ_{det}. The geometrical acceptance, ϵ_{geom}, is determined on the generator level and is given by the probability of the pions and the photons to be in the sensitive range of the detector. This means that transverse momentum and polar angle of the pions have to be in the acceptance region of the CJC and the energy and the polar angle of the photons have to be in the acceptance of the SpaCal. The detector efficiency, ϵ_{det}, is defined on the detector level and is based on the efficiency to reconstruct ρ^0 and π^0 (η) mesons in the detector after all cuts applied in the analysis. The total efficiency is the product of:

$$\epsilon_{tot} = \epsilon_{geom} \cdot \epsilon_{det} = \frac{N_{gen}^{MC}(\theta, p_t, E_{min})}{N_{gen}^{MC}} \quad \frac{N_{rec}^{MC}(final)}{N_{gen}^{MC}(\theta, p_t, E_{min})} = \frac{N_{rec}^{MC}(final)}{N_{gen}^{MC}} \tag{4.19}$$

where the first term corresponds to the geometrical acceptance and the second to the detector efficiency and

- N_{gen}^{MC} is the total number of generated events in the kinematical region $Q^2 < 0.01\,\mathrm{GeV}^2$ and $0.3 < y < 0.65$

- $N_{gen}^{MC}(\theta, p_t, E_{min})$ is the number of generated events (N_{gen}^{MC}) which passed the acceptance cuts on the polar angle of pion candidates ($20° < \theta_{\pi^\pm} < 160°$) and photon candidates ($154° < \theta_\gamma < 177°$), minimum transverse momentum of the pion candidates ($p_t > 150$ `MeV`) and minimum energy of the photon candidates ($E > 100$ `MeV`)
- $N_{rec}^{MC}(final)$ is the number of the fully reconstructed events which passed the kinematical restrictions described in table 4.1, the final selection shown in table 4.6 and the cuts summarized in tables 4.9 and 4.10.

4.7 Determination of the Kinematic Region

For the determination of the limits of the kinematical region it is necessary to use a MC model which produces particles in the full acceptance region of the SpaCal detector and the CJC. Therefore the ToyGenMod (see section 3.1) model with modified parameters is employed. In the following the total efficiency determined in two steps is shown: firstly the geometrical acceptance is determined and then the detector efficiency.

4.7.1 Geometrical Acceptance

The geometrical acceptance is determined separately for the π^0 (ϵ_{geom,π^0}), η ($\epsilon_{geom,\eta}$) and ρ^0 (ϵ_{geom,ρ^0}) as a function of their rapidities Y_{π^0}, Y_η and Y_{ρ^0}, respectively. By 'separately' it is meant that $\epsilon_{geom,\pi^0(\eta)}$ does not include ϵ_{geom,ρ^0} and vice versa. To ensure a reliable measurement of the momenta of the tracks originating from ρ^0 meson decay, their polar angle is restricted to the acceptance region of the central tracking detector, $20° < \theta_{\pi^\pm} < 160°$ and their transverse momentum to $p_t > 150$ `MeV`. For similar reasons the polar angle of both photons has to be in the region $154° < \theta_\gamma < 177°$ and their energy $E_{min} > 100$ `MeV`. The resulting acceptances for the $(\pi^0 - \rho^0)$ sample are shown in figure 4.10 for the a) π^0 and b) ρ^0 mesons as a function of Y_{π^0} and Y_{ρ^0}, respectively. The resulting acceptances for the $(\eta - \rho^0)$ sample are shown in c) for the η and d) the ρ^0 mesons as a function Y_η and Y_{ρ^0}, respectively.

The geometrical acceptance, ϵ_{geom,π^0}, of the π^0 meson is close to 100% in the whole SpaCal acceptance region since the photons are very close to each other, shown in figure 4.11 a). The distance between two photons from the η meson, figure 4.11 b), is larger and the probability that one of the photons will be lost at the edges of the SpaCal acceptance is much higher. Therefore the acceptance for the η meson falls down when approaching $Y_\eta \to -3.5$ and $Y_\eta \to -1.5$. In figures 4.11 one sees the distance (in the x-y plane) between two photons stemming from a) a π^0 and b) an η meson. The distance is calculated at the usual cluster position in the SpaCal ($160\,cm$) with respect to the nominal vertex. While the minimum distance of the photons from an η decay is about 8 `cm`, and the average is about 20 `cm`, the averaged distance between the photons from π^0 decay is about 5 `cm`. This is a consequence of the larger mass of the η meson: The phase space for the products of an η meson decay is much larger than for those from a π^0 meson decay. Mathematically it is described as

$$\cos(\theta_{\gamma_1\,\gamma_2}) \;=\; 1 - \frac{m^2_{\gamma_1\,\gamma_2}}{2\,E_{\gamma_1}\,E_{\gamma_2}} \tag{4.20}$$

where $\theta_{\gamma_1\,\gamma_2}$ and $m_{\gamma_1\,\gamma_2}$ are the angle between the decay photons in the laboratory system and the squared photon-photon invariant mass (either π^0 or η mass), respectively, with

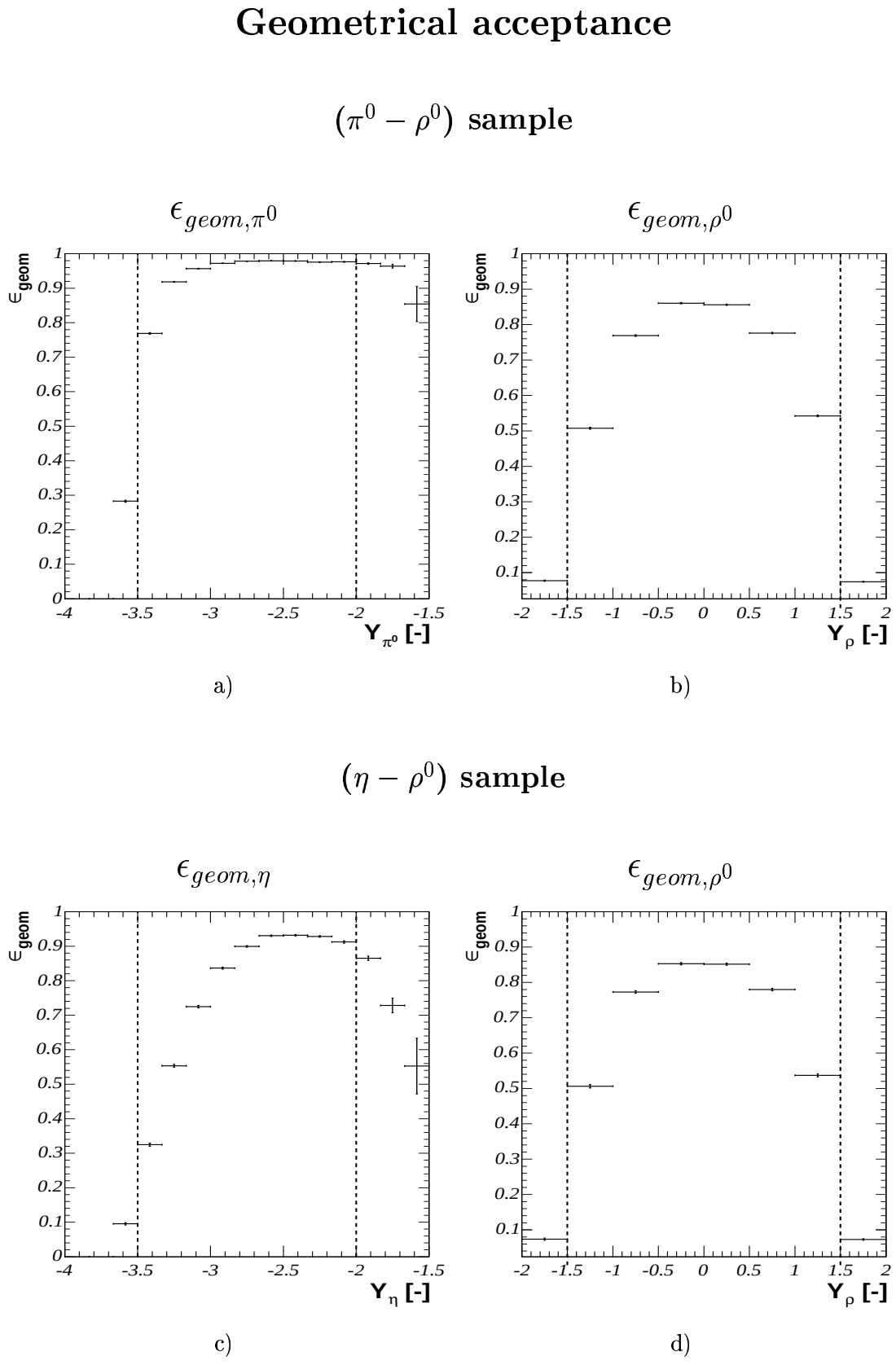

Figure 4.10: *Geometrical acceptances of the a) π^0 and b) ρ^0 mesons for the $(\pi^0 - \rho^0)$ sample as a function of the Y_{π^0} and Y_{ρ^0}, respectively. In c) and d) the geometrical acceptances of the η and ρ^0 for the $(\eta - \rho^0)$ sample are shown as a function of the Y_η and Y_{ρ^0}, respectively.*

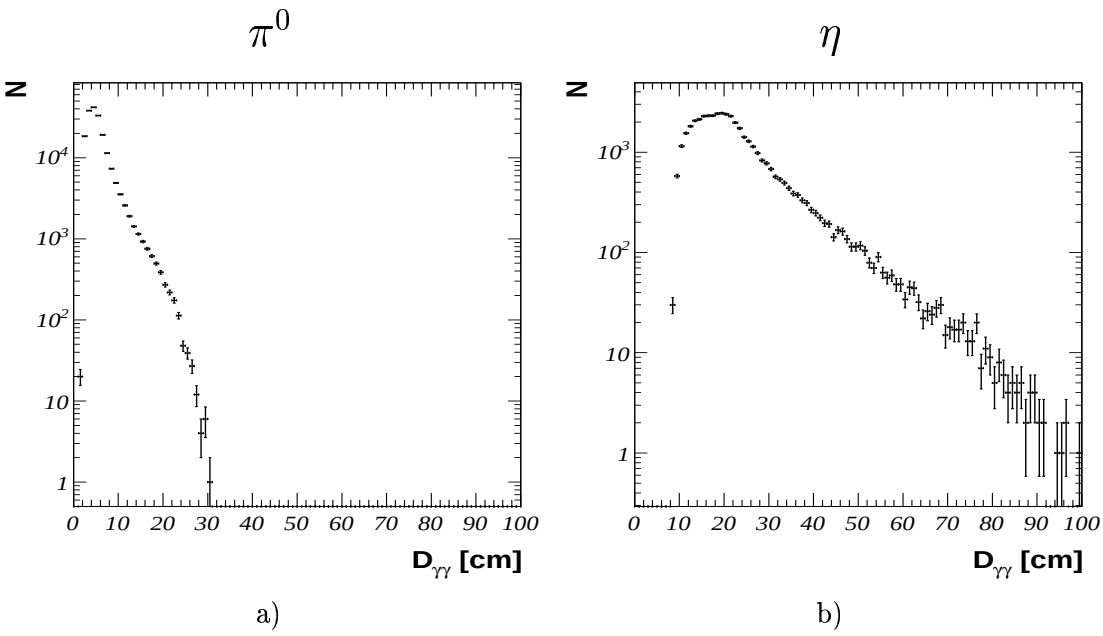

Figure 4.11: *Distance between two photons originating from a) π^0 meson decay and b) η meson decay, respectively, generated by the ToyGenMod Monte Carlo model.*

the energies E_{γ_1} and E_{γ_2}.

The acceptance for the ρ^0 meson is the same for the $(\pi^0 - \rho^0)$ and $(\eta - \rho^0)$ samples which is in agreement with the fact that the kinematics of the ρ^0 meson is similar in both samples. The probability that one of the pions from the ρ^0 decay will be outside of the CJC acceptance region is larger at the edges $Y_{\rho^0} \rightarrow \pm 1.5$ than for more central ρ^0 mesons and therefore the acceptance decreases, too.

4.7.2 Detector Efficiency

The detector efficiency, ϵ_{det}, determined for the $(\pi^0(\eta) - \rho^0)$ sample will include detector effects on both $(\pi^0(\eta)$ and $\rho^0)$ mesons, $\epsilon_{det} = \epsilon_{det}(\epsilon_{det,\pi^0(\eta)}, \epsilon_{det,\rho^0})$. The detector efficiency represents the efficiency of the π^0 (η) and ρ^0 reconstruction in the detector components and the efficiency of the applied analysis cuts. For both samples the efficiency is studied as a function of the rapidities of the two mesons. The reconstructed MC sample $(N_{rec}^{MC}(final))$ in equation 4.19) has to pass the preselection in table 4.1, final analysis cuts in table 4.6 and restrictions due to the trigger conditions mentioned in tables 4.9 or 4.10. The corresponding clusters are reconstructed in the backward SpaCal calorimeter within $154° < \theta < 177°$ fulfilling the photon selection criteria, table 4.3. The tracks from the ρ^0 decay have to be reconstructed in the central tracking detector within $20° < \theta < 160°$ fulfilling the standard cuts of the Lee West track selection criteria, table 4.4. The rapidity distributions after all the cuts (including cuts applied due to the trigger inefficiencies) are then compared with the generated sample $N_{gen}^{MC}(\theta, p_t, E_{min})$ determined in the geometrical acceptance.

The resulting detector efficiency for the $(\pi^0 - \rho^0)$ sample is shown in figure 4.12 as a function of the rapidities *a*) Y_{π^0} and *b*) Y_{ρ^0}. The efficiency decreases strongly towards lower rapidities of π^0. The reason is kinematics: Towards lower rapidities, $Y_{\pi^0} \to -3.5$, the pion energy rises resulting in more strongly collimated photons which has two consequences: 1) merging of the photons into one due to the SpaCal granularity 2) very low efficiency for the event candidates to pass the cut (of 20 or 30 cm, see table 4.9) applied to the radial distance of cluster. The detector efficiency in the Y_{ρ^0} distribution exhibits a shift to low rapidities of the ρ^0 which is related to the π^0 reconstruction efficiency.

The detector efficiencies for the $(\eta - \rho^0)$ sample are shown in figure 4.12 as a function of the rapidities *c*) of the η meson, Y_η and *d*) ρ^0 meson, Y_{ρ^0}. The strong decrease of the efficiency at $Y_\eta \to -3.5$ is a result of the cut applied to the radial distance of the clusters (table 4.9). For a decrease of the efficiency at $Y_\eta \to -1.5$ the fiducial cut (see table 4.3) requiring a radial distance of one of two clusters to be above 75 cm is responsible. When comparing the efficiencies of the $(\pi^0 - \rho^0)$ and $(\eta - \rho^0)$ samples one observes a much larger efficiency for the $(\eta - \rho^0)$ sample than for the $(\pi^0 - \rho^0)$, mainly because of the fact that the photons from η meson decay are much further apart from each other than the photons from π^0 meson decay (figure 4.11). In contrast to the $(\pi^0 - \rho^0)$ sample the efficiency as a function of Y_{ρ^0} is rather symmetric for the $(\eta - \rho^0)$ sample. The small asymmetry is due to misidentifying one of the charged pions from ρ meson decay in the SpaCal as a photon due to the small overlap between CJC and the SpaCal in acceptance. The relatively large asymmetry of the efficiency in Y_{ρ^0} distribution for the $(\pi^0 - \rho^0)$ sample is due to misidentifying one of the pions in the SpaCal as a photon. Approaching $Y_{\rho^0} \to \pm 1.5$ the efficiencies in both samples steeply fall down since the tracks are to short to pass the R_{length} condition in the track selection (table 4.4).

4.7.3 Total Efficiency

The total efficiency according to eq. (4.19) is the product of the geometrical and detector efficiency. The obtained total efficiencies for the $(\pi^0 - \rho^0)$ and $(\eta - \rho^0)$ are shown in figure 4.13 as a function a) Y_{π^0} and b) Y_{ρ^0} for the $(\pi^0 - \rho^0)$ sample and c) Y_η and d) Y_{ρ^0} for the $(\eta - \rho^0)$. In order to avoid large extrapolation uncertainties the cross sections are determined within a restricted kinematical region defined by the rapidities of the $\eta(\pi^0)$ and ρ mesons: $-3.5 < Y_\eta(\pi^0) < -2$ and $-1.5 < Y_{\rho^0} < 1.5$. The limits are shown by dashed lines in figure 4.13 and listed in table 4.11.

$-3.5 < Y_{\pi^0} < -2$
$-3.5 < Y_\eta < -2$
$-1.5 < Y_{\rho^0} < 1.5$

Table 4.11: *Definition of the kinematic region.*

4.8 Data Correction of the $(\eta - \rho^0)$ Sample

The procedure to determine the total efficiency correctly is discussed in Appendix B. It is shown that for the total efficiency, calculated as the ratio of the total number of the

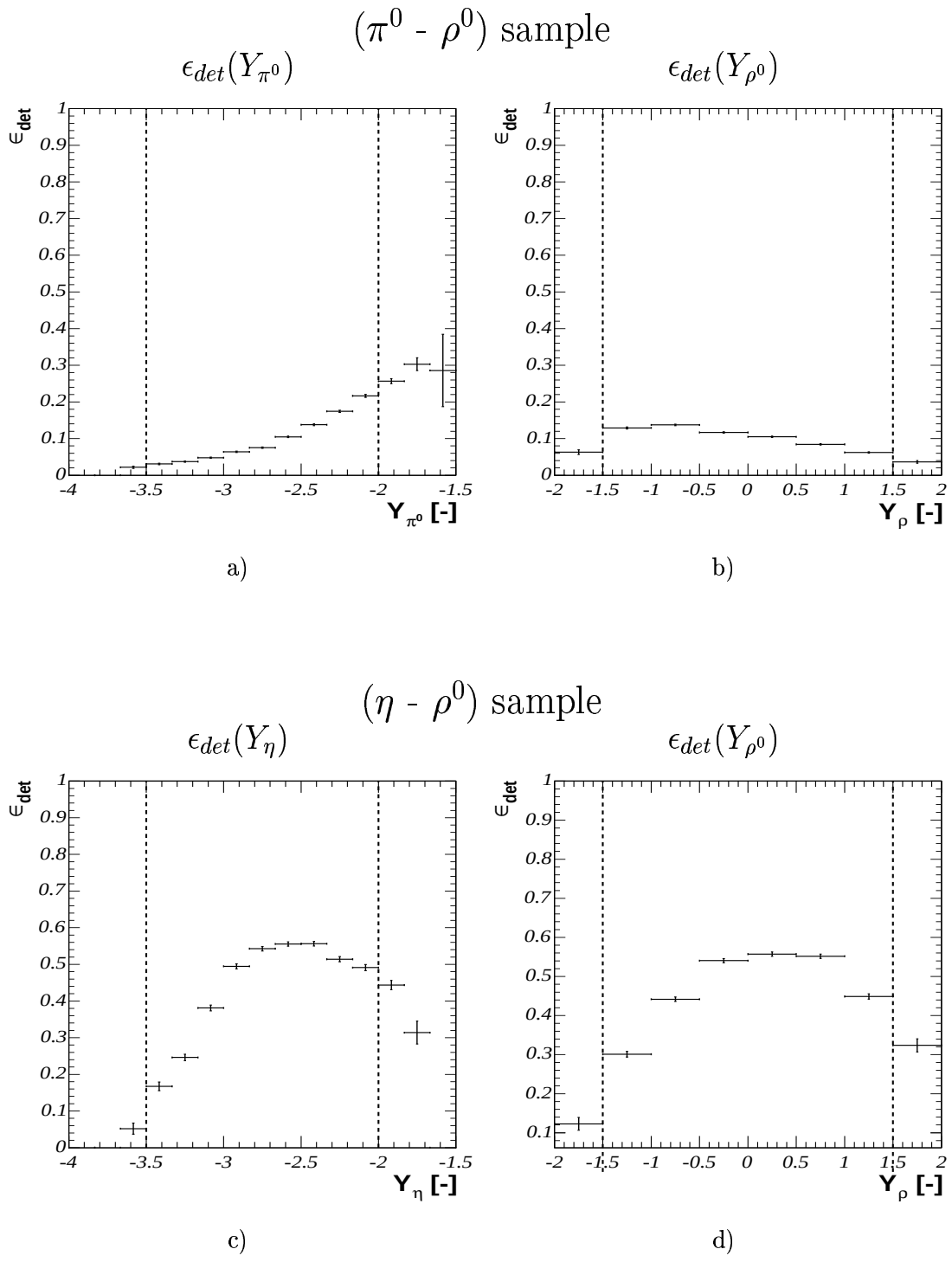

Figure 4.12: *Detector efficiency as a function of a) the π^0 meson rapidity, Y_{π^0}, and b) as a function of the rapidity of the ρ^0 meson, Y_{ρ^0}, for the $(\pi^0 - \rho^0)$ sample. c) and d) show the detector efficiency of the $(\eta - \rho^0)$ sample as a function of the rapidity of the η meson, Y_η, and the ρ^0 meson, Y_{ρ^0}, respectively.*

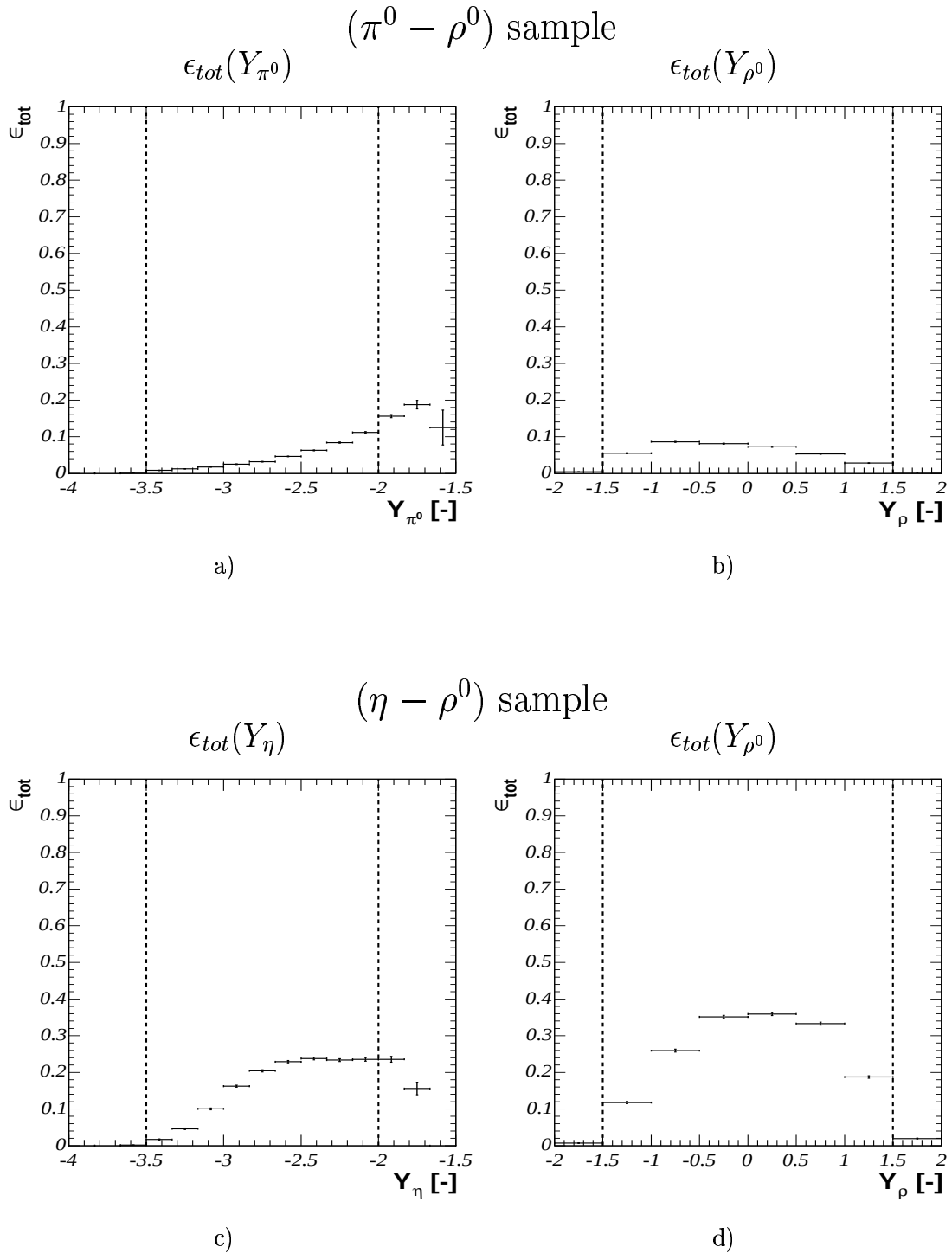

Figure 4.13: *Total efficiency as a function of a) the π^0 meson rapidity, Y_{π^0}, and b) as a function of the rapidity of the ρ^0 meson, Y_{ρ^0}, for the $(\pi^0 - \rho^0)$ sample. c) and d) show the total efficiency of the $(\eta - \rho^0)$ sample as a function of the rapidity of the η meson, Y_η, and of the ρ^0 meson, Y_{ρ^0}, respectively.*

reconstructed events after all analysis cuts and the total number of generated events (eq. (4.19)), the simulated and the data distributions have to agree. Therefore for the cross-section determination the ToyGenMod distributions have been weighted according to the distributions in data. This procedure is described in Appendix C.

To avoid large extrapolation uncertainties the kinematical region for the cross section calculation was defined in section 4.7 and listed in tab. 4.11. The total efficiency determined for this region is:

$$\epsilon_{tot} = \frac{N_{rec}^{MC}(final)}{N_{gen}^{MC}(Y_\eta, Y_{\rho^0})} = 6.62\% \pm 0.52\% \tag{4.21}$$

where $N_{rec}^{MC}(final)$ is defined in eq. (4.19) and $N_{gen}^{MC}(Y_\eta, Y_{\rho^0})$ is the number of the events generated by the weighted ToyGenModW within the kinematical constraints listed in tab. 4.11. The error of the efficiency is calculated as:

$$\Delta\epsilon_{tot} = \frac{1}{N_{gen}^{MC}} \sqrt{\left[\Delta N_{rec}^{MC}(final)\right]^2 - 2\epsilon_{tot}\left[\Delta N_{rec}^{MC}(final)\right]^2 + \epsilon_{tot}^2\left[\Delta N_{gen}^{MC}\right]^2}. \tag{4.22}$$

where ΔN_{gen}^{MC} and $\Delta N_{rec}^{MC}(final)$ are the corresponding absolute errors for N_{gen}^{MC} and $N_{rec}^{MC}(final)$. The relatively high error results from the weighting procedure described in Appendix C.0.1.

In order to correct the characteristic distributions of the $(\eta - \rho^0)$ sample the total efficiency has been studied as a function of the following variables: figure 4.14 *a)* the centre of mass energy of the gamma-proton system, $W_{\gamma p}$, *b)* the rapidity difference between ρ^0 and η mesons, $Y_{\rho^0} - Y_\eta$, *c)* the squared four momentum transfer at the photon vertex, t_1, *d)* the squared four momentum transfer at the proton vertex, t_2, *e)* the squared centre of mass energy of the $(\eta - \rho^0)$ subsystem, s_1, and *f)* the squared centre of mass energy of the $\rho^0 - proton$ subsystem, s_2.

The efficiency exhibits a similar behavior in the $W_{\gamma p}$ and $Y_{\rho^0} - Y_\eta$ distributions: the efficiency slightly rises with the steep decrease at the end. The lower number of events in the data sample than in PythiaMod results in an empty bin in the $Y_{\rho^0} - Y_\eta$ distribution. The t_1 and s_1 distributions exhibit a strong rise over the full acceptance region. The efficiency as a function of t_2 is for $t_2 < 0.6\,\mathtt{GeV}^2$ rather constant. Above $0.6\,\mathtt{GeV}^2$ the efficiency decreases due to the cuts applied to ensure rapidity gap in the forward region. The efficiency as a function of s_2 is highest for $s_2 \in (1500 - 4000)\,\mathtt{GeV}^2$. Below $1500\,\mathtt{GeV}^2$ the efficiency is low because of the detector acceptance limits. Above $4000\,\mathtt{GeV}^2$ it has a tendency to be rather flat. The efficiency dependence on the t_2 and s_2 is rather constant. In the next chapter these efficiency distributions will be used for the correction of the measured differential distributions.

4.9 Data Correction of the $(\pi^0 - \rho^0)$ Sample

In chapter 6 it is shown that the $(\pi^0 - \rho^0)$ signal can not be extracted and only the cross section for the $\pi^0 - 2\,track$ is determined. Therefore the efficiency will be determined for the $\pi^0 - 2\,track$ sample in which the $track - track$ mass is limited by the ρ^0 invariant mass window defined in eq. (5.5): $(0.6 < m_{tt} < 1)\,\mathtt{GeV}$. The same data correction procedure as for the $(\eta - \rho^0)$ sample is used. The respective efficiency is:

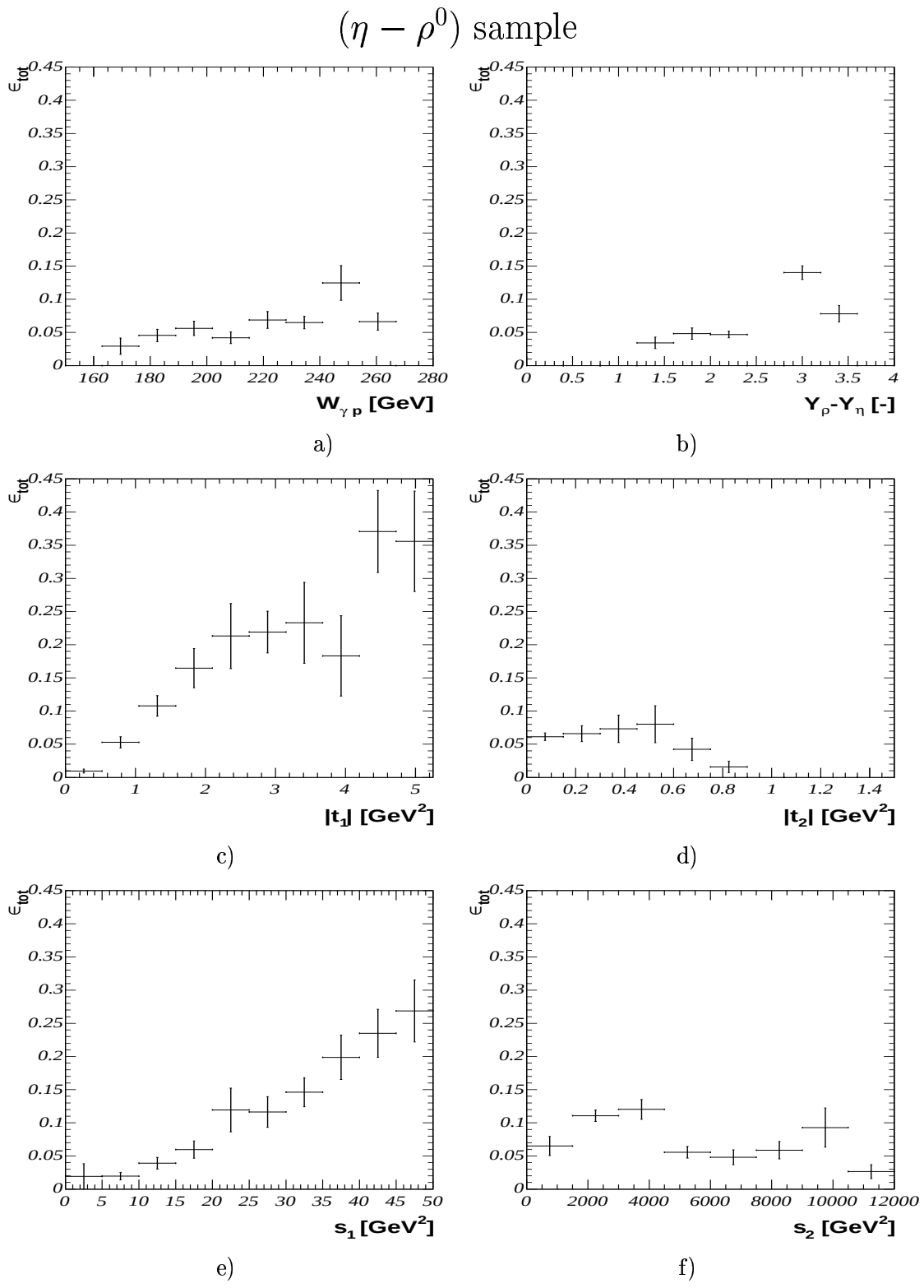

Figure 4.14: Total efficiencies for the $(\eta - \rho^0)$ sample as a function of: *a)* gamma-proton energy, $W_{\gamma p}$ *b)* rapidity difference between ρ^0 and η, $Y_{\rho^0} - Y_\eta$ *c)* momentum transfer at photon vertex, t_1 *d)* momentum transfer at photon vertex, t_2 *e)* $(\eta - \rho^0)$ system energy, s_1 *f)* $\rho^0 - proton$ system energy, s_2

$$\epsilon_{tot}((0.6 < m_{tt} < 1)\,\mathtt{GeV}) \quad = \quad \frac{N_{rec}^{MC}(final)}{N_{gen}^{MC}(Y_{\pi^0}, Y_{tt})} = 3.95\% \pm 0.43\% \qquad (4.23)$$

where $N_{rec}^{MC}(final)$ is defined in eq. (4.19) and $N_{gen}^{MC}(Y_\eta, Y_{tt})$ is the number of the events generated by the weighte ToyGenModW within the kinematical constraints listed in tab. 4.11. The error of the efficiency is calculated as in eq. (4.22). The relatively high error results from the weighting procedure described in Appendix C.0.2.

4.10 Summary on the Data Selection

In this chapter the signatures of the investigated exclusive double meson photoproduction of $(\eta - \rho^0)$ and $(\pi^0 - \rho^0)$ samples in the H1 detector were introduced. Also the data selection procedure in which many cuts have been introduced (they are summarized in tab. 4.13), was described. According to the data taking periods 1996, 1997, 1999 and 2000 the data were selected by the subtrigger $s50$ (for 1996 and first part of 1997) or subtrigger combination $s50 \,\|\, s61$ (second part of 1997, 1999 and 2000). Corrections on the data were derived from trigger element efficiencies, L1 prescale factors and from the corrections on the detector effects.

The kinematical region of the investigated processes in which the cross section will be determined has been defined by electron tagger and by the cuts applied due to detector efficiencies. They are summarized in table 4.12

$0.3 < y < 0.65$
$Q^2 < 0.01\,\mathtt{GeV}$
$-3.5 < Y_{\pi^0} < -2$
$-3.5 < Y_\eta < -2$
$-1.5 < Y_{\rho^0} < 1.5$

Table 4.12: *Summary of the kinematic restrictions: Kinematic region in which the cross section will be determined.*

<table>
<tr><td colspan="3">cuts according to the signatures:
existence of a primary vertex
$N_{central\,tracks} = 2$ reconstructed from the primary vertex, $q_1 \cdot q_2 = -1$
tagged electron
$N_{cluster} = 2$</td></tr>
<tr><td colspan="3">final selection
$\mathrm{N}(\mathrm{E}_{LAr\_cluster} > 500\,\mathtt{MeV}) = 0$ in forward LAr
$\mathrm{N}(\mathrm{E}_{LAr\_cluster} > 500\,\mathtt{MeV}) = 0$ in central LAr not connected to any track
$50\ \mathtt{GeV} < \mathtt{E} - \mathtt{p}_z < 60\ \mathtt{GeV}$</td></tr>
<tr><td colspan="3">the cuts for the events selected by</td></tr>
<tr><td colspan="2">subtrigger s50:
$E > 2.5\,\mathtt{GeV}$</td><td rowspan="3">subtrigger s61:
$E > 5.5\,\mathtt{GeV}$
$30^\circ < \theta < 150^\circ$
$p_t > 0.65\,\mathtt{GeV}$</td></tr>
<tr><td>L2TT: R20
$RD > 15\,\mathtt{cm}$</td><td>L2TT: R30
$RD > 25\,\mathtt{cm}$</td></tr>
</table>

Table 4.13: *Summary of all analysis cuts*

Chapter 5

Exclusive $\eta - \rho^0$ Photoproduction at HERA

In this chapter the events are selected which contain the η and ρ^0 meson-candidates. The η and ρ meson candidates are defined by the mass windows in the photon-photon and track-track mass spectra, the so called η and ρ^0 bands. The number of events entering the cross section is estimated from correlation of the η and ρ bands. To estimate the background contribution, the Monte Carlo models Pythia and RapGap are employed.

Since the purpose of Pythia in this analysis is background description and the interest is to investigate exclusive $\eta - \rho^0$ production of any origin, the process $\gamma p \to \eta\rho^0 X$ has been excluded from Pythia, and PythiaMod (see chapter 3.2.1) is used for the background description. For the signal expectation the signal Monte Carlo model ToyGen is used.

Concerning the event sample generated by ToyGen one has to distinguish between three types of generated samples:
a) ToyGen with original flux-factors which does not produce the particles in the region where the data are seen. This kind of simulation is not used in the analysis.
b) Therefore the flux factor at the photon vertex has been modified (see chapter 3.1) and this new generation of ToyGen is called ToyGenMod. This sample is only used in chapter 4.7 for efficiency determination to select the kinematical region and for selection of η and ρ^0 invariant mass bands. To study the ρ^0 invariant mass band the ToyGenMod includes also reweighting of the $track - track$ mass distribution according to a P-wave relativistic Breit-Wigner function. Therefore no normalization of the data is needed.
c) For comparison with the data, ToyGenMod distributions have been reweighted according to the difference between the data and PythiaMod distributions (see Appendix C) since the difference between data and PythiaMod is expected to represent the signal. The reweighted ToyGenMod MC model is called ToyGenModW. It also means that ToyGenModW is normalized to the signal expectation and will always be drawn as the sum of PythiaMod and the data distributions. The term 'expectation from ToyGenModW' will be used in the following only for simplicity since it is not an expectation in the sense of a real prediction, due to a missing theoretical prediction for the signal. ToyGenModW distributions are only normalized to the difference between the data sample and the background MC PythiaMod distributions selected by the final cuts.

All data distributions shown in this chapter are corrected by the $L1$ prescales (chapter

4.5), $L4$ weights (chapter 1.8) and by the corrections on the trigger element efficiencies (chapter 4.4). The background MC distributions are normalized to luminosity and corrected for the electron tagger acceptance.

Finally, the systematic errors are estimated, and the characteristic distributions for the upper and lower vertex are determined. The fitting procedure is based on the χ^2 minimization.

5.1 Preparation of the Sample

In order to select events with η and ρ^0 mesons, further cuts in addition to the final analysis cuts have to be applied. The obvious requirement to be fulfilled is the event to contain an η candidate, decaying into two photons, and a ρ^0 candidate, decaying into two charged pions. These decays are identified by looking at the invariant masses of the photon and track pairs. The mass window for η and ρ^0 bands will be determined from 'inclusively preselected' distributions due to the higher statistics. Here 'inclusively preselected' means the preselection of two clusters and two unlike-sign tracks.

For the inclusively preselected data sample the mass distribution of the $\gamma\gamma$ system, $m_{\gamma\gamma}$, is shown in fig. 5.1 a). The distribution is fitted with a Gaussian $G(m_{\gamma\gamma})$ to describe the η meson mass peak and a polynomial of third order $\mathcal{P}_3(m_{\gamma\gamma})$ for the background. The mass spectrum simulated by ToyGenMod is shown in c). This distribution is fitted only with a Gaussian due to the absence of any background. The parameters determined by the fits are displayed in the figure and the mean values, widths and χ^2/ndf are shown separately in table 5.1. Comparing measured and simulated mass distributions one observes an agreement in the mean value for the mass of the η, μ ($\mu_{data} = 526$ MeV for the data versus $\mu_{MC} = 529$ MeV for MC), and a slightly larger width, σ, for the data than for the simulation ($\sigma_{data} = 35$ MeV versus $\sigma_{MC} = 26$ MeV). The mean values in both cases are shifted toward lower values by $20 - 25$ MeV when comparing with the nominal value of 547.75 ± 0.12 MeV [37]. For the shift of the measured mass, μ, the large absolute energy scale uncertainty of the SpaCal is responsible which is about 6% for a 5 GeV electrons, (see chapter 1.4.2). The widths are dominated by the SpaCal resolution since the natural width of the η is only 1.29 ± 0.07 keV. Therefore the mass peak can be described by a Gaussian.

	Data	Monte Carlo
μ [MeV]	526.3±2.3	528.8±0.6
σ [MeV]	35.3±1.9	26±0.5
χ^2/ndf	16.7/9	35.8/18

Table 5.1: *Parameters fitted for η candidates: mean value, width and χ^2 per degree of freedom found by the fit for the data and the Monte Carlo (ToyGenMod) events.*

A pair of photon-candidates is considered as an η-candidate, if

$$0.42\,\text{GeV} < m_{\gamma\gamma} < 0.63\,\text{GeV}. \tag{5.1}$$

The lower and upper bounds of the mass window correspond roughly to 3σ (105 MeV) w.r.t. the mean value of 526 MeV measured in the data.

The track-track mass spectrum for the same data sample is shown in fig. 5.1 b). The distribution is fitted with a relativistic P-wave relativistic Breit-Wigner function $RBW(m_{tt})$ together with an exponential function multiplied by a square root $\mathcal{B}(m_{tt})$ defined in eq. (5.4) to describe the background. The Breit-Wigner function is given by [37]

$$RBW(m_{tt}) = A\frac{m_{tt}m_{\rho^0}\Gamma_{\rho^0}(m_{tt})}{(m_{tt}^2 - m_{\rho^0}^2)^2 + m_{\rho^0}^2\Gamma_{\rho^0}^2(m_{tt})}\,, \tag{5.2}$$

where m_{tt} marks the track-track mass, m_{ρ^0} is a free parameter which determines the mass of the ρ^0 meson. The mass-dependent width Γ_{ρ^0} is described by

$$\Gamma_{\rho^0}(m_{tt}) = \Gamma_{\rho^0}^0\left(\frac{q^*}{q_0^*}\right)^{2l+1}\frac{m_{\rho^0}}{m_{tt}}\,, \tag{5.3}$$

where $l = 1$ is the spin of the ρ^0 meson, $q^* = \frac{1}{2}\sqrt{m_{tt}^2 - (2m_{\pi^\pm})^2}$ and q_0^* are the momenta of the decay products in the rest frame of the ρ^0 and for $m_{tt} = m_{\rho^0}$, respectively.

The background is estimated via the function $\mathcal{B}(m_{tt})$ [96]:

$$\mathcal{B}(m_{tt}) = p_0 e^{-p_1 m_{tt}}\sqrt{m_{tt} - 2\cdot m_{\pi^\pm}}\,. \tag{5.4}$$

The parameters determined by the fit are displayed in the figure and the central values of the masses, m_{ρ^0}, with the widths, $\Gamma_{\rho^0}^0$, and χ^2/ndf are shown separately in table 5.2. The central value of the mass determined from the data (750 MeV) is lower than the nominal value of 775.8 ± 0.5 MeV, while the m_{ρ^0} obtained from the simulation is in agreement with the nominal value. The $\Gamma_{\rho^0}^0$ width is a bit larger in the simulation than in the data, (164 vs 147 MeV) but compatible within the large errors. The widths are dominated by the natural width of the ρ^0 ($\Gamma_{\rho^0}^0 = 150.3 \pm 1.6$ MeV [37]) which is the reason for a fit with a relativistic P-wave Breit-Wigner function.

	Data	Monte Carlo
m_{ρ^0} [MeV]	748.4±14.3	774.4±2.1
$\Gamma_{\rho^0}^0$ [MeV]	146.8±39.1	163.9±4.5
χ^2/ndf	17.65/16	20.43/18

Table 5.2: *Parameters fitted for ρ^0 candidates: the central value of the mass, m_{ρ^0}, the width, $\Gamma_{\rho^0}^0$, and the χ^2 per degree of freedom found by the fit for the data and Monte Carlo (ToyGenMod)*

Due to the asymmetry of the $RBW(m_{tt})$ a lower limit of 0.6 GeV and an upper limit of 1 GeV were chosen as mass region for the ρ^0 meson:

$$0.6\,\text{GeV} < m_{tt} < 1\,\text{GeV}\,. \tag{5.5}$$

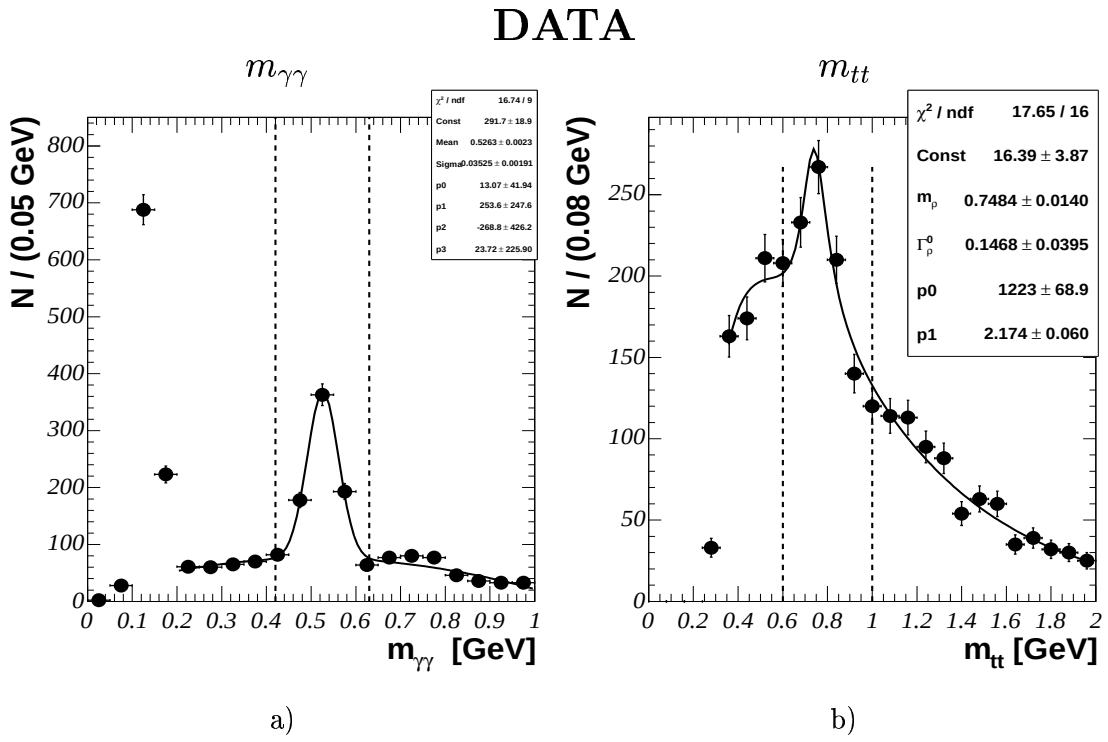

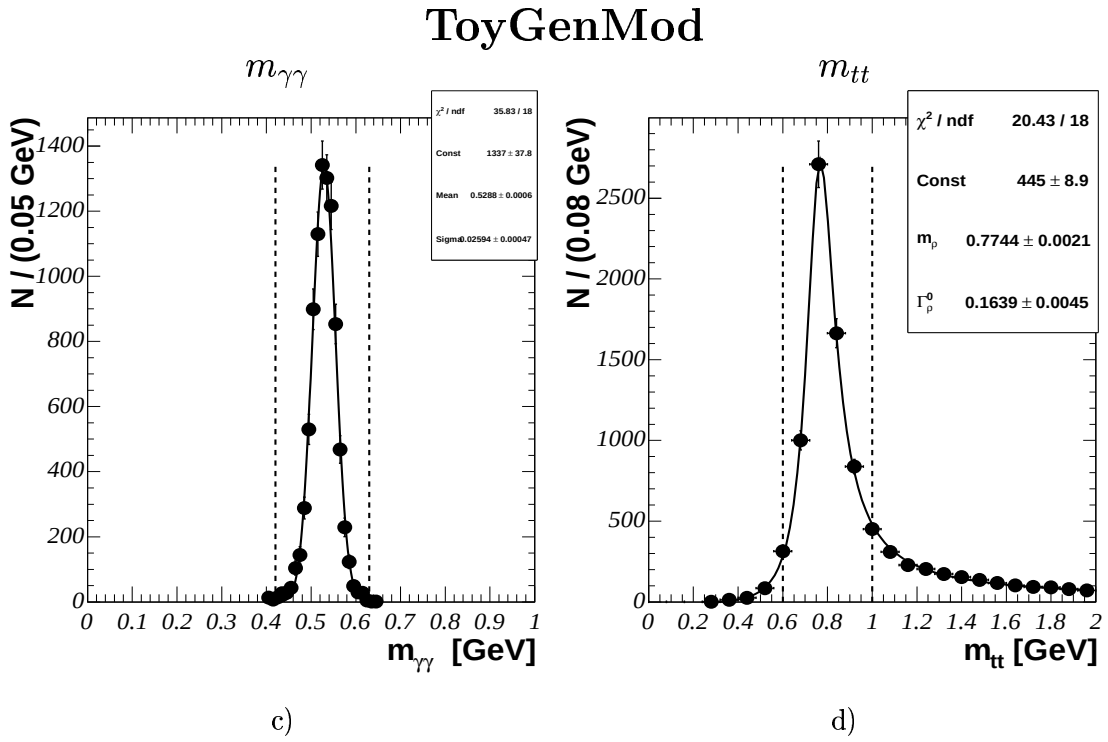

Figure 5.1: *Definition of the η and ρ^0 candidates: The photon-photon and track-track mass spectra are shown for data (upper plots) fitted with the sum of a Gaussian and a polynomial of third order $\mathcal{P}_3(m)$, and fitted with the sum of a P-wave relativistic Breit-Wigner function $RBW(m_{tt})$ and $\mathcal{B}(m)$, respectively. In the two lower plots the photon-photon and track-track mass distributions are shown for the Monte Carlo ToyGenMod fitted by a Gaussian and a P-wave relativistic Breit-Wigner function $RBW(m_{tt})$, respectively. The dashed lines illustrate the chosen mass region for the η and ρ^0 mesons.*

5.2 Signal Extraction and Background Treatment

In the previous chapter, from the inclusively preselected data, one observes the η peak in the photon-photon mass spectrum and the ρ^0 peak in the track-track mass spectrum. Whether these peaks survive the final selection and whether there is a correlation between them is discussed in the following.

The relative and absolute errors for the bins with N entries containing weighted events are calculated via the expression:

$$\Delta N = \sqrt{\sum_i w_i^2}, \qquad \frac{\Delta N}{N} = \frac{\sqrt{\sum_i w_i^2}}{\sum_i w_i}. \tag{5.6}$$

where the sum runs over all events in the bin.

Applying the cuts on exclusivity and cuts on the rapidity gap in addition to the preselection cuts, one obtains for the track-track and photon-photon mass spectra the distributions shown in fig. 5.2. The data are shown by dots, ToyGenModW as grey histogram and PythiaMod as empty histogram. In the track-track mass spectrum *a*) the data exhibit a signal in the ρ^0 mass range. The expectation from ToyGenModW from $\eta - \rho^0$ production is too low to describe the full peak in the data which means that some other processes may exist that contribute. The PythiaMod distribution does not exhibit any clear enhancement. The data also exhibit a peak in the η band in the photon-photon mass distribution, *b*). PythiaMod reasonably describes the distribution outside the η mass window, and no clear peak is seen. On the other hand the expected signal from ToyGenModW agrees with the data. The large errors in the data sample stem from the $L4$ weights. The correlation between the photon-photon and track-track mass spectrum is shown in *c*) for PythiaMod and *d*) for the data sample. For the data sample a clear correlation between the η and ρ^0 is observed while in PythiaMod the correlation is shifted to much higher track-track mass (about 1 GeV) and exhibits a very large spread.

In figure 5.3 the track-track mass is illustrated when selecting the η in the photon-photon mass spectrum according to eq. (5.1). The data (dots) are fitted by the sum of $RBW(m_{tt})$ (eq. (5.2)) and $\mathcal{B}(m_{tt})$ (eq. (5.4)). The parameters obtained from the fit are listed in table 5.3. The fitted mass and the width of the ρ^0 are compatible with the nominal values within the errors.

In fig. 5.3 also the contribution from the process $\gamma p \to \rho^0_{diff} X \to \eta\rho^0 X$ to the full signal is shown. From the difference between Pythia (full histogram) and PythiaMod (dashed histogram) distributions one gets 4.2 events which contribute to the total signal. But a much more probable process in Pythia is the production of non-bound $\pi^-\pi^+$ states: $\gamma p \to \rho^0_{diff} X \to \eta\pi^-\pi^+ X$ which is responsible for most of the background. The mechanism of ρ^0_{diff} production is described in chapter 3.2.1 in more detail.

The dot-dashed histogram shows background estimation from RapGap. Outside the ρ^0 band it agrees reasonable well with PythiaMod. The lower part of the m_{tt} distribution is better described by RapGap while the part of higher m_{tt} is better described by PythiaMod. The grey histogram demonstrates the track-track spectrum simulated by ToyGenModW.

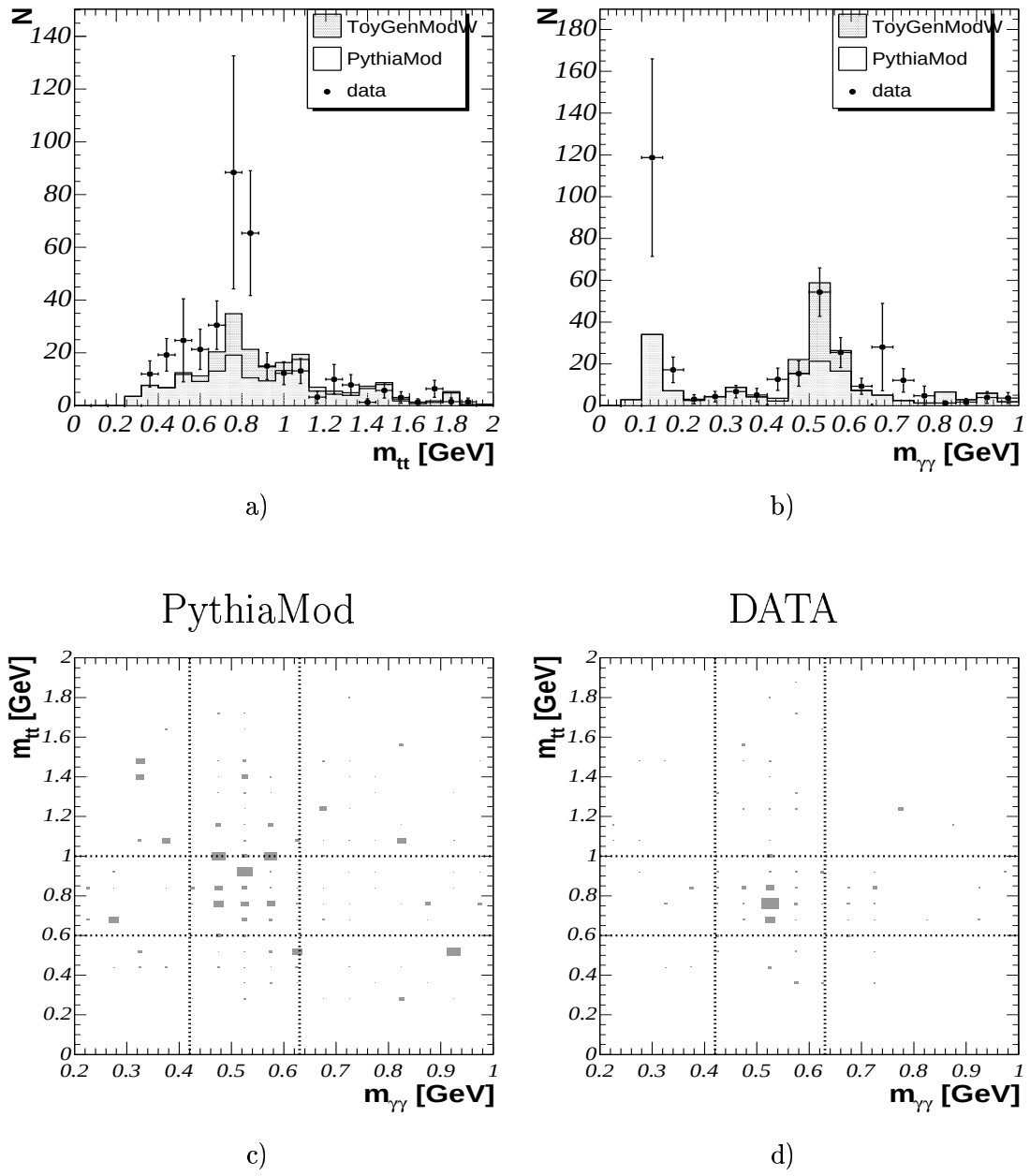

Figure 5.2: *Mass distribution of the (η-ρ^0)-sample: Comparison between data (dots), PythiaMod (white histogram) and ToyGenModW (grey histogram) for the track-track a) and photon-photon b) distribution after all analysis cuts (table 4.13). In c) and d) the correlation between photon-photon and track-track mass for PythiaMod and data, respectively, is shown.*

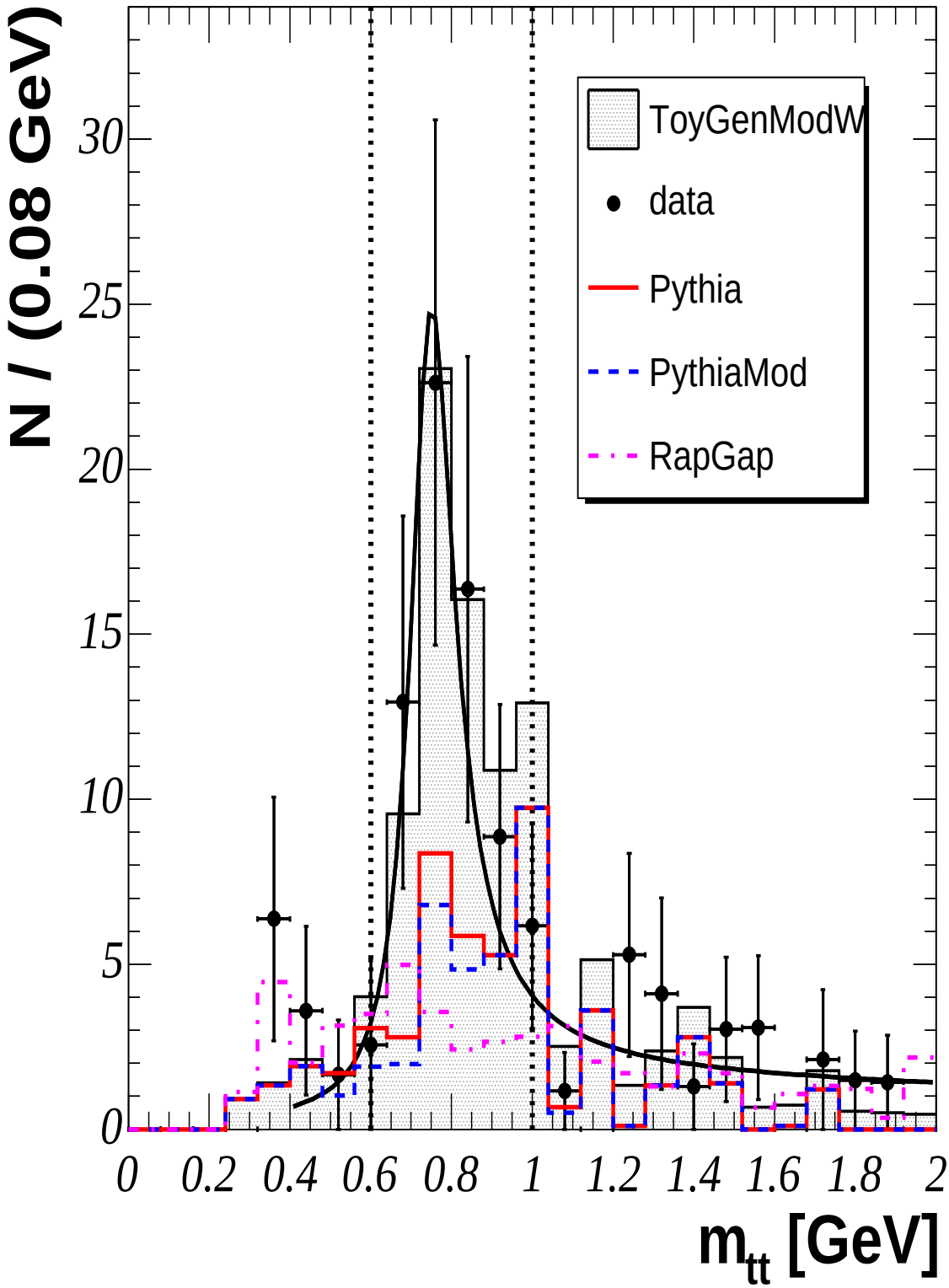

Figure 5.3: *Track-track mass distributions for the η band: Comparison between data (dots), Pythia(full-line histogram), PythiaMod (dashed histogram), RapGap (dot-dashed histogram) and ToyGenModW (grey histogram) for the track-track mass distribution after all analysis cuts (table 4.13). Also here the grey histogram is plotted as a sum ToyGenModW and PythiaMod distributions. The two dotted vertical lines demonstrate the ρ^0 band.*

A	3.08±1.22	[-]
m_{ρ^0}	(751.35±32.79)	GeV
$\Gamma^0_{\rho^0}$	(129.54±60.47)	GeV
p_0	14.85±19.67	$\mathrm{GeV}^{-3/2}$
p_1	19.44±14.82	GeV^{-1}
χ^2/ndf	7.35/13	[-]

Table 5.3: *Fitted Parameters of track-track mass distribution shown in figure 5.2: The table lists the parameters and their errors found by the fit together with the respective χ^2 per degree of freedom.*

It agrees with the data. In the RapGap MC sample only a negligible number of contributing events $N(\gamma p \to \eta\rho^0 X) = 0.3$ has been observed.

Control plots for the $(\eta - \rho^0)$ sample are shown in fig. 5.4 with a comparison between data (dots), PythiaMod (empty histogram) and expectation from ToyGenModW (grey histogram). In a) the variable $E - p_z$ is shown which is expected to be about 55 GeV, twice the electron beam energy. The data exhibit a slight shift towards lower values than seen in the simulation. The mean values from the data and from the simulation differ by roughly 1 GeV (54.4 GeV for the simulation and 53.8 GeV for the data) which is mainly due to the miscalibration of the SpaCal data in 1996 and 1997 and resolution effects. Also the shape of the background plays a rôle. In b) the z-Vertex position is shown. One observes reasonable agreement between the expectation from ToyGenModW and the data.

5.3 Comparison of Monte Carlo and Data

In this section the comparison between data, the background Monte Carlo model PythiaMod and the expectation from the signal MC, ToyGenModW, is discussed. All simulated and measured distributions shown in the following are obtained after application of all analysis cuts summarized in table 4.13 and also the cuts on the $\gamma - \gamma$ mass, equation 5.1, and *track* − *track* mass, equation 5.5, to ensure that events contain the η and ρ meson candidates.

The properties of the η candidates and the photon candidates originating from the η decay are shown in figure 5.5 for data (dots) and both Monte Carlos: the expectation from ToyGenModW is shown in grey on top of the background assumption of PythiaMod. The following distributions are shown: a) energy of all clusters, b) energy of the hottest cluster, c) energy of the η meson, d) distance between both clusters, e) transverse distance of the clusters from the beam line, f) radius of the clusters g) transverse momentum of the η meson and h) its rapidity. In general one observes reasonable agreement between ToyGenModW and the data. Only a small difference is observed in the E_η and p_t distributions: the simulation is distributed smoothly while the data are peaked at lower values.

The energy of the hottest cluster is above 2 GeV which is due to the cut applied in the analysis. The energy of the η meson is in the interval of $6-14$ GeV and the main part is carried

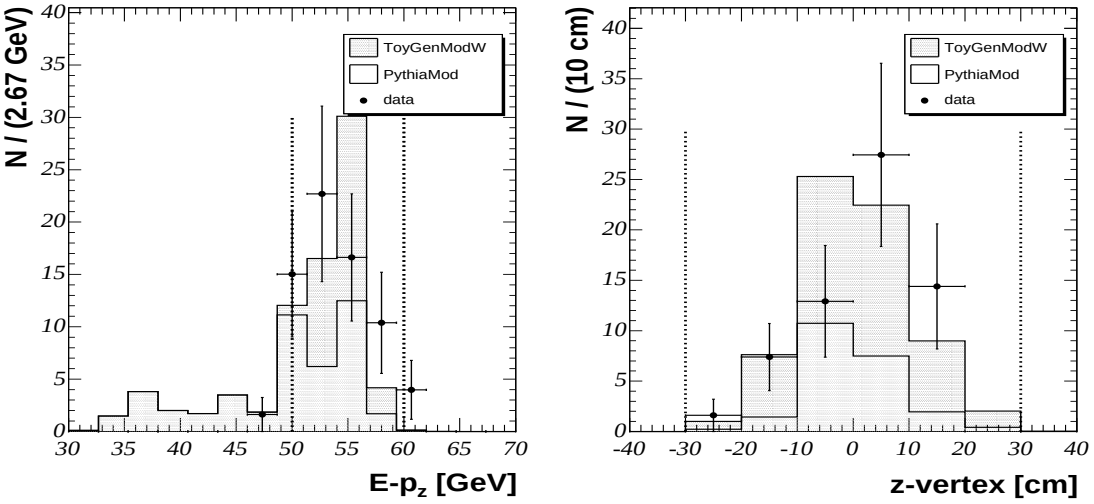

a) b)

Figure 5.4: *Control plots for the (η-ρ^0) sample: a) The variable $E - pz$ and b) z-coordinate of the vertex. The dots represent the data, the white histogram PythiaMod and the grey histogram ToyGenModW. The dotted lines demonstrate the applied cuts.*

by the hottest cluster which means that the energy of the η candidate is distributed between its decay products asymmetrically. The distance between clusters originating from the η meson is safely above the minimum of 4 `cm` for separate detection given by the SpaCal granularity. Also one can see that the clusters are dominantly produced in the very backward direction at the border of the SpaCal acceptance which is shown by RD_{cl} distribution. The cluster radius distribution, R_{cl}, shows a reasonable choice of an upper limit of 3 `cm`, used in this analysis. The p_t of the η meson is rather low which is characteristic for soft physics.

The properties of the ρ^0 candidates and pion candidates originating from the ρ^0 meson decay are shown in figure 5.6 for data (dots), ToyGenModW (grey histogram) and Pythia (empty histogram). The following distributions are shown: a) energy of all tracks, b) energy of the ρ^0 meson, c) transverse momentum of all tracks and d) the ρ^0 meson, e) polar angle of all tracks and f) the ρ^0 meson and g) rapidity of the ρ^0 meson. In h) the rapidity of the η meson versus rapidity of the ρ^0 meson in the data sample is depicted. The dashed lines indicate the region in which the cross section will be determined.

The typical energy of the tracks is below 1.5 `GeV`. It is an argument why no requirement on the identification of the pion candidate in the LAr calorimeter was imposed. The energy of the ρ^0 meson is $1-3$ `GeV` which is much less then the energy of the η meson. The transverse momenta of the tracks and ρ^0 meson are below 1.5 `GeV` which is also characteristic for soft processes. The polar angle distributions show that the tracks and also the ρ^0 meson are predominantly produced in the backward region at the end of the CJC acceptance which is also demonstrated by the rapidity distribution. Reasonable agreement can be observed between ToyGenModW and data in all distributions.

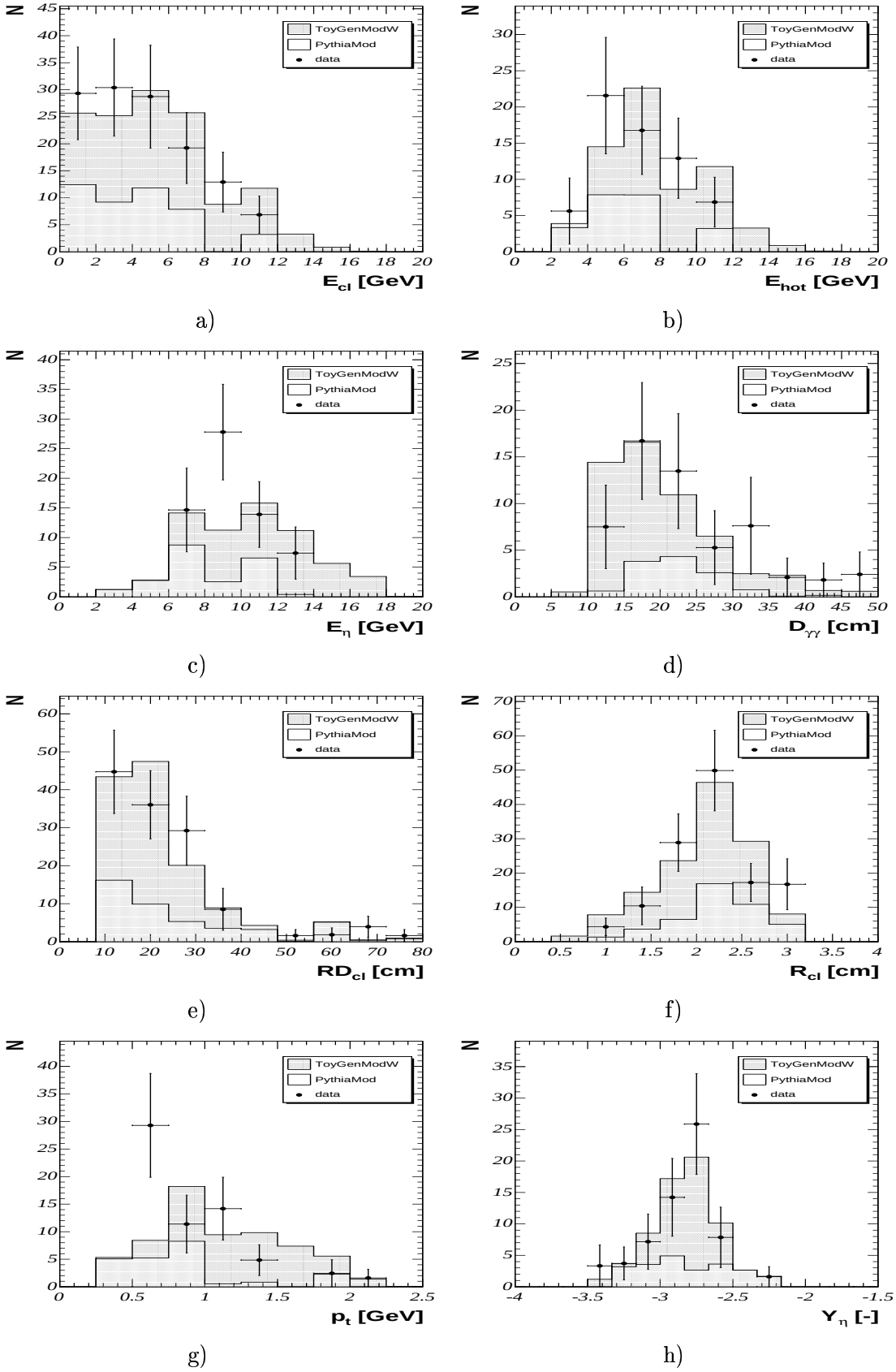

Figure 5.5: *Properties of the photon candidates of the decay $\eta \to \gamma\gamma$ after application of all analysis cuts (table 4.13) and the cuts on the $m_{\gamma\gamma}$ (eq. (5.1)) and m_{tt} (eq. (5.5)): a) the cluster energy, b) energy of the hottest cluster, c) η energy, d) distance between two photons originating from the η meson decay, e) radial distance of the cluster from the beam line, f) cluster radius, g) transverse momentum of the η meson, h) rapidity of the η meson.*

Figure 5.7 shows a collection of distributions for the $(\eta - \rho^0)$ sample together with the respective expectation from Monte Carlo, where the signal is plotted in grey. The distributions shown are: a) the rapidity difference between ρ^0 and η mesons, $Y_{\rho^0} - Y_\eta$, b) the center of mass energy of the $\gamma -$ `proton` system, $W_{\gamma p}$, c) the squared four-momentum transfer at the photon vertex, $|t_1|$, d) the squared four-momentum transfer at the proton vertex, $|t_2|$, e) the squared center of mass energy of the $\eta - \rho^0$ system, s_1, and f) the squared center of mass energy of the $\rho^0 -$ `proton` system, s_2, f). Also here, generally reasonable agreement between data and ToyGenModW is observed. The s_1, s_2, $Y_{\rho^0} - Y_\eta$ and $W_{\gamma p}$ distributions have strong influence from detector effects and therefore have to be corrected by these effects which is discussed in the next chapter.

5.4 Results

In this chapter the cross section calculation using different approaches for the signal and background extraction is executed. Also characteristic differential distributions for the upper and lower vertex are obtained.

5.4.1 Total Cross Section

The cross section $\sigma(\gamma p \to \eta\rho^0 X)$ is determined in the kinematical region defined by the scattered electron detected in the electron tagger and by restrictions on the rapidities of the η and ρ^0 mesons:

$$\begin{array}{rcccl} 0.3 & < & y & < & 0.65 \\ Q^2 & < & 0.01\,\texttt{GeV} & & \\ -3.5 & < & Y_\eta & < & -2 \\ -1.5 & < & Y_{\rho^0} & < & 1.5 \end{array} \tag{5.7}$$

It is obtained via the expression:

$$\sigma^*(\gamma p \to \eta\rho^0 X) = \frac{RBW_{corr}\,\mathcal{N}^{signal}}{\epsilon_{tot}\epsilon_{eTag33}\,BR_{tot}\,\mathcal{L}\,\mathcal{F}_{\gamma/e}}\,, \tag{5.8}$$

where the σ^* denotes the total cross section calculated in the kinematical region defined in (5.7), $\mathcal{N}^{signal}$ is the number of signal events corrected for trigger efficiencies, L1 and L4 prescale factors and weights, respectively, $\epsilon_{tot} = \epsilon_{geom}\epsilon_{det} = (6.62 \pm 0.52)\,\%$ is the total efficiency determined in section 4.22, $\langle\epsilon_{eTag33}\rangle = 0.5$ is the average of the electron tagger acceptance, $BR_{tot} = (BR_{\eta\to\gamma\gamma} = 39\,\%) \cdot (BR_{\rho^0\to\pi^+\pi^-} = 99\,\%) = 38\%$ is the total branching ratio calculated as the product of the branching ratios for the decays: $\eta \to \gamma\gamma$ and $\rho^0 \to \pi^+\pi^-$, $\mathcal{L} = 76$ pb^{-1} (table 4.7) is the integrated luminosity collected over the years 1996, 1997, 1999 and 2000, and $\mathcal{F}_{\gamma/e} = 1.32 \cdot 10^{-2}$ is the flux of photons stemming from the electron as given by the integral over y and Q^2 defined by the electron tagger (2.16). $RBW_{corr} = \int_{2m_{\pi^\pm}}^{2} RBW(m_{tt})\mathrm{d}m_{tt} / \int_{0.6}^{1} RBW(m_{tt})\mathrm{d}m_{tt} = 1.25$ is the correction on the integral of the relativistic Breit Wigner function (defined in (5.2)) limited by the

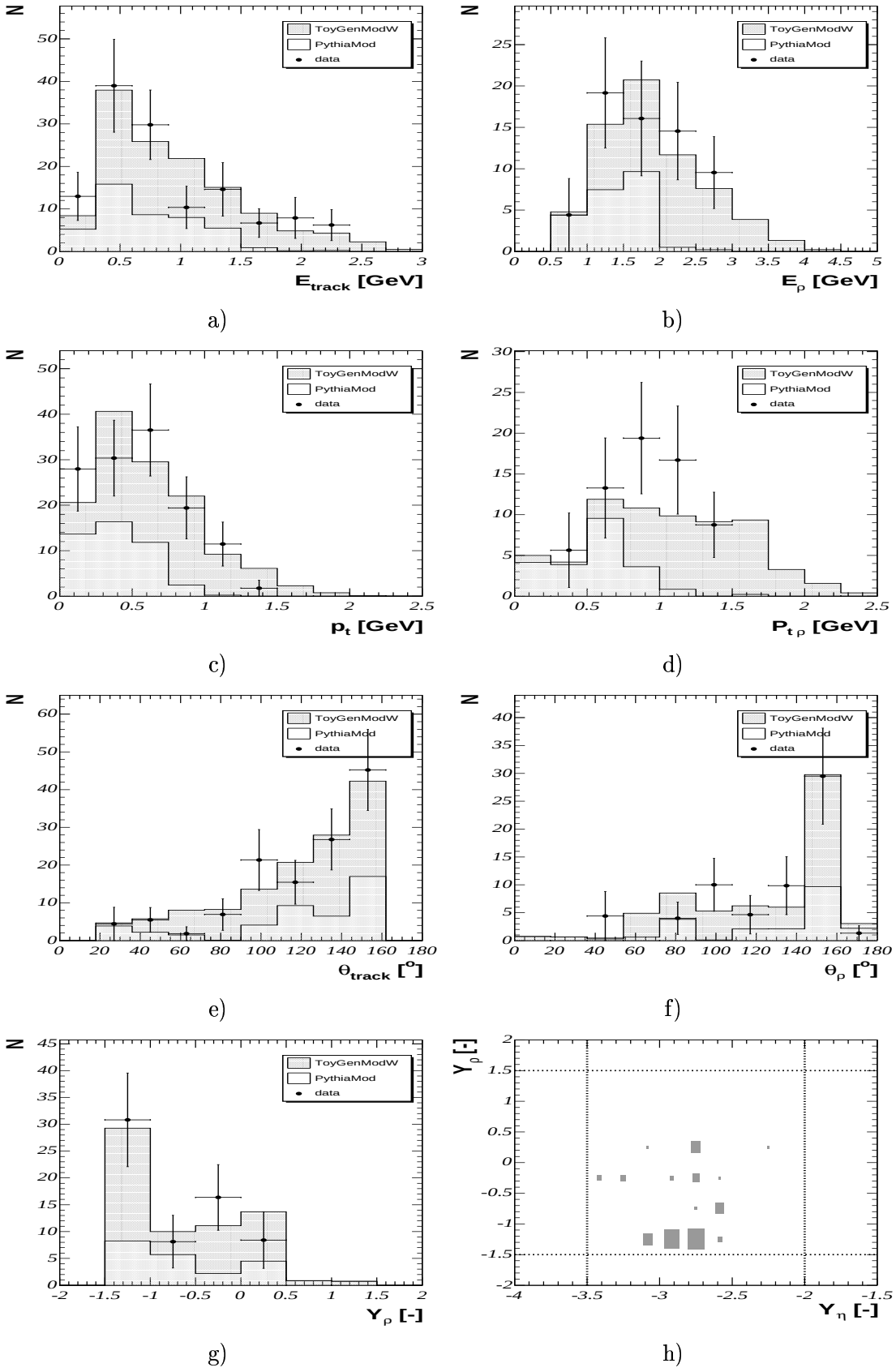

Figure 5.6: *Properties of the pion candidates of the decay $\rho^0 \to \pi^+\pi^-$ after application of all analysis cuts (table 4.13) and the cuts on the $m_{\gamma\gamma}$ (eq.5.1) and m_{tt} (eq.5.5): a) track energy, b) ρ^0 energy, c) and d) transverse momentum of the track and ρ^0, respectively, e) and f) polar angle of the track and the ρ^0, respectively and g) rapidity of the ρ^0 meson. In h) the rapidity of the η meson versus rapidity of the ρ^0 meson in the data sample is depicted. The dashed lines indicate the region in which the cross section will be determined.*

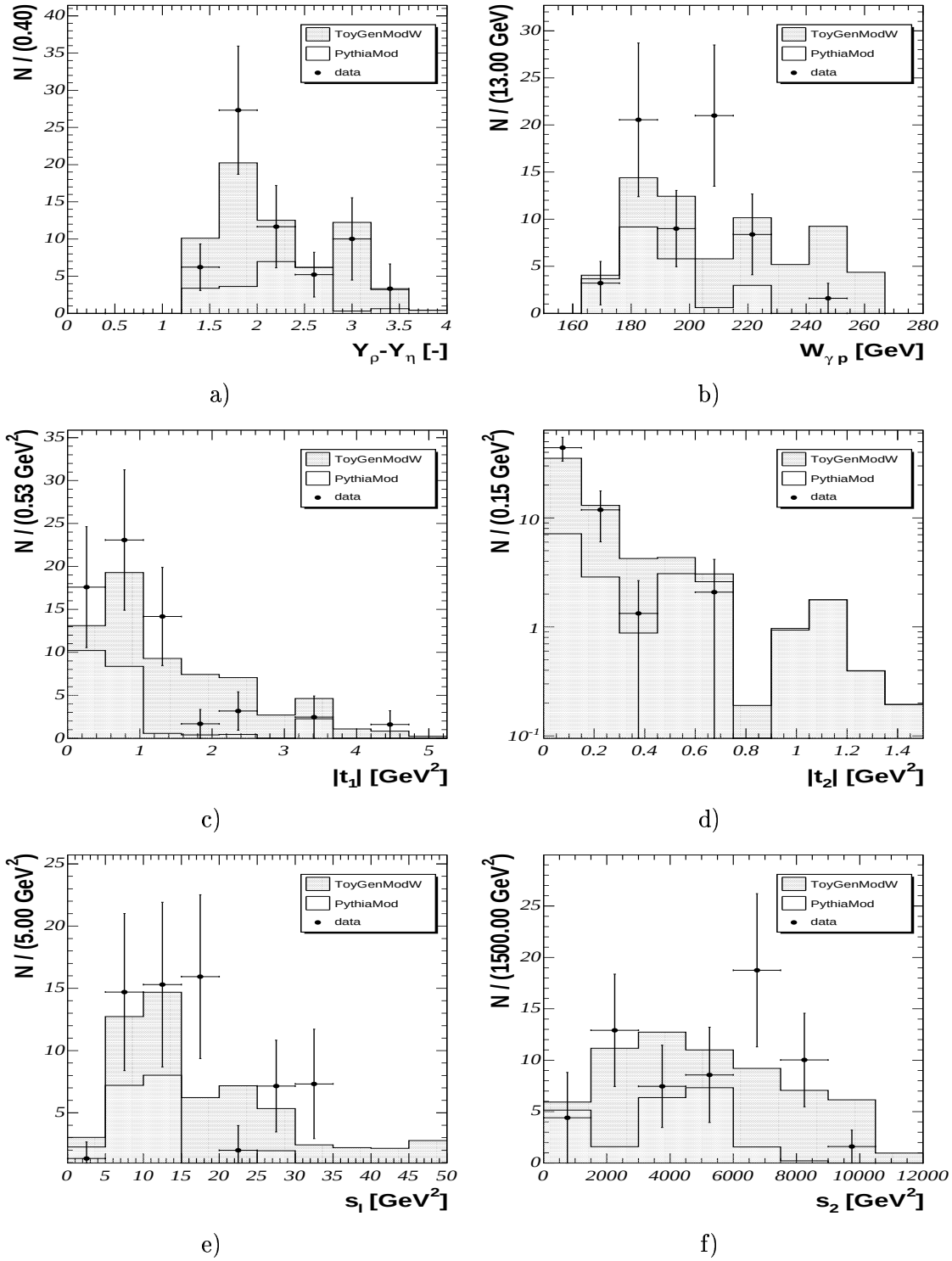

Figure 5.7: *Properties of the $\eta - \rho^0$ system after application of all analysis cuts (table 4.13) and the cuts on the $m_{\gamma\gamma}$ (eq.5.1) and m_{tt} (eq.5.5): a) Rapidity difference between ρ^0 and η mesons, $Y_{\rho^0} - Y_\eta$, b) center of mass energy of the γ-proton system, $W_{\gamma p}$, c) the squared four-momentum transfer at the photon vertex, t_1, d) the squared four-momentum transfer at the proton vertex, t_2, e) the squared center of mass energy of the $\eta - \rho^0$ system, f) the squared center of mass energy of the ρ^0 − proton system. The dots represent the data, the white histogram PythiaMod and the grey histogram ToyGenModW.*

ρ^0 mass window.

Two methods are used to get independent approaches for the extraction of $\mathcal{N}^{signal}$. In the first method $\mathcal{N}^{signal}$ will be obtained from the fit of the η signal in the $\gamma - \gamma$ invariant mass spectrum when selecting ρ band in the m_{tt} spectrum. In the second method it will be determined from the crossed η and ρ^0 mass bands shown in fig. 5.2 c). In principle $\mathcal{N}^{signal}$ could be obtained also from the fit of RBW but since the integral of the relativistic Breit-Wigner function is not normalized to one it is problematic to obtain the number of events from the fit and therefore this method is not employed. The two methods used are described in the following:

- $\mathcal{N}^{signal}$ is obtained from a Gaussian fit of the η invariant mass peak in the photon-photon mass distribution demanding the track-track invariant mass to be within four different invariant mass windows: $m_{tt} \in (0.6, 1.0)\,\mathtt{GeV}$, $m_{tt} \in (0.5, 1.15)\,\mathtt{GeV}$, $m_{tt} \in (0.5, 1.3)\,\mathtt{GeV}$ and $m_{tt} \in (0.5, 1.45)\,\mathtt{GeV}$. The corresponding $m_{\gamma\gamma}$ distributions are fitted by the sum of the Gaussian $G(m_{\gamma\gamma})$, to describe the η mass peak, and a polynomial of third order $\mathcal{P}_3(m_{\gamma\gamma})$, to describe non resonant background. The fitted distributions are shown in fig. 5.8. To estimate resonant background PythiaMod and RapGap distributions are shown.

  The Gaussian $G(m_{\gamma\gamma})$ has the form:

$$G(m_{\gamma\gamma}) = \frac{\mathcal{N}^{signal}}{\sqrt{2\pi}} \frac{\Delta m_{\gamma\gamma}}{\sigma_\eta} \exp\left[-\frac{1}{2}\left(\frac{m_{\gamma\gamma} - \mu_\eta}{\sigma_\eta}\right)^2\right] \tag{5.9}$$

  with the $\mathcal{N}^{signal}$ as the only free parameter. The values μ_η and σ_η are taken from the fits to the inclusively preselected sample (table 5.1). $\Delta m_{\gamma\gamma}$ is the width of the bins. The resonant background has been estimated by counting the events in PythiaMod above the polynomial. After subtraction of the resonant background, $\mathcal{N}_i^{res}$ from the value $\mathcal{N}_i^{tot}$ obtained from the Gaussians one obtains for $\mathcal{N}_i^{signal}$ the following values:

$$\begin{array}{lllllllll}
\mathcal{N}_1^{tot} & = & 38.0 \pm 12.8, & \mathcal{N}_1^{res} & = & 5 \pm 2.2 & \Rightarrow & \mathcal{N}_1^{signal} & = & 33 \pm 13.0 \\
\mathcal{N}_2^{tot} & = & 46.0 \pm 13.4, & \mathcal{N}_2^{res} & = & 13 \pm 3.6 & \Rightarrow & \mathcal{N}_2^{signal} & = & 33 \pm 13.9 \\
\mathcal{N}_3^{tot} & = & 49.4 \pm 13.7, & \mathcal{N}_3^{res} & = & 15 \pm 3.9 & \Rightarrow & \mathcal{N}_3^{signal} & = & 34 \pm 14.2 \\
\mathcal{N}_4^{tot} & = & 51.6 \pm 13.8, & \mathcal{N}_4^{res} & = & 16 \pm 4 & \Rightarrow & \mathcal{N}_4^{signal} & = & 36 \pm 14.4
\end{array}$$

  where $\mathcal{N}_i^{tot}$ is the number of events obtained from the Gaussian, $\mathcal{N}_i^{res}$ is the estimated number of events from the resonant background (events lying above the fitted polynomial) and $\mathcal{N}_i^{signal}$ is their difference with the absolute error of $\Delta\mathcal{N}_i^{signal} = \sqrt{(\Delta\mathcal{N}_i^{tot})^2 + \Delta\mathcal{N}_i^{res})^2}$. Making the ρ band wider the processes like $\gamma p \to \pi^-\pi^+\eta\,, \pi^-\pi^+\pi^0\eta\,, \ldots$ start to contribute significantly to the resonant background.

- Another possibility is to get $\mathcal{N}^{signal}$ as the difference of the total number of events measured in the data ($\mathcal{N}_5^{tot}$) and the number of background events ($\mathcal{N}^{bkg}$). They are obtained from the crossed region of the η and ρ^0 invariant mass bands illustrated in fig. 5.2 c) and d). From the data sample one gets: $\mathcal{N}_5^{tot} = 63.7 \pm 12.9$. Assuming that

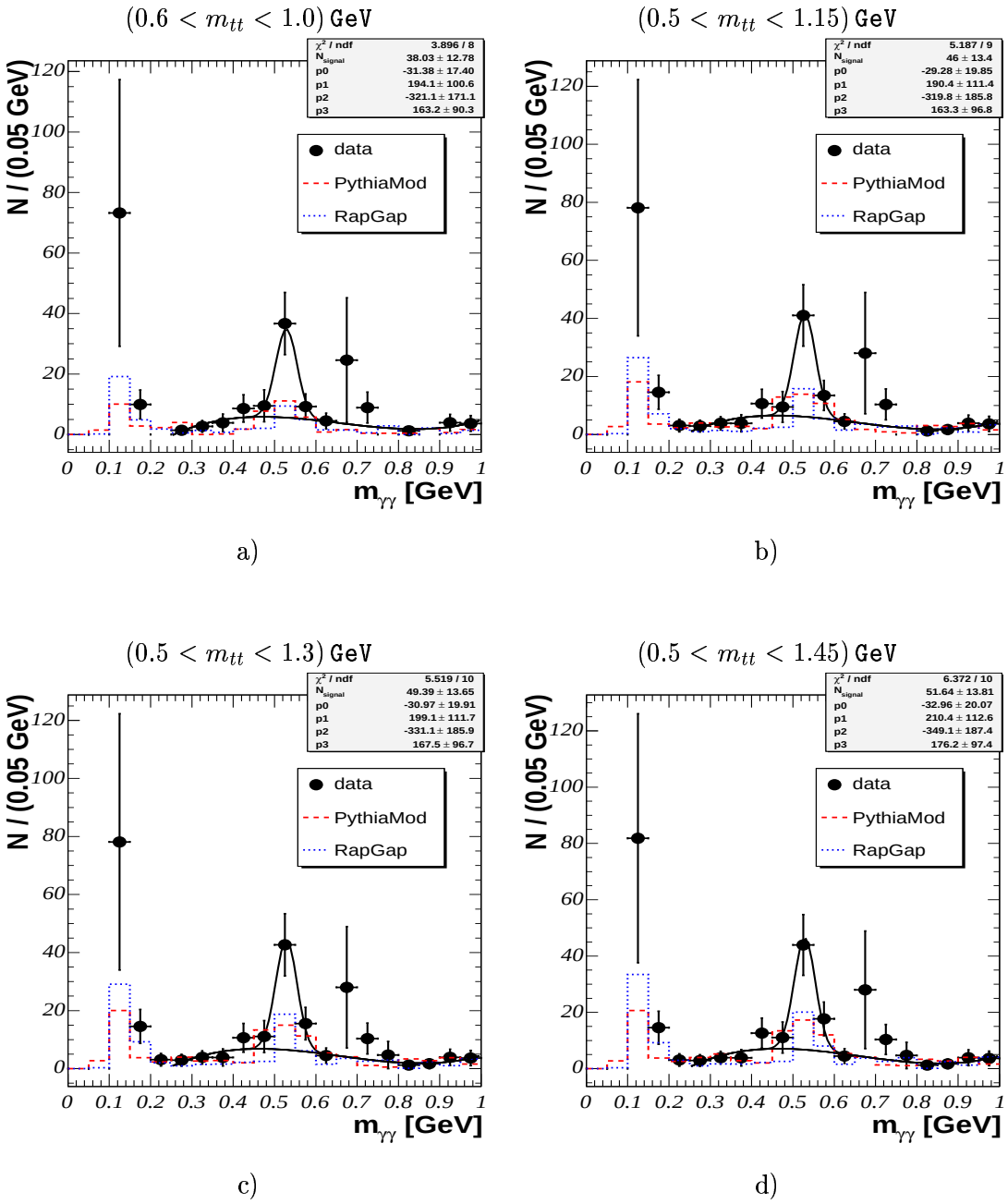

Figure 5.8: *The $m_{\gamma\gamma}$ distributions for four different ρ^0 invariant mass windows: a) $(0.6 < m_{tt} < 1.0)$ GeV, b) $(0.5 < m_{tt} < 1.15)$ GeV, c) $(0.5 < m_{tt} < 1.3)$ GeV, d) $(0.5 < m_{tt} < 1.45)$ GeV.*
The data (dots) were fitted by a Gaussian defined in eq. 5.9 and a polynomial of third order. Also background from PythiaMod (dashed histogram) and RapGap (dotted histogram) is shown.

the background is properly described by PythiaMod, the background is estimated to be $\mathcal{N}_{pyt}^{bkg} = 22.2 \pm 5.0$. Then:

$$\mathcal{N}_5^{signal} = \mathcal{N}_5^{tot} - \mathcal{N}_{pyt}^{bkg} = 41.5 \pm 13.8$$

with the absolute error calculated as: $\Delta\mathcal{N}^{signal} = \sqrt{(\Delta\mathcal{N}_5^{tot})^2 + (\Delta\mathcal{N}_{pyt}^{bkg})^2}$. Similar results of the background estimation provides also RapGap: $\mathcal{N}_{rap}^{bkg} = 18.6 \pm 3.6$ with only 0.3 events contributing to the signal via $\gamma p \to \eta\rho X$ which provides only 2% for the signal-to-background ratio. Pythia gives $4.2/22.2 \approx 16\%$ for the signal-to-background ratio.

The results from both methods differ by 22% but are consistent within the statistical errors when comparing $\mathcal{N}_1^{signal} = 34 \pm 13$ and $\mathcal{N}_5^{signal} = 41.5 \pm 13.8$. The difference is related mainly to the fact that in the second method the summing of events in the bins to obtain $\mathcal{N}_5^{tot}$ runs over the wider region defined by $0.42\,\mathtt{GeV} < m_{\gamma\gamma} < 0.63\,\mathtt{GeV}$, see (5.1), in which the PythiaMod distribution lies below the data. Another source of the difference is related to the principle on which the methods are based. The first method uses an integral of the fitted function over only three bins with relatively large bin-size which is lower than the sum of the events over the three bins. However only one parameter is free since μ_η and σ_η are fixed. A small incompatibility of the first method arises from the estimation of the $\mathcal{N}_i^{res}$ counting the events in the bins since no reasonable fit of the resonant background in PythiaMod can be performed. However this incompatibility is very low since it concerns only a few events. Comparing with the second method the first method is much less dependent on the background estimation via any Monte Carlo model. Since it is not clear how reliable Pythia and RapGap can describe such background it is a crucial point why the first method will be used for the cross section determination. Inserting the mean value from $\langle \mathcal{N}_1^{signal} \cdots \mathcal{N}_4^{signal} \rangle \pm \langle \Delta\mathcal{N}_1^{signal} \cdots \Delta\mathcal{N}_4^{signal} \rangle = 34 \pm 14$ into eq. 5.8 one obtains:

$$\sigma^*(\gamma p \to \eta\rho^0 X) \;=\; (3.5 \pm 1.4\,(stat))nb. \tag{5.10}$$

The statistical error for the cross section is calculated by adding the relative errors of the total efficiency ($\Delta\epsilon/\epsilon = 8\%$) and signal events $\langle\Delta\mathcal{N}^{signal}\rangle/\langle\mathcal{N}^{signal}\rangle = 14/34 = 41\%$ in quadrature. However the difference between the values obtained for $\mathcal{N}^{signal}$ of both methods will be taken as a systematic uncertainty.

5.4.2 Measurement of the Squared Four-momentum Transfer at the Photon and Proton Vertex

From the measured differential distributions of the squared four-momentum transfer at the photon vertex, $|t_1|$, and proton vertex, $|t_2|$, shown in figure 5.7 c) and d), respectively, one can determine the slopes b_{t_1} and b_{t_2} by fitting an exponential $\propto e^{-b_t|t|}$ to the data distribution. This is motivated by the expectation from eq. 2.29. To extract the true value of the slopes, the $|t_{1(2)}|$ distributions as they are measured have to be corrected for the total efficiency determined by means of ToyGenModW in chapter 4.8. Hence the correction function is obtained from the reconstructed distribution $f_{rec}^{\mathrm{MC}}(x)$ after applying all analysis cuts and the true (generated) distribution $f_{gen}^{\mathrm{MC}}(x)$:

$$\epsilon(x) = \frac{f_{rec}^{\mathrm{MC}}(x)}{f_{gen}^{\mathrm{MC}}(x)}\,, \tag{5.11}$$

and the corrected data distribution $f_{data}^{corr}(x)$ is obtained by multiplying the measured one, $f_{data}(x)$, by the correction defined in equation (5.11):

$$f_{data}^{corr}(x) = \epsilon(x) \cdot f_{data}(x)\,. \tag{5.12}$$

Applying this correction to the measured $|t_1|$ and $|t_2|$ spectrum the resulting distributions after background subtraction (PythiaMod) are shown in fig. 5.9 a) and b), respectively.

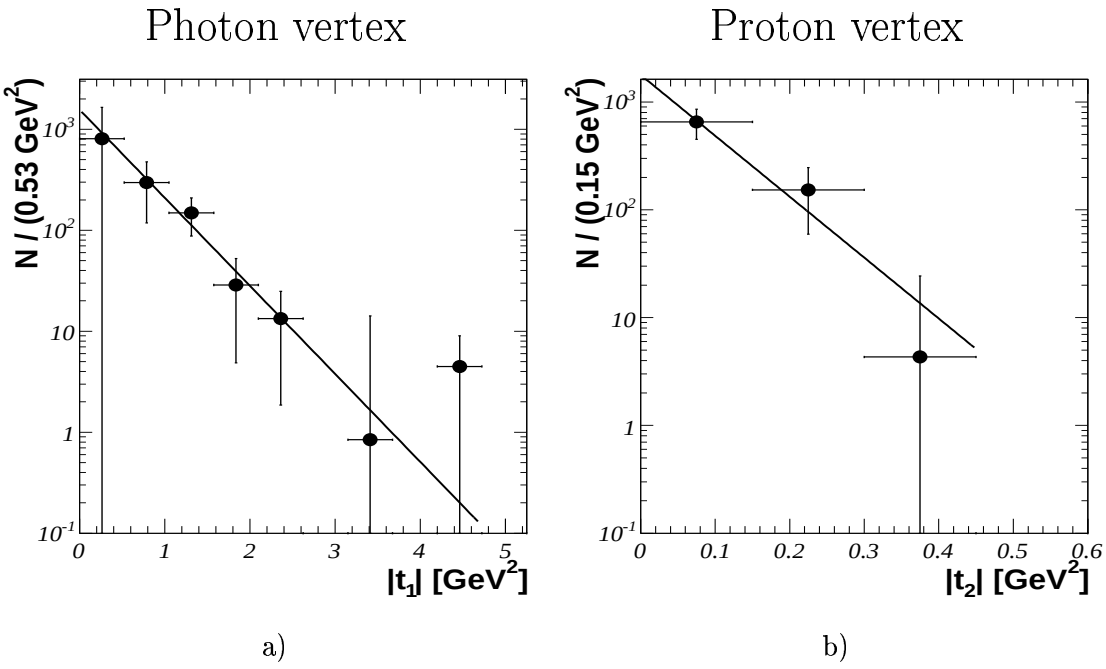

Figure 5.9: *Corrected differential distribution of the squared four-momentum transfer $|t_1|$ at the upper $\gamma - \eta$ vertex a) and $|t_2|$ at the lower proton vertex b).*

Fitting the results with

$$f_{data}^{corr}(|t_1|) = A_1 e^{-b_{t_1}|t_1|}, \quad f_{data}^{corr}(|t_2|) = A_2 e^{-b_{t_2}|t_2|}\,, \tag{5.13}$$

yields slopes of

$$b_{t_1} = (2.0 \pm 0.5)\,\mathtt{GeV}^{-2}, \quad b_{t_2} = (13^{-3}_{+6})\,\mathtt{GeV}^{-2}\,. \tag{5.14}$$

Parameters of the fits with χ^2/ndf are summarized in table 5.4.

For the mean values for $|t_1|$ and $|t_2|$ the following values are obtained:

$$\langle|t_1|\rangle \approx 0.6\ \mathtt{GeV}^2 \tag{5.15}$$
$$\langle|t_2|\rangle \approx 0.1\ \mathtt{GeV}^2. \tag{5.16}$$

	$\|t_1\|$	$\|t_2\|$	
A	$(1.6^{+1.2}_{-0.9}) \cdot 10^3$	$1.7^{+1.3}_{-0.7} \cdot 10^3$	$\mathtt{GeV}^{-2}$
b_t	2.0 ± 0.5	$13.0^{+2.9}_{-6.7}$	$\mathtt{GeV}^{-2}$
χ^2/ndf	1.4/5	0.7/1	[-]

Table 5.4: *The table lists the parameters determined from the fit of the squared four-momentum transfers t_1 and t_2 at the photon and proton vertex, respectively, with their errors together with their respective χ^2 per degree of freedom.*

5.4.3 Measurement of the Squared Center of Mass Energy of the Subsystems $\eta - \rho^0$ and $\rho^0 - proton$

From the differential distributions of the squared center of mass (CMS) energy of the subsystems $\eta - \rho^0$, s_1, and $\rho^0 - proton$, s_2, shown in figure 5.7 e) and f), respectively, one can measure the energy dependence. Again the corrections obtained in chapter 4.8 have been applied to the measured s_1 and s_2 distributions according to relation 5.12. The resulting distributions after background subtraction (PythiaMod) are shown in fig. 5.10 a) and b). The energy dependence motivated by the prediction from eq. 2.32 is expected in the form $\propto s^{-b_s}$. Fitting the corrected distribution via:

$$f^{corr}_{data}(s_1) = A_1 s_1^{b_{s_1}} \, , f^{corr}_{data}(s_2) = A_2 s_2^{b_{s_2}} \, , \tag{5.17}$$

yields for the s_1 dependence:

$$b_{s_1} = (-2.9^{+0.8}_{-0.7}) \, . \tag{5.18}$$

The fit of the s_2 distribution by 5.17 does not provides a reliable result since in the procedure of the χ^2 minimization the bins with low entries get very high 'weights' and the bins with high number of entries become less 'important' for the fit. Therefore the fit of the s_2 distribution via 5.17 is not presented. Parameters of the fits with χ^2/ndf are summarized in table 5.5.

	s_1	
A	$2.3^{+13}_{-1.5} \cdot 10^5$	$\mathtt{GeV}^{-2}$
b_s	$-2.9^{+0.8}_{-0.7}$	[-]
χ^2/ndf	6.2/5	[-]

Table 5.5: *The table lists the parameters determined from the fit for the squared center of mass energy of the $\eta - \rho^0$ system, s_1. Also the errors together with their respective χ^2 per degree of freedom are listed.*

For the mean values for s_1 and s_2 the following values are obtained:

$$\langle s_1 \rangle \approx 12.5 \ \mathtt{GeV}^2 \tag{5.19}$$

$$\langle s_2 \rangle \approx 6234 \ \mathtt{GeV}^2. \tag{5.20}$$

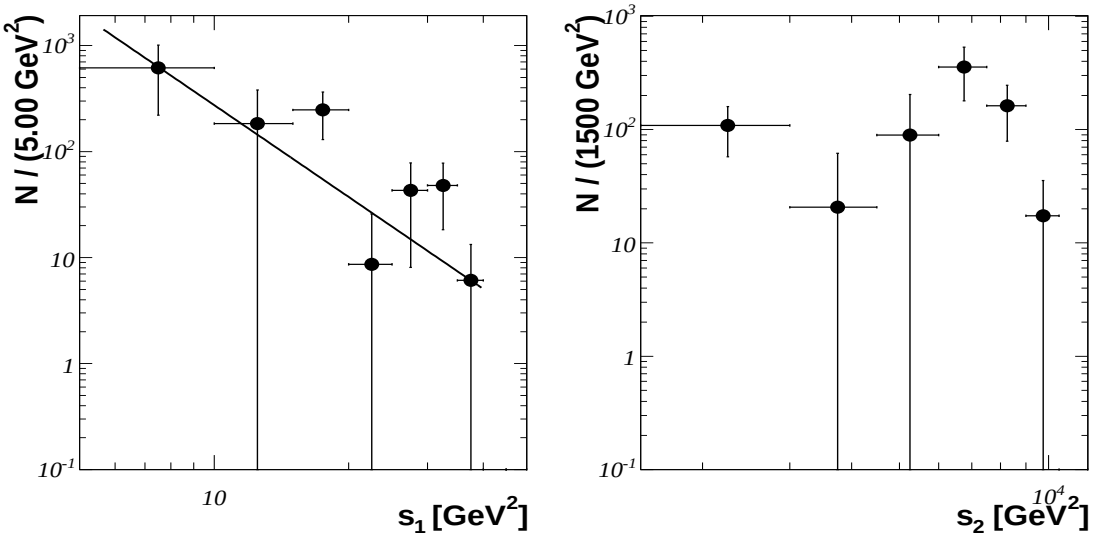

a) b)

Figure 5.10: *Corrected differential distributions for: a) the squared center of mass energy of the $\eta - \rho^0$ system, s_1, and b) the squared center of mass energy of the ρ^0 – proton system, s_2.*

5.4.4 Measurement of the Rapidity Difference between ρ^0 and η Mesons

Another important characteristics of the $\eta - \rho^0$ system is the dependence on the rapidity difference between the two mesons, $\Delta Y = Y_{\rho^0} - Y_\eta$. From the measured ΔY distribution (fig. 5.7) one gets the corrected one (shown in fig. 5.11) using the procedure described in chapter 5.4.2. According to (2.23) the distribution of the rapidity difference is expected in the form $\propto e^{b_{\Delta Y}(\Delta Y)}$ and therefore the corrected spectrum is fitted by:

$$f_{data}^{corr}(\Delta Y) = A\, e^{\Delta Y\, b}\,, \tag{5.21}$$

which results in the parameter $b_{\Delta Y}$ to be:

$$b_{\Delta Y} = (-0.8 \pm 0.5)\,, \tag{5.22}$$

All fitted parameters with χ^2/ndf are summarized in table 5.6.

	$Y_{\rho^0} - Y_\eta$	
A	$8.5^{+13.7}_{-6.3} \cdot 10^2$	[-]
$b_{\Delta Y}$	-0.8 ± 0.5	[-]
χ^2/ndf	2.1/2	[-]

Table 5.6: *Parameters determined from the fit of the rapidity difference between ρ^0 and η mesons with their errors and respective χ^2 per degree of freedom are listed.*

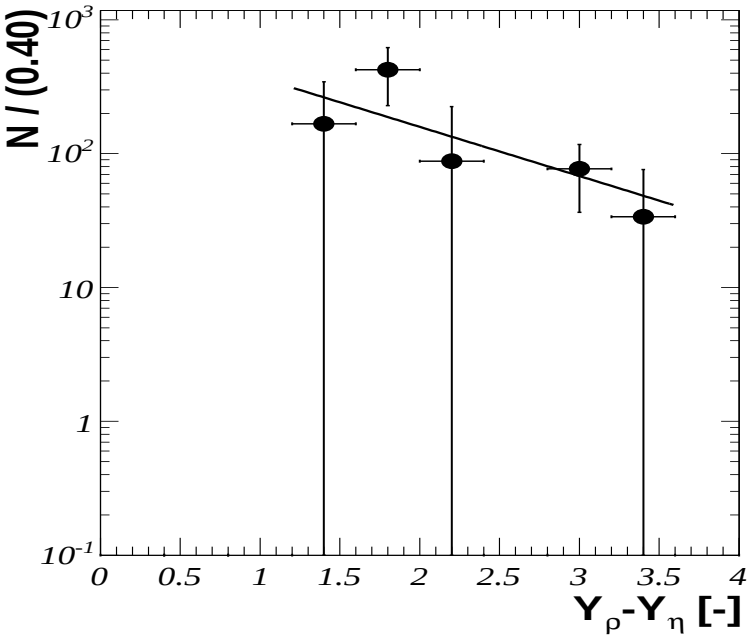

Figure 5.11: *Corrected distribution of the rapidity difference between ρ^0 and η mesons, ΔY.*

5.4.5 Measurement of the Center of Mass Energy of the $\gamma - p$ System $W_{\gamma p}$

The quantity characterizing the process in the photoproduction regime is the CMS energy of the $\gamma - proton$ system, $W_{\gamma p}$. The corrected $W_{\gamma p}$ distribution is shown in fig. 5.4.5. According to [104] the behavior of the $W_{\gamma p}$ distribution could be expected to be of the form $\propto W^{-2b_W}$, where b_W is the product of the intercepts of the Regge trajectories exchanged in the upper and lower vertex $b_W = \alpha(0)_1 \cdot \alpha(0)_2$. But the behavior of the corrected W distribution does not provide a meaningful result for the fit, and only the mean value for $W_{\gamma p}$ was extracted:

$$\langle W \rangle \approx 208 \text{ GeV} \tag{5.23}$$

5.5 Discussion of Systematic Errors

The main sources of the systematic errors for the cross section determination are discussed in the following:

- The systematic uncertainty related to the uncertainty of the energy scale and energy resolution of the electron tagger is estimated [95, 96] to be 4% when varying (increase/decrease) the energy deposited in the EM SpaCal by 2%.
- The relative uncertainty of the energy scale for the LAr and SpaCal calorimeters results in a systematic uncertainty of 10% [95]. The energy scale is varied by $\pm 4\%$ (see chapters 1.4.1 and 1.4.2).

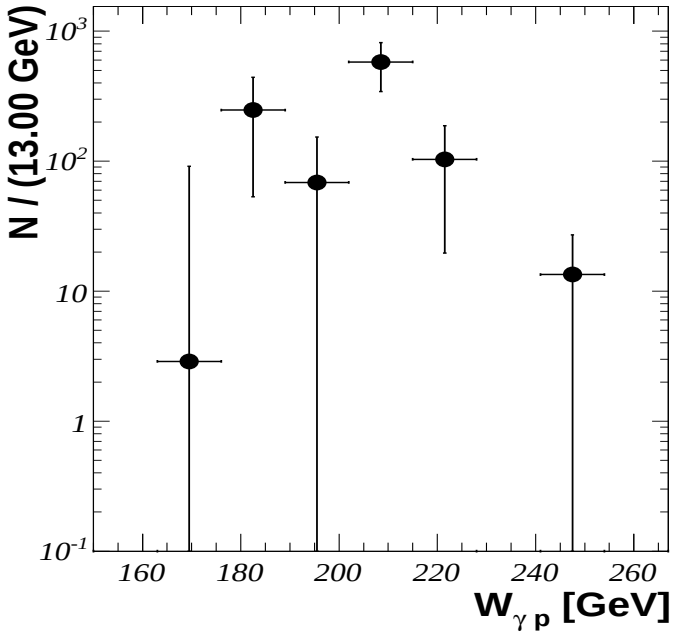

Figure 5.12: *Corrected differential distribution of the center of mass energy of the* $\gamma -$ `proton` *system,* $W_{\gamma p}$.

- The uncertainty of the track reconstruction efficiency is estimated to be 2 % [82] per track, resulting in an error of 4% for two reconstructed tracks ($(1 - 0.98^2) \cdot 100\% = 4\%$).
- The systematic uncertainty related to the contribution from beam-gas events could not be determined due to very low statistics and is taken to be $< 1\%$ from [95, 96].
- The systematic uncertainty on the $\eta - \rho^0$ reconstruction efficiency: The total efficiency was studied as a function of different variables which is shown in fig. 4.14. It exhibits the strongest dependence in t_1 distribution which also gives the largest uncertainty for the efficiency. The slope of the corrected t_1 distribution was measured to be $b_{t_1} = 2 \pm 0.5$. Therefore the reweighting of the slope t_1 of ToyGenMod was performed by $t^{\pm 0.5}$. The difference in the efficiency is taken as the systematic error and the uncertainty obtained is 20%.
- The comparison of the values obtained for the number of the signal events $\mathcal{N}^{signal}$ from four different method gives the uncertainty of 22%.
- The uncertainty on the Monte Carlo model is determined by calculating the cross section using the two different backgound Monte Carlo models RapGap and PythiaMod. The difference for the cross section is about 16%.
- The systematic errors on the luminosity are not uncorrelated and therefore the total error is determined as:

$$\frac{\Delta\mathcal{L}_{sys}}{\mathcal{L}_{tot}} = \frac{(\mathcal{L}_{96}\delta L_{96}) + (\mathcal{L}_{97}\delta L_{97}) + (\mathcal{L}_{99}\delta L_{99}) + (\mathcal{L}_{2000}\delta L_{2000})}{\mathcal{L}_{tot}} = 1.5\,\%.$$

The relative errors $\delta L_{96} = 1.77\,\%$, $\delta L_{97} = 1.5\,\%$, $\delta L_{99} = 1.5\,\%$, $\delta L_{2000} = 1.45\,\%$ include satellite corrections and are taken from [93].

- The systematic uncertainty on the efficiency of subtriggers s50 and s61: A variation of the fitted parameters according to their errors (see table A.1) leads to a change of the cross section by less than 1 %.

The total systematic uncertainty is determined by adding all systematic uncertainties in quadrature and amounts to 36%. The systematic errors are summarized in table 5.7.

	source	method	error [%]
1)	electron tagger energy scale	energy scale variation by 2%	4
2)	LAr and SpaCal energy scale	energy scale variation by 4%	10
3)	track reconstruction	2 traks	4
4)	beam-gas	pilot bunchies	< 1
5)	efficiency	reweighting by $t^{\pm 0.5}$	20
6)	$\mathcal{N}^{signal}$	different methods	22
7)	MC model	Pythia $\leftrightarrow$ RapGap	16
8)	Luminosity		1.5
9)	subtrigger s50 and s61	variation of fitted parameters	< 1
	all added in quadrature		**36**

Table 5.7: *Summary on the systematic errors*

5.6 Discussion of the Results

In this chapter a measurement of exclusive $\eta - \rho^0$ photoproduction at a mean photon-proton centre of mass energy (CMS) of 200 GeV is presented. The main quantity measured is the cross section $\sigma^*(\gamma p \to \eta\rho^0 X)$:

$$\sigma^*(\gamma p) \to \eta\rho^0 X = (3.5 \pm 1.4(stat) \pm 1.3(syst)) \text{ nb}, \tag{5.24}$$

The models which can explain exclusive $\eta - \rho^0$ photoproduction are discussed in chapter 3. One of them is the phenomenological model based on Regge theory which tries to explain the investigated process via exchange of a ρ trajectory at the photon vertex and the Pomeron trajectory at the proton vertex. The coupling $\gamma - \rho^0 - \eta$ is finite which is demonstrated i.e. by the existing ρ^0 meson decay into γ and η (with relatively very small branching ratio of $3 \cdot 10^{-4}$). The diffractive proton vertex with the ρ^0 meson production is very well known from many analyses on vector meson production. Finite values of all these couplings allow the process to proceed via ρ – Pomeron exchange.

One way to confirm/exclude that the process measured in this analysis is induced via the exchange of the ρ^0 and Pomeron trajectories is to look at the differential distributions like $|t_1|$, $|t_2|$, s_1, s_2 and ΔY. The Regge model was used as a hypothesis for the expectation of the behavior of these distributions. The measured spectra give the following dependences:

$$
\begin{array}{lcllcl}
b_{t_1} & = & (2.0 \pm 0.5(stat))\,\mathtt{GeV}^{-2} & \langle t_1 \rangle & \approx & -0.6\,\mathtt{GeV}^2\,, \\
b_{t_2} & = & (13^{-3}_{+6}(stat))\,\mathtt{GeV}^{-2} & \langle t_2 \rangle & \approx & -0.1\,\mathtt{GeV}^2\,, \\
b_{s_1} & = & (-2.9^{+0.8}_{-0.7}(stat))\,\mathtt{GeV}^{-2} & \langle \sqrt{s_1} \rangle & \approx & 3.5\,\mathtt{GeV}\,, \\
b_{s_2} & = & \text{not measured} & \langle \sqrt{s_2} \rangle & \approx & 80\,\mathtt{GeV}\,, \\
b_{\Delta Y} & = & (-0.8 \pm 0.5(stat)) & \langle \Delta Y \rangle & \approx & 2\,.
\end{array}
\tag{5.25}
$$

The measured value $b_{t_2} = 13^{-3}_{+6}\,\mathtt{GeV}^{-2}$ is consistent within errors with the expected value for the diffractive slope ($b \sim 11\,\mathtt{GeV}^{-2}$ at $\sqrt{s} \approx 80\,\mathtt{GeV}$) obtained from [96]. From the s_1 dependence $b_{s_1} \approx -2.9\,\mathtt{GeV}^{-2}$ one may estimate an intercept of the trajectory exchanged at the photon vertex: Using (2.46) one obtains $b_{s_1} = \alpha(0) - 1 \Rightarrow \alpha(0) = -1.9^{+0.8}_{-0.7}$. which within $1\,\sigma$ is not compatible with the expected value of 0.5 from (2.36). The reason might be related to the fitting procedure not suited for the fluctuating s_1 spectrum. On the other hand the intercept obtained from the rapidity difference distribution is within error compatible with the ρ trajectory hypothesis: $b_{\Delta Y} = \alpha(0) - 1 \Rightarrow \alpha(0) = 0.2 \pm 0.5$. The measured very low mean value of $\sqrt{s_1}$ is characteristic for non-diffractive processes as a consequence of (2.46), and the relatively high values of $\sqrt{s_2}$ for diffractive processes which is compatible with the hypothesis used.

The production of η and ρ^0 mesons from diffractively excited state V_{diff} is another possibility for the explanation. However the signal-to-background ratio of these processes determined from Pythia (1 : 5) is very low when comparing with the data (6 : 5). The contribution from RapGap via $\gamma p \to \eta \rho X$ is negligible with 1 : 50 signal-to-background ratio. With the present very low statistics and the resulting difficulties to obtain differential cross distributions and meaningful fit results (e.g. for the s_2 distribution) it is not possible, however, to draw any definitive conclusion on the production process.

Chapter 6

Search for Exclusive $\pi^0 - \rho$ Photoproduction at HERA

The analysis of exclusive $\pi^0 - \rho$ photoproduction proceeds in an analogous way as the analysis of exclusive $\eta - \rho$ photoproduction, described in the previous chapter 5. In particular the photon and track selection and the analysis cuts to be applied to ensure exclusivity, a rapidity gap and ρ meson definition are the same. The major difference is the selection of events containing a π^0 meson instead of an η meson.

The selection of events which contain neutral pions is performed by selection of a mass window in the photon-photon invariant mass spectra of the data and signal Monte Carlo model ToyGenMod distributions. The Monte Carlo models Pythia and RapGap are employed for background description. In this case no ToyGenModW is needed since the data are compared only with RapGap and Pythia.

Due to the fact, that no clear signal for $\pi^0 - \rho$ production is found, the cross section for $\pi^0 - 2track$ and an upper limit for $\pi^0 - \rho$ production is determined with the estimation of the systematic errors.

6.1 Preparation of the sample

In order to select events with neutral pions and ρ mesons, the π^0 and ρ invariant mass bands have to be defined. They are determined from the same 'inclusively preselected' data sample as used for the η and ρ selection. Therefore, the mass window defining the ρ meson is taken from the previous chapter:

$$0.6\,\mathtt{GeV} < m_{tt} < 1\,\mathtt{GeV}\,. \tag{6.1}$$

For more details of the ρ band selection see chapter 5.1.

To select a neutral pion decaying into two photons, the mass window for the π^0 band is obtained from the invariant mass of photon pairs. For the inclusively preselected data sample the photon-photon invariant mass spectrum, $m_{\gamma\gamma}$, is shown in fig. 6.1 a). The π^0 peak is fitted with a Gaussian $G(m_{\gamma\gamma})$. To fit the background a polynomial of third order, $\mathcal{P}_3(m_{\gamma\gamma})$, is employed. The mass spectrum simulated by ToyGenMod is shown in

the figure in b). The fit was carried out with a Gaussian only due to the absence of any background in the Monte Carlo model.

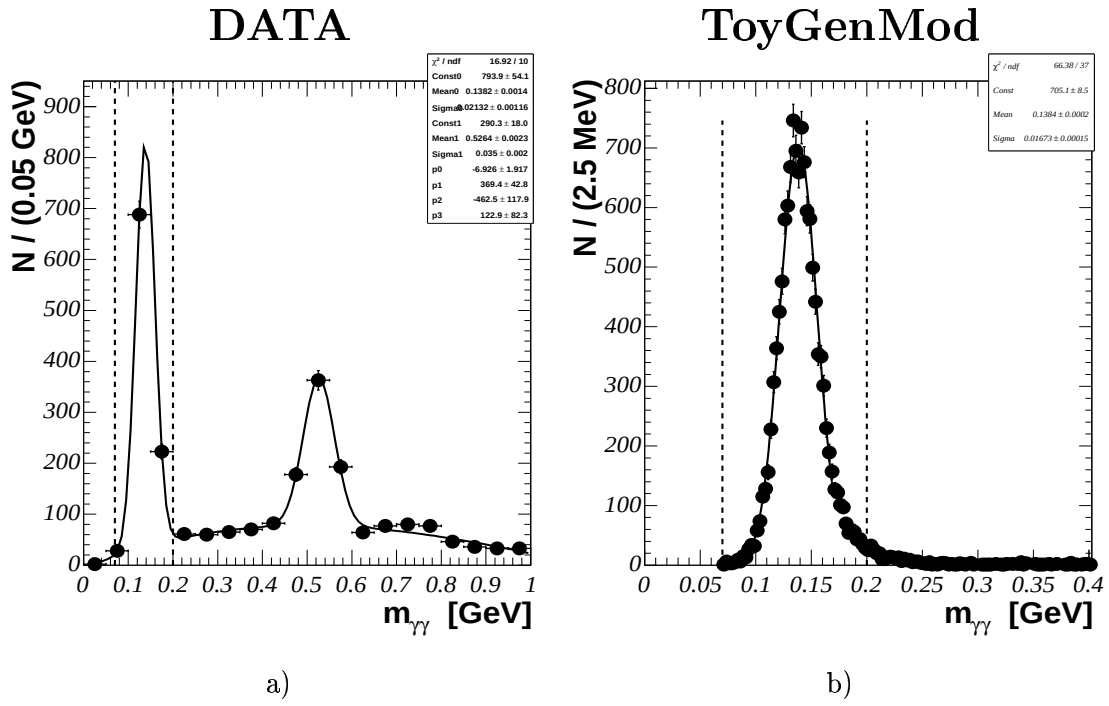

Figure 6.1: *π^0 candidates in data and Monte Carlo: a) photon-photon mass spectrum for data fitted by a Gaussian together with a polynomial of third order $\mathcal{P}_3(m_{\gamma\gamma})$. The $m_{\gamma\gamma}$ mass distribution simulated by ToyGenMod, shown in b), is fitted by a Gaussian only. The dashed lines illustrate the mass region for the selection of π^0 mesons.*

The values found in the fit are displayed in the figure, and the mean values, widths and χ^2/ndf are listed separately in table 6.1. A comparison of measured and simulated mass distributions exhibits compatibility for the mean value of the π^0 mass, μ ($\mu_{data} = \mu_{MC} =$ 138 MeV), and slightly larger width, σ, for the data than for the simulation ($\sigma_{data} = 21.3$ MeV versus $\sigma_{MC} = 16.7$ MeV). The masses in both cases are only slightly shifted toward higher values when compared with the nominal value of 134.98 MeV [37]. The widths are dominated by the SpaCal resolution since the natural width of the π^0 is negligible.

	Data	Monte Carlo
μ [MeV]	138.2±1.4	138.4±0.2
σ [MeV]	21.3±1.2	16.7±0.2
χ^2/ndf	16.9/10	66.4/37

Table 6.1: *Parameters fitted for π^0 candidates: The table shows the mean value, the width and the χ^2 per degree of freedom found by the fit for the data and Monte Carlo (ToyGenMod)*

Choosing the upper and lower bound of the π^0 mass window to be roughly 3σ (65 MeV)

w.r.t. the nominal value of 135 MeV, a pair of photon-candidates is considered as a π^0-candidate, if

$$70\,\mathtt{MeV} < m_{\gamma\gamma} < 200\,\mathtt{MeV}. \tag{6.2}$$

6.2 Signal Extraction and Background Treatment

Looking at the photon-photon and track-track mass spectra (shown in fig. 5.1 a) and 5.1 b)) for the inclusive data sample one observes π^0 and ρ signals in the corresponding distributions. The impact of the application of all analysis cuts and the correlation between both signals is studied in the following.

The respective mass spectra after applying the final analysis cuts on exclusivity and rapidity gap have been already shown in fig. 5.2 a) and b), respectively. In the $m_{\gamma\gamma}$ mass distribution a π^0 peak is apparent, and also an enhancement in the track pair spectrum in the ρ-band is observed. But from this distribution is it not clear whether the enhancement can be attributed to a ρ mass peak. Looking at the track-track versus photon-photon mass distributions, shown in fig. 6.2 a), a correlation is evident in the region crossed by the ρ and π^0 invariant mass bands. A good check whether the enhancement in m_{tt} corresponds to the invariant mass distribution of the ρ meson is to check the track-track mass spectrum after selecting the π^0 band in the $m_{\gamma\gamma}$ distribution according to eq. (6.2). The corresponding m_{tt} distribution is shown in fig. 6.2 b). In the data sample (dots) some 'space' for a ρ mass peak is possible but due to the poor statistics the signal can not be assigned to a mass peak of the ρ meson. The large errors in the data sample are caused by the L4 downscaling. These are also responsible for the correlation between ρ and π^0 bands shown in fig. 6.2 a). Also a comparison with the background Monte Carlo models Pythia and RapGap is shown. The agreement of the Monte Carlo description of the data is quite satisfactory, although a possible contribution of the ρ appears to be rather small.

Since RapGap describes the mass distribution better than Pythia, RapGap will be used to describe the data/background in the following. RapGap shows that the main processes which produce the spectrum take place via boson gluon fusion where the gluon originates from the Pomeron: $\gamma p \to \gamma I\!P X \to q\bar{q}ggX$. Quark-antiquark and gluon pairs produced in the interaction fragments into the following states:

- The main contribution comes from $q\bar{q}gg \to \pi^0\pi^+\pi^-$.
- Processes like: $q\bar{q}gg \to \pi^0\rho^\pm\pi^\mp(\pi^0K^+K^-, \pi^0\pi^0\pi^+\pi^-, ...)$ in which some particles are misidentified as pions, or neutral daughter particles are not seen in the Liquid Argon calorimeter due to their low energy.
- The contribution to the signal process $\pi^0\rho$ via $\gamma I\!P \to q\bar{q}gg \to \rho^0\,\pi^0$ is negligible.

The distribution of the variable $E - p_z$ characterizing the exclusivity is shown in figure 6.3 a). The peak of the variable $E - p_z$ is expected to be about 55 GeV. Also in this distribution the main part of the data is reasonably described by the background MC RapGap. Most of the events in this distribution are shifted to the lower limit of 50 GeV applied in the analysis. That means that most of the events are not exclusive and can be considered as background. However there is a small discrepancy between data and simulation at around

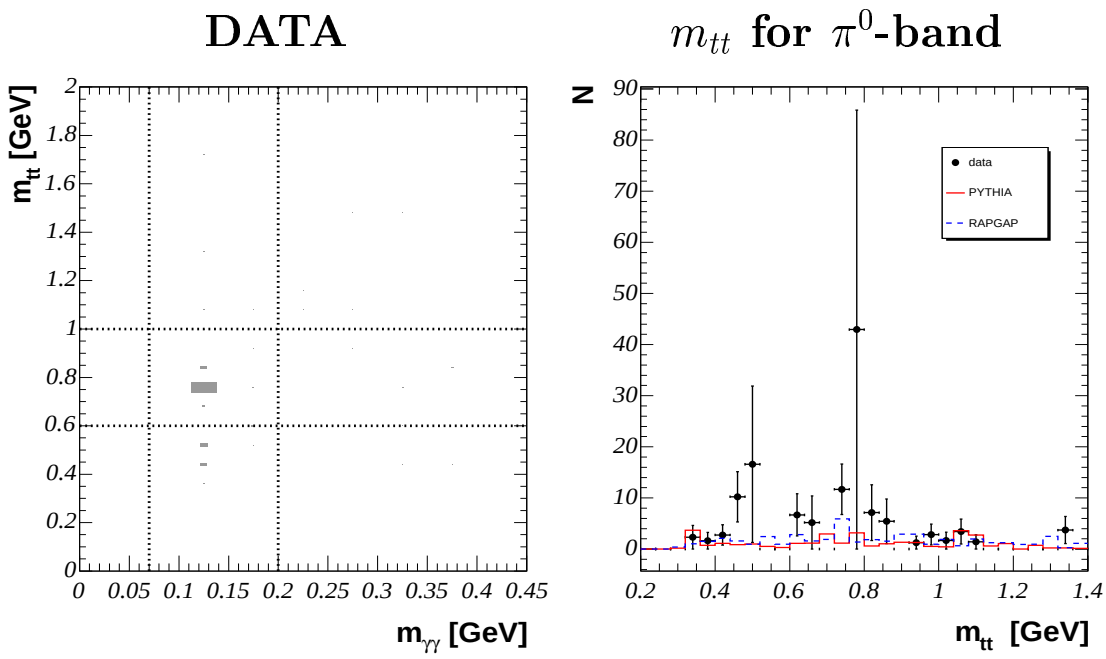

Figure 6.2: *Extraction of the $\pi^0 - \rho$ signal: a) photon-photon versus track-track mass distribution. The dashed lines indicate the π^0 and ρ invariant mass bands. In b) the track-track mass distribution is shown requiring $m_{\gamma\gamma}$ to be within the π^0 mass band. Here also the Pythia and RapGap contributions are shown.*

55 GeV where the exclusive signal is expected.

From the discussion above one may conclude that while the π^0 signal is evident (see also fig. 5.2) the ρ signal can not be confirmed. Therefore the cross section for exclusive $\pi^0 - \rho$ photoproduction can not be determined. However due to an enhancement in the ρ band in the track pair mass spectrum the signal may exist. To estimate an upper limit for the expectation of the process, the cross section of the process $\gamma p \to \pi^0\, 2\, track\, X$ will be determined.

6.3 Comparison of Monte Carlo and Data

In this section a comparison between the data and the background Monte Carlo model RapGap is shown. All simulated and measured distributions shown in the following are obtained after application of all analysis cuts summarized in table 4.13, and only those events are considered which contain neutral pions and where the track-track invariant mass lies in the mass window defined by the ρ band in (6.1). Since it is not possible to extract the signal from the difference between the data and background MC, no comparison with the distributions simulated by ToyGen will be performed but the data will be compared with the distributions simulated by the RapGap MC model.

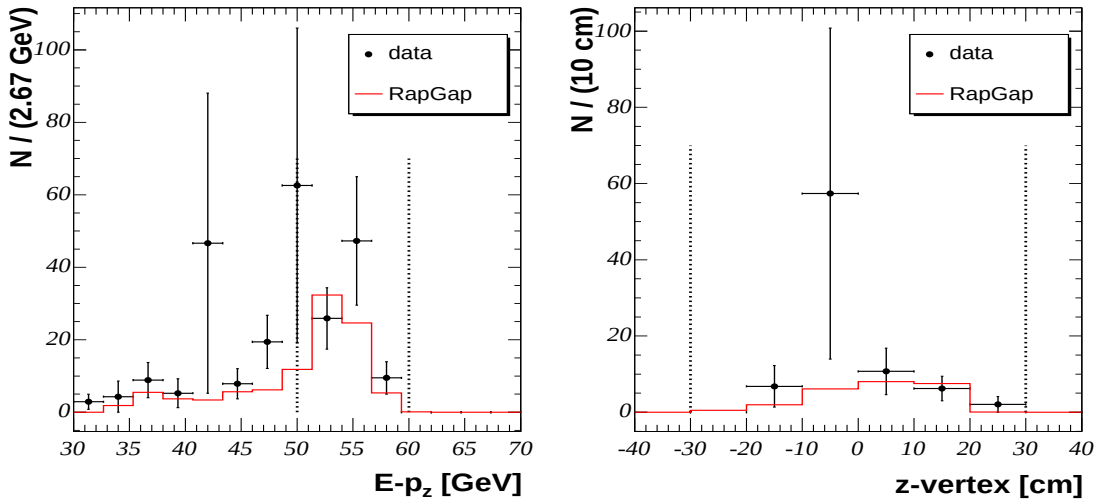

a) b)

Figure 6.3: *Control plots for the ($\pi^0 - 2\,tracks$) sample are shown: a) The variable $E - pz$ and b) z-coordinate of the vertex. The dots represent the data and the histogram Monte Carlo RapGap model. The dotted lines indicate the cuts applied.*

The properties of the π^0 candidates and photon-candidates originating from the π^0 decay are shown in figure 6.4 in a) - d) for data (dots) and RapGap (histogram). The following distributions are shown: a) energy of all clusters, b) energy of the hottest cluster, c) energy of the π^0 meson and d) distance between both clusters. From a) and b) one may conclude that the energy is distributed asymmetrically between the clusters stemming from a π^0 which is necessary for the separation of the clusters in the SpaCal as a consequence of eq. (4.20) and the energy of the π^0 above 4 `GeV`, shown in c). Also the distance between the clusters is peaked at the minimum value of 4 `cm` determined by the SpaCal granularity. The RapGap distributions marginally agree with the data distributions and also the shape of the spectra is in agreement.

Figure 6.4 e) - g) show the properties of the tracks and track-track system. The transverse momentum of all tracks is shown in e), the polar angle of all tracks is depicted in f) and the polar angle of the track-track system in g). From the polar angle distributions one observes that the tracks and the track-track system are predominantly produced in the backward region. Most tracks have a transverse momentum below one `GeV` which is the region where the properties of the track are measured with very good precision. Also from these distributions one may conclude that RapGap describes the data distributions marginally. In the last plot of this figure h) the π^0 rapidity versus rapidity of the two track system for the data sample is shown; The dashed lines show the region in which the cross section will be determined. The neutral pion is mainly produced in the central region of the SpaCal acceptance. The enhancement at $Y_{\pi^0} \approx -2.2$ and $Y_{tt} \approx 0.4$ is not relevant since it corresponds to one event only with a very high weight and a 100% error.

Figure 6.5 shows a collection of distributions for the $\pi^0 - 2\,track$ system together with

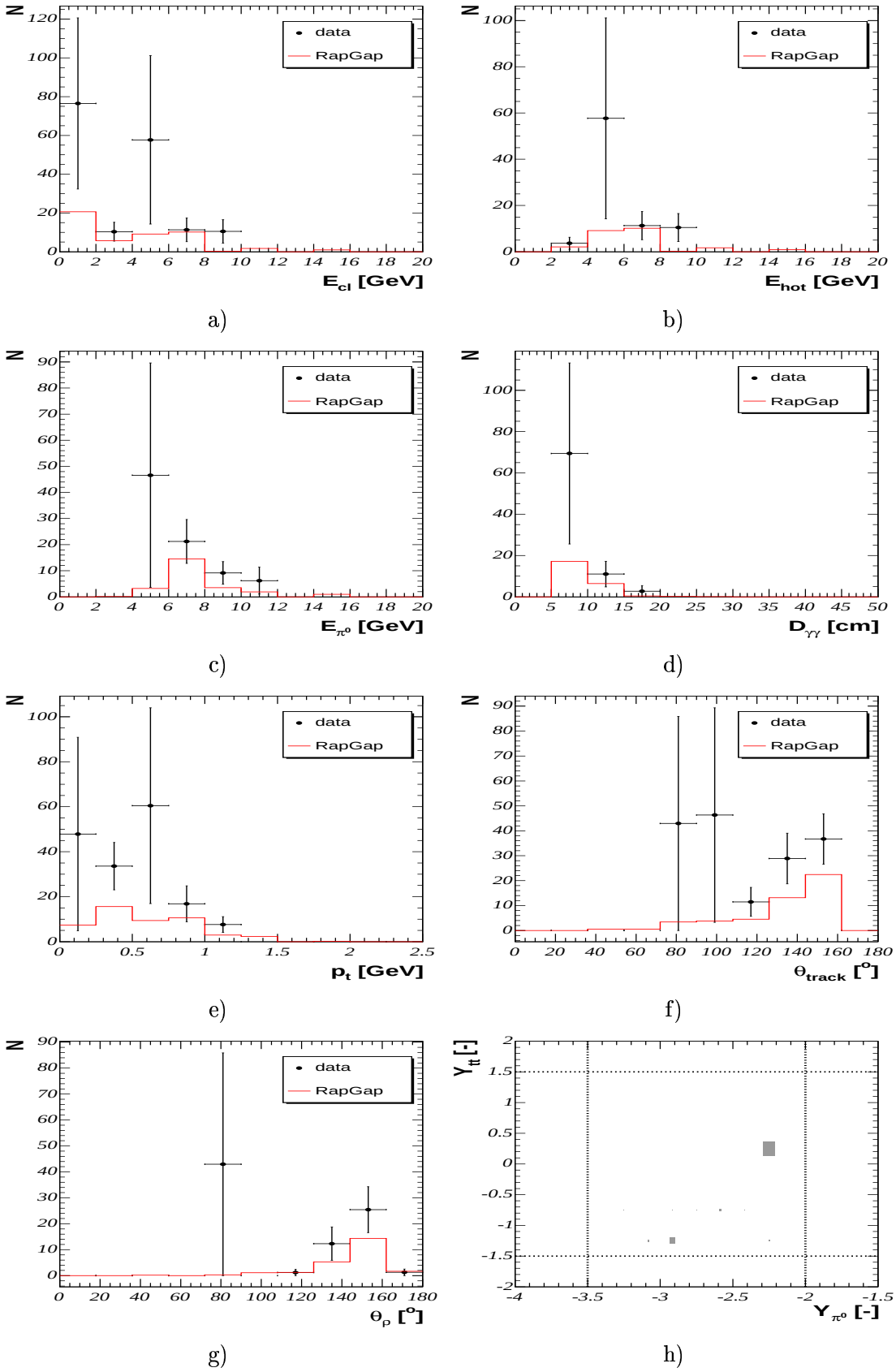

Figure 6.4: *Properties of the $\pi^0 - 2$ track system: a) the energy of all clusters, b) energy of the hottest cluster, c) π^0 energy, d) distance between two photons originating from the π^0, e) transverse momentum of all tracks, f) polar angle of all tracks, g) polar angle of the 2 track system, h) rapidity of the π^0 meson versus rapidity of the 2 track system. The dashed lines illustrate the region in which the cross section will be determined.*

the comparison from RapGap. The distributions shown are: a) The rapidity difference between the $track-track$ system and the π^0 meson, $Y_{tt}-Y_{\pi^0}$, b) the center of mass energy of the $\gamma - proton$ system, c) the squared four-momentum transfer at the photon vertex, $|t_1|$, d) the squared four-momentum transfer at the proton vertex, $|t_2|$, e) the squared center of mass energy of the $\pi^0 - 2\,track$ subsystem, s_1, f) the squared center of mass energy of the $2\,track - proton$ subsystem, s_2.

The rapidity difference distribution exhibits a maximum around 1.5 similarly to the $\eta - \rho$ sample. The $W_{\gamma p}$ spectrum has a mean value of 183 GeV. Comparing the $|t_1|$ and $|t_2|$ spectra one observes higher values for the squared four-momentum transfer at the photon vertex as at the proton vertex. Comparing the s_1 and s_2 distributions one observes that s_1 is peaked at low values while the s_2 distribution acquires much higher values, as also seen in $\eta - \rho$ sample. Also here, generally good agreement between the data and RapGap is seen. Comparing with the distributions from $\eta - \rho$ sample one observes similar behavior of all distributions.

6.4 Results

6.4.1 Cross Section

The cross section $\sigma(\gamma p \to \pi^0\, 2track\, X)$ is determined in the kinematical region defined by the scattered electron detected in the electron tagger and by restrictions on the rapidities of the π^0 meson and $track - track$ system:

$$\begin{array}{rcccl} 0.3 & < & y & < & 0.65 \\ Q^2 & < & 0.01\,\mathrm{GeV} & & \\ -3.5 & < & Y_{\pi^0} & < & -2 \\ -1.5 & < & Y_{tt} & < & 1.5 \end{array} \tag{6.3}$$

The cross section is obtained via the expression:

$$\sigma^*(\gamma p \to \pi^0\, 2track\, X) = \frac{\mathcal{N}}{\epsilon_{tot}\epsilon_{eTag33}\, BR_{\pi^0\to\gamma\gamma}\, \mathcal{L}\, \mathcal{F}_{\gamma/e}}\,, \tag{6.4}$$

where the σ^* denotes the total cross section calculated in the kinematical region defined in (6.3), $\mathcal{N}^{signal}$ is the number of events corrected for trigger efficiencies, L1 and L4 prescale factors and downscaling, respectively, $\epsilon_{tot}((0.6 < m_{tt} < 1)\,\mathrm{GeV}) = \epsilon_{geom}\epsilon_{det} = (3.95 \pm 0.43)\,\%$ is the total efficiency determined in section 4.9, $\langle\epsilon_{eTag33}\rangle = 0.5$ is the average of the electron tagger acceptance, $BR_{\pi^0\to\gamma\gamma} = 99\,\%$ is the branching ratio for the decay $\pi^0 \to \gamma\gamma$, $\mathcal{L} = 76$ pb^{-1} (table 4.7) is the integrated luminosity collected over all run periods: 1996, 1997, 1999 and 2000, and $\mathcal{F}_{\gamma/e} = 1.32\cdot 10^{-2}$ is the flux of photons stemming from the electron as given by the integral over y and Q^2 defined by the electron tagger (eq. (2.16)).

$\mathcal{N}$ is the number of events observed in the data in the rapidity region shown in fig. 6.4 h) which is found to be 83.2 ± 44.3. Then for the cross section one obtains:

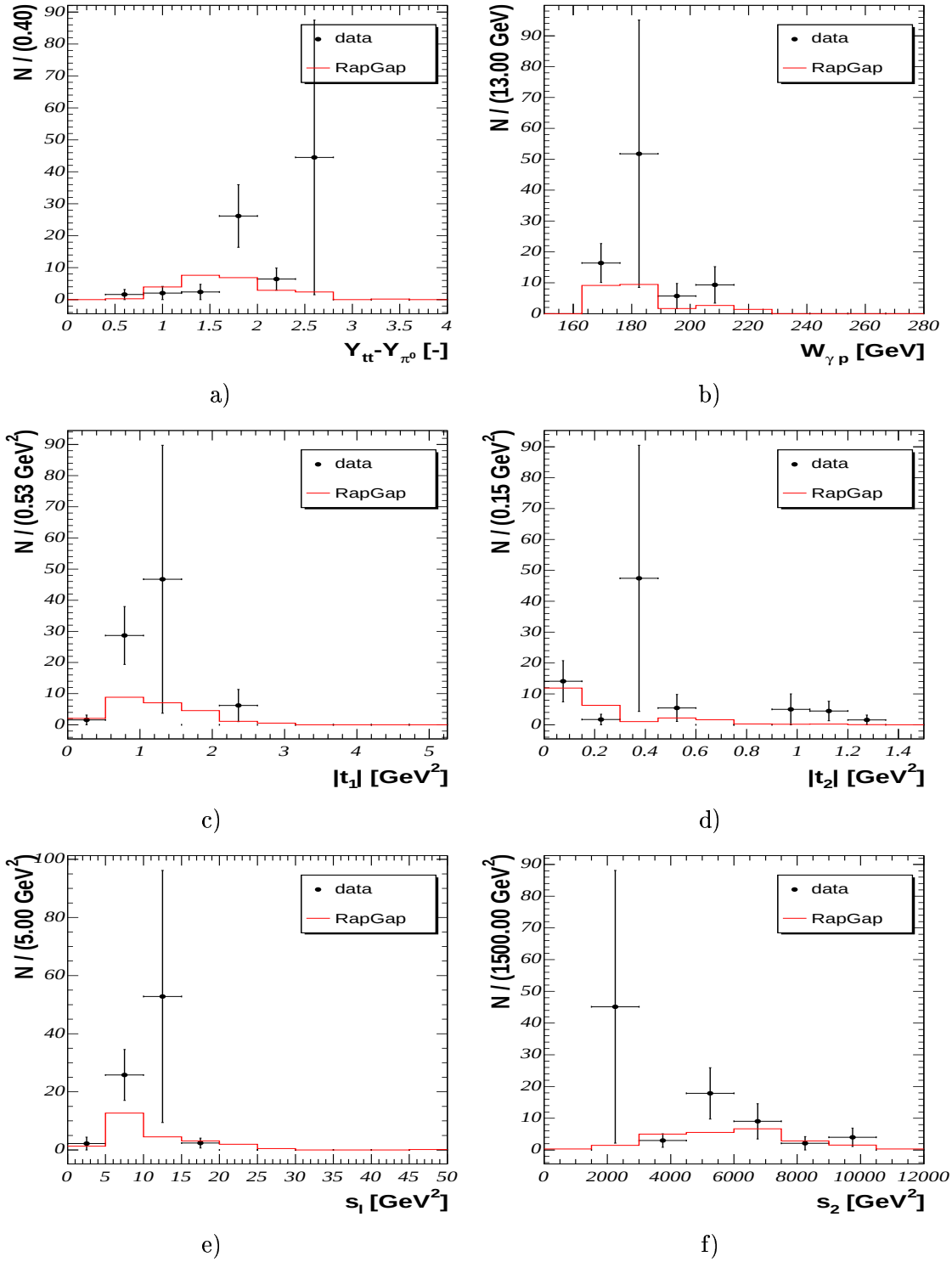

Figure 6.5: *Kinematical distributions of the $\pi^0 - 2$ track system: a) Rapidity difference between the track − track system and π^0, $Y_{tt} - Y_{\pi^0}$, b) center of mass energy of the γ-proton system, $W_{\gamma p}$, c) the squared four-momentum transfer at the photon vertex, t_1, d) the squared four-momentum transfer at the proton vertex, t_2, e) the squared center of mass energy of the $\pi^0 - 2$ track system, f) the squared center of mass energy of the 2 track − proton system. The dots illustrate the data, the histogram the Monte Carlo RapGap model.*

$$\sigma^*(\gamma p \to \pi^0\, 2track\, X) \;=\; (4.2 \pm 2.3\,(stat))\;\; \texttt{nb}. \tag{6.5}$$

The statistical error for the cross section determination was calculated adding the relative errors of the total efficiency ($\Delta\epsilon/\epsilon = 11\%$) and the events $\Delta\mathcal{N}/\mathcal{N} = 53.2\%$ in quadrature.

The background contribution determined from RapGap is $\mathcal{N}^{rap} = 24.2 \pm 5.9$ including roughly 0.3 events contributing to the signal via $\gamma p \to \pi^0 \rho X$ with 1 : 50 for the signal-background ratio. The Pythia event generator gives for the background $\mathcal{N}^{pyt} = 14.3 \pm 3.2$ events including 2.3 events contributing to the signal via $\gamma p \to \pi^0 \rho X$ which provides the signal-to-background ratio of 1 : 5. For the comparison of the inclusive data sample the RapGap has been chosen to estimate background since it better describes the data and therefore also for the determination of the upper limit will be used for background estimation. Conservatively, it is assumed that all events after the background subtraction is signal which yields the cross section:

$$\sigma^*(\gamma p \to \pi^0\, \rho\, X) = \frac{RBW_{corr}\left(\mathcal{N}^{data} - \mathcal{N}^{rap}\right)}{\epsilon_{tot}\epsilon_{eTag33}\, BR_{\pi^0\to\gamma\gamma}\, \mathcal{L}\, \mathcal{F}_{\gamma/e}} \;=\; (3.7 \pm 2.8\,(stat))\;\; \texttt{nb}. \tag{6.6}$$

where $\mathcal{N}^{data} - \mathcal{N}^{rap} = 59 \pm 44$, $\Delta\sigma^* = \sqrt{(44/59)^2 + (0.11)^2}$ and $RBW_{corr} = 1.25$ is the correction on the integral of the relativistic Breit-Wigner function taken from chapter 6.4.1.

6.5 Discussion of Systematic Errors

In the following the main sources of systematic errors are discussed:

- Due to the similarity of the investigated process with the $\eta - \rho$ sample, most of the sources caused systematic errors are taken over from table 5.7. Namely the uncertainties related to the energy scale and resolution of the electron tagger, LAr and SpaCal, labeled by 1)-2) in the table, uncertainty on the track reconstruction and contribution from beam-gas events labeled by 3)-4) and uncertainty on the luminosity measurement and the efficiency of the subtriggers s50 and s61 mentioned as point 8)-9) in the table.

- The systematic uncertainty on the $\pi^0 - 2track$ reconstruction efficiency: ToyGenMod has been weighted according to RapGap and Pythia distributions by the same way as according to the data described in appendix C.0.2. The difference in the efficiencies yields 25% which is taken as a systematic error.

- For the upper limit the uncertainty on the Monte Carlo model has to be taken into account. It is determined by calculating the cross section using two different background Monte Carlo models RapGap and PythiaMod which results in the difference of 20%.

The total systematic uncertainty is determined by adding all systematic uncertainties in quadrature and amounts to 28% for the $\sigma^*(\gamma p \to \pi^0 2\, trackX)$ cross section determination and 34% for the upper limit of $\pi^0 - \rho^0$ photoproduction. They are summarized in table 6.2.

	source	method	error [%]
1)	electron tagger energy scale	energy scale variation by 2%	4
2)	LAr and SpaCal energy scale	energy scale variation by 4%	10
3)	track reconstruction	2 tracks	4
4)	beam-gas	pilot bunches	< 1
5)	efficiency	using Pythia and RapGap	25
6)	Luminosity	–	1.5
7)	subtrigger s50 and s61	from fits	< 1
8)	MC model	Pythia $\leftrightarrow$ RapGap	20*
	all added in quadrature		**28/34***

Table 6.2: *Summary on the systematic errors. Two values are given. The value with * includes also the uncertainty on the Monte Carlo model.*

6.6 Discussion of the Results

In this chapter measurements of the exclusive $\pi^0 - 2\,track$ photoproduction at a mean photon-proton center of mass energy (CMS) of 180 GeV is presented. The quantity measured is the cross section $\sigma^*(\gamma p \to \pi^0 2\,track X)$. Taking into account the systematic error of 28% the value obtained is:

$$\sigma^*(\gamma p \to \pi^0\, 2track\, X) \;=\; (4.2 \pm 2.3\,(stat) \pm 1.2\,(sys))\ \texttt{nb} \tag{6.7}$$

which can be converted onto an upper limit using (6.6) and taken into account systematical uncertainty of 34%:

$$\sigma^*_{upper\,limit}(\gamma p \to \pi^0\,\rho\, X) \;<\; 8.6\ \texttt{nb} \quad (95\%\ \mathrm{CL}). \tag{6.8}$$

on the $\pi^0 - \rho$ photoproduction.

Also exclusive $\pi^0 - \rho$ photoproduction can be interpreted in the terms of Regge theory via exchange of a ρ trajectory at the photon vertex and Pomeron trajectory at the proton vertex. The only difference from the $\eta - \rho$ sample is the different coupling at the photon vertex. One of the possible reasons why the process is not seen in contrast to $\eta - \rho$ production is a smaller efficiency for π^0 reconstruction than for η, (compare plots in fig. 4.13 a) and c)) or a smaller detector acceptance for the $\pi^0 - \rho^0$ production.

Chapter 7

Summary and Conclusion

This analysis of double meson photoproduction was performed using the H1 detector at HERA on the data sample corresponding to an integrated luminosity of $\mathcal{L} = 76.21$ pb^{-1}. The processes under investigation were exclusive photoproduction of $\eta - \rho^0$ and $\pi^0 - \rho^0$ meson pairs. The kinematical range of the measurements are limited by the kinematics of tagged photoproduction and by the limits on the rapidity ranges (defined in the laboratory system) of the ρ^0 and $\eta(\pi^0)$ mesons:

$$\begin{array}{rcccl} Q^2 & < & 0.01 \text{ GeV}^2 & & \\ 0.3 & < & y & < & 0.65 \\ -3.5 & < & Y^{lab}_{\eta(\pi^0)} & < & -2 \\ -1.5 & < & Y^{lab}_{\rho^0} & < & 1.5 \end{array} \tag{7.1}$$

The measurement of the cross section for exclusive $\eta - \rho^0$ photoproduction has been performed at an average γp centre of mass energy of $\langle W_{\gamma p} \rangle \approx 208$ GeV. The background expectation from the event generators Pythia and RapGap are consistent to each other and capable to describe the background but not the signal. From the difference between the data and the background the cross section for $\eta - \rho^0$ photoproduction in the kinematical region defined in (7.1) was obtained:

$$\sigma^*(\gamma p \to \eta \rho^0 X) = (3.5 \pm 1.4(stat) \pm 1.3(syst)) \text{ nb}. \tag{7.2}$$

In the measurement of exclusive $\pi^0 - \rho^0$ photoproduction, performed at an average γp centre of mass energy of $\langle W_{\gamma p} \rangle \approx 180$ GeV, no significant signal of the ρ^0 meson could be extracted. The generator models RapGap and Pythia were used to estimate the background. Both models marginally describes the data. Due to the absence of a ρ signal, the cross section for $\pi^0 - 2track$ was determined to be:

$$\sigma^*(\gamma p \to \pi^0\, 2track\, X) \;=\; (4.2 \pm 2.3\,(stat) \pm 1.2\,(sys)) \text{ nb}\,. \tag{7.3}$$

After background subtraction, an upper limit for $\pi^0 - \rho^0$ production was derived:

$$\sigma^*_{upper\,limit}(\gamma p \to \pi^0\, \rho^0\, X) \;<\; 8.6 \text{ nb} \quad (95\%\text{ CL})\,, \tag{7.4}$$

both determined in the kinematical region given in (7.1).

In the term of Regge theory the measured processes can be interpreted as: 1) a diffractively produced high mass mesonic state decaying into two mesons, or 2) the meson measured in the central region is generated in a fusion process of the ρ^0 trajectory originating at the photonic vertex, and the Pomeron originating at the proton. It was shown that the available data do not allow a definite distinction between these mechanisms. The analysis of the accessible differential distributions shows, however, that the processes observed are consistent with a sizeable contribution from Pomeron exchange, and the mere existence of e.g. $\eta - \rho^0$ meson pair production at energies as high as HERA energies suggest a contribution from Pomeron exchange.

Appendix A

Summary on the Trigger Element Efficiencies

For the data sample the efficiencies of the subtriggers s50 and s61 are determined via their trigger elements (TE) by the procedure described in chapter 4.4.1.

The efficiencies of the L1 and L2TT SpaCal trigger elements for the given data taking periods are shown in fig. A.1, namely for $IET > 1 \,\|\, IET\_cen\_2$ in the first row, $IET > 2 \,\|\, IET\_cen\_3$ in the second row, $R20$ in the third row and $R30$ in the fourth row. The efficiencies for both IET trigger elements are determined as functions of the energy of the hottest cluster, $\epsilon_{IET}(E_{hot})$. The efficiencies of the radius trigger elements are determined as functions of the radial distance of the farthest cluster from the beam-line, $\epsilon_R(RD_{cl})$. The energy of this cluster has been required to be above 2.5 `GeV` in order to be independent of the IET trigger element. The dots demonstrate the calculated efficiency which are fitted by the Fermi function of eq. (4.6). The fitted parameters with χ^2 per degree of freedom are listed in table A.1. From the parameters obtained one observes that the maximum efficiency for all SpaCal trigger elements is very close to 100%. Only the trigger element $IET > 1 \,\|\, IET\_cen\_2$ for 1996 has a maximum efficiency of about 98%. The vertical lines illustrate the cuts applied to the energy and radial distance of the cluster. The large χ^2/ndf for the fit of the trigger element $IET > 2 \,\|\, IET\_cen\_3$ is caused by discrepancies between the fit and the calculated efficiency at low energies E_{hot} which are safely below the cuts to be applied. Therefore these discrepancies have no influence on the data correction.

The efficiency for the DCRϕ trigger element is determined as a function of the transverse momentum of the highest p_t track (fig. A.2 first row), $\epsilon_{DCR\phi}(p_{t,high})$, and the polar angle θ_{high} of this track (fig. A.2 second row), $\epsilon_{DCR\phi}(\theta_{high})$. For the $\epsilon_{DCR\phi}(p_{t,high})$ distribution it is demanded that the polar angle of the track has to be between 40 and 140 degrees in order to be independent of $\epsilon_{DCR\phi}(\theta_{high})$. For $\epsilon_{DCR\phi}(\theta_{high})$ the p_t of the track has to be above one `GeV` to be independent of $\epsilon_{DCR\phi}(p_{t,high})$. The dots representing the calculated efficiency are fitted by a 'double Fermi' function, defined in eq. (4.11) for the θ_{high} dependence and a Fermi function for the $p_{t,high}$ dependence. The efficiency for the `zVtx` trigger element is obtained as a function of the momentum of the highest p_t track (fig. A.2 third row), $\epsilon_{zVtx}(p_{t,high})$. The fitted parameters with χ^2 per degree of freedom are listed in table A.1. The maximum of the $\epsilon_{DCR\phi}(p_{t,high})$ and $\epsilon_{DCR\phi}(\theta_{high})$ reaches $(85-90)\%$ and in any given data taking period they are compatible within one percent. The $\epsilon_{zVtx}(p_{t,high})$ reaches a maximum of $(72-75)\%$. This rather low efficiency is caused by the zVtx de-

TE			1996	1997	1999	2000
$IET > 1$	Eff	[%]	98.64 ± 0.30	99.59 ± 0.11	99.99 ± 0.11	99.89 ± 0.14
	Thr	[GeV]	1.91 ± 0.01	1.79 ± 0.01	1.90 ± 0.01	1.95 ± 0.01
	Width	[GeV]	0.18 ± 0.01	0.13 ± (< 0.01)	0.15 ± 0.01	0.18 ± (< 0.01)
	χ^2/ndf		43.53/127	127.45/152	39.85/151	28.68/165
$IET > 2$	Eff	[%]	–	100.0 ± 0.06	100.0 ± (< 0.01)	99.68 ± 0.10
	Thr	[GeV]	–	5.07 ± (< 0.01)	5.48 ± 0.01	5.67 ± 0.01
	Width	[GeV]	–	0.41 ± (< 0.01)	0.47 ± < 0.01	0.54 ± (< 0.01)
	χ^2/ndf		–	1755.70/93	574.16/87	766.90/88
R20	Eff	[%]	98.92 ± 0.25	97.93 ± 0.31	–	–
	Thr	[cm]	15.59 ± 0.09	15.27 ± 0.10	–	–
	Width	[cm]	1.13 ± 0.05	1.17 ± 0.06	–	–
	χ^2/ndf		31.36/12	24.68/12	–	–
R30	Eff	[%]	–	100.0 ± 0.45	99.65 ± 0.09	99.85 ± 0.06
	Thr	[cm]	–	25.59 ± 0.27	25.49 ± 0.09	25.66 ± 0.09
	Width	[cm]	–	1.10 ± 0.20	0.90 ± 0.04	0.93 ± 0.05
	χ^2/ndf		–	0.18/23	17.95/25	22.18/27
DCR$\phi(p_{t,high})$	Eff	[%]	–	89.52 ± 0.43	84.85 ± 0.53	88.10 ± 0.48
	Thr	[GeV]	–	0.60 ± (< 0.01)	0.65 ± (< 0.01)	0.65 ± (< 0.01)
	Width	[GeV]	–	0.11 ± (< 0.01)	0.09 ± (< 0.01)	0.09 ± (< 0.01)
	χ^2/ndf		–	153.12/17	165.47/17	179.19/17
DCR$\phi(\theta_{high})$	Eff	[%]	–	89.60 ± 0.51	85.10 ± 0.64	88.41 ± 0.57
	Thr1	[°]	–	22.48 ± 0.54	25.24 ± 0.54	25.59 ± 0.59
	Width1	[°]	–	4.66 ± 0.45	4.43 ± 0.50	4.44 ± 0.50
	Thr2	[°]	–	156.32 ± 0.32	154.24 ± 0.28	155.79 ± 0.29
	Width2	[°]	–	4.87 ± 0.30	3.62 ± 0.22	4.15 ± 0.25
	χ^2/ndf		–	90.8/21	88.37/21	84.57/21
$zVtx(p_{t,high})$	Eff	[%]	–	71.17 ± 0.48	71.35 ± 0.54	72.89 ± 0.55
	Thr	[GeV]	–	0.07 ± 0.02	0.04 ± 0.04	0.0 ± (< 0.01)
	Width	[GeV]	–	0.18 ± 0.02	0.18 ± 0.02	0.22 ± 0.01
	χ^2/ndf		–	16.80/17	22.87/17	22.59/17

Table A.1: *Fitted parameters of the trigger element efficiencies with χ^2/ndf per a year are listed.*

pendence on the number of reconstructed tracks fitted to the vertex. In [82] it is shown that the ϵ_{zVtx} increases with the number of assigned tracks.

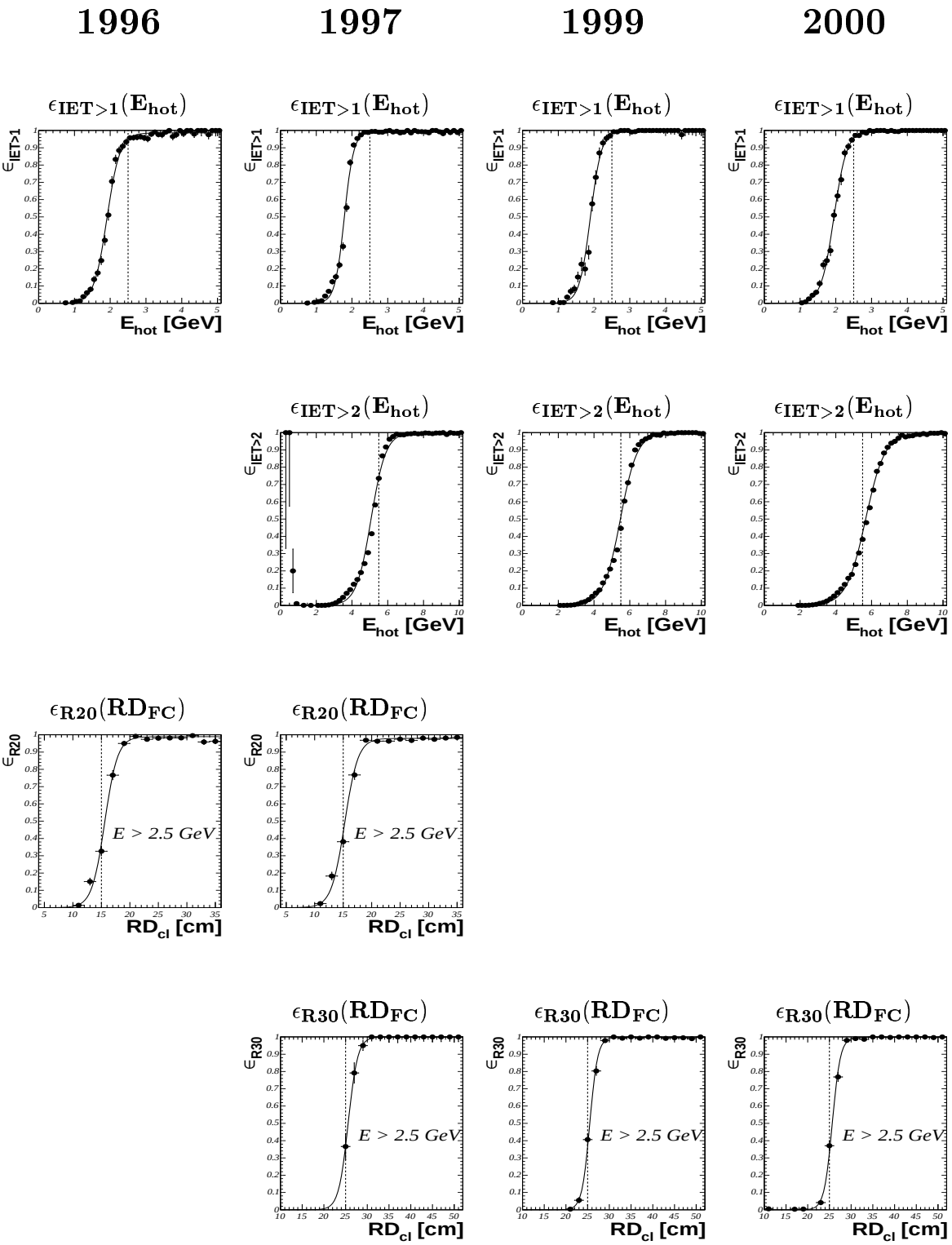

Figure A.1: *Distributions of the SpaCal trigger element efficiencies for data taking periods* 1996 − 2000*: The first (second) row shows the efficiency of the IET*> 1 *(IET*> 2*) trigger element as a function of the energy of the hottest cluster. The third (fourth) row shows the efficiency of the R*20 *(R*30*) trigger element as a function of the radial distance of the farthest cluster w.r.t. the beam line. The dots representing the obtained efficiencies are fitted by Fermi functions. The vertical dashed lines indicate the cuts applied to the energy and distance of the cluster.*

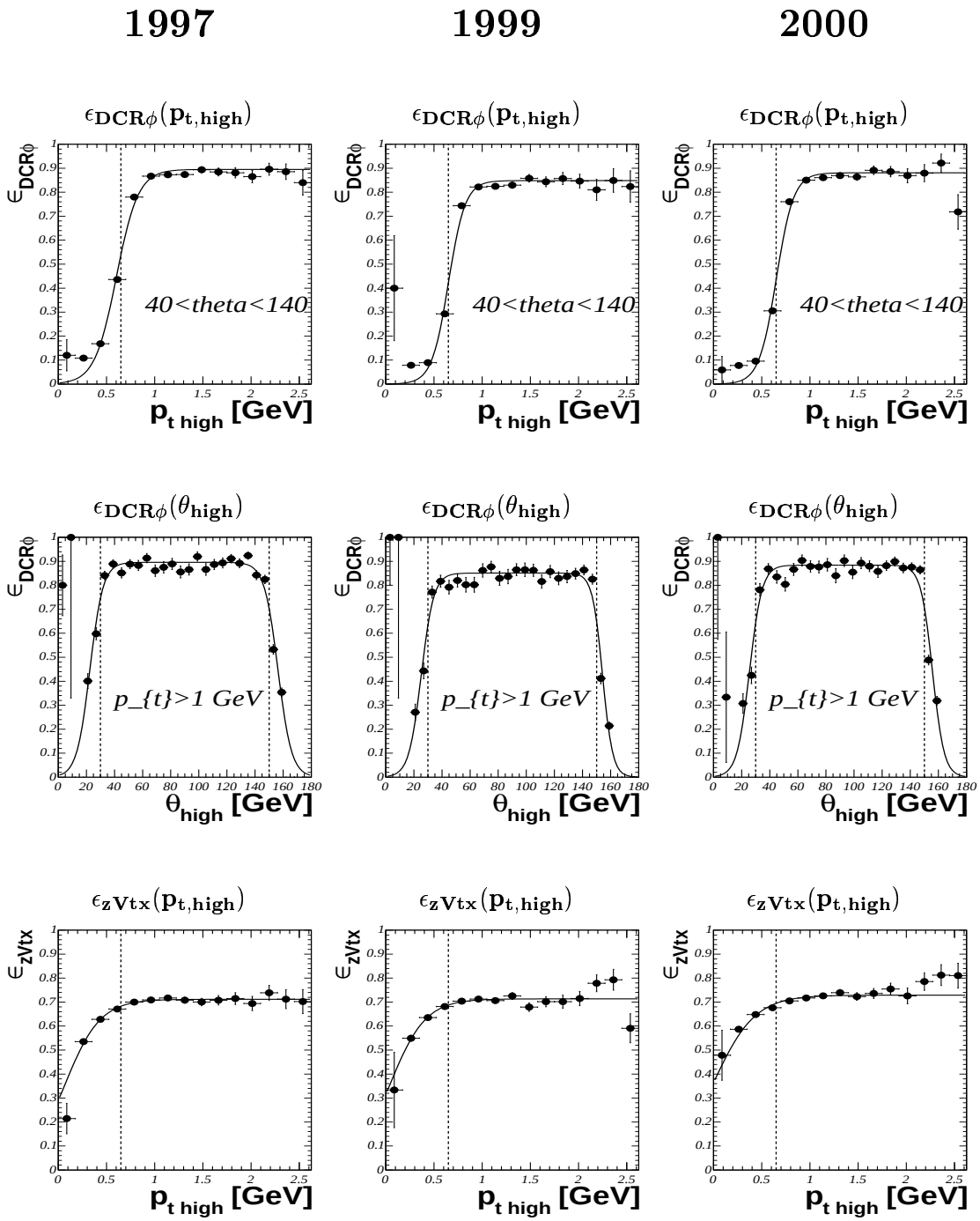

Figure A.2: *Distributions of the DCRϕ and* `zVtx` *trigger element efficiencies for the* 1997, 1999 *and* 2000 *data taking periods: The first (second) row shows the efficiency of the DCRϕ trigger element as a function of the transverse momentum (polar angle) of the highest p_t track. The third row shows the efficiency of the* `zVtx` *trigger element as a function of the transverse momentum of the highest p_t track. The dots represent the obtained efficiencies. They are fitted by a Fermi ($\epsilon_{DCR\phi}(p_{t,high})$, $\epsilon_{zVtx}(p_{t,high})$) and a 'double Fermi' ($\epsilon_{DCR\phi}(\theta_{high})$) function. The vertical dashed lines indicate the cuts applied to the p_t and θ of the track.*

Appendix B

Determination of the Total Efficiency

For the cross-section determination the data have to be corrected for several detector effects. There are two ways how to take the corrections into account:

1. The corrections are included in the so called total efficiency, ϵ_{tot}. Then the cross-section can be written as:

$$\sigma = \frac{N_{sig}}{L \quad \epsilon_{tot}} . \tag{B.1}$$

   The detector effects are usually obtained by means of Monte Carlo events. It is determined as the ratio of the number of reconstructed events, N^{rec}_{total}, which passed all analysis cuts and the number of generated events, N^{gen}_{total}:

$$\epsilon_{tot} = \frac{N^{rec}_{total}}{N^{gen}_{total}} . \tag{B.2}$$

   Due to the cuts applied on the energy of the cluster, transverse momentum of the track and the others, N^{rec}_{total} is a function of all the variables used for the cuts. All *uncorrelated* variables will in the following be called $x_1, x_2, ...x_n$ and therefore $N^{rec}_{total} = N^{rec}_{total}(x_1, x_2, ...x_n)$ and also $\epsilon_{tot} = \epsilon_{tot}(x_1, x_2, ...x_n)$.

2. The corrections, $\epsilon(x_1, x_2, ...x_n)$, are calculated as a function of uncorrelated variables $x_1, x_2, ...x_n$. Then the measured distribution $f^{DATA}_{measured}(x_1, x_2, ...x_n)$ is corrected by $\epsilon(x_1, x_2, ...x_n)$ via the following formula:

$$f^{DATA}_{true}(x_1, x_2, ...x_n) = \frac{f^{DATA}_{measured}(x_1, x_2, ...x_n)}{\epsilon(x_1, x_2, ...x_n)}. \tag{B.3}$$

   where $f^{DATA}_{true}(x_1, x_2, ...x_n)$ is the distribution of the true physics events. The number of the events entering the cross section is then the integral of the corrected spectrum $f^{DATA}_{true}(x_1, x_2, ...x_n)$:

$$N_{sig} = \int\int \ldots \int f^{DATA}_{true}(x_1, x_2, ...x_n) \quad dx_1 dx_2 \ldots dx_n \tag{B.4}$$

Then the cross section is calculated via:

$$\sigma = \frac{N_{sig}}{L} \tag{B.5}$$

One observes that the efficiencies calculated by both methods depend on the uncorrelated variables $x_1, x_2, ...x_n$ which are used in the analysis as cuts. If the generated distribution has the form of $f_{gen}(x_1, x_2, ...x_n)$ and after the reconstruction passing all analysis cuts $f_{(\texttt{rec+all analysis cuts})}(x_1, x_2, ...x_n)$, one can define the efficiency as a function of the variables $x_1, x_2, ...x_n$:

$$\epsilon(x_1, x_2, ...x_n) = \frac{f_{(\texttt{rec+all analysis cuts})}(x_1, x_2, ...x_n)}{f_{gen}(x_1, x_2, ...x_n)}, \tag{B.6}$$

which represents the efficiency in the point $[x_1, x_2, ...x_n]$ of the parameter-space.

The total efficiency can be written via $\epsilon(x_1, x_2, ...x_n)$ by the following expression:

$$\epsilon_{tot} = \frac{\int\int \dots \int f_{gen}(x_1, x_2, \dots, x_n) \quad \epsilon(x_1, x_2, \dots x_n) \quad dx_1 dx_2 \dots dx_n}{\int\int \dots \int f_{gen}(x_1, x_2, \dots, x_n) \quad dx_1 dx_2 \dots dx_n}, \tag{B.7}$$

where the function $f_{gen}(x_1, x_2, \dots, x_n)$ plays the role of a weight for $\epsilon(x_1, x_2, ...x_n)$. Here and in the following it will be assumed that the function $f_{gen}(x_1, x_2, \dots, x_n)$ is finite in the whole region $(x_1, x_2, ...x_n)$, $f_{gen}(x_1, x_2, \dots, x_n) > 0$ since there is no possibility to calculate an efficiency for $f = 0$ and negative values are forbidden due to unphysical meaning.

In the ideal case the efficiency is calculated from the data. But obviously in this analysis there is not enough statistics and the efficiency is obtained from the signal MC which describes the kinematics of the investigated precesses. Thereby one assumes that the simulation of the detector is reasonably well described. Then the efficiency obtained from MC and the efficiency determined from data are equal:

$$\epsilon^{MC}(x_1, x_2, \dots x_n) \approx \epsilon^{DATA}(x_1, x_2, \dots, x_n). \tag{B.8}$$

In the following it is discussed how to get the right corrections from both methods studying the properties of the integral in eq. (B.7).

B.1 Efficiency as a Function of one Variable x

For simplicity one assumes that the efficiency depends only on one variable,x , $\epsilon = \epsilon(x)$. The integral in B.7 becomes a simple one:

$$\epsilon^{MC}_{tot} = \frac{\int f_{gen}(x) \quad \epsilon^{MC}(x) \quad dx}{\int f_{gen}(x) \quad dx}. \tag{B.9}$$

Since $\epsilon^{MC}(x)$ is obtained from MC as a discrete function of bins, the integral changes to the sum over all bins, and the continuous function $f(x)$ to the discrete spectrum of the number of events N_i:

$$\epsilon^{MC}_{tot} = \frac{\sum_{i=1}^{m} N_i^{gen} \quad \epsilon_i^{MC}}{\sum_{i=1}^{m} N_i^{gen}}, \quad N_i^{gen} > 0, \tag{B.10}$$

where ϵ_i^{MC} is the efficiency determined in the `i-th` bin. Also the number of events N_i has to be finite in all m bins ($m > 0$), $N_i^{gen} > 0$.

From B.10 one sees the following consequences:

1. If N_i is a constant which means that the distribution N is flat, the total efficiency is the averaged efficiency $< \epsilon >$:

$$\epsilon_{tot}^{MC} = \frac{\sum_{i=1}^{m} N_i^{gen} \quad \epsilon_i^{MC}}{\sum_{i=1}^{m} N_i^{gen}} = \frac{\sum_{i=0}^{m} \epsilon_i}{m} =< \epsilon > \ . \tag{B.11}$$

   Remark: For the total cross-section the total efficiency may be used and therefore the constant can be employed. But for the correction of differential cross-section the bin-wise efficiency has to be applied!

2. If the efficiency is constant: $\epsilon_i = Const$, then the total efficiency is the same constant:

$$\epsilon_{tot}^{MC} = \frac{\sum_{i=1}^{m} N_i^{gen} \quad \epsilon_i^{MC}}{\sum_{i=1}^{m} N_i^{gen}} = Const \tag{B.12}$$

   In this case a constant efficiency can be used for the total and for the differential cross section.

3. In the following it is shown that if the measured data and reconstructed MC distributions agree on the bin level, $N_i^{DATA}(measured) = N_i^{MC}(rec)$, the total efficiency can be obtained as a ratio of $N_{total}^{MC}(rec)$ and $N_{total}^{MC}(gen)$ according to the expression B.2.

   In analogy to B.6 and using B.8 one can write down an equation for the efficiency ϵ obtained for the data and the MC in the `i-th` bin :

$$\epsilon_i = \frac{N_i^{DATA}(measured)}{N_i^{DATA}(true)} = \frac{N_i^{MC}(rec)}{N_i^{MC}(gen)} \tag{B.13}$$

   where $N_i^{DATA}(true)$ is the number of events in the `i-th` bin in the data sample which are expected to be true physics events. Since the data and MC distributions are assumed to be the same, $N_i^{DATA}(measured) = N_i^{MC}(rec)$, and using B.13 one gets an equality of DATA and MC distributions on the generator level $N_i^{DATA}(true) = N_i^{MC}(gen)$, too. Then for the total efficiency one gets:

$$\epsilon_{tot}^{DATA} = \frac{\sum_{i=0}^{m} N_i^{DATA}(true)\epsilon_i}{\sum_{i=0}^{m} N_i^{DATA}(true)} = \frac{\sum_{i=0}^{m} N_i^{DATA}(true)\frac{N_i^{MC}(rec)}{N_i^{MC}(gen)}}{\sum_{i=1}^{m} N_i^{MC}(gen)} = \frac{N_{total}^{MC}(rec)}{N_{total}^{MC}(gen)} \tag{B.14}$$

   The advantage of this method is that there is no necessity to determine the efficiency as a function $f(x)$ which is useful in the case of low (data or MC) statistics. Therefore if the MC does not describe the data distributions and the statistics in the data is very low, it is necessary to reweight the MC distributions by a weight $w_i = N_i^{data}(measured)/N_i^{MC}(rec)$ according to data distributions for all uncorrelated variables which are used for the analysis cuts.

4. Now it will be shown that the efficiency, obtained as a function of x (or bine-wise if one treat with the histograms), does not depend on the agreement/disagreement between data and MC distributions. In this case more practical way then to calculate the total efficiency by formula B.10 is to get N_{signal} using expressions B.3 and B.4.

   Assuming that the data and MC spectra do not agree in the bin i, $N_i^{DATA}(measured) \neq N_i^{MC}(rec)$ one obtains the factors w_i^{rec} and w_i^{gen}:

$$\mathtt{w_i^{rec}} = \frac{\mathtt{N_i^{DATA}(measured)}}{\mathtt{N_i^{MC}(rec)}} \qquad \mathtt{w_i^{gen}} = \frac{\mathtt{N_i^{DATA}(true)}}{\mathtt{N_i^{MC}(true)}} \tag{B.15}$$

   Going back to B.8 one gets:

$$w_i^{gen} = w_i^{rec}\,. \tag{B.16}$$

   Eq. (B.15) can be generalized to arbitrary weights w_i. Important is the equality between w_i^{gen} and w_i^{rec} which cancel in the efficiency calculations:

$$\epsilon_i = \frac{N_i^{MC}(rec)\, w_i^{rec}}{N_i^{MC}(gen)\, w_i^{gen}} = \frac{N_i^{MC}(rec)}{N_i^{MC}(gen)} \tag{B.17}$$

   Since it is fulfilled for any bin the efficiency does not depend on the agreement or disagreement of the data and MC distributions. The data are then corrected by the following:

$$N_{true}^{DATA} = \sum_{i=1}^{n} \frac{N_i^{DATA}(measured)}{\epsilon_i} \tag{B.18}$$

   The disadvantage of this method is the need for high statistics if the efficiency depends on several uncorrelated variables.

5. Going from the continuous function $\epsilon(x)$ to the discrete one, ϵ_i, the error due to finite bin size has to be taken into account in the systematics. Therefore it is convenient to choose the bin size reasonably small.

B.2 Efficiency as a Function of two Variables x and y

Now one assumes that the efficiency depends on two variables x and y, $\epsilon = \epsilon(x, y)$. If x and y are uncorrelated, factorization is possible:

$$\epsilon(x, y) = \epsilon(x)\,\epsilon(y). \tag{B.19}$$

In this case the efficiency is calculated in the two dimensional plane $x - y$. If the number of bins in the x distribution is m_1 and m_2 in the y distribution, the number of the bine-wise determined efficiencies is $m_1 \times m_2$:

$$\begin{pmatrix} \epsilon_{11} & \epsilon_{12} & \dots & \epsilon_{1\,m_2} \\ \epsilon_{21} & \epsilon_{22} & \dots & \epsilon_{2\,m_2} \\ \vdots & \vdots & \dots & \vdots \\ \epsilon_{m_1\,1} & \epsilon_{m_1\,2} & \dots & \epsilon_{m_1\,m_2} \end{pmatrix} \tag{B.20}$$

The consequences from the study of the one-dimensional case are also valid here.

B.3 Summary on the Efficiency Calculation

In the more general case one assumes `n` uncorrelated variables and the total number of bins is $m_1 \times m_2 \times \ldots m_n = m_{tot}$. From the shown examples one sees two possibilities how to correct the data:

1. The data are corrected by the total efficiency calculated as:

$$\epsilon_{tot}^{DATA} = \frac{N_{total}^{MC}(rec)}{N_{total}^{MC}(gen)} \tag{B.21}$$

   In this case an agreement between the MC and data distributions is required.

2. The efficiency is determined bin-wise according to:

$$\epsilon_{bin} = \frac{N_{bin}^{MC}(\texttt{rec} + \texttt{all analysis cuts})}{N_{bin}^{MC}(gen)} \tag{B.22}$$

   and the data are then corrected by:

$$N_{true}^{DATA} = \sum_{bin=1}^{m_{tot}} \frac{N_{bin}^{DATA}(measured)}{\epsilon_{bin}} \tag{B.23}$$

   entering the cross section calculation as:

$$\sigma = \frac{N_{true}^{DATA}}{L} . \tag{B.24}$$

   In this case no requirement on the agreement of the distributions between data and MC is employed. Only enough statistics for reasonable binning is necessary.

- General remark: It is assumed that the number of generated entries in all bin is always positive and the bins with no entries have to be excluded for efficiency determination.

Due to the very poor statistics for the measured signal the method two can not be employed and the first method (eq. B.21) had to be used. Therefore the Monte Carlo distributions had to be reweighted according to the data distributions which is shown in the next chapter.

Appendix C

Reweighting of the Monte Carlo Generator ToyGen

Due to a poor statistics of the data sample in this analysis it is not possible to determine the efficiency bine-wise, described in the second method in the previous chapter (Appendix B). Therefore the data has to be corrected by the total efficiency defined by relation B.2. It requires an agreement between the data and Monte Carlo for all 'uncorrelated' distributions on which the analysis cuts have been applied. The signal Monte Carlo model employed in this analysis is ToyGen. But since ToyGen with original parameters does not produce the particles in the region where the data are seen, the flux-factor and the kinematical constraints at the photon vertex have been changed. The procedure is described in chapter 3.1. ToyGen after this modifications is called ToyGenMod. Afterwards the regions are populated, but the distributions do not agree with the data. Therefore ToyGenMod will be reweighted which is described in the following for the $\eta - \rho^0$ and $\pi^0 - 2track$ sample, respectively.

C.0.1 Reweighting of ToyGenMod according to the Distributions of the $\eta - \rho^0$ Sample

The data and simulated distributions will be compared for the variables that are restricted by cuts in this analysis (summarized in table 4.13): cluster energy, hottest cluster energy, radius of the cluster, radial distance of the cluster, transverse momentum of the track, polar angle of the track and rapidities of the η and ρ^0 mesons, respectively. The comparison of all this distributions between the data and ToyGenMod is shown in fig. C.1 a) - h). The data are represented by the dots and ToyGenMod by the histogram. One observes reasonable agreement for the cluster properties and a small difference in the distribution of the rapidity of the η meson. On the other hand the spectra of the ρ^0 and track properties show significant differences. The polar angle of the tracks and the rapidity of the ρ^0 meson are flat in ToyGenMod while in the data they are peaked at the edge of the CJC-SpaCal acceptance. Due to this large discrepancy it was decided that the ToyGenMod distributions will be reweighted according to the rapidities of the η and ρ^0 mesons and the rapidity difference between them. Since the ρ^0 rapidity and the polar angle of the track are correlated, no additional weighting is applied. Since the efficiency strongly depends on the η and ρ^0 rapidities, also the rapidity difference has been taken into account in the weighting procedure.

Since it is assumed that the PythiaMod reasonably describes the background, the difference between the data and PythiaMod is expected to represent the signal. Therefore ToyGenMod has been weighted according to this difference. It is assumed that due to the flat distribution of the ρ^0 rapidity the weighting according to Y_η and Y_{ρ^0} is independent. The weighting procedure has been performed in the four following steps:

$$\begin{array}{ll} \text{1) rapidity of the } \eta \text{ meson:} & Y_\eta^{DATA} - Y_\eta^{PythiaMod} \\ \text{2) rapidity of the } \rho^0 \text{ meson:} & Y_{\rho^0}^{DATA} - Y_{\rho^0}^{PythiaMod} \\ \text{3) rapidity difference of the } \rho^0 \text{ and } \eta \text{ mesons:} & (Y_{\rho^0} - Y_\eta)^{DATA} - (Y_{\rho^0} - Y_\eta)^{PythiaMod} \\ \text{4) track-track mass} & m_{tt} \text{ according to the RBW} \end{array} \quad \text{(C.1)}$$

Due to the steps 1) – 3) of the reweighting procedure the $track - track$ mass distribution is affected. Therefore, to avoid higher statistical uncertainties the reweighting according to a P-wave relativistic Breit-Wigner function is performed at the end of the reweighting procedure. The reweighted ToyGenMod is called ToyGenModW.

After the complete weighting procedure the corresponding distributions are shown in fig. C.2. One observes reasonable agreement between the data and ToyGenModW in all the characteristic distributions.

C.0.2 Reweighting of ToyGenMod according to the Distributions of the $\pi^0 - 2\,$`track` Sample

The reweighting procedure of the ToyGen MC generator for the distributions generated for the $\pi^0 - 2\,$`tracks` sample has been performed analogously to the $\eta - \rho^0$ sample. The major difference are: a) the cross section is determined for the $\pi^0 - 2\,$`tracks` production with any origin which means that the ToyGen events were weighted according to the data and not the difference between data and background MC. b) Due to the absence of the ρ^0 signal the events were weighted according to the mass distribution measured in the data. The rest of the reweighting procedure remains the same:

$$\begin{array}{ll} \text{1) rapidity of the } \pi^0 \text{ meson:} & Y_{\pi^0}^{DATA} \\ \text{2) rapidity of the } 2\,\texttt{tracks} \text{ system:} & Y_{tt}^{DATA} \\ \text{3) rapidity difference of the } \rho^0 \text{ and } \eta\text{:} & (Y_{tt} - Y_{\pi^0})^{DATA} \\ \text{4) track-track mass } m_{tt} & \text{according to the } m_{tt}^{DATA} \end{array} \quad \text{(C.2)}$$

The respective distributions of data with comparison with simulation before and after weighting procedure are shown in figures C.3 and C.4. The ToyGenMod reweighted by the procedure is called ToyGenModW. However in the reweighting procedure the event at $Y_t \approx 0.25$ with very high weight which is responsible for high fluctuations in all distributions (i.e at $Y_{\pi^0} \approx -2.65$ in the Y_{π^0} distribution) have been 'downgraded' to the event with the weight one in order to avoid high uncertainties for the efficiency determination. Comparing the data and ToyGenModW distributions one observes reasonable agreement and the same tendency of both distributions.

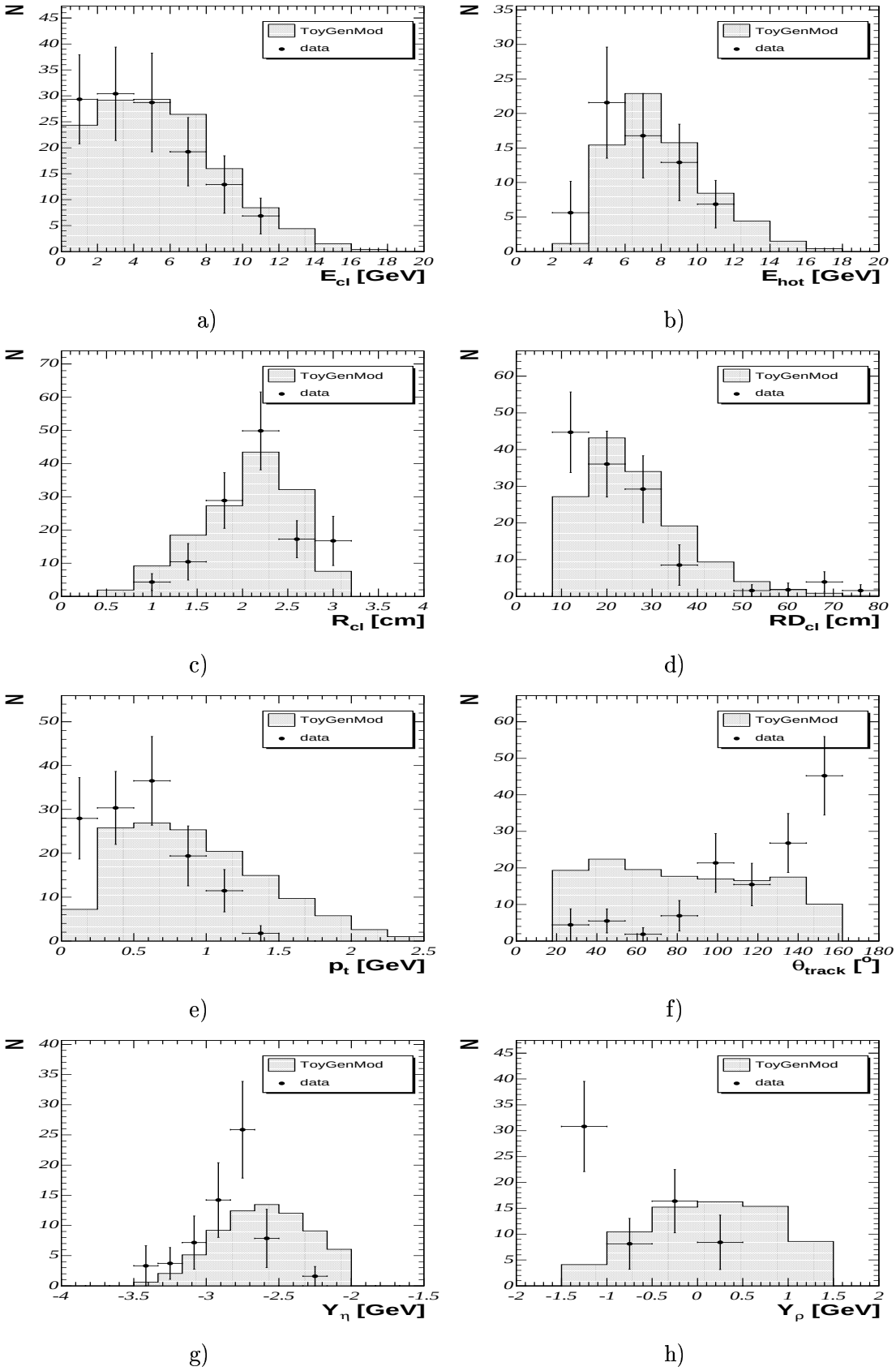

Figure C.1: *Characteristic distributions of ToyGenMod for $\eta - \rho^0$ sample: a) cluster energy, b) hottest cluster energy, c) radius of the cluster, d) radial distance of the cluster from the beam line, e) transverse momentum of the tracks, f) polar angle of the tracks and rapidities of the g) η and h) ρ^0 mesons, respectively.*

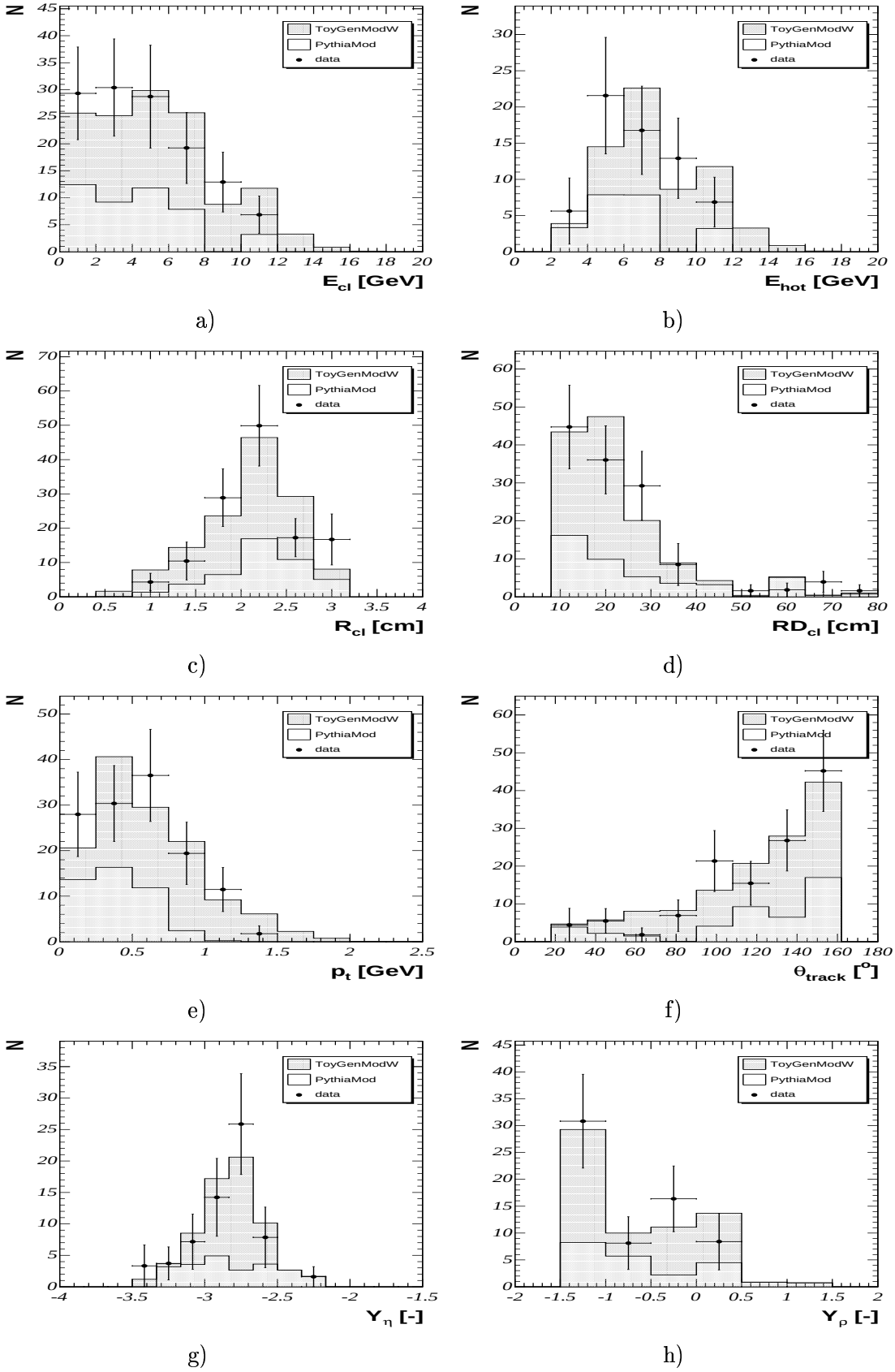

Figure C.2: *Characteristic distributions of ToyGenModW for $\eta - \rho^0$ sample: a) cluster energy, b) hottest cluster energy, c) radius of the cluster, d) radial distance of the cluster, e) transverse momentum of the track, f) polar angle of the track and rapidities of the g) η and h) ρ^0 mesons, respectively.*

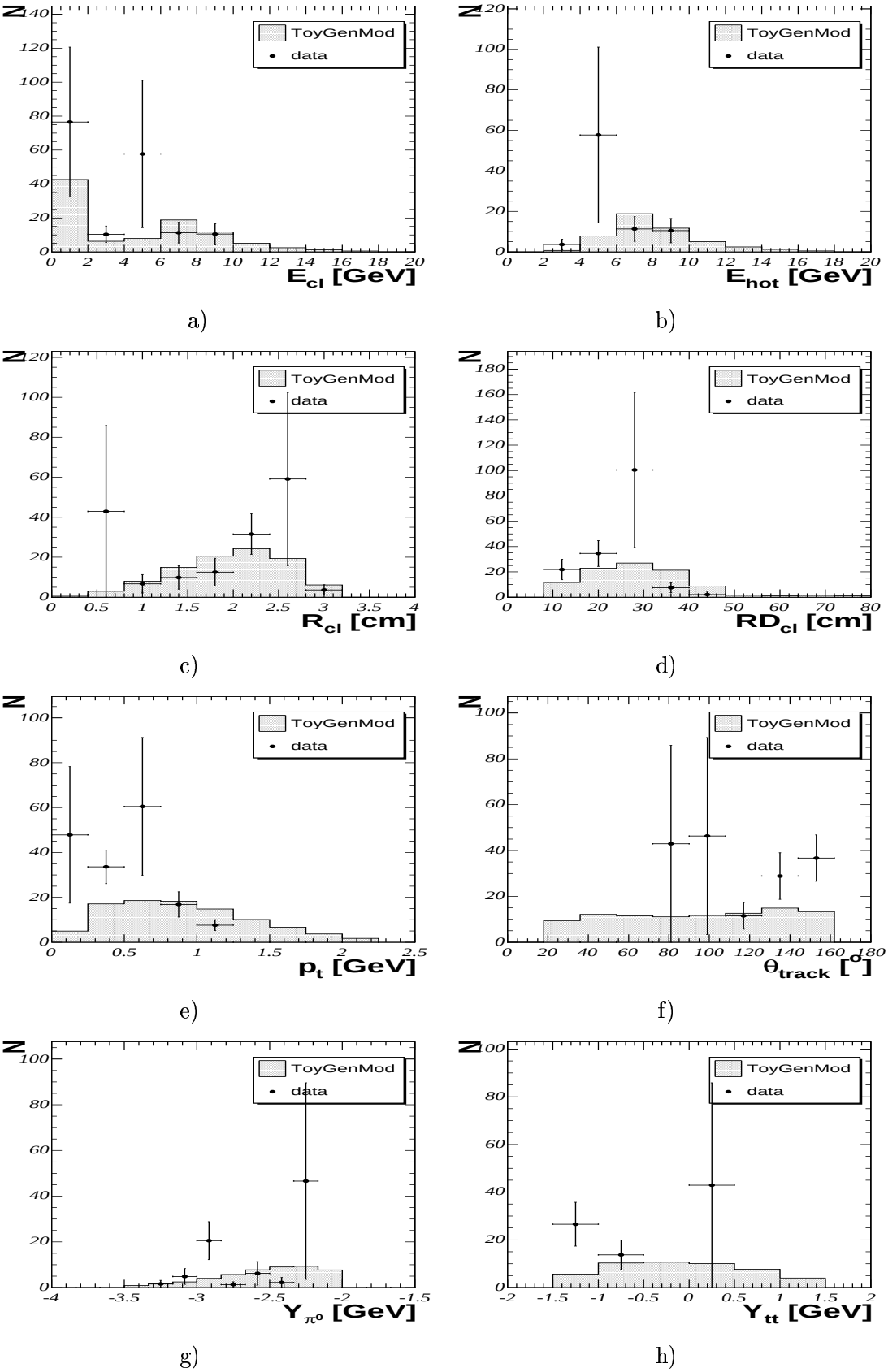

Figure C.3: *Characteristic distributions of ToyGenMod for $\pi^0 - 2track$ sample: a) cluster energy, b) hottest cluster energy, c) radius of the cluster, d) radial distance of the cluster from the beam line, e) transverse momentum of the tracks, f) polar angle of the tracks and rapidities of the g) π^0 meson and h) track − track system, respectively.*

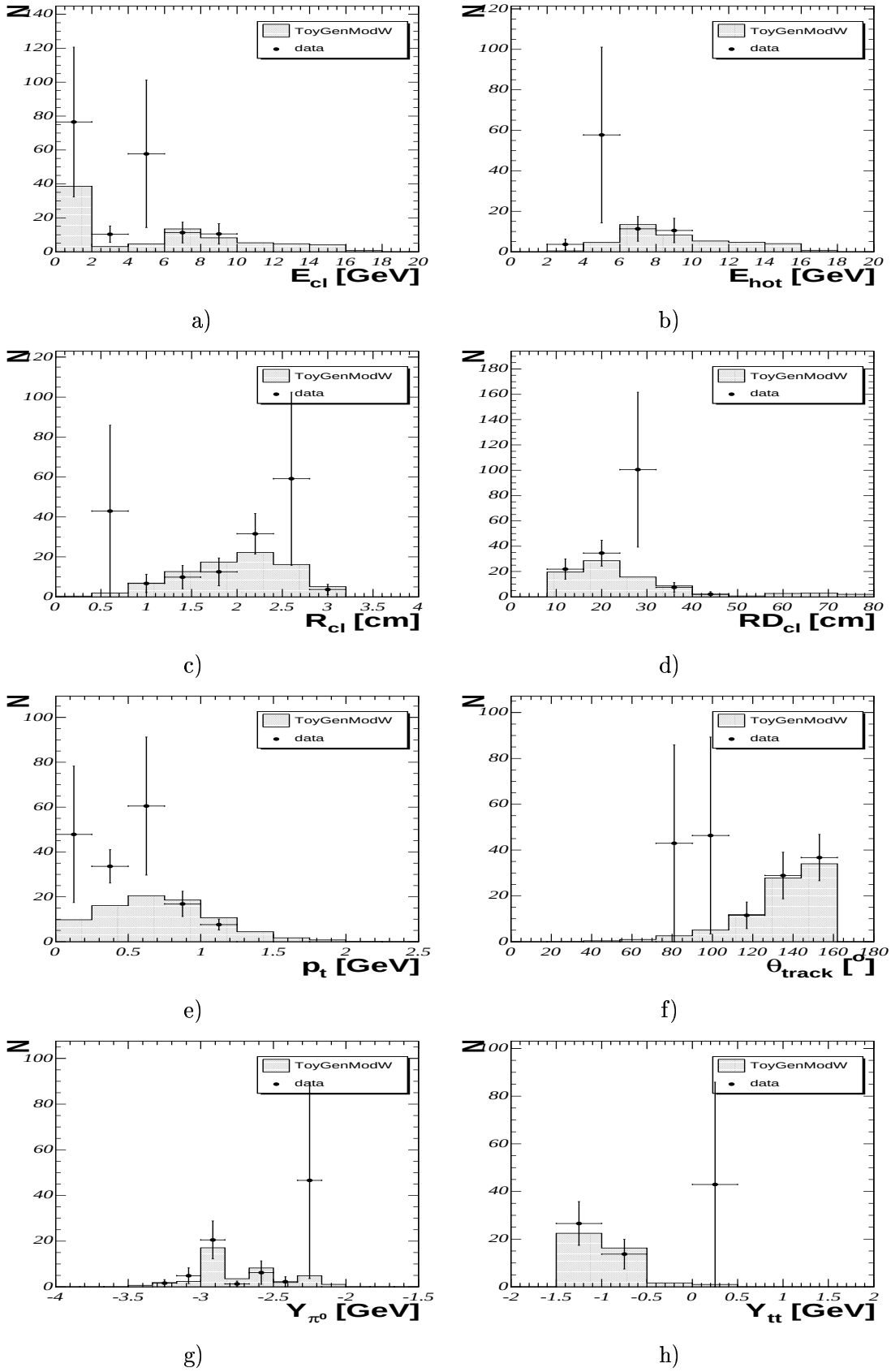

Figure C.4: *Characteristic distributions of ToyGenModW for $\pi^0 - 2track$ sample: a) cluster energy, b) hottest cluster energy, c) radius of the cluster, d) radial distance of the cluster, e) transverse momentum of the track, f) polar angle of the track and rapidities of the g) π^0 meson and h) track−track system, respectively.*

Bibliography

[1] H1 Collaboration, I.Abt et al., *Nucl. Instrum. Methods* **A386** (1997) 310-396.

[2] J. Bürger et al., *Nucl. Instrum. Methods* **A279** (1989) 217.

[3] S. Egli et al., *Nucl. Instrum. Methods* **A283** (1989) 487.

[4] K. Müller et al., *Nucl. Instrum. Methods* **A312** (1992) 457.

[5] S. Burke et al., RAL. **95-037**, DESY **95-132**.

[6] H1 Collaboration, *Technical Proposal to Upgrade the Backward Scattering Region of the H1 Detector*, DESY PRC 93/02.

[7] H1 Calorimeter Group, *Nucl. Instrum. Methods* **A336** (1993) 460.

[8] J. Ebert, *The H1-Tail Catcher Hardware and software Performance*, H1 Internal Note **95-448**.

[9] B. Andrieu et al. *Nucl. Instrum. Methods* **B350** (1994) 57.

[10] H1 Calorimeter Group, *Nucl. Instrum. Methods* **A386** (1997) 310.

[11] H1 SPACAL Group, *The H1 Lead/Scintillating-Fibre Calorimeter.* DESY **96-171.**

[12] H1 SPACAL Group, A. Stellberger et al., *Nucl. Instrum. Methods* **A374** (1996) 149.

[13] H. Cronström et al., *Nucl. Instrum. Methods* **A340** (1994) 304.

[14] H1 Collaboration, *Luminosity Measurement in the H1 Experiment at HERA* contributed paper pa17-026 to ICHEP 1996, Warsaw.

[15] H. Bethe, W. Heitler, Proc. Roy. Soc. **146** (1934) 83.

[16] H1 Collaboration, *Proposal for a Forward Proton Spectrometer for H1*, DESY **94-03**.

[17] M. Beck et al., *Nucl. Instrum. Methods* **A355** (1995) 351.

[18] J. C. Bizot et al., *Status of Simulation for a Topological Level 2 Trigger* H1 Internal note **92-212**.
J. C. Bizot et al., *Strategy Studies for the H1 Topological L2-Trigger (L2TT)* H1 Internal note **97-508**.

[19] J. H. Köhne et al., *Realization of a Second Level Neural Network Trigger for the H1 Experiment at HERA* H1 Internal note **97-509**.

[20] D. Hoffmann, F. Tomasz, *Time measurements and Calibration with the H1 Spaghetti Calorimeter*, H1 Internal Note (in preparation).

[21] J. Janoth et al., *Nucl. Instrum. Methods* **A350** (1994) 221-225.

[22] E. Eisenhandler et al,. IEEE Transactions on Nuclear Science **42** (1995) 688.

[23] E. Eisenhandler et al,. *H1 SPACAL TDC System description*, (March 1994) Internal Project Document, RAL Electronics Division.

[24] V. Boudry et al,. *The Inclusive Electron Trigger for the SPACAL: Design and CERN test results*, H1 Internal Note H1-03/95-430.

[25] S. Spielmann, *H1 SPACAL TDC System description*, PhD Thesis, Ecole Polytechnique, Paris, France (1996), (H1 Thesis H1T-0796-029).

[26] A. Stellberg et al., *Nucl. Instrum. Methods* **A515** (2003) 543-562.

[27] see e.g. references in: C. Grupen, *Teilchendetectoren*, (1993) Mannheim; Leipzig; Wien; Zürich: BI-Wiss.-Verl.

[28] A. Donnachie, H.G. Dosch, P. V. Landshoff and O. Nachtmann, *Pomeron Physics and QCD* (2002), Published by the press Syndicate of the University of Cambridge.

[29] P. Bruni, A. Edin and G. Ingelmann, Pompyt version 2.6 - A Monte Carlo to Simulate Diffractive Hard Scattering Processes September 12, (1996) ISSN 0418-9833.

[30] T.Berndt, "ToyGen V 2.0", (2003) unpublished.

[31] H. Jung, *Hard Diffractive Scattering in High Energy ep Collisions and the Monte Carlo Generator RAPGAP*, (December 1993, DESY 93-182).

[32] T. Sjöstrand, *PYTHIA 5.7 and JETSET 7.4 Physics and Manual*, (August 1995, hep-ph/9508391).

[33] T. Sjöstrand, *Comp. Phys. Comm.* **39** (1986) 347.

[34] T. Sjöstrand *Comp. Phys. Comm.* **82** (1994) 347.

[35] T. Sjöstrand and M. Bengtsson, *Comp. Phys. Comm.* **43** (1987) 367.

[36] Ch. Friberg and T. Sjöstrand. *JHEP 0009:100 (*`hep-ph/0007314`*)*, 2000.

[37] D. E. Groom et al. *Eur. Phys. J.* **C15** (2000) 1.

[38] G. A. Schuler and T. Sjöstrand. *Nucl. Phys.* **B 407** (1993) 539.

[39] T. Nicholls et al. *Nucl. Instrum. Methods* **B374** (1996) 149.

[40] R. D. Apphun et al. *Nucl. Instrum. Methods* **B382** (1996) 395.

[41] R. D. Apphun et al. *Nucl. Instrum. Methods* **B386** (1997) 397.

[42] T. Sjöstrand. *Computer Physics Commun.* **82** (1994) 74.

[43] L.D.Landau and I.Ya. Pomerunchuk, *Zh. Eksp. Teor. Fiz.* **24**, 505.

[44] E.Feinberg and I.Ya. Pomerunchuk, *Nuovo Cim. Suppl.* **3**, 652.

[45] J.D.Bjorken, Phys. Rev. **D47**, (1993) 101.

[46] A. Donnachie and P. V. Landshoff. *Nucl. Phys.* **B231** (1984) 189.

[47] A. Donnachie and P. V. Landshoff. *Phys. Lett.* **B296** (1992) 227.

[48] A. Donnachie and P. V. Landshoff. *Phys. Lett.* **B437** (1998) 408.

[49] A. Donnachie et al., private communication: Meeting in Heidelberg, 23th of February 2005.

[50] see e.g. references in: P.D.B. Collins, *An Introduction to Regge Theory and High Energy Physics* (Cambridge University Press, Cambridge 1977).

[51] TOTEM Collaboration Letter of Intent, CERN/LHCC 97-49

[52] G.F.P.Chew and S.C.Frautschi, *Phys. Rev. Lett.* **7** (1961) 394.

[53] V.N.Gribov, *Zh. Eksp. Teor. Fiz.* **41**, 667 [transl. Sov. Phys. JETP **14** (1962) 478].

[54] V.N.Gribov, *Soviet Journal of Nuclear Physics 5* (1967) 138.

[55] D.R.O. Morrison, *Phys. Rev.* 165 (1968) 1699.

[56] K. K. Seth, *Modern Phys. Lett.* **A 18** (2003), 330-339.

[57] S. Abatzis et al., *Phys. Lett.* **B324** (1994) 509.

[58] S. Nusinov. *Phys. Lett.* **34** (1975) 1286.

[59] A. Donnachie and P. V. Landshoff. *Nucl. Phys.* **B311** (1989) 509.

[60] J. Cudell. *Nucl. Phys.* **B336** (1990) 1.

[61] D. Joynson et al., *Nuovo Cimento* **30A** B (1975) 345.

[62] V.N.Gribov et al., *Sov. J. Nucl. Phys.* **12** (1971) 699.

[63] A. Levy, *Low-x physics at HERA* DESY preprint DESY-97-013 (1997).

[64] D. Jansen, *The H1 Reconstruction Program.* `http://www-h1.desy.de/h1/www/general/home/intra_home.html` .

[65] The H1 SpaCal Group. *DESY-report* **95-250**, 1995.

[66] V. Boudry et al. *H1-internal report* **H1-0395-430**, 1995.

[67] D. Schmidt, *Diffraktive Photoproduktion von Charmonium im H1-Detector bei HERA*, PhD thesis, Universität Hamburg, 2001.

[68] D. Schildknecht and H. Spiesberger. `hep-ph/9707447`, 1997.

[69] Ch. Wissing et al. *The H1 ToF system in 1996 and 1997* H1 internal note **H1-01/98-533**, 1998.

[70] J. Meyer, *Guide to the simulation program H1SIM,.* H1 internal software manual (1991).

[71] *GEANT - Detector description and Simulation Tool,.* CERN Program Library Long Writeup W5013 Detector; R. Brun, R. Hagelberg, M. Hansroul and J.C Lassalle, CERN-DD-78-2-REV.

[72] L. West *How to use the Heavy Flavour Working Group Track, Muon and Electron Selection Code, H1,*. H1 internal software manual (2000).

[73] E. Elsen, *The H1 Trigger and Data Acquisition.* Proceedings of the International Symposium on Electronic Instrumentation in Physics, Dubna, May 1991.

[74] E. Elsen, *Experience with the First Level Trigger of H1.* Proceedings of the IEEE Nuclear Science Symposium, Norfolk, Virginia, July 1994.

[75] S. Egli et al., *Calculating event weights in case of downscaling on trigger levels 1-4*, H1 Internal Note, H1-04/97-517.

[76] T. Regge, *Nuovo Climento* **14** (1959) 951.

[77] T. Regge, *Nuovo Climento* **18** (1960) 947.

[78] V. N. Gribov, *Zh. Eksp. Teor. Fiz.* **41**, 667, (1961), [transl. Sov. Phys. JETP **14** (1962) 478].

[79] H1 Collaboration, T. Ahmed et al., *Phys. Lett.* **B299** (1993) 372.

[80] H1 Collaboration, S. Aid et al., *Nucl. Phys.* **B470** (1995) 471,

[81] Ch. Brunne, *Bestimmung der Protonstrukturfunktion* $F_2(x_{bj}, Q^2)$ PhD thesis, Universität Heidelberg, 1996.

[82] K. Krüger, *Photoproduction of J/Psi Mesons at Medium and Low Elasticities at HERA* PhD thesis, Universität Hamburg, 2001.

[83] A.M.Cooper-Sarkar, R.C. Devenish and A.De Roeck, *Int. J. Mod. Phys.* **13** (1998) 3385, DESY-97-226, hep-ph/9712301.

[84] G.A.Schuler, T. Sjöstrand, *Phys. Lett.* **B300** (1993) 169.

[85] H.-C. Schultz-Coulon et al., IEEE Trans. Nucl. Sci. **46** (1999) 915.

[86] S. Egli et al., H1 internal note (1997) 517.

[87] B. Heinemann, PhD thesis, University of Hamburg,1999 DESY-THESIS-99-046.

[88] C. Wissing, Diploma Thesis, University of Dortmund, 1998

[89] M. Paterno, *Calculating Efficiencies and Their Uncertainties*, FERMILAB-TM-2286-CD, May 22, 2004.

[90] see e.g. references in: V. Barone, E. Predazzi, *High-Energy Particle Diffraction*, Springer-Verlag Berlin Heidelberg 2002.

[91] R. Feynmann, *Phys. Rev. Lett.* **23** (1969) 1415
J. Bjorken, E. Paschos, *Phys. Rev.* **185** (1969) 1975.

[92] H1PHAN routine written by Sergey Levonian,
`http://www-h1.desy.de/~levonian/QPETAC.html` .

[93] home page of luminosity system
`http://www-h1.desy.de/h1det/lumi/summary_tables.html` .

[94] home page of luminosity system
`http://www-h1.desy.de/h1/www/h1det/lumi/doc/` .

[95] M. Swart. *Mass Spectroscopy of Neutral Mesons in the Photon Hemisphere at HERA.* PhD thesis, Universität Heidelberg, 2000. HD-KIP-00-17.

[96] T. Berndt, *Exclusive Pomeron- and Odderon Induced Photoproduction of ω and f_2 Mesons at HERA.* PhD thesis, Universität Heidelberg, 2002. HD-KIP-001-22.

[97] V. Lendermann, *Measurement of the QED Compton Scattering Cross Section with with the H1 Detector at HERA.* PhD thesis, Universität Dortmund, 2001. DESY-THESIS-2001-004.

[98] T. Ch. Nicholls *A Measurement of the Diffractive Proton Structure Function at HERA.* PhD thesis, The University of Birmingham, 1997.

[99] Ch. von Cube. *Exklusive Photoproduktion der Mesonen b_1 und a_2 bei HERA.* Diplomarbeit, Universität Heidelberg, 2001.

[100] F. Bigiel *Search for Exclusive Photoproduction of $\omega - \phi$ Vector meson Pairs at HERA.* Diplomarbeit, Universität Heidelberg, 2004, HD-KIP 04-13.

[101] H1 Collaboration *Search for Odderon-Induced contributions to exclusive π^0 photproduction at HERA.* Phys. Let. **B544** (2002) 35-43.

[102] J. Engelen, M. Klein, and R. Rückel. *Reconstruction of (x, Q^2) and extraction of of structure functions in neutral current scattering at HERA.* In *Physics at HERA*, volume 1, pages 23–43, 1991.

[103] H. Abramowicz and A. Caldwell, *HERA Collider Physics.* DESY preprint DESY-98-192 (1998).

[104] A. Kirk, *Resonance production in central pp colisions at the CERN Omega Spectrometer* hep-ph/0008053

Acknowledgment

Finally I would like to thank all the people who supported me during my studies as a Ph.D. student. I am especially grateful to:

Prof. Karlheinz Meier for the very interesting topic he proposed and many stimulating and encouraging discussions.

Prof. Hans-Christian Schultz-Coulon for supervising me kindly and carefully during the last year of my work.

Prof. Ulrich Uwer for being so kind to take over the task to referee this thesis.

Tommy Berndt for developing and explaining the Monte Carlo program ToyGen. Katja Krüger and Jürgen Stiewe for their endless supply of critical thoughts and many ideas from which I really learned a lot. I would like to thank them also for the invaluable patience during reading and commenting this theses.

Prof. Nachtmann for useful discussions. My thanks also belong to Victor Lendermann for his many helpful ideas.

The convenors of the H1 diffractive group at DESY in Hamburg, namely Hannes Jung, Laurent Favart and Xavier Janssen for their helpful suggestions.

Dirk Hofmann and Prof. Etienne Barrelet for their support during the two years I spent working on the SpaCal timing. Of course, I can't forget also Marián Repašan.

Kamil Sedlák for his support and help during my first months at DESY, Christoph von Cube for the nice time spent together in Heidelberg and also Karel Saksl from whom I learned about diffraction from another point of view.

František Kriváň who gave me the best introduction to the SpaCal electronics and Florian Keil for the introduction to the SpaCal CAM system.

All the PhD- and Diploma students of the H1- and the ATLAS groups with whom I had the pleasure to have a nice time.

All friends in Hamburg for four unforgettable years in Hamburg, my parents for everything, and finally also to my Evul'a for her encouragement throughout my time as a student and for tolerating my antisocial behavior during writing my thesis.